



The
University
Of
Sheffield.

Study of the Microstructure and Oxidation of Alloys of the Al-Hf-Nb-Si-Ti System

by:

Mohammad Hossein Ghadyani

Supervisor:

Professor Panos Tsakirooulos

**A thesis submitted in fulfilment of the
degree of Doctor of Philosophy**

**In the
Department of Materials Science and Engineering
University of Sheffield**

April 2017

Abstract: This research aimed to find out how the synergy of Al, Hf and Ti affects phase stability and oxidation in Nb-silicide based alloys, in particular the stability of specific type(s) of silicide(s), of the Nb_{ss}, whether other phase(s) is (are) stabilised, and whether α -Al₂O₃ could form and pest oxidation could be suppressed. The alloys MG1, MG2, MG5 and MG6, respectively with nominal compositions (at%) Nb-22Si-24Ti-5Al-5Hf, Nb-22Si-24Ti-30Al-5Hf, Nb-25Si-23Ti-30Al-4Hf and Nb-23Si-23Ti-38Al-4Hf were studied in the as cast (AC) and heat treated (HT) conditions and after isothermal oxidation at 800 °C and 1200 °C for 100 h. The alloys were produced using arc melting and were heat treated in an Ar atmosphere. Characterisation was carried out by DSC, TG, XRD (Bragg-Brentano, GXR), SEM and EDS.

In MG1-AC there was macrosegregation of Si and Ti and the phases were the Nb_{ss}, β Nb₅Si₃ and γ Nb₅Si₃ with Nb_{ss} + β Nb₅Si₃ eutectic, and separate Ti and Hf rich Nb₅Si₃ and normal Nb₅Si₃ grains. In MG1-HT (1300 °C/100 h) the γ Nb₅Si₃ was stable. At 800 °C MG1 did not pest, exhibited parabolic oxidation and the thick layered scale did not spall-off. Scale spallation occurred at 1200 °C. The Nb_{ss} and Nb₅Si₃ were contaminated by oxygen, the former more severely than the latter and the contamination of both phases became less severe with increasing depth below the scale. At both temperatures the oxides Nb₂O₅, TiO₂, SiO₂ and HfO₂ and Ti niobates formed in the scale but not Al niobate.

In MG2-AC there was macrosegregation of Al, Hf, Si and Ti, the ingot was severely cracked and the microstructure consisted of the β Nb₅Si₃ and γ Nb₅Si₃, Al₃TM, TiAl, and Ti₂Al₅ and metastable TM_{3.7}Al₃Si and TM_{2.35}Al_{1.65}Si. There was strong partitioning of Hf and Ti in Nb₅Si₃. In MG2-HT (1300 °C/100 h) the β Nb₅Si₃ and γ Nb₅Si₃, Al₃TM, TiAl, and Ti₂Al₅ were present. The Nb_{ss} was not stable in MG2 but the γ Nb₅Si₃ was. MG2 did not pest at 800 °C, at 1200 °C formed a thin α -Al₂O₃ scale that did not spall off and at both temperatures followed parabolic oxidation kinetics. The contamination of Nb₅Si₃ was more severe than TiAl and Al₃TM. At both temperatures Nb₂O₅, TiO₂, SiO₂, HfO₂, TiAl₂O₅ and Ti niobates were in the scale plus α -Al₂O₃ at 1200 °C but not Al niobate.

The MG5-AC had macrosegregation of Al, Si and Ti, was very brittle and its microstructure consisted of γ Nb₅Si₃, Ti₅Si₄, TiSi and Al₃TM. The MG5-HT at 800 °C and 1200 °C consisted of the γ Nb₅Si₃, TiAl, Al₃TM, Ti₅Si₄ and TiSi. The 5-4 silicide formed a fibrous structure growing towards Al₃TM. The Nb_{ss} was not stable in MG5. The MG5 did not pest at 800 °C, did not oxidise catastrophically at 1200 °C, in both temperatures it formed a thin and adherent alumina scale which did not spall off at 1200 °C. The MG5 oxidised at 800 °C had the same phases as MG5-HT800, plus Ti₂Al₅, Ti(Al,Si)₂, TM₂Si_{1.5}Al and TM₈Al₁₁Si₃ and the oxides were Ti niobates, TiO₂, SiO₂, Nb₂O₅, TiAl₂O₅ and HfO₂ but no Al niobate. The MG5 oxidised at 1200 °C had the same phases as MG5-HT1200 plus hexagonal (Ti,Nb)₅Si₃, Ti₂Al₅ and TM₂Si_{1.5}Al and the oxides were Ti niobates, TiO₂, Nb₂O₅ and HfO₂, and SiO₂, α -Al₂O₃, TiAl₂O₅ and TiO and no Al niobate. The contamination of the 5-4 silicide was less severe than the Ti₂Al₅ aluminide.

The MG6-AC had macrosegregation of Al, Si and Ti and consisted of γ Nb₅Si₃, Ti₅Si₄, Al₃TM and TiAl. The MG6-HT800 consisted of γ Nb₅Si₃, TiAl, Al₃TM, Ti₅Si₄ and TiSi and the TM₉Si₇Al₄. The MG6-HT1200 consisted of γ Nb₅Si₃, TiAl, Al₃TM, Ti₅Si₄ and TiSi and Ti₃Al. The Nb_{ss} was not stable. There was localised melting where the Ti₅Si₄, Al₃Ti, TiSi and TiAl were present. The MG6 did not pest at 800 °C, but oxidised linearly, and at 1200 °C followed parabolic oxidation. At both temperatures a thin and adherent alumina scale formed, which did not spall off at 1200 °C. The oxidation of MG6 at 1200 °C was better than the Ni superalloy CMSX-4. At 800 °C the scale consisted of Ti niobates, TiO₂, SiO₂, Nb₂O₅, TiAl₂O₅ and HfO₂. At 1200 °C the same oxides were present in the scale plus α -Al₂O₃. The latter was thick and continuous even around corners and did not spall off during handling of the oxidised specimen. The oxidised microstructure at 800 °C consisted of γ Nb₅Si₃, Ti₅Si₄, TiSi, Al₃TM, TiAl and TiAl₂. The silicides and aluminides below the scale were contaminated, with worse contamination of Nb₅Si₃ compared with Ti₅Si₄. The oxidised microstructure at 1200 °C consisted of γ Nb₅Si₃, (Ti,Nb)₅Si₃, Ti₅Si₄, Al₃TM, TM_{2.7}AlSi_{0.3} and TiAl₂.

Acknowledgments

There is no shadow of doubt on the fact that achievement cannot be acquired without the help of others directly or indirectly. It has been stated that the meaning of acknowledgment can reside in its place once it has been done verbally, wholeheartedly and concretely. There are numerous people to whom I am greatly beholden. First of all, I must thank the almighty God for his grace without which it would have all impossible.

I am sincerely grateful to my supervisor, *Panos Tsakirooulos*, who accepted me as a PhD student and exhausted all possible methods to guide me through learning, researching, and my doctoral dissertation. Throughout the more than five years in which I worked with him he has always been an example of an archetypal researcher and erudite professor in my mind, whenever I jolt my memory.

I must express my gratitude to my Family: my father, *Ali*, my mother, *Parvin*, and my sister, *Maryam*, to whom I am relentlessly and inexorably indebted. Their supports have been ubiquitous and the river of their love and passion has been interminably vociferous and clamorous. Not a day goes by that I regret for not being able to reciprocate, and this is one of the existential equations which could be added to the “unbearable lightness of being”.

All my friends have been supportive and sympathetic. However, I should like to name two of them, *Karim and Sajjad*, whose supports were inexhaustible toward the PhD chapter of my life. They selflessly helped me when I was inundated with the PhD and I profoundly hope that I shall be able to reciprocate in their other life’s chapters.

Table of contents

Chapter 1: Literature review	1
1.1 The need for high temperature materials	1
1.2 Aims and Objectives	4
1.3 Niobium silicide based in-situ composites.....	5
1.4 Phase equilibria relevant to this work.....	8
1.4.1 The Nb-Si binary system	8
1.4.2 The Nb-Si-Ti ternary system	10
1.4.3 The Nb-Si-Hf ternary system.....	15
1.4.4 The Nb-Si-Al ternary system.....	18
1.5 Oxidation.....	20
1.5.1 Oxidation of Nb	21
1.5.2 Pest oxidation.....	25
1.5.3 Oxidation of Nb-silicide in situ composites.....	27
1.5.3.1 Role of alloying additions.....	30
1.5.3.2 Scale formers	35
1.6 Mechanical properties	38
1.6.1 Fracture toughness	39
1.6.1.1 Fracture mechanism	40
1.6.1.2 The effect of alloying additions on fracture toughness.....	40
1.6.2 Intermediate and high temperature strength	45
1.6.2.1 Creep resistance	47
Chapter 2: Experimental procedures	53

2.1 Selection of alloys	53
2.2 Alloy making.....	55
2.3 Heat treatment	56
2.4 Specimen preparation	56
2.4.1 Specimens for SEM and EDS study	56
2.4.2 Specimens for XRD study	57
2.4.3 Specimens for TGA study.....	57
2.5 Alloy characterization	57
2.5.1 X-ray diffraction	57
2.5.2 Scanning electron microscopy	58
2.5.3 Energy dispersive X-ray spectrometry.....	58
2.5.4 Differential scanning calorimetry	59
2.5.5 Thermo-gravimetric analysis	59
Chapter 3: The alloy Nb-24Ti-22Si-5Al-5Hf.....	61
3.1 Alloy Nb-24Ti-22Si-5Al-5Hf (MG1).....	61
3.1.1 As cast.....	61
3.1.2 Heat treated	68
3.1.3 Oxidation behaviour.....	74
3.1.3.1 Isothermal oxidation at 800 °C for 100 h.....	74
3.1.3.2 Isothermal oxidation at 1200 °C for 100 h.....	76
3.1.3.3 Microstructure of oxidised MG1	78
3.1.4 Discussion.....	84
3.1.5 Summary	95

Chapter 4: The alloy Nb-24 Ti-22Si-30Al-5Hf..... 97

4.1	Alloy Nb-24Ti-22Si-30Al-5Hf (MG2)	97
4.1.1	As cast.....	97
4.1.2	Heat treated	106
4.1.3	Oxidation behaviour.....	115
4.1.3.1	Isothermal oxidation using TGA	116
4.1.4	Discussion	125
4.1.5	Summary	136

Chapter 5: The alloy Nb-23Ti-25Si-30Al-4Hf..... 139

5.1	Alloy Nb-23Ti-25Si-30Al-4Hf (MG5)	139
5.1.1	As cast.....	139
5.1.2	Heat treated	145
5.1.2.1	Heat treatment at 800 °C	145
5.1.2.2	Heat treatment at 1200 °C.....	149
5.1.3	Isothermal oxidation	153
5.1.3.1	Oxidation at 800 °C.....	153
5.1.3.2	Oxidation at 1200 °C.....	154
5.1.4	Discussion	168
5.1.5	Summary	187

Chapter 6: The alloy Nb-23Ti-23Si-38Al-5Hf..... 189

6.1	Alloy Nb-23Ti-23Si-38Al-5Hf (MG6)	189
6.1.1	As cast.....	189
6.1.2	Heat treated	194

6.1.2.1 Heat treated at 800 °C	195
6.1.2.2 Heat treated at 1200 °C	199
6.1.3 Oxidation behaviour.....	204
6.1.3.1 Thermogravimetry	204
6.1.3.1.1 Isothermal oxidation at 800 °C for 100 h.....	204
6.1.3.1.2 Isothermal oxidation at 1200 °C for 100 h.....	206
6.1.3.2 Muffle furnace oxidation experiments.....	208
6.1.3.2.1 Isothermal oxidation at 800 °C	208
6.1.3.2.2 Isothermal oxidation at 1200 °C	213
6.1.4 Discussion.....	220
6.1.5 Summary.....	236

Chapter 7: Conclusions and Suggestions for future work 239

7.1 Conclusions	239
7.2 Suggestions for future work.....	244

References..... 246

Chapter 1: Literature review

1.1 The need for high temperature materials

The gas turbine, as used in aero engines and land-based power generators, is unequivocally the main field of application of high temperature structural materials. It is 30 years since Ni based superalloys have gained a monopoly in aerospace industries: they have become an integral part of the turbofan aeroengines. It is worth mentioning that there has not been any other class of structural metallic materials able to bequeath the same mechanical and engineering properties while operating at high service temperature. The operating temperature of high-pressure turbine blades has been increased by 125 °C owing to developments in casting technology (directional solidification and single crystal casting) and the composition of Ni base super alloys (Jackson et al, 2003 and Bewlay and Jackson, 2003).

The temperature of the metal surface at the hottest section of the advanced gas turbine engine airfoils reaches approximately 1150 °C, which is considered the limit for employing Ni based superalloys (Jackson et al, 2003). However, the thermal barrier coating (TBC) surface temperature can be higher than 1150 °C as it insulates the airfoils from the hot gases (Jackson et al, 1996).

New classes of materials are needed to overcome the barrier imposed by Ni based superalloys, whereby the turbine inlet temperature (TIT) can be increased. The need to increase the efficiency and performance of the aeroengine is the main reason for seeking new materials to survive at temperatures beyond the limit of Ni based

superalloys irrespective of their brilliant structural properties particularly at elevated temperatures (Perepezko, 2009).

Basically, similar to all heat engines, an increase in working fluid temperature results in an increase in jet engine performance (Taub et al, 1989). Hence, increasing the combustion temperature of the jet engine enhances the efficiency. Thermal efficiency is increased by raising the turbine inlet temperature or rotor inlet temperature in the aero engine, which dictates the operating temperature of the engine. (Perepezko, 2009 and Taub et al, 1989). In view of the fact that some of the work performed in the compressor for combustion must be consumed to cool the air, eliminating this step is of particular importance as it saves the mechanical energy produced in the compressor, which is lost to cooling (Perepezko, 2009 and Jackson et al, 2003). Besides, the centrifugal stress on the rotor can be considerably reduced by decreasing the airfoil mass, which results in an increase in thrust to weight ratio performance (Jackson et al, 2003 and Balsone et al, 2001).

Further development of alloy composition of Ni based superalloys beyond the fourth generation single crystal alloys for operating above 1150 °C seems to be impossible since they melt at approximately 1350 °C (Jackson et al, 1996). There are two main hindrances in increasing the temperature capability of Ni based superalloys. Firstly, incipient melting can occur at 1270 °C as a result of chemical segregation in the superalloys. This mostly depends on heat treatment and solidification processes by which supperalloy has formed (Jackson et al, 2003). Moreover, the interaction zone between metal surface and thermal barrier coating can melt at 1250°C (Jackson et al, 2003 and Bewlay and Jackson, 2003). Thus it could be deduced from the above

description that there are some inherent obstacles that make it very difficult if not impossible to increase further the operating temperature of Ni based superalloys.

Paradoxically, inefficiency has been increased as a result of the advancements in raising the service temperature of Ni based superalloys employed in state-of-the art jet engines most certainly due to the fact that extra flow in the compressor must be provided for cooling air. It has been pointed out that operating without auxiliary cooling air at 1350 °C can increase the performance by 50% (Perepezko 2009) see figure 1. Hence, it signifies that eliminating cooling air, meaning employing the ultra-high temperature class of materials able to surpass the temperature limit imposed by Ni based superalloys, would improve the performance by approximately 50%.

Essentially, materials must possess some fundamental characteristics in order for them to be able to be employed in high temperature sections of the jet engine and those properties encompass: (1) good creep strength, (2) excellent oxidation resistance, (3) low density, (4) high elastic modulus, (5) acceptable fracture toughness (Anton et al, 1989).

High temperature materials include intermetallic compounds, refractory metal based intermetallic materials and composite materials (Jackson et al, 1996 and Subramanian et al, 1996,1997).Among ultra-high temperature refractory metal intermetallic composites, those based on Mo and Nb have attracted attention owing to their promising characteristics in high temperature applications (Bewlay and Jackson, 2003). Both of them have been researched by metallurgists. Nb silicide in-situ composite materials offer better high temperature properties than the Mo based ones (Balsone et

al, 2001). In accordance with the prerequisite properties for high temperature applications, Nb silicide in-situ composites are the most favorable and promising alternatives to Ni based superalloys. First, compared with Ni and Mo, Nb has lower density, which is very important for aerospace applications (Balsone et al, 2001, Bewlay and Jackson al,2003 and Taub et al, 1989). Second, Nb is more ductile at room temperature than Mo therefore has better fracture resistance (Bewlay and Jackson, 2003).

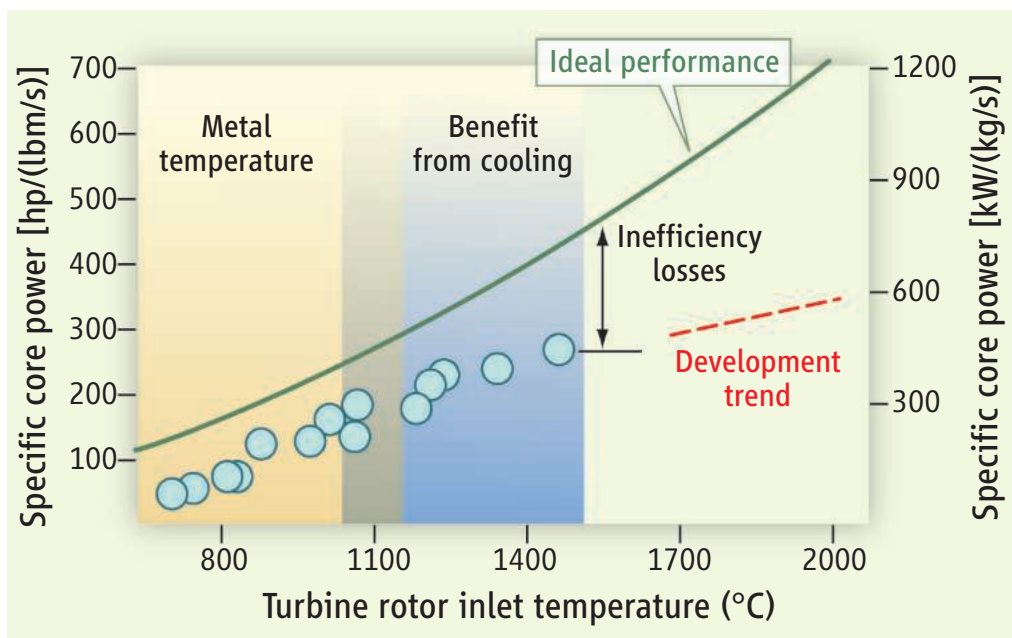


Figure 1 : The turbine rotor inlet temperature versus specific core power is extrapolated denoting the importance of eliminating the auxillary cooling air to improve the efficiancy (Perepezko, 2009).

1.2 Aims and Objectives

The aim of this research was to find out how the synergy of Al, Hf and Ti, which are three key elements that control the properties of Nb silicide based alloys, affects phase

stability and oxidation behaviour when the Al concentration in the alloy increases at the expense of Nb.

The objectives of the research were to find out (a) whether the synergy of Al, Hf and Ti promotes the stability of specific type (s) of silicide(s), (b) whether the Nb₃Si is stabilised, (c) what the synergy effect of Al, Hf and Ti is on the stability of the bcc Nb_{ss} and (d) which other phase(s) is (are) stabilised in the microstructures.

1.3 Niobium silicide based in-situ composites

As mentioned previously, Nb silicide based in-situ composites are considered to be the main alternative to Ni based superalloys. Basically, Nb silicide in-situ composites have good thermodynamic and thermophysical stability, which is a prerequisite for high temperature applications (Jackson et al, 2003). Thermodynamic stability denotes that the constituent phases of the material will not react with each other at high temperature: thermophysical stability implies that there will be no morphological or physical change in the material at high temperature. Therefore, the state of being thermophysically and thermodynamically stable is of importance at elevated temperature. Monolithic intermetallic compounds cannot be employed in high temperature applications due to their poor toughness (Taub et al, 1989 and Subramanian et al, 1994). For that reason, a composite like material can be developed in which intermetallic materials are combined with metallic second phase(s) (Mendirata et al, 1991). Such a material would address the poor toughness of monolithic intermetallic compounds. Incidentally, the level of toughness can be adjusted by alloying additions so that a balance of properties can be achieved and the materials can be used in high temperature applications (Bewlay and Jackson, 2003). Solid solution strengthening of the phases in Nb-silicide based in-

situ composites (Jackson et al, 2003) enables the metallic phase to provide toughness. Depending on alloy composition the volume fraction of Nb_{ss} can vary from 35 to 60 % (Jackson et al, 2003 and Bewley et al, 2003).

The key silicide in Nb silicide in-situ composites is the Nb₅Si₃ in which Nb and Si can be substituted by transition metals and simple metals (Tsakiroopoulos, 2001). The alloying behavior of 5-3 silicide and the Nb_{ss} offer a significant advantage for achieving a balance of properties with improved oxidation resistance of Ni silicide in-situ composites (Tsakiroopoulos , 2001). The latter is a key requirement for their employment in long term working service at high temperature (Mendiratta et al, 1991).

Nb-silicide based in-situ composites based on different alloy systems have been investigated and scrutinized by metallurgists in order to find an alloy with a good balance of low and high temperature properties required for high temperature applications (Tsakiroopoulos, 2001).

The important alloy systems for the development of Nb silicide based in-situ composites are Nb-Si-Ti , Nb-Si-Hf and Nb-Si-Ti-Hf-Al owing to the importance of Al, Ti, Hf for achieving a balance of properties. These systems lay the foundations for developing new alloy compositions capable of meeting the requirements of high temperature structural applications. The latter system will be discussed in this chapter as it is important for one of the alloys investigated in this project.

The role of alloying additions on mechanical properties, specifically on high temperature properties, will be briefly discussed here. A full elucidation of the role of

alloying additions on mechanical properties and oxidation behaviour of Nb silicide based in-situ composites shall be given in the mechanical properties section of this literature review.

Alloying additions X in Nb-Si-Ti-Hf-Al-X can be simple metal (SM) and / or transition metals (TM) (Tsakirooulos, 2001). Si has beneficial effect on density and oxidation resistance (Tsakirooulos, 2001). The concentration of silicon in the composite is important in terms of high temperature mechanical properties, for instance creep performance and tensile strength, as it governs the silicide's volume fraction. Indeed, the creep performance and high temperature strength are affected by the volume fraction of silicide (Bewlay and Jackson, 2003). It has been pointed out that for obtaining best creep performance the concentration of Si ought to be in the range of 18% and 20% (Bewlay and Jackson, 2003).

Titanium is a strong solid solution strengthener and imparts the toughness to Nb-silicide based in-situ composites (Bewlay et al , 1995b and 2003, Chan , 2005 and Davidson et al, 1999). The concentration of Ti should not exceed 25 at % to ensure that the alloy melts above 1700 °C (Bewlay and Jackson, 2003).

Room temperature ductility is enhanced in the same way as the strength at elevated temperature by an increase in Hf concentration (Tsakirooulos, 2001). The Ti:Hf ratio is important for creep performance. It has been suspected that the ratio should be below 3 in order to reach the creep rate goal (Bewlay et al, 1995b and 2003).

1.4 Phase equilibria relevant to this work

1.4.1 The Nb-Si binary system

The phase diagram of the Nb-Si binary system is given in figure 2. The melting temperature of Nb is 2467 °C. At the eutectic temperature (1915 °C), the amount of Si soluble in Nb solid solution is 3.5 at% (Schlesinger et al ,1993). According to figure 2 the peritectic reaction at 1975 °C leads to the formation of Nb₃Si. The αNb₅Si₃ is formed from the decomposition of Nb₃Si or βNb₅Si₃ via a eutectoid reaction (Kocherzhinskii et al, 1980,Schlesinger et al 1993, and Zhao et al, 2004) see table 1.

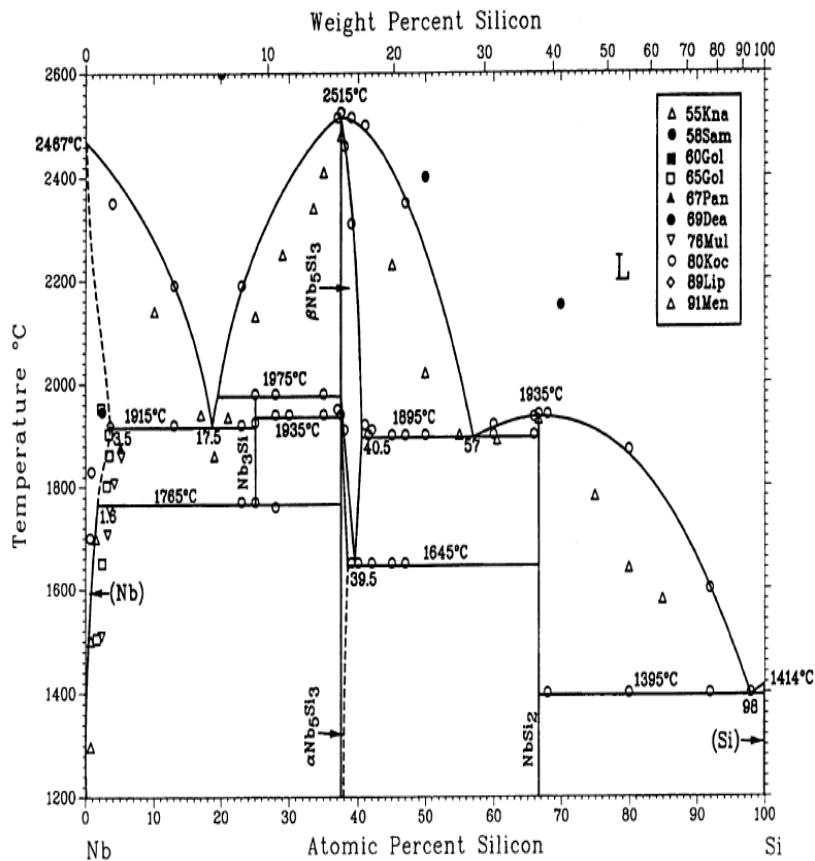


Figure 2: The Nb-Si binary phase diagram (Schlesinger et al, 1993)

The α Nb₅Si₃ is the low temperature form in comparison with the high temperature form, β Nb₅Si₃. The Nb₅Si₃ and β Nb₅Si₃ silicides have the same crystal structure (*tI32*) but with different lattice parameters (Schlesinger et al, 1993). Both of them possess the tetragonal crystal structure (Schlesinger et al, 1993)

Table 1: Summary of phase transformations in the Nb-Si system (Schlesinger et al, 1993)

Reaction	Composition of the respective phases, at% Si			Temperature (°C)	Reaction type
L \leftrightarrow (Nb)	0			2467	Melting
L \leftrightarrow (Nb)+Nb ₃ Si	17.5	3.5	25	1915	Eutectic
L+ β Nb ₅ Si ₃ \leftrightarrow Nb ₃ Si	19.5	37.5	25	1975	Peritectic
NbSi ₃ \leftrightarrow (Nb)+ α Nb ₅ Si ₃	25	1.6	35.5	1765	Eutectoid
L \leftrightarrow β Nb ₅ Si ₃	37.5			2515	Melting
NbSi ₃ + β Nb ₅ Si ₃ \leftrightarrow α Nb ₅ Si ₃	25	37.5	37.5	1935	Peritectoid
β Nb ₅ Si ₃ \leftrightarrow α Nb ₅ Si ₃ +NbSi ₂	39.5	38.5	66.7	1645	Eutectoid
L \leftrightarrow β Nb ₅ Si ₃ +NbSi ₂	57	40.5	66.7	1895	Eutectic
L \leftrightarrow NbSi ₂	66.7			1935	Melting
L \leftrightarrow NbSi ₂ +(Si)	98	68.8	100	1395	Eutectic
L \leftrightarrow (Si)	100			1414	Melting

The metastable γ Nb₅Si₃ has a hexagonal crystal structure and is stabilized by impurities (Alyamovskii et al, 1962).

The crystal structure of the phases in the Nb-Si binary system is given in table 2.

Table 2: Crystal structure data of Nb-Si system (Schlesinger et al, 1993)

Phase	Composition, at% Si	Pearson symbol	Space group	Strukturbericht designation	Prototype
(Nb)	0 to 3.5	<i>cI2</i>	<i>Im$\bar{3}m$</i>	<i>A2</i>	W
Nb ₅ Si ₃	25	<i>tP32</i>	<i>P4₂/n</i>	...	Ti ₃ P
α Nb ₅ Si ₃	36.7 to 39.8	<i>tI32</i>	<i>I4/mcm</i>	<i>D8₁</i>	Cr ₅ Si
β Nb ₅ Si ₃	37.5 to 40.5	<i>tI32</i>	<i>I4/mcm</i>	<i>D8_m</i>	W ₅ Si ₃
NbSi ₂	64.9 to 68.8	<i>hP9</i>	<i>P6₄22</i>	<i>C40</i>	CrSi ₂
(Si)	100	<i>cF8</i>	<i>Fd$\bar{3}m$</i>	<i>A4</i>	C(diamond)
Metastable phases					
Nb ₇ Si	8 to 13	<i>C**</i>
Nb ₄ Si	20	<i>hP*</i>	...	<i>C6?</i>	ϵ -Fe ₃ N
Nb ₃ Si.m	10 to 22	<i>cP8</i>	<i>Pm$\bar{3}n$</i>	<i>A15</i>	Cr ₃ Si
Nb ₃ Si.m'	10 to 27	<i>cF4</i>	<i>Fm$\bar{3}n$</i>	<i>A1</i>	Cu
Nb ₃ Si.m''	25	<i>cP4</i>	<i>Pm$\bar{3}n$</i>	<i>L1₂</i>	AuCu ₃
Nb ₃ Si I	25	<i>t**</i>
Nb ₅ Si ₃	37	<i>hP16</i>	<i>P6₃/mcm</i>	<i>D8₈</i>	Mn ₅ Si ₃

1.4.2 The Nb-Si-Ti ternary system

Figure 3 shows the space diagram of the metal rich region of the Nb-Ti-Si ternary system. The crystal structure data are shown in table 3. Basically, five phases form during solidification, namely: Nb, Nb₅Si₃, Nb₃Si, Ti₅Si₃, and Ti₃Si (Bewlay et al, 1997). The addition of Ti shifts the eutectic transformation $L \rightarrow \text{Nb}_{ss} + \text{Nb}_3\text{Si}$ from 1860 °C in the binary to 1330 °C in the ternary Nb-Si-Ti (Bewlay and Jackson, 2003). The Nb₃Si and Ti₃Si are isomorphous and have the *tP32* structure. Incidentally, the (Nb,Ti)₃Si is stabilized by Ti to lower temperature (Bulanova and Fartushna, 2010).

The formation of Nb₅Si₃ with Ti₅Si₃ (hexagonal) is promoted by an increase in Ti concentration as the Nb₅Si₃ (*tI32*) and Ti₅Si₃ (*hp16*) are not isomorphous (Bewlay et al, 1997 and Massalski et al, 1990).

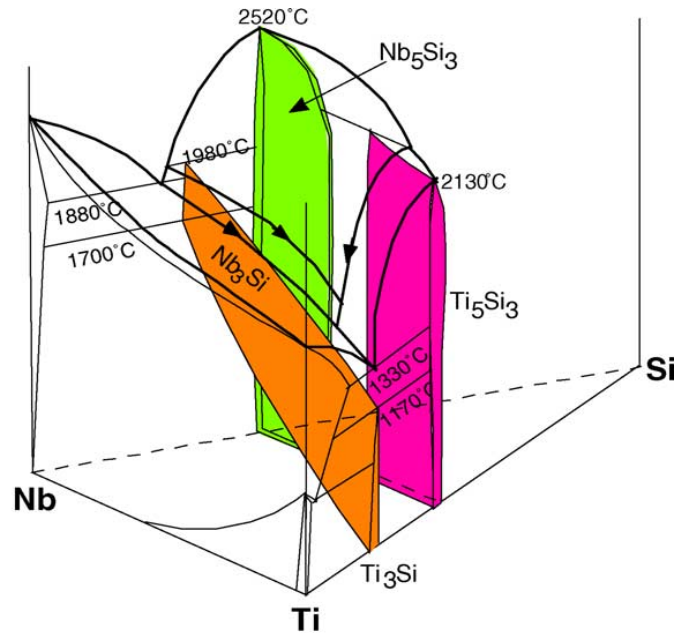


Figure 3: The ternary diagram of the Nb-Ti-Si ternary system(Zhao et al, 2004)

The solid solubility of Si in (β Ti,Nb) with 60 at% Ti at 1100 °C is reported to be 0.5 at% (Bulanova and Fartushna, 2010). The solubility of Ti in Nb₅Si₃ is 28 at% (Bewlay et al, 1997). But the exact form of the silicide phase was not specified.

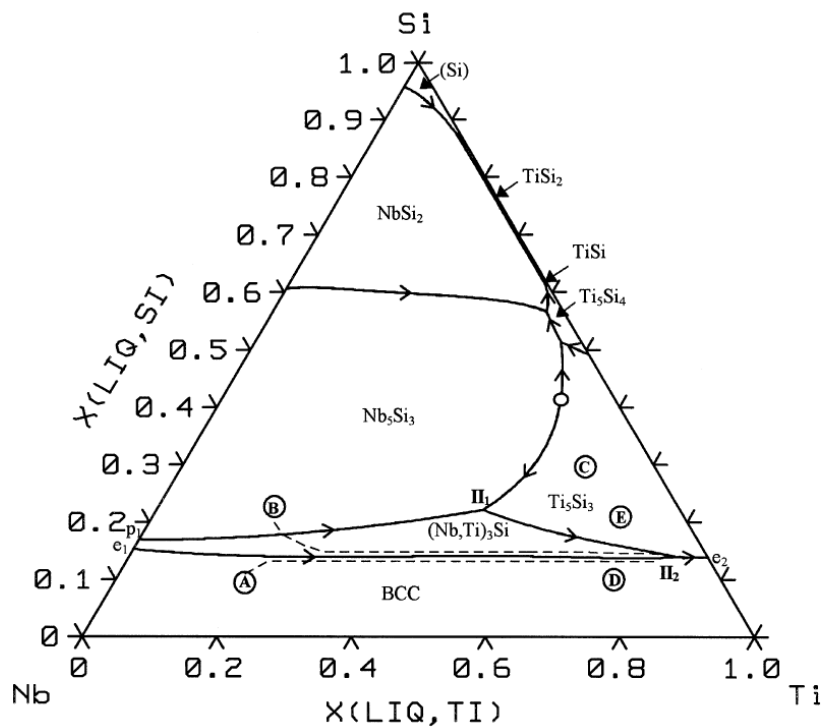
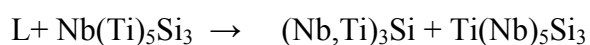


Figure 4: Calculated liquids projection of Ti-Nb-Si system (Liang and Chang, 1999)

The liquidus projection and isothermal sections at different temperatures namely 1500°C, 1350 °C, 1340 °C, 1320 °C and 1150 °C have been calculated by (Bewlay et al, 1997,1998 and Yan et al, 2007). The experimental results of (Bewlay, 1997) have been used as a base for the thermodynamic modelling of the liquidus projection by (Yan, 2007), the data of which are in contrary with (Bewlay, 1997). Figure 4 shows the calculated liquidus projection of the Nb-Si-Ti system by Liang and Chang (1999).

The main transition reactions in the Nb-Ti-Si ternary system in accordance with the liquidus projection of this system Figure 5 are as follows (Yan et al, 2007):



The II_1 reaction occurs at 1850 °C which is 200 °C higher than the one which Bewlay et al (1997) estimated, which was around 1600 °C. Furthermore, the type of primary Nb_5Si_3 is not specified in the projection. This was also the case in the experimental liquidus projection of Bewlay et al, (2007). The liquidus projection calculated by Yan et al (2007) shows the primary solidification of $\alpha(\text{Nb},\text{Ti})_5\text{Si}_3$, see figure 5. In other words, the primary solidification of $\alpha(\text{Nb},\text{Ti})_5\text{Si}_3$ was stabilized by Ti additions. This has not been accepted by Bulanova and Fartushna, (2010). In their assessment of the Nb-Ti-Si system there is no XRD data to contain the $\alpha(\text{Nb},\text{Ti})_5\text{Si}_3$. Concerning the controversy over the $\alpha\text{Nb}_5\text{Si}_3$ as a primary phase Geng et al, (2009) assessed the Nb-Ti-Si system and provided a liquidus projection see figure 6. In the liquidus projection calculated by Geng et al (2009) a large phase field is devoted to the $\alpha(\text{Nb},\text{Ti})_5\text{Si}_3$ as a primary phase.

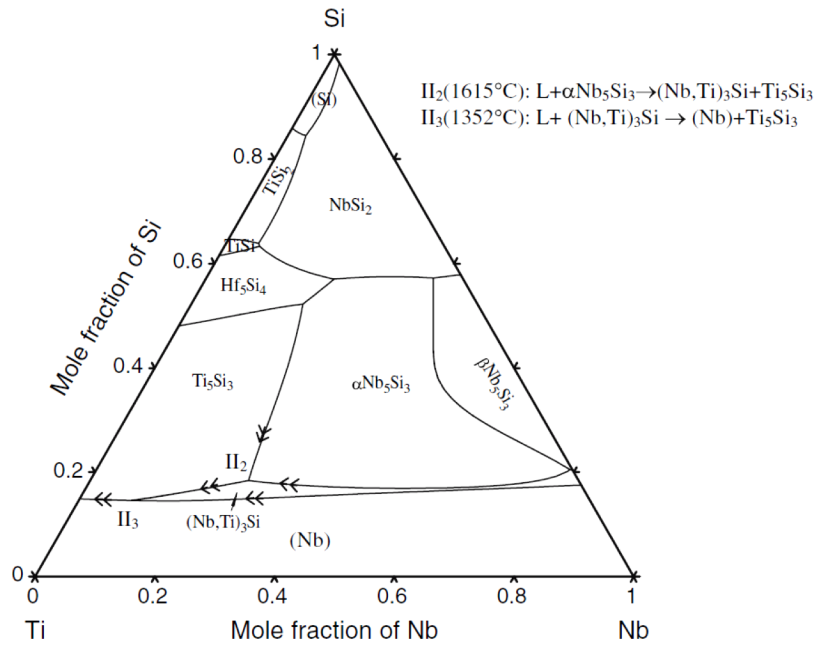


Figure 5: The liquidus projection calculated for the Nb-Ti-Si ternary system by Yan et al, (2007)

The liquidus projection of the Nb-Ti-Si ternary system has been studied by Li et al (2013) and is shown in figure 7 . In this projection the field of β Nb_5Si_3 is large but the existence of α Nb_5Si_3 as a primary phase is suggested in a narrow field. The latter has not been confirmed by research in our group (Tsakiroopoulos, 2016).

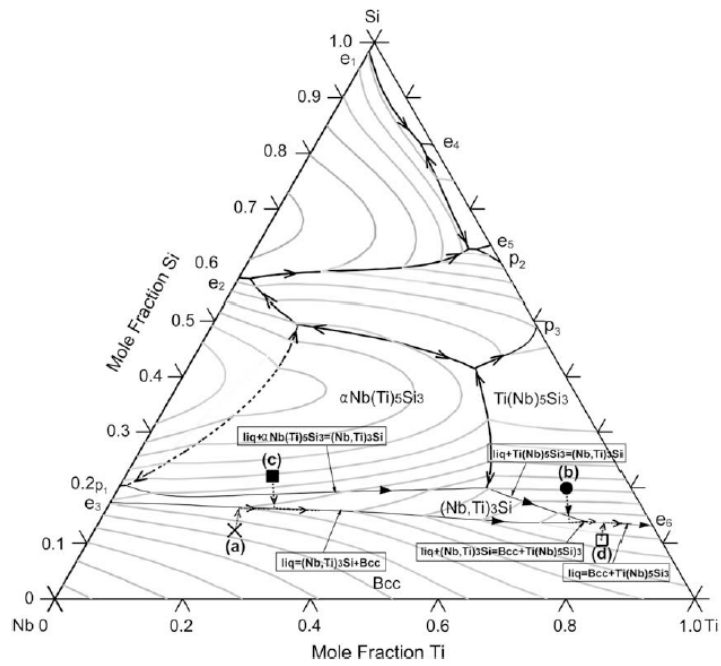


Figure 6: The liquids projection of the Nb-Ti-Si ternary system calculated by Geng et al, (2009)

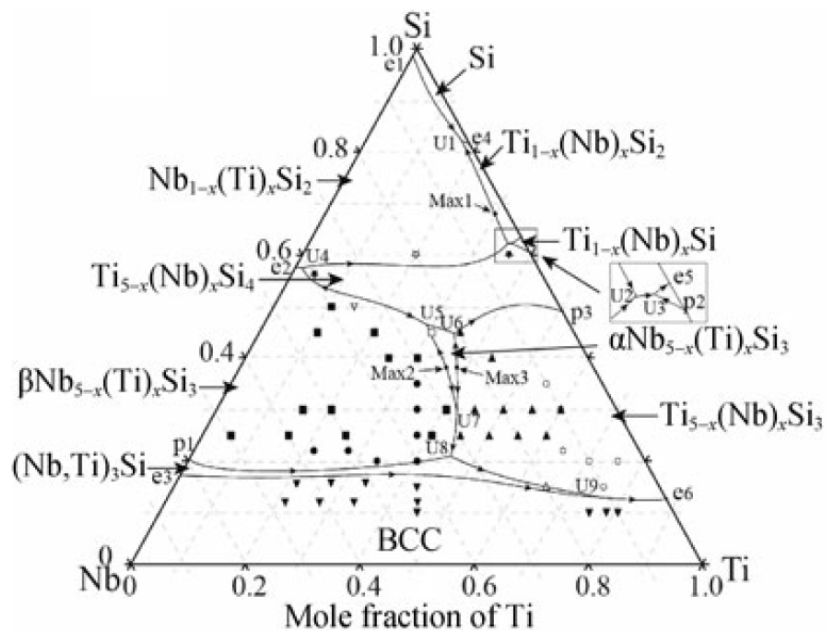


Figure 7: The calculated liquidus projection of the Nb-Ti-Si System (Li et al, 2013)

Table 3: Crystal structure data of the Nb-Si-Ti ternary system (Zhao et al, 2004)

System	Conditions (°C)	Pearson symbol	Space group
α -Ti	≤ 882	<i>hP2</i>	<i>P6₃/mmc</i>
B-Ti	882-1670	<i>cI2</i>	<i>Im$\bar{3}m$</i>
Nb	≤ 2489	<i>cI2</i>	<i>Im$\bar{3}m$</i>
Si	≤ 1414	<i>cF8</i>	<i>Fd$\bar{3}m$</i>
Nb ₃ Si	1770-1980	<i>tP32</i>	<i>P4₂/n</i>
β -Nb ₅ Si ₃	1650-2520	<i>tI32</i>	<i>I4/mcm</i>
α -Nb ₅ Si ₃	≤ 1940	<i>tI32</i>	<i>I4/mcm</i>
NbSi ₂	≤ 1940	<i>hP9</i>	<i>P6₂22</i>
TiSi	≤ 1570	<i>oP8</i>	<i>Pnma</i>
TiSi	≤ 1570	<i>oP8</i>	<i>Pmm2</i>
Ti ₃ Si	≤ 1170	<i>tP32</i>	<i>P4₂/n</i>
TiSi ₂	≤ 1485	<i>oF24</i>	<i>Fddd</i>
Ti ₅ Si ₃	≤ 2130	<i>hP16</i>	<i>P6₃/mcm</i>
Ti ₅ Si ₄	≤ 1920	<i>tP36</i>	<i>P4₁2₁2</i>

1.4.3 The Nb-Si-Hf ternary system

Figure 8 shows a space diagram of the Nb-Hf-Si ternary system. There is a eutectic trough between the Nb₃Si+Nb and Hf₂Si+ Hf binary eutectics (Abbaschian et al, 1989 and Bewlay et al, 1999a). There is a change in the nature of the liquidus surface with an increase in Hf concentration and a decrease in Nb concentration (Bewlay and Jackson, 2003), see figure 9.

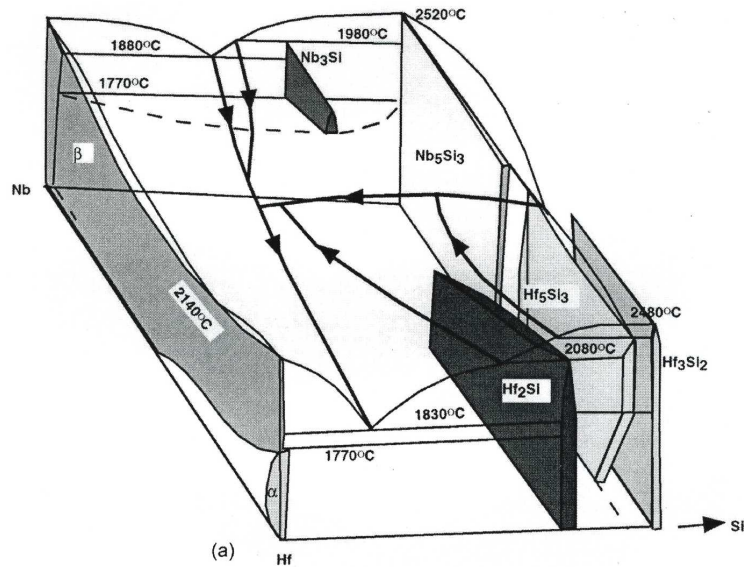
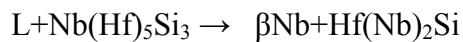
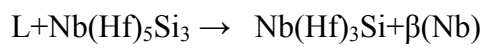


Figure 8: Space diagram of the metal-rich end of the Nb-Hf-Si ternary system (Bewlay and Jackson, 2003)

Three main transition reactions according to the liquidus projection in figure 9 are (Bewlay and Jackson, 2003):



The temperature at which the first reaction occurs is approximately 1850 °C with the composition (at%) Nb-2Hf-16Si and reaction 2 occurs at 2040 °C with the composition Nb-27Hf-22Si; the third reaction occurs at 1840 °C with the composition Nb-26Hf-14Si (Zhao et al, 2001 and Bewlay and Jackson, 2003).

Bewlay and Jackson (2003) reported that the contrast in backscattered images taken by SEM was poor owing to the partitioning of Hf. Moreover, the peritectic reaction can be suppressed in ternary alloys with higher Hf concentration and the eutectic reaction can be accelerated (Bewlay and Jackson, 2003). Incidentally, the peritectic reaction is

missed in Nb Silicide in-situ composites with higher Hf concentration, and therefore two phase Nb(Hf)₅Si₃ and Nb composites are formed (Bewlay and Jackson, 2003).

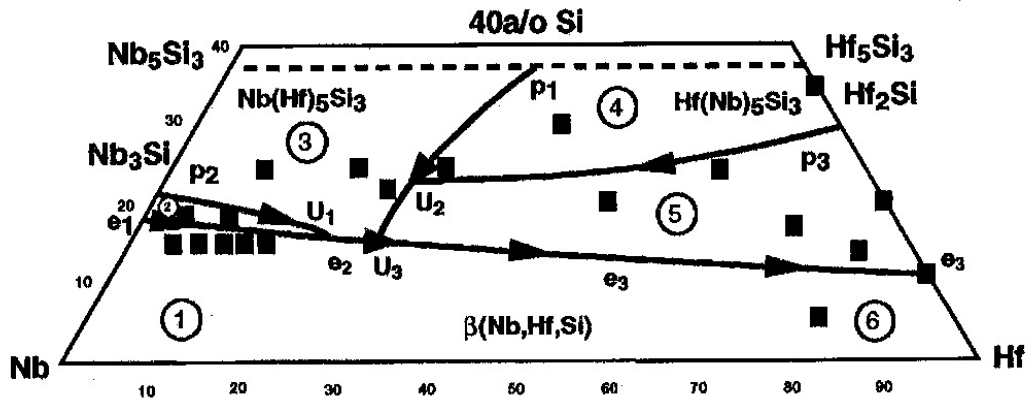


Figure 9: The liquidus projection of the Nb-Hf-Si ternary system. Three main transition reactions associated with regime 1, 2 and 3 circled in the picture, have been set out in the text (Bewlay and Jackson, 2003).

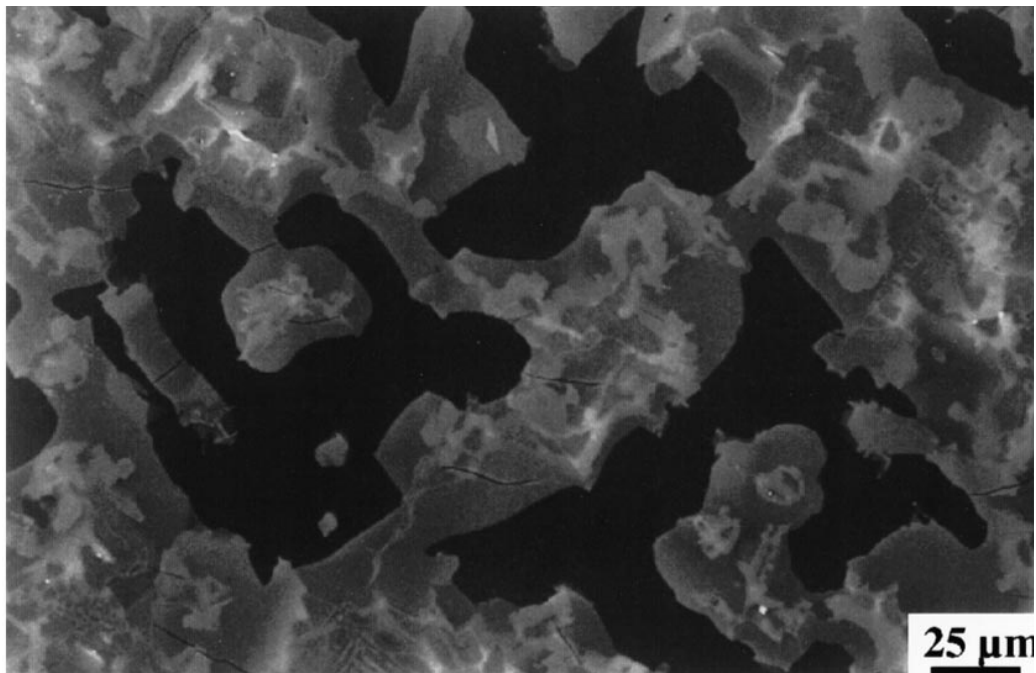


Figure 10: Backscattered electron image of the microstructure of the Nb-15Hf-16Si alloy (at%). Three phases have formed during solidification namely: Nb (light gray phase), Nb(Hf)₃Si (large black phase) and Nb(Hf)₃Si (large dark gray) which is Hf rich. The poor contrast between the gray and light gray phases is attributed to the partitioning effect of Hf (Bewlay and Jackson, 2003).

Figure 10 demonstrates a backscattered image of the microstructure of the alloy Nb-15Hf-16Si. As can be seen three different phases formed during solidification. The large scale dark phase is the $\beta(\text{Nb})$ and the interdendritic eutectic cells of $\text{Nb}(\text{Hf})_3\text{Si}$ can be seen as the light gray phase. In addition, the brighter gray phase represents the Hf rich $\text{Nb}(\text{Hf})_3\text{Si}$. As mentioned above, owing to higher concentration of Hf, the contrast between the two gray phases is poor, which was attributed to the partitioning effect of Hf (Bewlay and Jackson, 2003).

1.4.4 The Nb-Si-Al ternary system

Figure 11 shows reported isothermal sections of the Nb-Si-Al ternary system at different temperatures. Two ternary compounds have been identified by Brukl et al (1961), namely the $\text{Nb}_3\text{Si}_5\text{Al}_2$ and $\text{Nb}_3\text{Si}_{10}\text{Al}_3$. Figure 11b shows the isothermal section of the Nb-Si-Al at 1500 °C reported by Pan et al (1984).

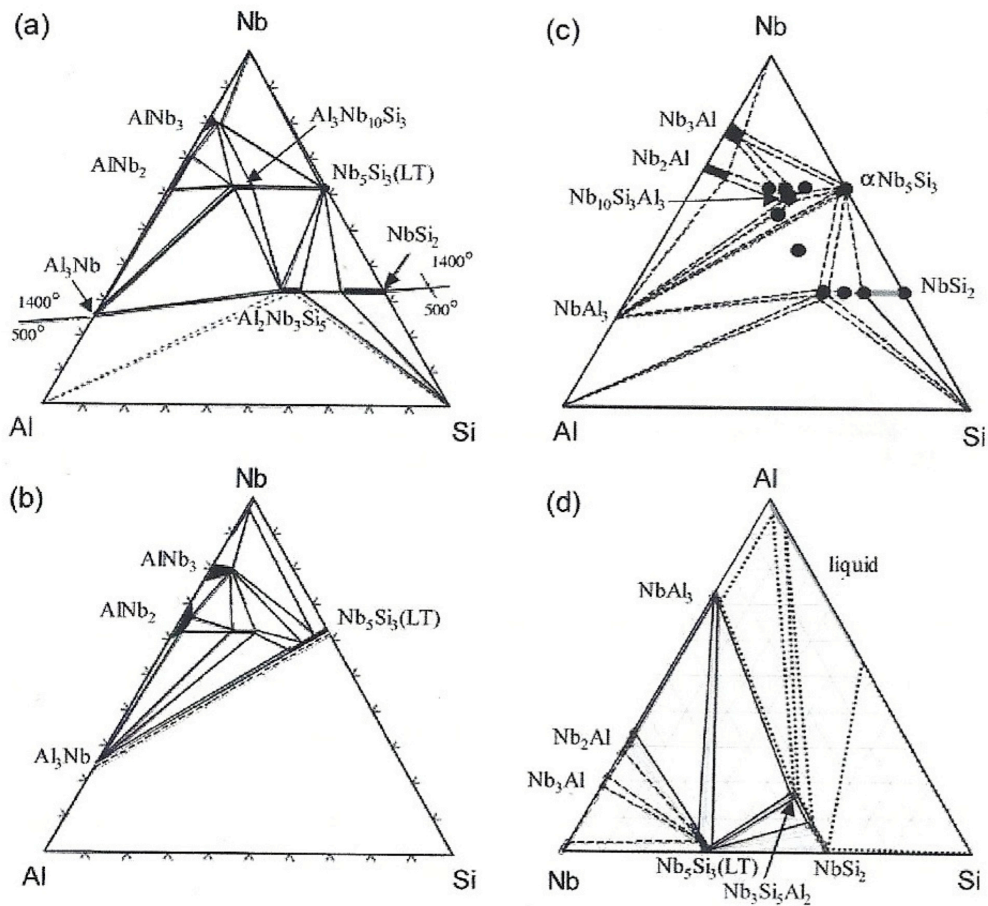


Figure 11: Isothermal sections of the Nb-Si-Al ternary system (a) upper part is for 1400 °C and the lower part for 500 °C, (b) isothermal section at 1500 °C, (c) 1200 °C-1600 °C isothermal section, (d) the calculated isothermal section at 1000 °C and 2000 h annealed (Brukl et al, 1961, Pan et al, 1984, Murakami et al, 2001a and Zhao et al, 2003b)

The equilibrium between NbAl_3 and $\alpha\text{Nb}_5\text{Si}_3$ was confirmed by Murakami et al (2001a) who proposed the isothermal section for the temperature from 1200 °C-1600 °C, see figure 11c. There has been a considerable discrepancy concerning the solubility of Al in $\alpha\text{Nb}_5\text{Si}_3$: Pan et al (1984) reported Al solubility of 10 at% and Murakami et al (2001a) approximately zero. The solubility of Al in Nb_5Si_3 at 1000 °C has been reported to be 8 at % (Zhao et al, 2003b). The isothermal section of the annealed Nb-Si-Al system for

2000 h calculated by Zhao et al (2003b) is presented in figure 11d. It has been pointed out that as a result of the Al addition in the Nb-Si-Al ternary system, the β Nb₅Si₃ is stabilized to a lower temperature form by the Nb₁₀Si₃Al₃ compound (Murakami et al, 2001a).

1.5 Oxidation

To increase the thermal efficiency and decrease the fuel consumption in turbofan aero-engines, new high temperature alloys are required to outstrip the Ni-based superalloys. Nb-silicide based in situ composites are the main candidate materials. The oxidation behaviour of Nb alloys was enhanced via alloying in the 1960s and 1970s. However, because of lack of funding and scientific literature about phase equilibria and the role of alloying additions in Nb, no breakthrough was achieved.

The oxidation behaviour of alloys and materials employed in long term high temperature working service and their resistance to oxidation are of utmost importance, as failure can lead to a disastrous and costly catastrophe. The oxidation resistance of Nb based silicide in-situ composites is the main hindrance to their use because the composites can have poor oxidation resistance, particularly at high temperatures.

Considering the service temperature of the high-pressure turbine and the constituent elements of the fuel, such as sulphur, it is appreciated that alloys and materials must be capable of operating in a very corrosive environment. Therefore understanding the oxidation mechanism is the first step towards improving oxidation resistance. Nb-silicide based in-situ composites are multiphase materials. Different oxidation behaviours can be observed during their exposure. Nb₂O₅ is the stable oxide formed at

the temperature of interest for future application of Nb silicide based in-situ composites in the turbine engines. High temperature and low temperature oxidation in Nb silicide based in-situ composites can be differentiated and the oxidation kinetics and mechanisms through which oxidation occurs at ambient temperature and high temperature oxidation and scale forms can be different.

1.5.1 Oxidation of Nb

Niobium has high affinity to oxygen and thus high solid solubility for oxygen, see figure 12.

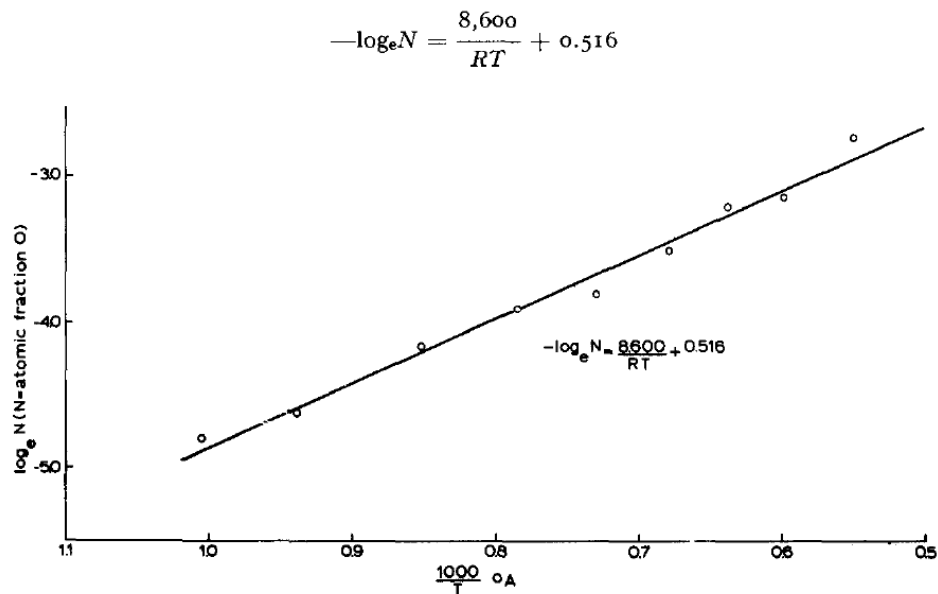


Figure 12: Solubility of oxygen in pure Niobium (Brayant, 1962)

Nb₂O₅ is reported by Kofstad et al (1961) and Hurlen (1960) to be white when stoichiometric. However, it will turn dark in event of departure from stoichiometry. Nb₂O₅ is a polymorphic oxide. The dissolved oxygen causes an expansion of the bcc Nb lattice (Hurlen 1960). In accordance with the lattice parameter measurements, the

solubility of oxygen in Nb in the temperature range of 770 °C to 1100 °C was reported to be between 1.38 to 5.52 at% (Hurlen 1960). Kofstad et al (1961), Hurlen (1960) and Kubaschewski and Hopkins (1960) confirmed the formation of suboxides in the early stages of oxidation with the assigned formula of NbO_x.

Principally, 5 stages have been proposed for the oxidation of Nb at different temperatures, namely linear 1, parabolic 2, linear 3, parabolic 4 and parabolic 5 (Hurlen.T 1960). Figure 13 is a schematic representation of the abovementioned stages. The weight gain has been drawn versus time based on which oxidation behaviour of Nb has been assessed by Hurlen (1960). It has been suggested that the transition from stage 2 to stage 3 is of particular importance, and is the most influential stage. This is because a transition from protective to non-protective type of oxidation occurs. A noticeable extension in both time and oxygen uptake associated with this transition phase has been found (Hurlen (1960)). Based on the mechanism put forward by Hurlen (1960) which was also accepted by Kofstad et al (1961), at lower temperature, linear 1 stage dominates at low pressure and parabolic (2) dominates at higher pressures. Consequently, at higher temperatures, the linear (3) and subsequent parabolic stages 4 and 5 will prevail.

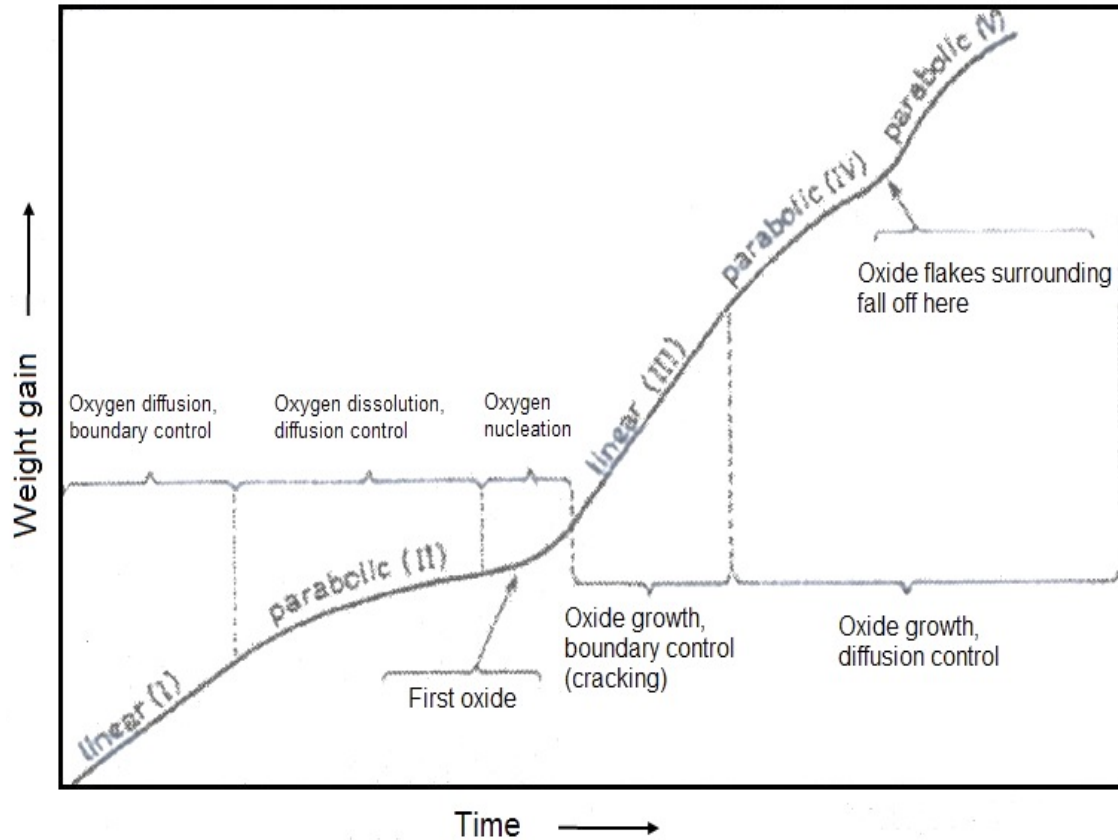


Figure 13: Oxidation of Nb and different stages, namely parabolic and linear.
Redrawn from Hurlen, (1960)

It has been pointed out that the scale on Nb at 1000 °C, is more compact. However, at 1250 °C, the scale becomes non-adherent and exfoliates at the slightest provocation (Kubaschewski and Hopkins, 1960). This is called break-away oxidation, a name which is self-explanatory. The complicated oxidation behaviour of Nb has been considered as a stalemate to determine the temperature dependence over large temperature and oxygen pressure ranges in terms of activation energies (Kofstad et al, 1961).

The complicated oxidation behaviour is referred to as irregular oxidation behaviour by those who examined the oxidation behaviour of Nb. With regard to the oxide scale formation at elevated temperature, Kofstad et al (1961) described that the oxide scale is thick and porous at high oxygen pressures. They attributed the irregular temperature

dependence to different plastic properties of different Nb₂O₅ modifications and set out that those differences change the degrees of compactness and in effect change the protective ability of the oxide scale. Kofstad et al (1961) and Kubaschewski and Hopkins (1960) attributed the irregular behaviour to the different disorder structures of Nb₂O₅.

Kubaschewski and Hopkins (1960) put forward a mechanism, along with the above explanation, to account for the break-away or onset of the break-away. In accordance with their proposal, the diffusion of O ions through the film consisting of the highest oxide is the prevailing mechanism at intermediate temperature and consequently the next oxide forms at the metal-oxide interface. In view of the fact that the volume ratios for the highest oxide are notably high (2.45 to 3.5), the new oxide develops and expands against the resistant oxide layer and subsequently drastic biaxial stresses develop causing the oxide film to spall off.

According to Kubaschewski and Hopkins (1960), different modifications of Nb₂O₅ are the main reasons for the complex oxidation behaviour of Nb. The first formation of Nb₂O₅ has been reported by Hurlen (1960) to occur during the transition from stage 2 to stage 3, which is a significant stage of the Nb oxidation, as mentioned above. Kofstad et al (1961) pointed out that oxygen dissolution is a function of temperature, oxygen pressure and length of oxidation, and that oxygen diffusion controls the oxygen dissolution.

1.5.2 Pest oxidation

Pest oxidation is a well-known phenomenon observed in intermetallics and in Nb-silicide based in-situ composites at intermediate temperature (500 °C to 800 °C). In the latter, pest oxidation is thought to occur through the diffusion of oxygen along grain boundaries into the Nb_{ss} grains (Mitra, 2006), and owing to oxygen embrittlement, self-pulverization occurs at intermediate temperature (Balsone et al, 2001).

Figure 14 shows a schematic representation of pest oxidation at 815 °C of Nb-silicide based in-situ composites leading to crack formation and propagation. At 815 °C, a volume expansion of approximately 15% is induced due to the formation of a large amount of small oxide scales, and consequently the induced volume expansion leads to crack formation within the silicide (Mathieu et al, 2012). Isothermal enrichment of oxygen accelerates crack development and increases the rate of volume expansion. Shear stress is introduced at the interface of the matrix (Nb solid solution) and silicide, inducing internal stress within the silicides (Mathieu et al, 2012). Consequently, the induced tensile stress reaches the local critical value: crack initiation and propagation occur, leading to rupture (Knittel et al, 2012). Furthermore, the main reason for introducing the shear stress at the interface is that the expansion was possible in one direction, which was towards the external surface (Mathieu et al, 2012).

Embrittlement of grain boundaries by providing a short circuit diffusion path for oxygen has been put forward as a mechanistic basis for occurrence of pest oxidation by Westbrook and Wood (1964) (Yang et al, 2007). However, it has been demarcated that the onset of pesting is not merely related to grain boundary embrittlement as it does not

occur only in dense and porous specimens, rather, it has been known to occur in specimens with poorer density (Mitra, 2006).

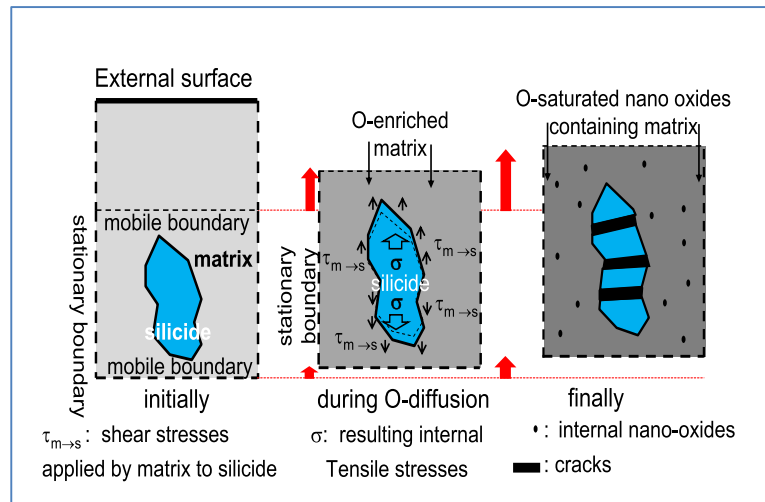


Figure 14: Schematic representation of pest oxidation of Nb silicide based in-situ composites at 815 °C (Mathieu et al, 2012).

Incidentally, it has been reported that the chance of self-pulverization increases with an increase in the level of porosity within the alloy (Mitra, 2006). Yanagihara et al, (1993) have reported that the cracks induced during processing have more prominent effects on pesting and are deemed more accountable than grain boundaries. The detailed analysis of the oxide of Mo-Si-O is in accord with the abovementioned. Accordingly, the initial oxide was seen to involve 200% volume expansion at crack tips along with increased stress concentration (Mitra, 2006, Yanagihara et al, 1993). It has been reported by Menon et al (2001) that the generation of residual stress in Nb solid solution is attributed to fine scale precipitation of the oxide and negative thermal expansion coefficient of Nb₂O₅.

Pest oxidation is limited to intermediate temperatures and has not been reported to occur at high temperature. Regarding the latter, the lower thermal expansion coefficient of silicides and their ability to sustain plastic flow could be the reason for the non-occurrence of pesting at high temperature (Menon et al, 2001).

The residual stress in Nb solid solution phase during the initial stages of oxidation is shown in figure 15. Compressive stress is developed. It has been pointed out that fracture of the brittle phase, which is the silicide, occurs preceded by stresses reaching a critical value in order for the stresses to be relieved.

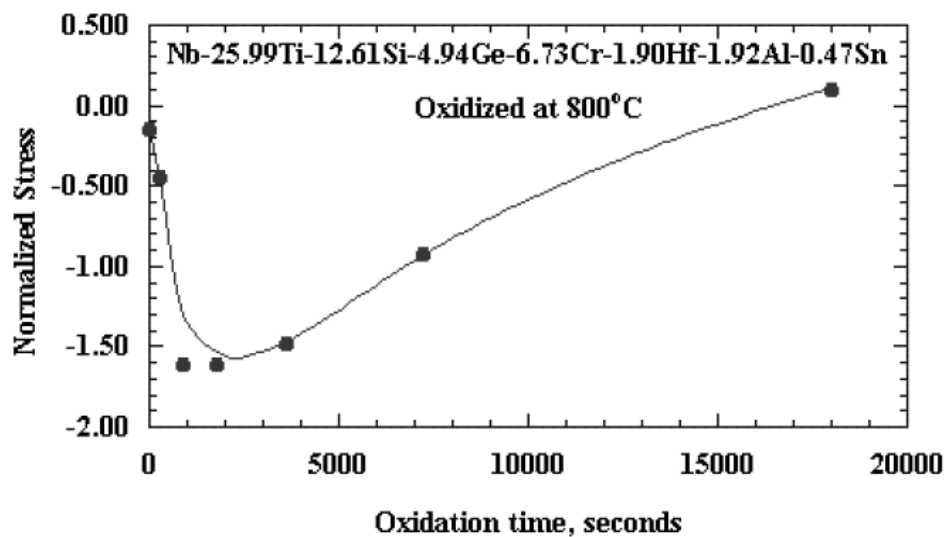


Figure 15: Residual stress in Nb solid solution during the initial stage of oxidation (Menon et al, 2001)

1.5.3 Oxidation of Nb-silicide in situ composites

Nb silicide based in-situ composites display poor oxidation resistance at high temperature. Alloying additions improve the oxidation resistance but other mechanical properties might be adversely affected. This necessitates the rigorous assessment of the role of alloying additions to avoid gaining an improvement in the oxidation resistance at the expense of mechanical properties.

Nb_2O_5 is the main Nb-based oxide layer present after oxidation. Due to high affinity of Nb to oxygen, the oxide layer formed during oxidation will, once it has been broken, provide a diffusional pathway for oxygen, meaning the oxide layer will no longer be able to act as a protective layer (Jackson et al, 2003). Basically, the oxide layer contains 3 zones: an oxide scale where spallation is expected due to the brittle nature of the layer, a diffusion zone and the base metal (substrate) (Jackson et al, 2003).

It has been reported that Nb oxides form at lower temperature in company with SiO_2 in spite of their having higher energy of formation which is attributed to the lower diffusivity of Si (Mitra, 2006). Consequently, owing to the non-protective nature of the oxide, oxygen is able to diffuse to the lattice through the grain boundaries succeeded by embrittlement and crack introduction (Mitra, 2006).

The role of alloying additions in Nb silicide based in-situ composites is of paramount importance as they can enhance oxidation resistance. As mentioned above, Nb is susceptible to both internal and external oxidation followed by non-protective scale formation owing to its high affinity to oxygen. The non-protective Nb_2O_5 upon exposure at high temperature cracks and acts as a diffusional pathway for more oxidation.

The role of alloying additions in Nb silicide based in-situ composites can be described through the mechanism by which the oxidation resistance is improved. Some elements are added to reduce the diffusivity of Nb and reduce the depth of internal oxidation. Some elements are scale formers which form a passive layer protecting the alloy from more oxygen uptake and embrittlement.

The oxidation of multiphase Nb silicide based in-situ composites has been significantly improved in comparison with the monolithic Nb₅Si₃ owing to the addition of reactive elements, figure 16 and figure 17, which have been beneficial in scavenging oxygen, thereby reducing the oxygen dissolution (Tsakiroopoulos, 2001). Figure 16 compares different Nb alloys with Ni-based superalloys, in terms of metal loss at 100 h at the temperature of interest. Considering figure 16, it is appreciated that the rate of metal loss at 100 h in Nb silicide based in-situ composites has been greatly enhanced as compared with binary Nb-Nb₅Si₃. The effect of adding Al, Cr, Hf and Ti in decreasing the metal recession is evident in figure 16.

It is worth mentioning a promising Nb silicide in-situ composite designed by GE researchers that is often referred to as the MASC alloy. It is evident in figure 16 that the metal loss rate of the MASC alloy has been significantly improved through alloying additions. It has been reported that the oxidation performance of the MASC alloy (metal loss rate) is between IN 738 and third generation single crystal Ni-based superalloys (Bewlay and Jackson, 2003).

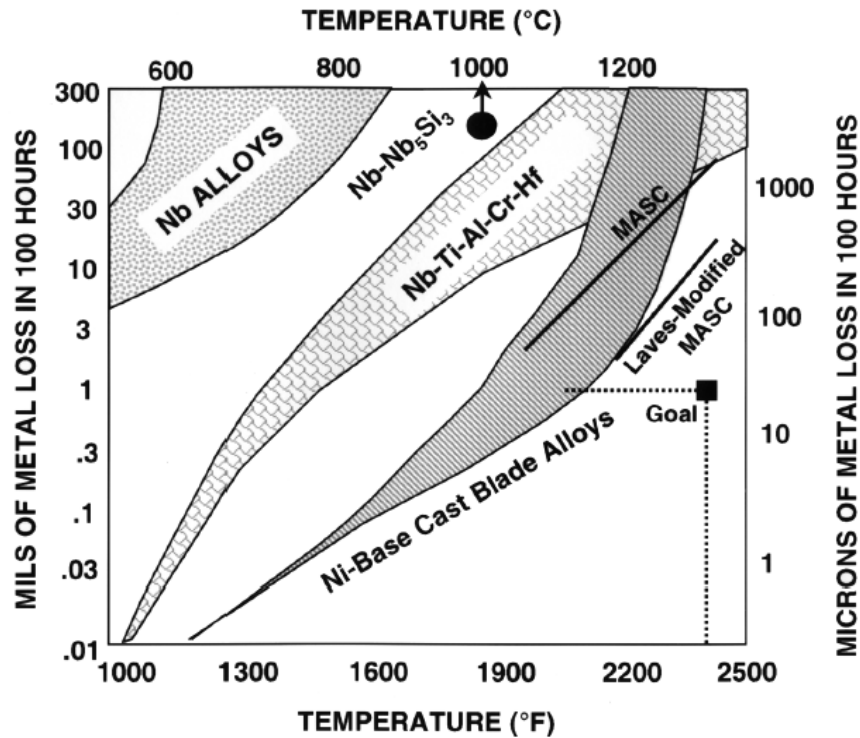


Figure 16: Oxidation behaviour of Nb alloys along with Nb alloys bearing silicide in comparison with Ni-based superalloys (Bewlay and Jackson, 2003)

1.5.3.1 Role of alloying additions

Hf is regarded as an oxygen scavenger which traps the oxygen and forms Hafnia. Additionally, it reduces the oxygen diffusivity, resulting in a reduction of embrittlement which occurs at high service temperature due to oxygen uptake (Subramanian 1996, Jackson 1996). The depth of internal oxidation is reduced by the addition of Hf to Nb silicide based in situ composites (Verma et al 2011, Bewlay and Jackson, 2003 and Mathieu et al, 2012).

Ti also improves the oxidation resistance of Nb silicide based in-situ composites (Bewlay and Jackson, 2003, Jackson et al 1996). Ti has high affinity for oxygen, thereby reducing the solubility of oxygen in Nb. Incidentally, oxidation of Nb₅Si₃ has been reported to be improved by the substitution of Nb with Ti. The concentration in

the component is very important as it affects significantly the mechanical properties and melting temperature of the composite. The importance of the concentration of alloying addition is not just limited to Ti, because the balance of mechanical and environmental properties is affected by the majority of the alloying additions. Silicon is the main addition in Nb silicide based in-situ composites as it governs the volume fraction of the silicide phase and has a startling effect on oxidation performance (Bewlay and Jackson, 2003). Based on the effect of the major alloying additions on weight loss during thermal exposure, it has been reported that Si, Cr and Al are the most effective elements (Bewlay and Jackson, 2003, Meier, 1989 and Pint et al, 2006).

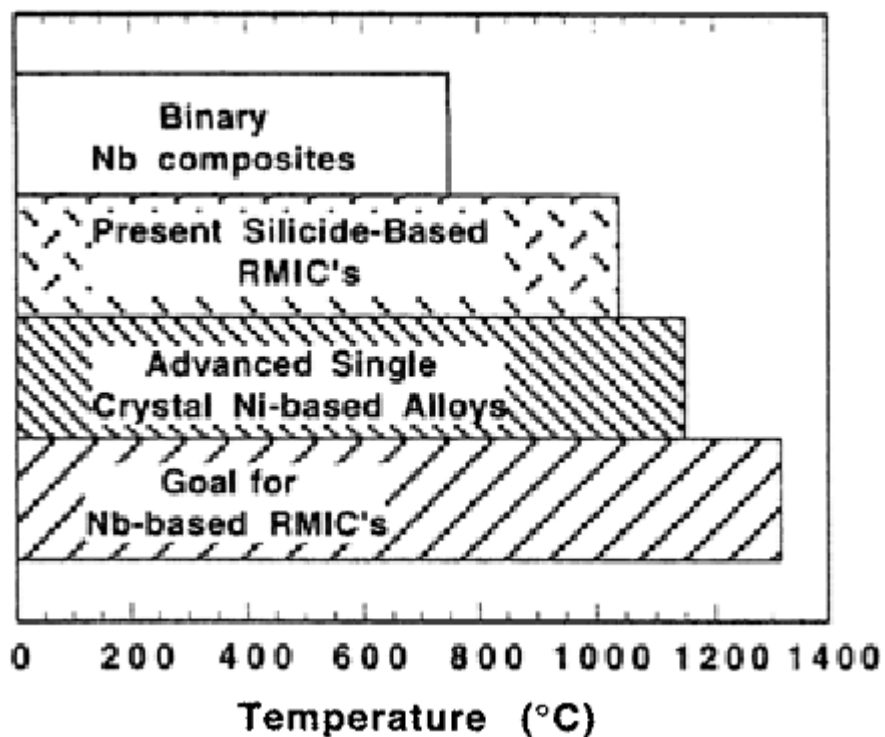


Figure 17: Temperature dependence of less than 25 μm of metal loss at 100 h for monolithic Nb_5Si_3 , silicide based RMIC and Nb based silicide in-situ composites (Bewlay et al, 1997)

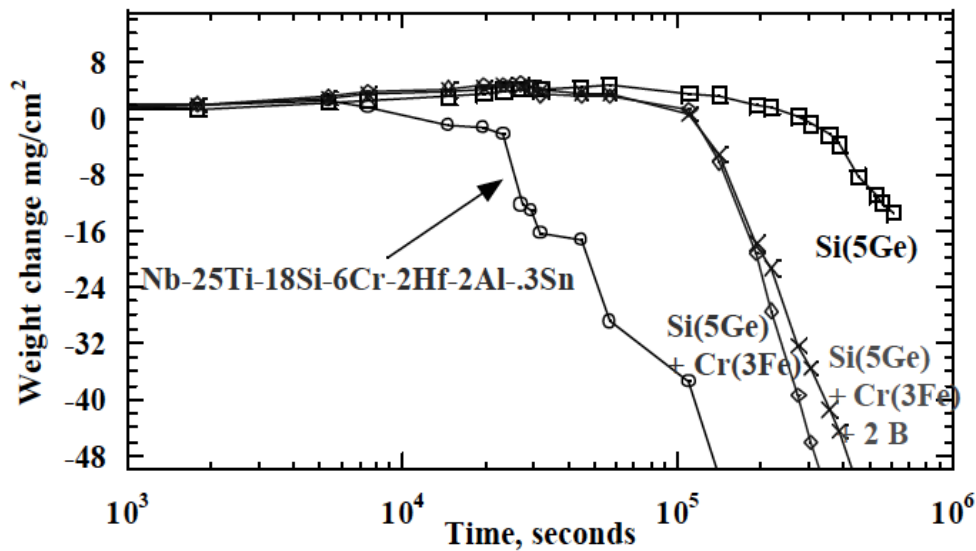


Figure 18: Effect of alloying on cyclic oxidation performance of Nb silicide based in-situ composites (Menon et al, 2001 and Menon et al, 2004)

Some Nb silicide based in-situ composites have shown a two-stage oxidation response: initial weight gain followed by rapid weight loss, see figure 18 (Menon et al, 2001). During the second stage, a break away stage, oxide scale spallation will occur. The weight change versus time data has been analysed using the equation:

$$\ln(\Delta w) = \ln K + n \ln t$$

In accordance with the value n , the oxidation could be linear or parabolic. The oxidation of Nb silicide based in-situ composites has been reported to be much better than Nb-Al alloys in which the value of n was found to be close to unity (Menon et al, 2001). Figure 18 and figure 19 clearly illustrate that the oxidation of Al-rich Nb base alloys is inferior to that of high Si-bearing Nb alloys. Furthermore, volume diffusion of oxygen through the oxide is surmised as a main factor determining parabolic law for oxide growth which sidesteps the effect of short circuit diffusion (Menon et al, 2001 and Mathieu et al, 2012).

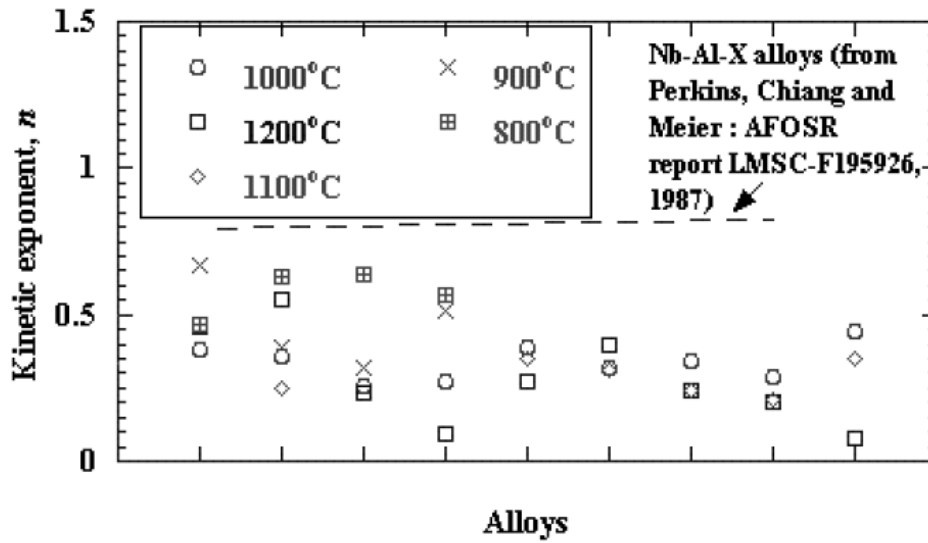


Figure 19: Determined values of the kinetic exponent n , for different multicomponent Nb base alloys. Symbols are representative of the alloying additions illustrated in figure 18 (Menon et al, 2001)

In case of break away or occurrence of cracks or internal oxidation, which are relevant in Nb-based alloys, oxygen will diffuse to the metal-oxide interface at a much higher rate, which renders the above discussion problematic (Menon et al, 2001).

Addition of Si is also considered one of the measures to form a protective oxide layer, regardless of the fact that it is an integral part of the composite. However, its addition imposes some complications as its applicability becomes limited at high temperature owing to its becoming volatile (Pint et al, 2006). In general, an increase in the volume fraction of the Nb_{ss} , meaning a decrease in silicide volume fraction, decreases the oxidation resistance of the composites and vice versa. Considering the free energy of formation of oxides, the formation of HfO_2 deep inside Nb-silicide based in-situ composites could be justified (Menon et al, 2001). The free energy of formation of the oxides according to the alloying additions employed in Nb silicide based in-situ composites is given in table 4.

Table 4: Free energy of formation of oxides (Menon et al, 2001)

$$\Delta G_{HfO_2} < \Delta G_{Al_2O_3} < \Delta G_{TiO_2} < \Delta G_{SiO_2} < \Delta G_{NbO} < \Delta G_{Cr_2O_3} < \Delta G_{NbO_2} < \Delta G_{Nb_2O_5}$$

Having studied different Nb silicide based in-situ composites, Menon et al (2001) concluded that the silicide phase remained unaffected while the Nb solid solution phase was oxidized selectively. It has been documented by Smarin (1965) that the oxidation resistance of Nb₅Si₃ is much better than dilute alloys and the oxidation resistance of the silicide decays above 1100 °C. Based on the above explanations and observations using EDS and BSE by Menon et al (2001), the silicide phase is assumed to be unaffected or at least resistant to internal oxidation as opposed to the Nb_{ss} phase. However, an opposite account has been proposed by Mathieu et al (2012) based on which the silicide phase was found to be affected by oxygen penetration and the outer part of the silicide was observed to be fully oxidized, namely the area in which the mixture of different oxides was observed. The heart of the silicide did not seem to be affected (Mathieu et al, 2012). The fast solid state transport of oxygen at high temperature was held responsible for a prominent effect of oxygen penetration on internal zone formation and changes within the zone (Mathieu et al, 2012). Despite the claim of Mathieu et al (2012) regarding their results in contrast with those obtained by Menon et al (2001), the results do not seem to be refuting each other, since Menon et al (2001) stated that the outer part of Nb₅Si₃ and its interface with Nb_{ss} were “decorated” with oxide particles, the very same claim which was put forward by Mathieu et al (2012) regarding the precipitation of the oxide particles within the Nb_{ss}/Nb₅Si₃ interface. BSE images taken from the oxidized specimens by Mathieu et al (2012) and Menon et al (2001) are shown in figure 20. Figure 20, shows that the heart of the silicide in both figures is unaffected

while the outer part of the silicide at the Nb_{ss} and Nb₅Si₃ interface is oxidized. This was also reported by (Geng et al 2006 and 2007).

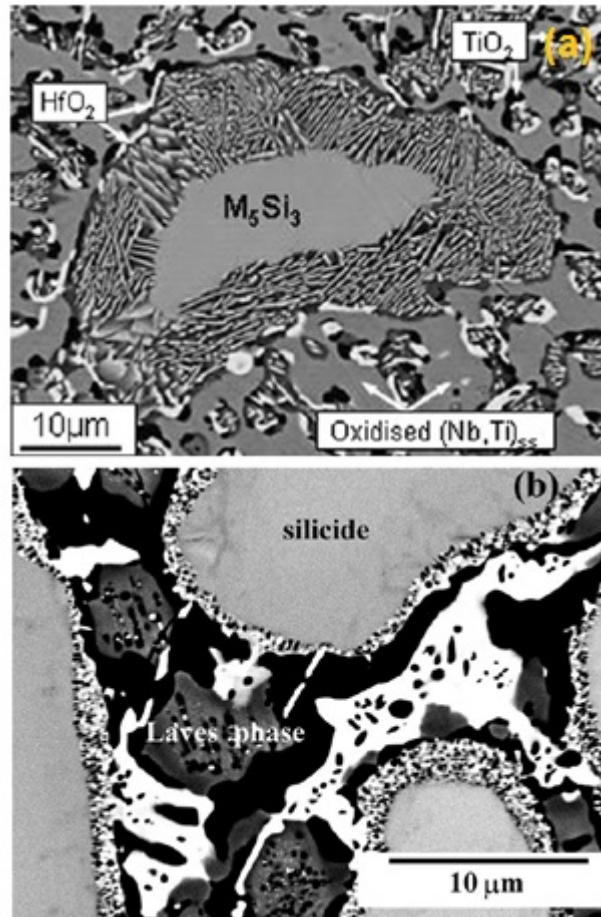


Figure 20: Precipitation of oxide particles in the Nb_{ss}/Nb₅Si₃ interface. a) BSE image taken by Mathieu et al (2012) signifying the presence of unaffected silicide after exposure. b) BSE image taken by Menon et al (2001) showing the unaffected silicide phase after exposure

1.5.3.2 Scale formers

Nb silicide based in-situ composites to be employed in aircraft engines will require coating (Pint et al, 2006). Relying solely upon a coating is not reasonable and the performance of the coating itself cannot be relied upon. The alloy must have an inherent and acceptable oxidation resistance for applications in gas turbine engines

(Bewlay and Jackson, 2003). Thus the development of Nb silicide based in-situ composites must also consider the effect of alloying additions and their compositions on the performance of the materials required (substrate + coating). Developing coatings is itself an arduous task, as several conditions must be met so that its employment could be warranted. Among different alloying additions, Al, Si and Cr are the most well-known protective scale formers that have been studied widely (Meier and Petit, 1992).

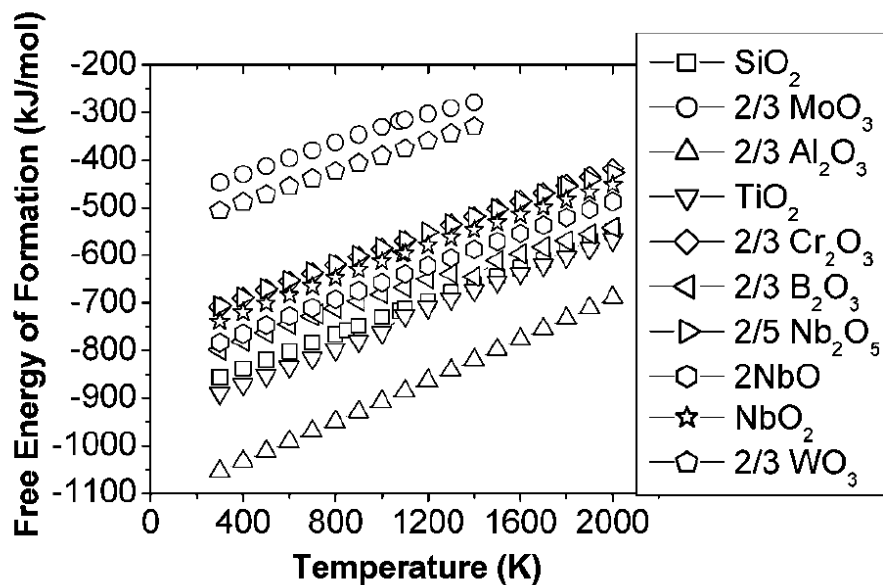


Figure 21: Free energy of formation for different oxides. Data is given per mole of oxygen with absolute temperature (Mitra, 2006)

Notwithstanding their advantageous attributes over Nb₂O₅, their influence on mechanical and high temperature properties (in excess of certain limits) and their working limitation at very high operating temperature are insurmountable issues. As mentioned above, oxidation behaviour of Al- or Si-bearing intermetallic alloys is proven to be superior owing to the formation of passive scales of Al₂O₃ or SiO₂ (Mitra, 2006).

Figure 21 shows the free energy of formation of different oxides. It is seen that Al_2O_3 has the lowest free energy of formation compared with other oxides. Al_2O_3 and SiO_2 were considered as the most protective scales due to their low diffusivity for anions and cations and their thermodynamic stability (Meier and Petit, 1992). The former implies low parabolic rate constant for the growth of SiO_2 and Al_2O_3 (Mitra, 2006).

Compared with other oxides, particularly Al_2O_3 , SiO_2 is considered to be an optimal scale owing to its ability to form an amorphous scale in comparison with a crystalline state which might provide a short circuit path for diffusion (Menon et al, 2001 and Mitra, 2006). It has been pointed out that silica scale is more stable at elevated temperature than alumina due to having lower activation energy for oxygen (Menon et al, 2001 and Mitra, 2006). However, the evidence points to the fact that complex oxide scale formation would be expected during the oxidation of Nb silicide based in-situ composites (Menon et al, 2001). The rationale behind the abovementioned is the fact that oxides that are more stable than silica can form during the oxidation chiefly due to the presence of Al, Hf and Ti as alloying additions (Menon et al, 2001). Incidentally, the presence of stable oxides could be coupled with SiO_2 and Nb_2O_5 , both of which have virtually no solubility in the solid state (Menon et al, 2001). Notwithstanding the described advantages, silica's employability is systematically affected in humid conditions and temperature above 1100 °C at which it becomes volatile. Considering the proposed working temperature for Nb silicide based in-situ composites, which is above the working temperature of current Ni-based superalloys (>1350 °C), it is appreciated that alumina scale is deemed to be the best scale. This is owing to its stability at high temperature (not becoming volatile) and the fact that its workability is not affected by humid conditions (Pint, 2006).

1.6 Mechanical properties

A balance of high temperature and low temperature mechanical properties in Nb-silicide based in-situ composites seems to be an oxymoron, as improving some properties compromises other properties. Achieving acceptable high temperature yield strength and room temperature fracture toughness is the main instantiate of this oxymoron. Raising the volume fraction of Nb₅Si₃ will increase the yield strength and creep performance of the composite. However, it has a deleterious effect on room temperature fracture toughness, demonstrating the importance of finding optimum fracture toughness, yield strength and creep strength. Moreover, the oxidation of Nb-silicide in-situ composites and the role of alloying additions to improve it, are not excluded from this scenario. As described in the preceding section, some alloying additions will improve the oxidation resistance at the expense of attenuating other mechanical properties. This section elucidates the role of alloying additions on creep strength, fracture toughness and yield strength. An explanation of the role of alloying additions will be succeeded by a short account of the ability of the developmental alloy MASC to reach the property goals. The property goals for Nb silicide based in-situ composite are given in table 5.

It is helpful for that account to consider the MASC alloy and the roles of alloying additions in this particular alloy. The MASC alloy and specific Nb silicide based in-situ composites investigated in this project happen to have almost the same alloying additions although with different concentrations. The MASC alloy has received significant attention due to its improved mechanical properties as a result of alloying additions and has been considered as a baseline for investigating the role of alloying additions on mechanical properties (Bewlay and Jackson, 2003). The MASC alloy

comprises Nb,Ti,Hf,Si,Al and Cr with minor additions of Ge and Sn which are not given (Bewlay and Jackson, 2003). It contains $M_5(\text{Si,Al})_3$ type phases and $M_3\text{Si}$ silicide phase (Bewlay and Jackson, 2003). The nominal composition of the MASC alloy containing Ge and Sn, is Nb-24.7Ti-8.2Hf-16.0Si-2Cr-1.9Al (at%). Table 5 shows that the MASC alloy meets the goals of fracture toughness and yield strength.

Table 5: Property goals and present (2002) capability of Nb-silicide based in-situ composites (Bewlay and Jackson, 2003).

	<i>Property goal</i>	<i>Present capability</i>
Density	$< 7.0 \text{ g cm}^{-3}$	7.3 g cm^{-3}
1400 °C phase stability	Total stability	Demonstrated in silicide-based composites
RT fracture toughness	$> 20 \text{ MPa}\sqrt{\text{m}}$	$> 20 \text{ MPa}\sqrt{\text{m}}$
Fatigue-Paris law slope	< 5	2-5
ΔK_{th}	$> 10 \text{ MPa}\sqrt{\text{m}}$	6-13 $\text{MPa}\sqrt{\text{m}}$
Creep rupture	100 F improvement	Similar to CMSX10
Creep rate (s^{-1}) at 1200 °C	3×10^{-8}	1.2×10^{-8} : Nb-8Hf-25Ti-16Si (140 MPa) 1.5×10^{-8} : Nb-16Si (140 MPa)
Oxidation	$\sim 25 \mu\text{m}/100 \text{ h}$	$\sim 250 \mu\text{m}/100 \text{ h}$

1.6.1 Fracture toughness

Fracture toughness is an important mechanical property for turbine blades. Components must have acceptable fracture toughness to sustain impact throughout service (Bewlay and Jackson, 2003). The fracture toughness desired for Nb silicide based in-situ composites must exceed $20 \text{ MPa}\sqrt{\text{m}}$ (Bewlay and Jackson, 2003). In view of the fact that alloying additions added to Nb silicide based in-situ composites to improve the fracture toughness might have a negative impact on oxidation resistance because of changes in the Nb_{ss} to Nb_5Si_3 volume fraction and microstructure, reaching the goal is an arduous task.

1.6.1.1 Fracture mechanism

There are two possible options for Nb-silicide based in situ composites. They can have a ductile phase in a brittle matrix or a brittle phase in a ductile matrix (Chan , 2002). As Nb_{ss} is the ductile phase, Nb_{ss} is the phase that is responsible for the fracture toughness of the composite (Chan, 2005). Cleavage fracture happens through moving crack tips along grains by hitting the brittle phase (Davidson et al, 1999). Additionally, atomic bonds will be broken by moving a crack tip along the grains. The ductile phase can pin the crack when the crack moves through a ductile phase (Davidson et al, 1999 and Chan, 2002). In essence, the ductile phase's plastic dissipation in the microstructure (occurring under high plastic constraint) controls the fracture toughness of the composite (Davidson et al, 1999).

It has been pointed out that decreasing the Peierls-Nabarro barrier energy increases the fracture toughness of Nb-silicide in situ composites (Davidson et al, 1999 and Chan et al, 2005). With regard to this, it is inferred that alloying additions can increase the fracture toughness by reducing the Peierls-Nabarro barrier energy and (antiphase boundary and stacking fault energy). Furthermore, the microstructure of the composite can be altered by alloying additions in order to promote slip, for instance by partial dislocations (Davidson et al, 1999 and Chan et al, 2005).

1.6.1.2 The effect of alloying additions on fracture toughness

Fundamentally, the main mechanism in Nb silicide based in-situ composites to improve fracture toughness is to change the Nb_{ss}/Nb_5Si_3 ratio (Chan , 2002). Since Nb_{ss} is the phase responsible for the ductility of the composite, increasing the Nb_{ss} volume fraction will result in an increase in fracture toughness of the composite (Chan , 2002

and Kim et al, 2001). Additionally, increasing the volume fraction of Nb_5Si_3 (the brittle phase), will decrease the fracture toughness of the composite. Ti has a positive effect on the fracture toughness of Nb_5Si_3 (Chan, 2002). The measured fracture toughness of the latter alloyed with Ti was 50 % greater than unalloyed Nb_5Si_3 (Bewlay and Jackson, 2003 and Jackson et al, 2003) see figure 22.

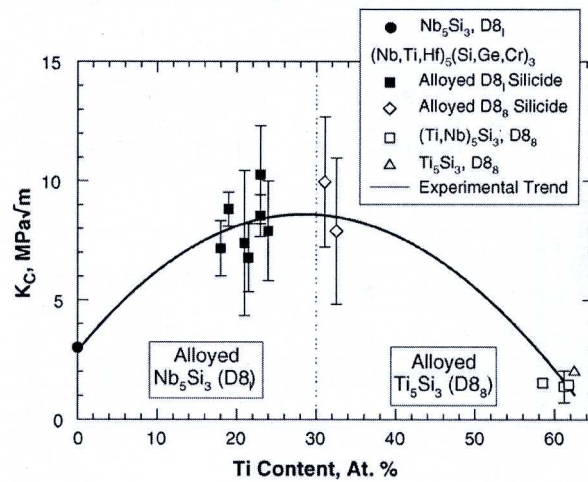


Figure 22: Effect of Ti on the fracture toughness of Nb-based silicide. Increasing the Ti concentration more than 30% led to a decrease in fracture toughness by stabilizing the Ti_5Si_3 (Chan, 2005).

Figure 22 shows that increasing the Ti content in $(Nb,Ti)_5Si_3$ up to 30 % increases the fracture toughness significantly and that Ti concentrations more than 30 % became detrimental to fracture toughness. The crystal structures of the Nb_5Si_3 and Ti_5Si_3 silicides are indicated in the figure. It can be deduced that the $D8_1$ is a desirable crystal structure and by increasing the Ti content beyond 30 %, the crystal structure changes to $D8_8$, leading to a decrease in fracture toughness. Hf has been reported to improve the fracture toughness of Nb silicide based in-situ composites (Tian et al, 2008 and Bewlay and Jackson, 2003). It has been reported that an increase in Hf content will change the fracture behaviour of Nb_{ss} from brittle cleavage to plastic behaviour (Tian et al, 2008).

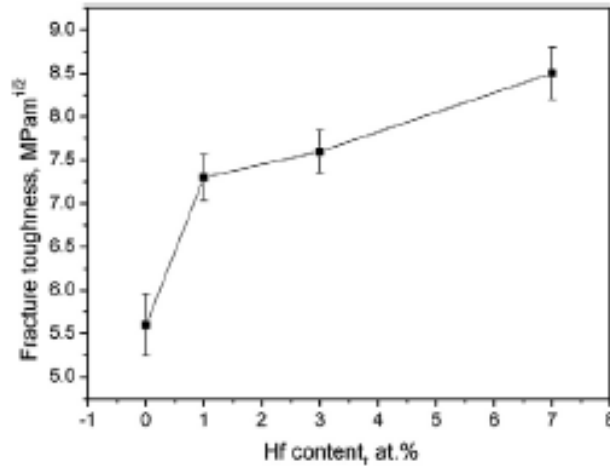


Figure 23: Effect of Hf on the room temperature fracture toughness of Nb-16Si (Tian et al, 2008)

With regard to figure 23, increasing the Hf content to 7 at% increased the fracture toughness of the Nb-16Si from 5.5 to 8.5 MPa√m. As it can be seen, there was a dramatic increase in the fracture toughness with 1 at% Hf addition that was followed by a steady increase in fracture toughness by raising the Hf content. It should be noted that figure 22 is for a single phase while figure 23 is for an alloy containing Nb_{ss} and Nb₅Si₃.

Regarding the positive effect of Hf on fracture toughness, it should be noted that the formation of primary Nb_{ss} particles will be promoted and the eutectic phases will be reduced as a result of the Hf addition (Tian et al, 2008 and Kim et al, 2001).

Given the fact that the existence of primary Nb_{ss} and the reduction in volume fraction of Nb₅Si₃ has a positive effect on fracture toughness, the promotion of the formation of Nb_{ss} will enhance the fracture toughness (Davidson et al, 1999 and Chan , 2002) and

most likely will deteriorate the oxidation resistance. Furthermore, Hf and Ti are the only elements that do not increase the ductile to brittle transition temperature (DBTT) of Nb but also improve the oxidation resistance (Chan , 2002).

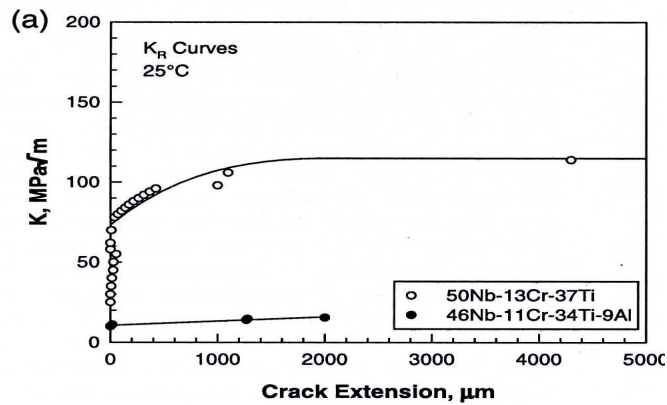


Figure 24: The deleterious effect of Al on fracture toughness is evident in the figure comparing the fracture toughness of 46Nb-11Cr-34Ti-9Al and 50Nb-13Cr-37Ti (Davidson et al, 1999 and Chan , 2002)

Al has been reported to prevent the nucleation of dislocations at the crack tip, confirming its detrimental effect on the fracture toughness of Nb-silicide based in-situ composites (Chan, 2002). Preventing dislocation formation at the crack tip will limit the plastic zone formation at the crack tip, thereby accelerating cleavage cracking (Davidson et al, 1999 and Davidson , 1999a).

Al and Cr also increase the DBTT, unlike Hf and Ti (Chan et al , 2002). Figure 24 shows the negative effect of Al on fracture toughness. As can be seen, the fracture toughness of the alloy 46Nb-11Cr-34Ti-9Al was decreased significantly compared with the alloy 50Nb-13Cr-37Ti. For ease of demonstration, the cleavage crack formation in the alloy 46Nb-11Cr-34Ti-9Al is shown in figure 25 (Chan , 2002 and Davidson et al, 1999).

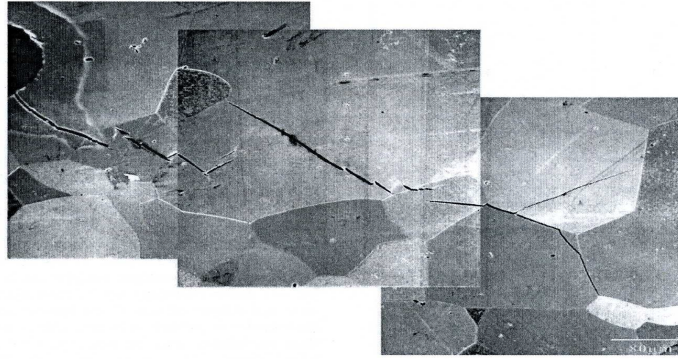


Figure 25: The occurrence of cleavage in Nb-11Cr-34Ti-9Al (Chan , 2002)

As mentioned above, Si has a deleterious effect on fracture toughness by increasing the volume fraction of Nb_5Si_3 thereby increasing the brittleness of the composite (Bewlay et al, 2003). According to Bewlay et al (1995b and 2003), decreasing the Si concentration from 18 at% to 10 at%, increased the fracture toughness from 6 to 14 $MPa\sqrt{m}$. Alloying additions that increase the volume fraction of Nb_{ss} will increase the fracture toughness, and those that increase the volume fraction of Nb_5Si_3 will decrease the fracture resistance of the composite. Considering the exceptional effect of Si on creep and oxidation resistance and its negative effect on fracture toughness, it is a major challenge to achieve a balance between high temperature and low temperature properties. Figure 26 shows the measured fracture toughness of Nb silicide based in-situ composites with different alloying additions. The horizontal line shows the fracture toughness goal, which has been set as 20 $MPa\sqrt{m}$. The MASC alloy fracture toughness exceeded 20 $MPa\sqrt{m}$, as reported by Bewlay and Jackson (2003).

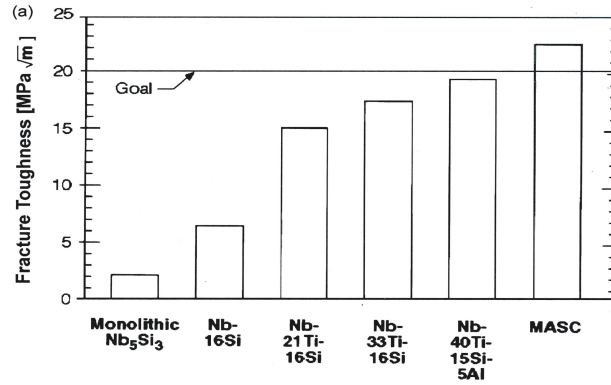


Figure 26: Fracture toughness of different Nb-silicide based in-situ composites including monolithic Nb₅Si₃ (Bewlay and Jackson, 2003)

1.6.2 Intermediate and high temperature strength

Grain size and solid solution strengthening play a vital role in high temperature yield strength, and predominantly control it. Heat treatment controls the grain size, and the microstructure of the composite can be refined by alloying additions (Subramanian et al, 1996 and Mendiratta et al, 1991).

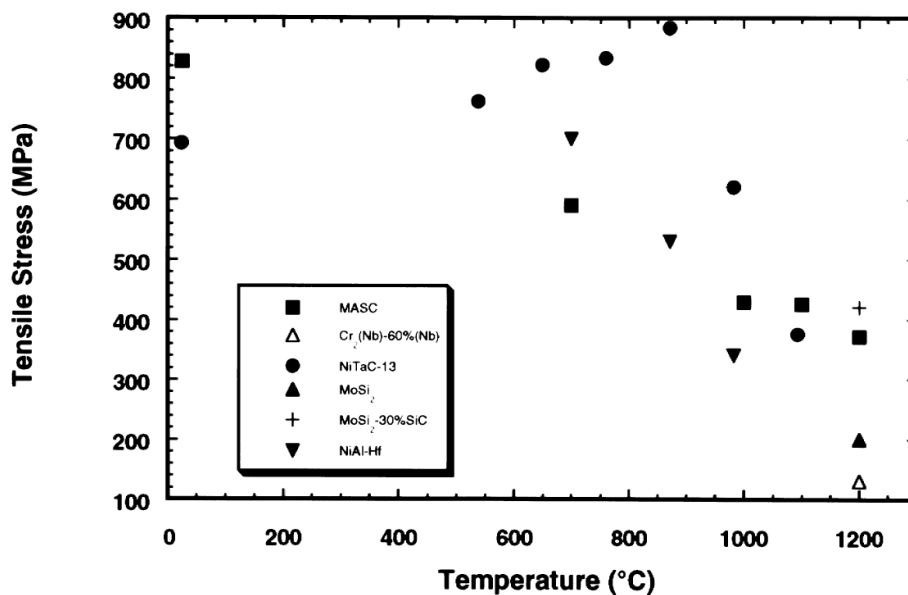


Figure 27: Tensile strength of a variety of in situ composites as a function of temperature. The circle indicates a Ni-based superalloy and the square shows the tensile strength of the MASC alloy at different temperatures. The improved tensile

strength of the MASC as compared with Ni-based superalloy is evident in the picture (Bewlay and Jackson, 2003).

Figure 27 compares the tensile strengths of different in situ composites as a function of temperature with a Ni-based superalloy, the latter indicated as NiTaC-13 in the figure. The MASC alloy's high temperature strength (1200 °C) is similar to the Ni-based superalloy confirming the potential of Nb silicide based in-situ composites to outperform the Ni-based superalloys. There are two ways to effectively enhance the high temperature strength of Nb silicide in-situ composites. Additions of refractory and high modulus elements can influence the solid solution strengthening (Bewlay et al, 2003 and Anton et al, 1989). Precipitation strengthening, such as dispersion strengthening, can be performed by using refractory nitrides or MC carbides (Bewlay and Jackson, 2003 and Anton et al, 1989).

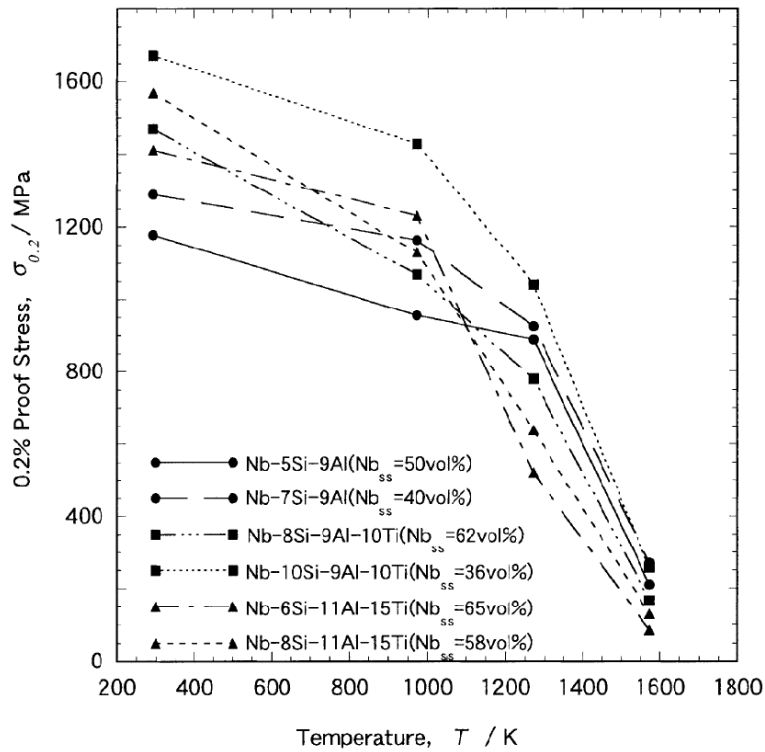


Figure 28: Yield strength as a function of temperature for a range of Nb-silicide based in-situ composites (Murayama et al, 2002).

As can be seen in figure 28, which shows compressive yield strength of Nb-Si-Al-Ti alloys as a function of temperature, the addition of Ti leads to an increase in yield strength from room temperature up to 827 °C (Murayama et al, 2002). However, the compressive yield strength decreases drastically when increasing the Ti addition beyond 827 °C. Moreover, it can be inferred from the diagram that the high temperature strength is vastly affected by the Nb_{ss} volume fraction. The compressive yield strength has been decreased by an increase in Nb_{ss} volume fraction (Murayama et al, 2002).

1.6.2.1 Creep resistance

Creep resistance is of paramount importance for the components employed at elevated temperature. When operating at high temperature under load, for instance centrifugal load, it is important to decrease the creep rate of the high temperature components of

the jet engine, for instance high-pressure turbine blades. Dislocation creep and diffusion creep (Nabarro Herring and Coble creep) are the dominant creep mechanisms at a homologous temperature ≤ 0.8 (Dieter, 1986).

The diffusion of Nb in the Nb₅Si₃ silicide controls the creep deformation in Nb₅Si₃ (Subramanian et al , 1995). The combined function of creep in the silicide and solid solution phase controls the creep of the composite (Bewlay and Jackson, 2003). Alloying additions' effects on creep strength can be interpreted by the Sherby model in accordance with which high temperature creep strength is enhanced by valance and high melting temperature (Tsakiropoulos, 2010). Valance signifies that diffusion rate is decreased by increasing the bonding electrons (Tsakiropoulos 2010). Hence, substitutional elements in Nb that have high melting temperature, high elastic modulus and large electron-atom ratio are effective in enhancing the creep strength of the composite (Tsakiropoulos 2010).

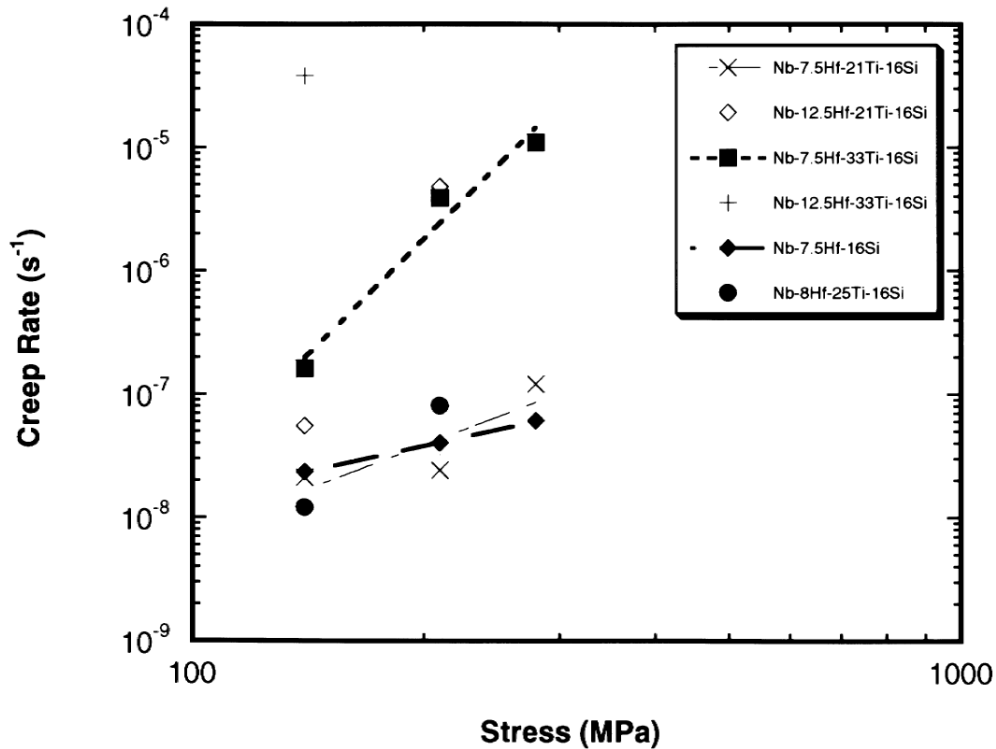


Figure 29: Secondary creep rate of quaternary Nb-Hf-Si-Ti in situ composites at 1200 °C (Bewlay and Jackson, 2003)

The detrimental effect of increasing the Ti content on the creep strength of Nb-silicide based in-situ composites is illustrated in figure 29 that shows the creep rate at 1200 °C of different Nb-Si-Ti-Hf alloys. The data shows that an increase in Ti content led to an increase in the creep rate. It can be seen in figure 29 at different stress levels, raising the Hf content increased the creep rate confirming the deleterious effect of increasing the Hf content (Bewlay and Jackson, 2003). It has been suggested that for obtaining the best creep performance, the Nb/(Ti+Hf) ratio should be above 1.4 and the Ti concentration must be less than 21% (Bewlay and Jackson, 2003 and Chan, 2002). It is postulated that at a high (Ti:Hf) ratio, the formation of Nb₅Si₃ is suppressed and hexagonal Ti₅Si₃ is stabilized. Since Nb₅Si₃ has a rather high melting point, the formation of Ti₅Si₃ is unfavourable to the creep strength of the composite (Bewlay et al, 1995b, 2003, and Chan 2002).

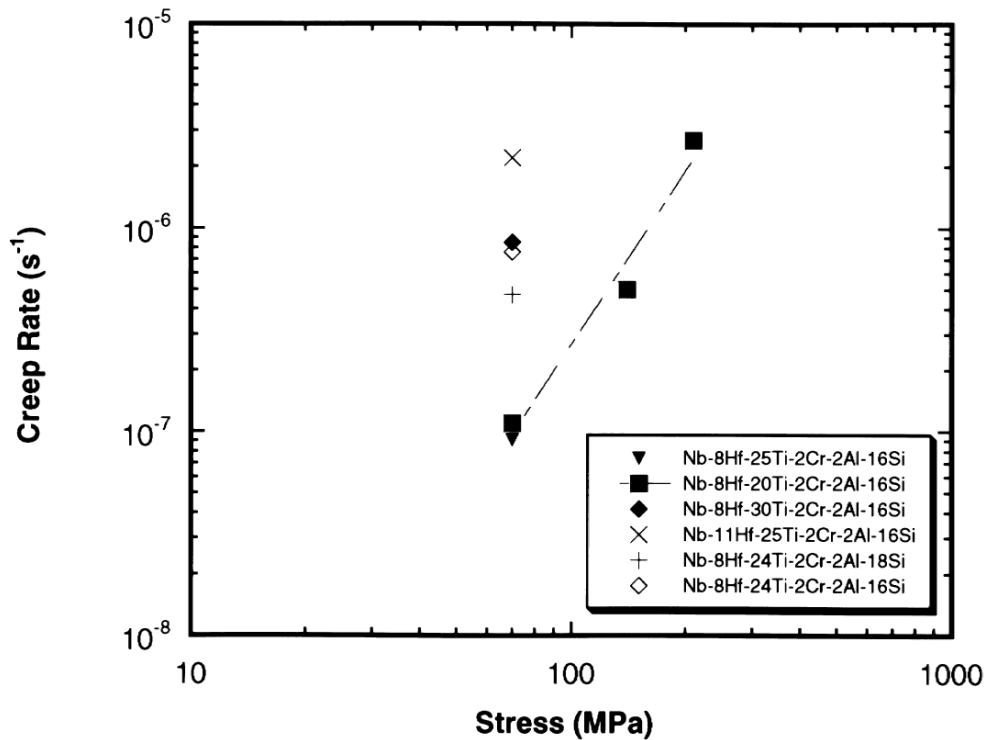


Figure 30: The deleterious effect of Ti on creep strength is shown by the data for the secondary creep rate of a range of Nb-Al-Ti-Si-Hf-Cr in at% composition at temperature 1200 °C. All alloys failed at stress greater than 70 MPa except Nb-8Hf-20Ti-2Cr-2Al-16Si containing the lowest Ti addition (Bewlay and Jackson, 2003).

The secondary creep rate of different Nb-Hf-Ti-Si-Cr-Al alloys at 1200 °C is shown in figure 30. Some significant points have to be made regarding the variations in creep rate as a result of alloying additions. The creep rate decreases with an increase in the Si concentration from 16% to 18%. This can be attributed to promoting the formation of Nb₅Si₃ thereby increasing the volume fraction of Nb₅Si₃, which is the phase responsible for the creep performance of the composite (Bewlay and Jackson, 2003 and Subramanian et al, 1995). The creep rate is increased by an increase in Ti concentration, confirming the detrimental effect of Ti on creep performance in concentrations of more than 21% (Bewlay and Jackson, 2003). As mentioned previously, increasing the

concentration of Ti and Hf helps to promote the formation of Ti_5Si_3 and Hf_5Si_3 type hexagonal silicide having a lower melting temperature than Nb_5Si_3 , which is an undesirable outcome for creep strength. Concerning the negative effect of Ti on the creep strength and an increase in the creep rate, Hf bears strict resemblance to Ti in a sense that increasing the Hf from 8% to 11% caused the creep rate to increase (Bewlay and Jackson, 2003).

Starting with W, the most effective solute in Nb for enhancing creep strength, effective solutes in Nb in terms of creep strength can be descendingly ranked as follows: W, Os, Ir, Re, Mo, Ru, Ta and Cr (Tsakiroopoulos, 2001 and McAdam, 1964).

Chapter 2: Experimental procedures

2.1 Selection of alloys

Nb silicide based alloys that meet mechanical property goals and have inherent oxidation resistance will be candidate materials for structural engineering applications in future aero-engines where they will be used with a suitable coating system, most likely of the bond coat (BC)/thermally grown oxide (TGO)/ceramic top coat type (such coating systems are often referred to as thermal barrier coatings or TBCs). Inherent oxidation resistance means (i) no pest oxidation in the pest regime and (ii) stable adherent scale with acceptable oxidation (growth) rate at $T \geq 1200$ °C, the latter compared with the single crystal Ni superalloy CMSX-4 at 1100 °C.

Scales consisting of Al_2O_3 , Cr_2O_3 and SiO_2 can protect alloys from high temperature oxidation. Cr_2O_3 is suitable up to about 1000 °C because at higher temperatures gaseous CrO_3 is formed and the stability of Al_2O_3 is better than SiO_2 in humid environments. Only alumina and silica are desirable above 1000 °C. Nb silicide based alloys are Si rich (so that silicides can be stable in their microstructures) but their concentration of Al cannot be high (to ensure alumina stability) owing to the adverse effect high Al contents have on toughness and high temperature strength. Furthermore, the concentration of Cr in these alloys needs to be controlled because high Cr contents stabilise a Laves phase in their microstructure, and the oxidation is improved but at the expense of fracture toughness. To date, the scales formed on developmental Nb silicide based alloys can contain silica in the presence of Ti and/or Al, Cr niobates. Pest oxidation is suppressed by additions of B, Ge or Sn which can also improve scale adhesion depending on the other elements present in the alloy.

The main objective of this research was to find out if Cr free Nb-Ti-Al-Si-Hf alloys that do not pest can form stable α -Al₂O₃ scales that do not spall off. The alloys selected for this work are given in table 6.

Table 6: The alloys selected for this work, composition at%

Alloy	Nb	Si	Ti	Al	Hf	$\frac{[\text{Hf}+\text{Ti}]}{[\text{Al}+\text{Si}]}$	sd/sp	Al/Si	Al/Ti	Si/Ti
MG1	44	22	24	5	5	≈ 1.1	2.7	0.2	0.2	0.92
MG2	19	22	24	30	5	0.56	0.92	1.36	≈ 1.3	0.92
MG5	18	25	23	30	4	0.49	0.82	1.2	1.3	≈ 1.1
MG6	12	23	23	38	4	0.44	0.64	1.65	1.65	1

It was decided to study first the alloy Nb-24Ti-22Si-5Al-5Hf (alloy MG1 in table 6) in order to improve our understanding of phase stability and oxidation in Nb-Ti-Si based alloys with Al or Hf addition. This knowledge would then link with that emerging from other research in the group on the oxidation of Nb-24Ti-22Si-5Al based alloys with additions of B, Ge, Sn with/out Hf.

The alloy MG1 was used as reference to design the alloy MG2 with same Si/Ti ratio and higher Al/Si and Al/Ti ratios to understand what the effect of increased Al content is on phase stability and oxidation. In the table 6 the sd/sp ratio is the ratio of sd electronic configuration elements over sp ones, thus as the Al content increases the sd/sp ratio will decrease. The (Hf+Ti)/(Al+Si) ratio considers the sd elements that improve oxidation (numerator) over the sp ones (denominator).

The alloy MG2 was then used as reference to explore the effect of higher Al content (Al substituting Nb) on oxidation in the alloys MG5 and MG6. The latter alloys were selected:

(i) with $Al/Ti \approx 1.3$, increase Si content and have the same Al/Si and Si/Ti ratios (alloy MG5) and

(ii) with $Si/Ti \approx 1$, increase Al and have the same Al/Ti and Al/Si ratios (alloy MG6)

2.2 Alloy making

The arc-melting method was chosen for alloy making. This is standard method used for making intermetallic and high temperature alloys even though it has the following drawbacks: no control of the melt superheat, variation of cooling rate along thickness of the ingot, loss of low melting elements due to vaporization and thus limited control of alloy composition and macrosegregation in the ingot. High purity elements (Ti 99.99 %, Nb 99.99 %, Si 99.99 %, Al 99.99 %, Hf 99.99 %) were arc melted in a water cooled crucible in an argon atmosphere using a non-consumable tungsten electrode. 15 g ingots were prepared. Materials were placed in the crucible and the chamber was closed to be vacuumed. The chamber was evacuated to 10^{-5} mbar via a rotary pump succeeded by a diffusion pump. After reaching the aimed vacuum pressure, the arc-melter was left for roughly an hour to be rest assured of any leaking. Consequently, the chamber was filled with argon. A voltage of 20 V and a current of 850 A were used. The melting procedure was repeated 3 times. At the end of each cycle, the sample was flipped in order for homogeneity to be improved.

2.3 Heat treatment

A tube furnace was chosen for the heat treatments. The cut specimens were wrapped in Ta foil and placed in an alumina boat and put in the tube furnace. The alumina boat was placed in the centre of the furnace along with Ti-sponge boats on each side. Three different temperatures were selected for heat treatment, namely 800, 1200 and 1300 °C based on the composition of the alloy (alloys MG1 and MG2 were heat treated at 1300 °C for 100 h and alloys MG5 and MG6 were heat treated at 800 and 1200 °C for 100 h) . Each heat treatment was performed in an argon atmosphere.

2.4 Specimen preparation

2.4.1 Specimens for SEM and EDS study

The alloy button ingot was cut using an ISOMET5000 precision saw with a diamond blade. Thick slices from the centre of the ingot were cut for microstructural characterization. Samples were mounted in conductive Bakelite. Some oxidised samples, due to their brittle nature, were cold mounted to avoid the pressure of hot mounting which could have conceivably crushed them. Subsequently, the samples were grounded using different ranges of grinding papers (240, 420, 800, 1200, 2500, and 4000) they were finally polished with 1 µm cloth.



Figure 31: a labelled diagram showing where the samples have been obtained

2.4.2 Specimens for XRD study

The prepared samples for SEM/EDS analysis were used for Bragg-Brentano and glancing angle X-ray diffractometry. For powder XRD, the powder of alloy MG1-AC was prepared from the as cast ingot and crushed. The spalled off scale of the alloy MG1 oxidized at 1200 °C was crushed and the powder was used for XRD powder analysis.

2.4.3 Specimens for TGA study

Cube shaped (where possible) samples from the as cast ingots were prepared for TGA analysis. They were cut into 0.4 cm x 0.4 cm x 0.4 cm cubes. However, cutting some samples in a cube shape was impossible and therefore the optical microscope and its related software were used to measure the surface area of the prepared specimen for TGA analysis. The samples were polished using 800 and 1200 grinding papers.

2.5 Alloy characterization

2.5.1 X-ray diffraction

A Siemens D5000 diffractometer with a $\text{CuK}\alpha$ ($\lambda = 1.54178\text{\AA}$) was used for bulk phase identification in as cast, heat treated and oxidized samples. The XRD experiment was performed at a scan speed of 2° min over a 2θ range of 20 to 100. The same machine was used for glancing angle XRD to study the oxide products formed on the oxidized specimens. The glancing angle XRD was performed at a scan speed of 2° min over a 2θ range of 20 to 100 with $\theta = 5^\circ$.

A STOE-STADI P (CUIP) was used for powder XRD of the as cast alloy MG1 and the spalled off scale of the alloy MG1 oxidized at 1200 °C. For phase identification the WINXPO and PDF4 databases were used. The PDF4 software was extensively used owing to its broad entries and its filter algorithms for better results and more accuracy. The produced file by the XRD machine and the possible existent elements within the alloy were imported into the software. The existent phases were matched against the database and the phases were recorded. The user had a choice to insert different PDF cards manually and to check whether the sought-after phases could fit, the process which was widely used in this research particularly in terms of identifying the oxide products. The identification process of some niobates was possible due to the broad entries in the PDF4 software. Data about crystal structure, lattice parameter, etc were also available.

2.5.2 Scanning electron microscopy

Three different SEM microscopes were used. Secondary and backscatter electron imaging was used. A FEI INSPECT F50, JEOL 6400 and PHILIPS 30S XL FEG were used. The FEI INSPECT F50 and PHILIPS 30S XL FEG were equipped with field emission gun and therefore almost all BSE images were taken using those machines. The image acquisition was performed at 20 Kv.

2.5.3 Energy dispersive X-ray spectrometry

The JEOL 6400 and PHILIPS 30S XL FEG microscopes were equipped with EDS detectors and were used for quantitative analysis. Large area and spot analysis were performed with an acceleration voltage of 20 Kv. A large area analysis was done at 300 X magnification. Both microscopes were equipped with INCA software and were

equipped with elemental standards of Nb, Hf, Ti, Al, Si. The calibration of the detector was conducted each time before starting the quantitative analysis and was repeated every 2 hours. The procedure used pure Co standard and was done twice each time to yield an acceptable dead time between 25 to 30 %. At least 10 spectra were acquired from the top, bulk and bottom of the as cast, heat treated and oxidized alloys for large area analysis.

2.5.4 Differential scanning calorimetry

A NETSZCH machine was used for DSC analysis. The DSC was performed to determine the melting temperature of the alloy to make sure that the alloy will not melt at the temperature of interest .ie. 800, 1200 and 1300 °C. The samples were run along with the balance at the designated heating rate (10 degrees per minute or 20 degrees per minute) to 1500 °C and were cooled using the same rate. (A DSC trace) was produced at the end of the experiment showing the exothermic reaction through which any melting up to the targeted temperature was detected. DSC samples were taken from the centre of the ingots, with less than 5 g. The samples were weighed before the test and the weight was inserted into the software linked with the machine so that the DSC graph could be produced. They were finally put into an alumina crucible. The DSC experiments were done under argon flow. The machine was left at least one hour with the balance and argon flowing before starting the experiment in order for it to be calibrated and stabilized.

2.5.5 Thermo-gravimetric analysis

A NETSZCH machine was used for study of the isothermal oxidation of the alloys MG1, MG2 and MG6 using TGA. Cube specimens whose surface area had been

measured were weighed and placed in an alumina crucible. The 800 and 1200 °C temperatures were selected for the TGA experiment. The TGA tests were performed with a heating and cooling rate of 3 degrees per minute. Samples were heated at the designated heating rate to the temperature of interest where they were kept for 100 h and then cooled at the same rate to room temperature. The curve of weight gain against time and temperature at the end of each experiment was produced measured to calculate the oxidation behaviour of each alloy.

Chapter 3: The alloy Nb-24Ti-22Si-5Al-5Hf

3.1 Alloy Nb-24Ti-22Si-5Al-5Hf (MG1)

3.1.1 As cast

The nominal composition of the alloy MG1 is shown in table 7. The actual composition was Nb-22.3Ti-21.3Si-4.5Al-5.4Hf. The latter was determined by EDS analyses of the top, bulk and bottom of the ingot. The EDS data is shown in table 8. There was small deviation from the nominal composition, which is not uncommon in alloys produced with arc melting and with alloys that contain elements that have high vapour pressure, like Al, the loss of which by evaporation is common in arc melting.

Table 7: Nominal composition (at %) of alloy MG1-AC

Alloy	Nb	Si	Ti	Al	Hf
MG1	44	22	24	5	5

There was macrosegregation of Si and Ti. The concentration of Si varied between 26.2 at% and 18.8 at% and the concentration of Ti between 25.3 at% and 20.1 at%. Given that Si and Ti are the two major alloying elements in the alloy MG1, their macrosegregation led to variation in the Nb concentration in the top, centre, and bottom of the ingot. The Nb concentration in the centre of the ingot reached 49.8 at%.

The microstructure of the alloy MG1-AC is shown in figure 32 and figure 33. The XRD data for the phases is shown in figure 34a and the quantitative EDS analysis data is shown in table 8. The cast microstructure of the alloy MG1 consisted of bulky Nb₅Si₃ grains with Nb_{ss} and Nb_{ss} + Nb₅Si₃ eutectic (figure 35). The latter was fine and had formed with a low volume fraction in the top and centre of the ingot, particularly in the

latter area. Some of the bulky Nb₅Si₃ grains exhibited cracking, similar to that reported by Geng et al (2006). The cracking was more severe in the bulk microstructure.

There was microsegregation of Hf in the Nb₅Si₃ (figure 32, figure 33 and figure 35). This made the characterisation of the microstructure using BSE imaging in the SEM very difficult as often different phases could not be distinguished by their contrasts. The Hf rich silicide was observed in the bottom and in the transition from bottom to bulk microstructure where it exhibited brighter contrast (see figure 33 and figure 35) compared with the silicide in the top and bulk of the ingot. In the latter parts, the “normal” Nb₅Si₃ was observed.

According to the XRD data (figure 34a) both the tetragonal βNb₅Si₃ and hexagonal γNb₅Si₃ were present in the microstructure. It should be noted that the compositions of the “normal” and Hf-rich Nb₅Si₃ in table 8 are the averages of the analysis data from all parts of the ingot. Whilst in the “normal” Nb₅Si₃ the standard deviation of Ti was small and the minimum and maximum analysis values close to each other, in the Hf-rich Nb₅Si₃ in the bottom of the ingot the maximum Ti values with the corresponding high Hf concentrations gave Nb/(Ti+Hf) < 1, which according to the empirical rule of Bewlay (Bewlay and Jackson, 2003) would indicate the presence of hexagonal γNb₅Si₃, in other words the XRD and EDS data for the silicide were in agreement.

In the Nb_{ss} the average Si concentration was very close to the maximum solid solubility of Si in Nb at the eutectic temperature, but in the top and bulk of the ingot the standard deviation of Si in the Nb_{ss} (like that of Ti in the Nb_{ss}) was larger compared with the values in the bottom. In other words, there was some microsegregation of Ti in the Nb_{ss},

but this was not accompanied by micro-segregation of Hf or Al. The average concentration of Ti in the Nb_{ss} was essentially the same as that in the alloy. In the Nb_{ss} + Nb₅Si₃ eutectic, the standard deviations of Si and Ti were significant, reflecting the variations of the concentrations of these elements in the Nb_{ss}.

Table 8: EDS analysis data (%at) of the as cast MG1 alloy

Area and Phase analysis		Element				
		Nb	Si	Ti	Al	Hf
Large area	Top	47.5±2 44.8-49.7	20.5±1.8 18.8-22.0	22.2±1.2 21.4-23.5	4.6±0.4 4.4-4.9	5.2±0.4 4.8-5.6
	Bulk	45.4±2.0 43.0-49.8	22±1.8 19.4-26.2	22.3±1.2 20.5-24.2	4.67±0.4 3.5-5.2	5.6±0.4 4.9-6.0
	Bottom	46.3±2 42.1-49.1	21.1±1.8 19.3-23.7	22.5±1.2 20.1-25.3	4.6±0.4 3.94-5.1	5.5±0.4 4.5-5.6
	Average	46.2±2.1 42.1-49.8	21.3±1.8 18.8-26.2	22.3±1.2 20.1-25.3	4.5±0.4 3.5-5.2	5.4±0.4 4.5-6
Phase (spot) analysis		Nb _{ss}				
	Top	64.7±2.6 61.9-68.6	3.9±1.2 2.5-5.3	21.9±1.3 19.6-23.2	6.4±0.1 6.4-6.7	3.1±0.2 2.9-3.5
	Bulk	63.6±3.3 58.9-68.6	4.1±1.3 2.8-5.4	22.5±2.0 19.5-25.7	6.2±0.2 6.0-6.5	3.6±0.3 3.1-4.0
	Bottom	67.1±0.5 66.7-67.8	2.8±0.1 2.7-3.0	20.9±0.6 20.3-21.5	6.0±0.4 6.0-6.1	3.1±0.1 3.1-3.1
	Average	64.8±2.9 58.9-68.6	3.8±1.2 2.5-5.4	21.9±1.6 19.5-25.7	6.2±0.2 6-6.7	3.3±0.3 2.9-4
		Nb ₅ Si ₃				
	Hf-rich	36.2±2.2 31.5-38.1	36.1±1.5 32.7-37.5	17.7±3 15.9-24.7	2.9±0.4 2.5-3.8	6.9±0.5 6.5-7.8
	Normal	43.5±1.2 40.5-44.5	35.3±1.4 34.1-36.5	14.4±0.3 14-14.9	3.4±0.3 3-3.9	3.8±0.3 3.6-4.4
Large area		Eutectic				
	Average	52.6±2.4 49.3-57.8	15.5±1.2 12.1-17.9	22.1±2.1 18.5-26.1	5.1±0.4 4.5-5.7	4.6±0.3 3.9-5.2

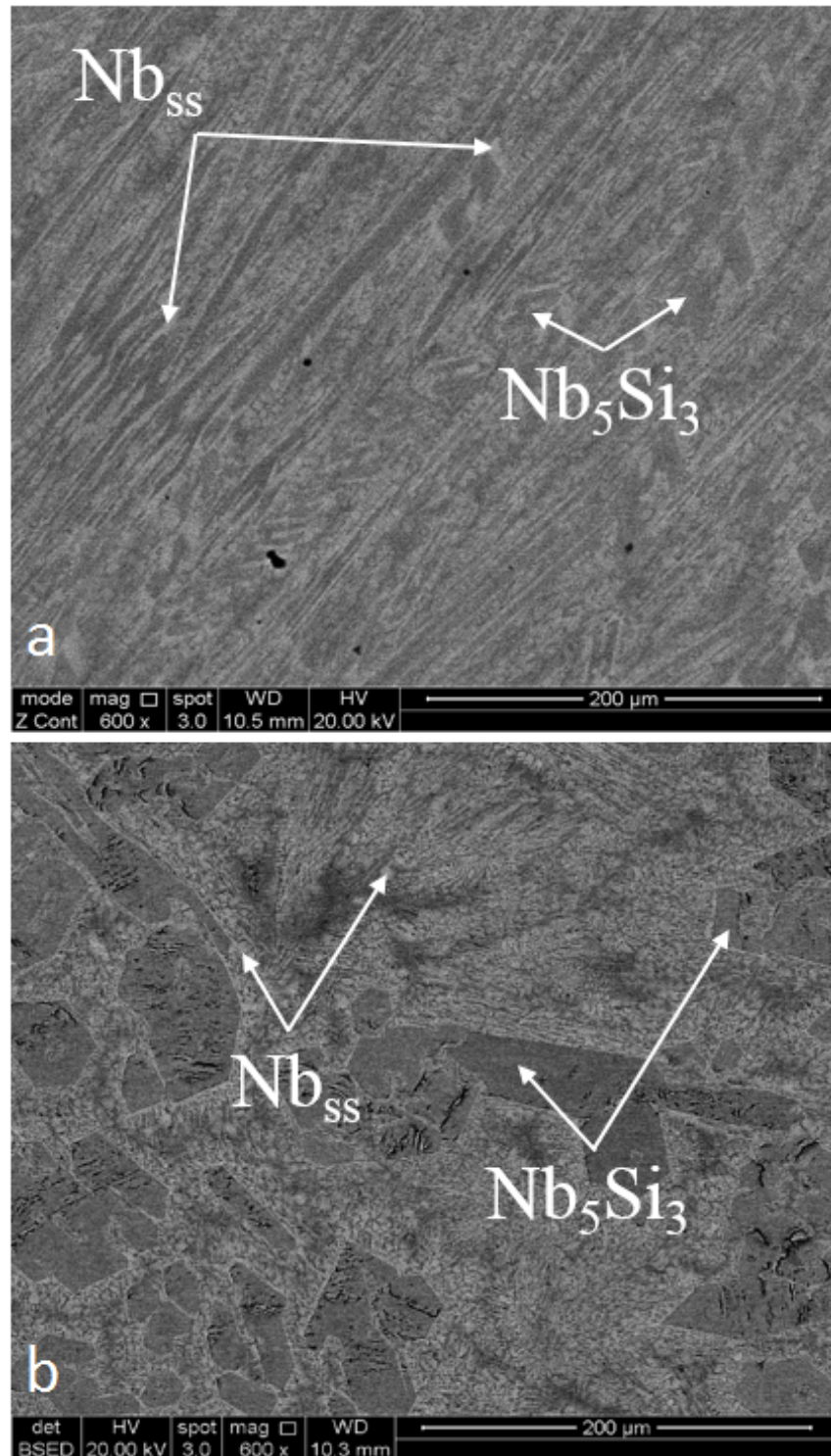


Figure 32: SEM backscatter electron images of the microstructure of MG1-AC in the top (a) and centre (b) of the ingot

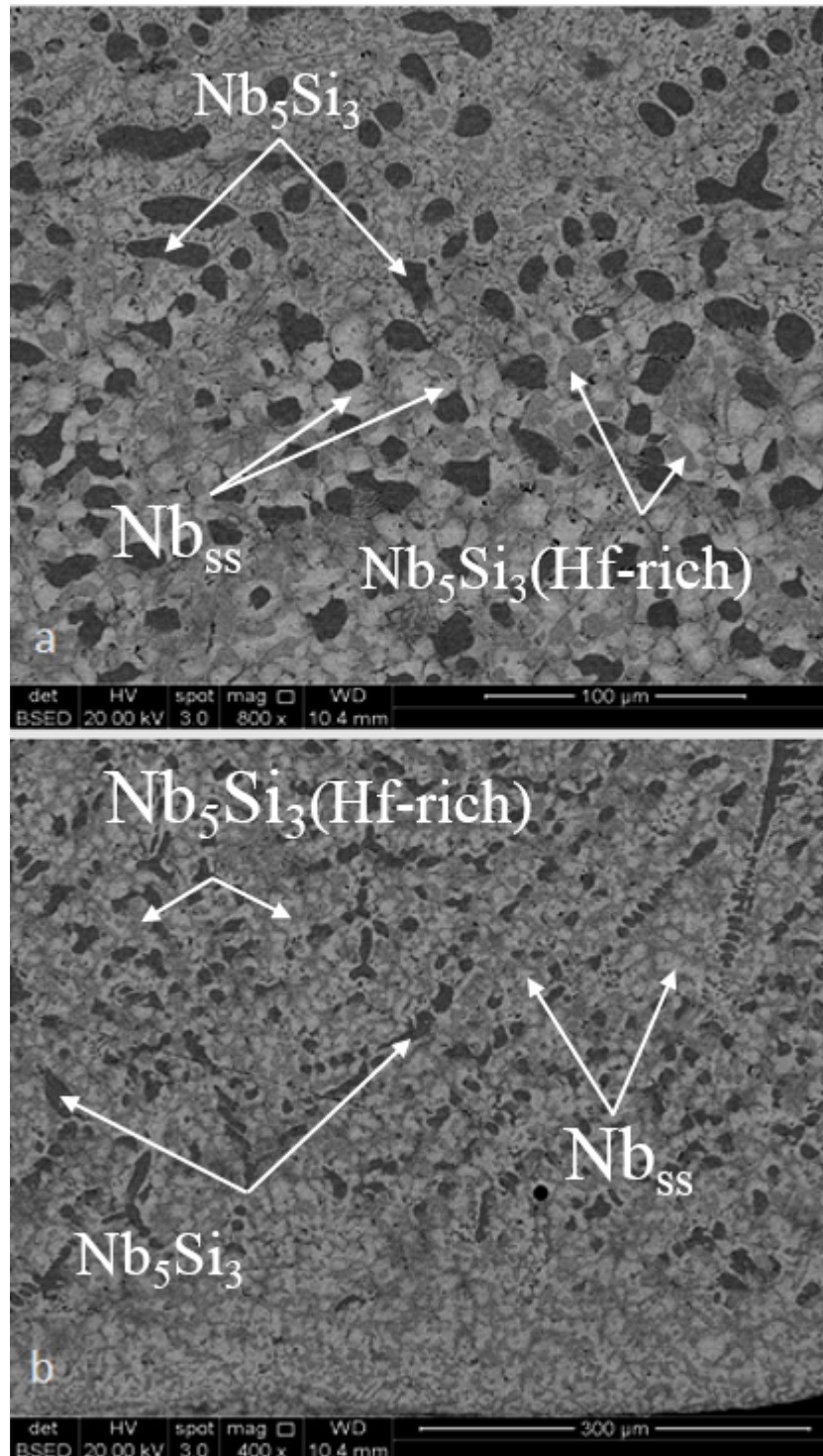


Figure 33: BSE images taken from the bottom of the ingot. The microstructure formed at the very bottom, where the melt was in contact with the water cooled Cu crucible, is shown in (b).

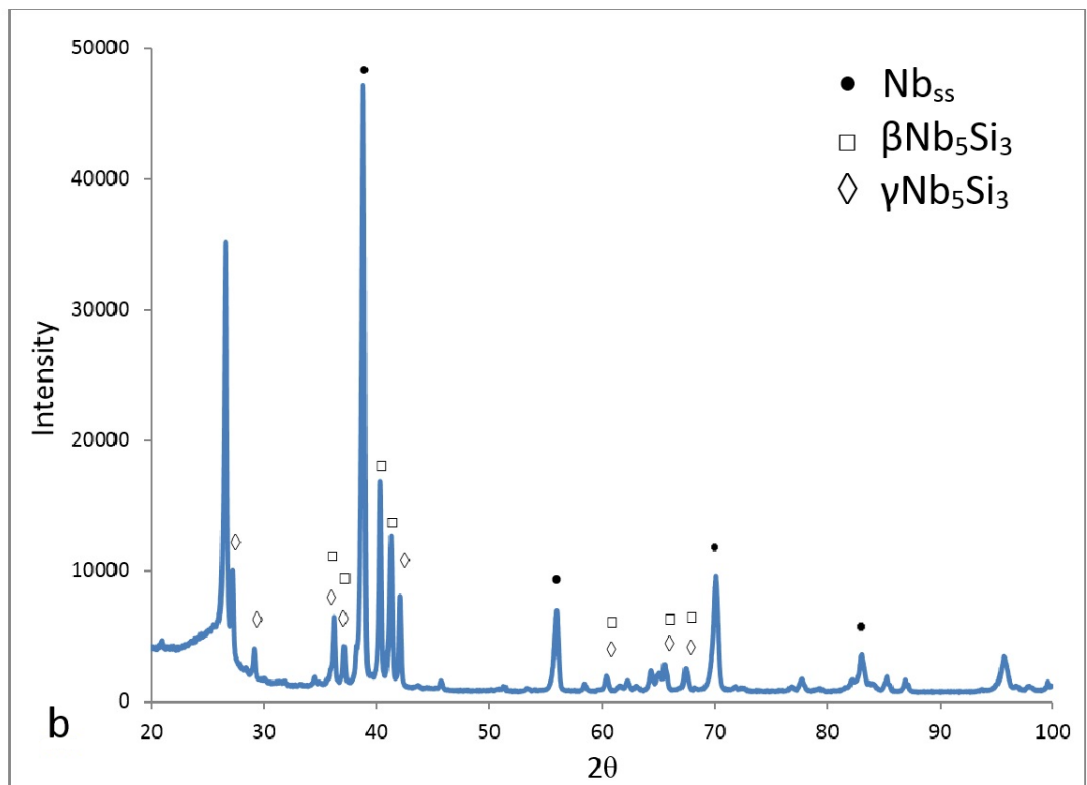
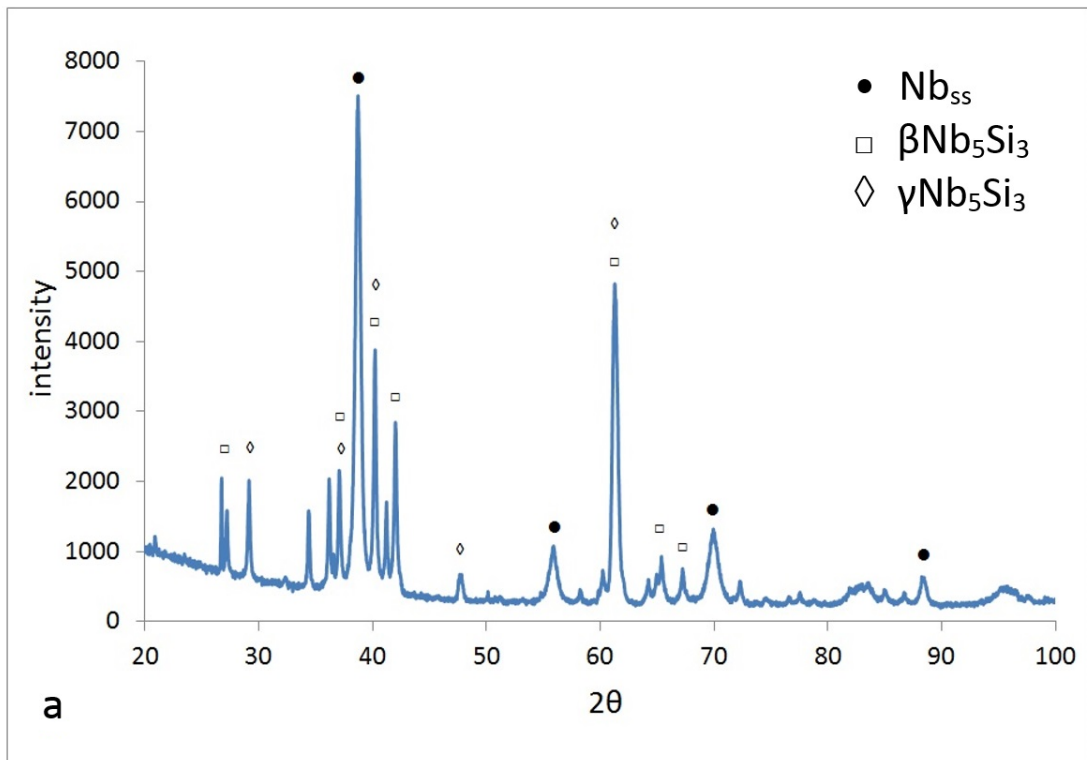


Figure 34: X-ray diffractograms of powder of the as cast (a) and solid specimen of the heat treated alloy (b)

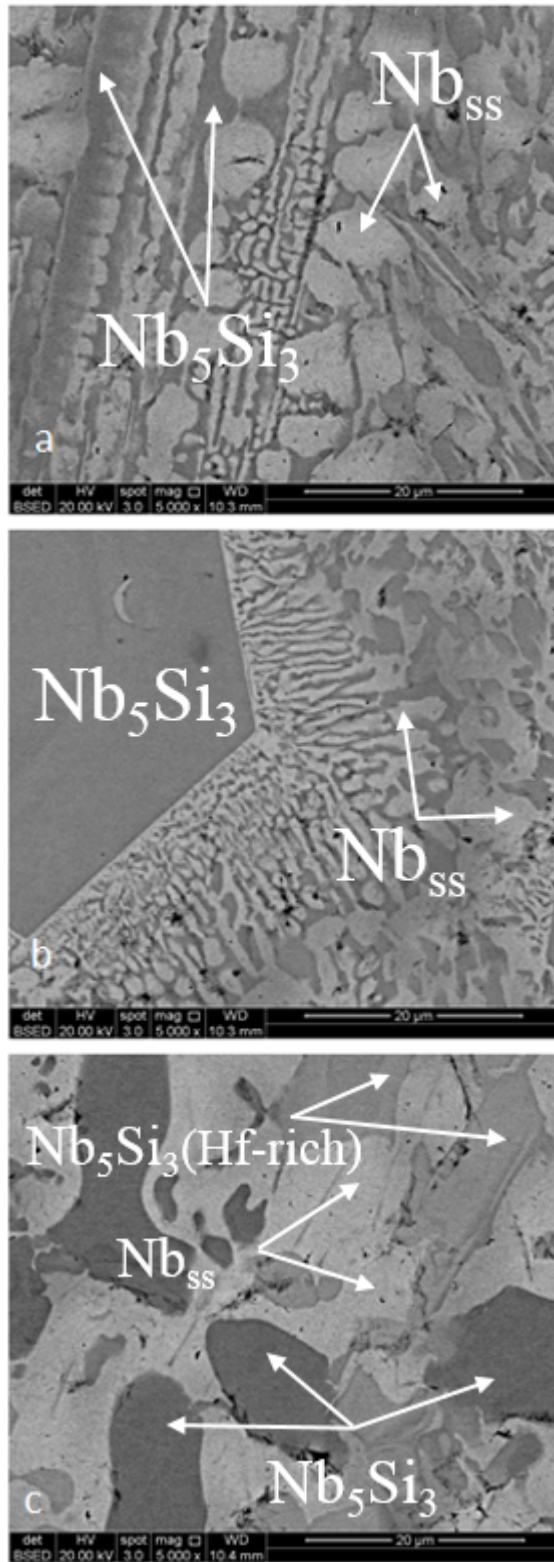


Figure 35: BSE images taken from different areas of the MG1-AC, where a,b and c represent the top, centre and bottom of the ingot, respectively.

3.1.2 Heat treated

The alloy MG1 was heat treated at 1300 °C for 100 h. The average composition of MG1-HT was Nb-21.3Ti-20.5Si-4.3Al-5.7Hf, not significantly different from that of MG1-AC (table 8). The aforementioned composition was the average of all large area analyses taken from the top, bulk and bottom of MG1-HT, see table 9. There was still chemical inhomogeneity of Si and Ti, for which the differences between maximum and minimum concentrations were 9.1 and 5.9 at%, respectively.

The microstructure of MG1-HT is shown in figure 36, figure 37 and figure 38 and the XRD data in figure 34b. Figure 37 shows that there was contamination by nitrogen and oxygen near the top and bottom surface areas of MG1-HT where TiN and HfO₂ were formed. The latter two phases were not observed in the top, bottom or the bulk of MG1-HT, which would suggest that the synergy of Al and Hf was effective in decreasing the diffusivity of interstitials to the bulk of the alloy.

The microstructure was essentially stable, as comparison of figure 32, figure 33 and figure 35 with figure 36 and figure 38 would confirm. The same phases were present, namely β and γ Nb₅Si₃ and Nb_{ss} (figure 34b), prior eutectic could still be observed in the centre and the volume percentage of the silicide in the top of MG1-HT had increased from 4% to 7% compared with MG1-AC. There was still Hf rich Nb₅Si₃ with essentially similar Ti and Hf concentrations and similar Ti standard deviation as in MG1-AC, with the high Ti and Hf concentrations corresponding to Nb/(Ti+Hf) <1 and thus hexagonal γ Nb₅Si₃, as discussed above. However, in the “normal” Nb₅Si₃ in the bulk of MG1-HT the Ti concentration had increased compared with MG1-AC, as did the Hf

concentration. In other words as a result of the heat treatment the silicide tended to become richer in Ti and Hf and thus for the silicide the ratio $Nb/(Ti+Hf)$ was reduced, which would suggest potential for increased stability of the hexagonal silicide.

In the Nb_{ss} the average Si concentration was reduced to a value that is consistent with other data in the literature for heat treated Nb silicide in-situ composites and the Ti concentration was essentially the same as that of the heat treated alloy. However, there was still chemical inhomogeneity of Ti in the Nb_{ss} in the bulk of the MG1-HT, where the standard deviation for Ti was 3.7 with minimum and maximum concentration values 14.7 and 24.1 at %, respectively. The Hf concentration in the Nb_{ss} was reduced owing to its consumption to form hafnia. Prior eutectic areas could still be seen in the bulk of MG1-HT in which the standard deviations of Al, Hf and Ti were reduced compared with MG1-AC as did the difference between minimum and maximum values for Si (3.2 at% compared with 5.8 at% in the cast alloy).

Table 9: EDS analysis data (at%) of the heat treated alloy MG1

Area and Phase analysis		Element					
		Nb	Si	Ti	Al	Hf	
Large area	Top	47.7±1.9	20.5±2.6	21.6±1.3	4.4±0.4	5.7±0.2	
		45.4-51.6	16.3-24.1	19.6-25.1	3.9-5	5.5-6.2	
	Bulk	47.4±2.2	20.8±3.5	21.6±1.2	4.2±0.6	5.9±0.3	
		44.5-50.1	16.8-25.4	20.1-23.2	3.4-5.1	5.4-6.4	
Bottom	49±1.3	20.2±1.7	20.8±0.7	4.4±0.3	5.5±0.3		
		47-50.4	18.6-24.5	19.2-21.8	4-4.8	5.1-6.1	
Average		48±1.9	20.5±2.6	21.3±1.2	4.3±0.4	5.7±0.3	
		44.5-51.6	16.3-25.4	19.2-25.1	3.4-5.1	5.1-6.4	
Phase (spot) analysis			Nb _{ss}				
	Average		68.2±2.5	0.9±0.3	22.6±2.5	6.1±0.5	2.1±0.3
			65.8-75.5	0.4-1.5	14.7-24.1	4.1-7	1.4-2.6
			Nb ₅ Si ₃				
	Bulk	Normal	34±1.1	36.3±1.4	20.5±0.6	3.8±0.1	5.4±0.1
			33.2-34.8	35.2-37.3	20.1-20.9	3.8-3.9	5.3-5.5
	bottom	Normal	42.8±1	34.4±0.6	15.7±1.2	3.1±0.4	3.7±0.3
41.3-43.9			33.5-35.1	14.4-17.5	2.5-3.6	3.3-4.2	
Hf-rich		35.7±3.1	35.8±2.1	18.2±3.1	2.9±0.6	7.4±0.7	
		27.9-38.6	30.7-38	14.5-24.6	2-4.1	6.3-8.6	
		Prior Eutectic					
Large area	Bulk	48.7±1.4	17.7±1.2	23.4±0.6	4.7±0.3	5.5±0.2	
		46.2-51.7	15.2-19.4	22.4-23.9	4.4-5.1	5.2-5.9	

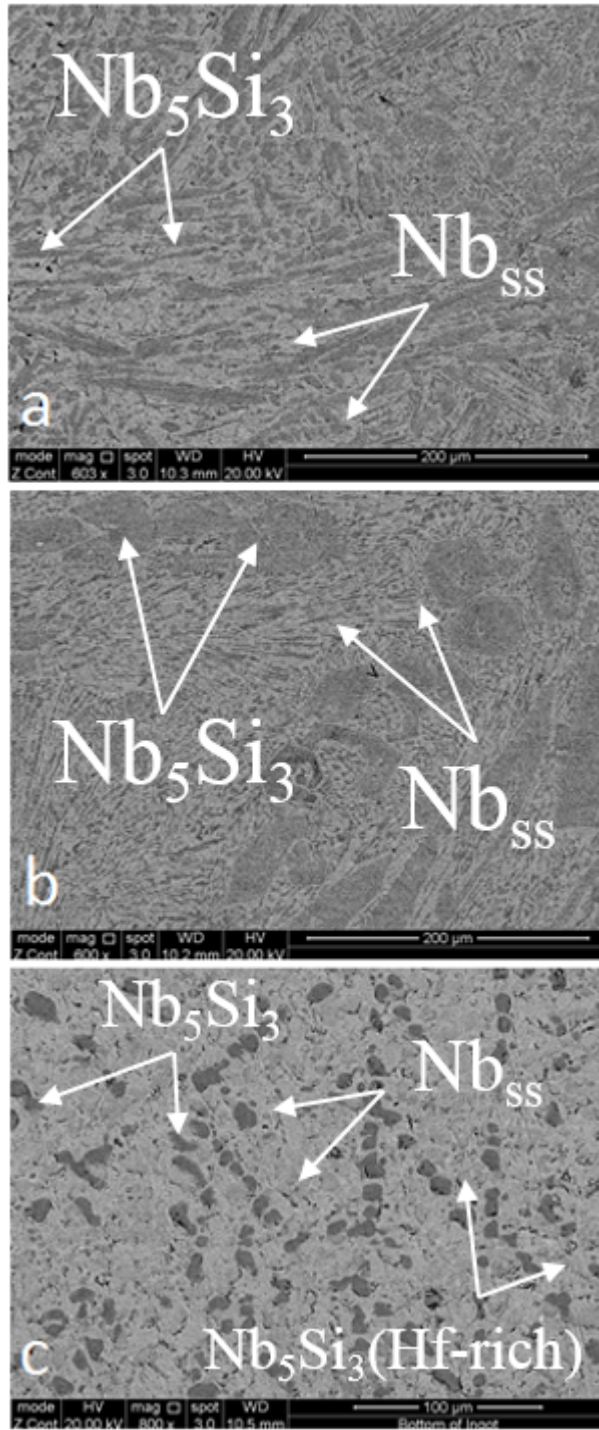


Figure 36: BSE images taken from different areas of MG1-HT, (a) top, (b) centre and (c) bottom

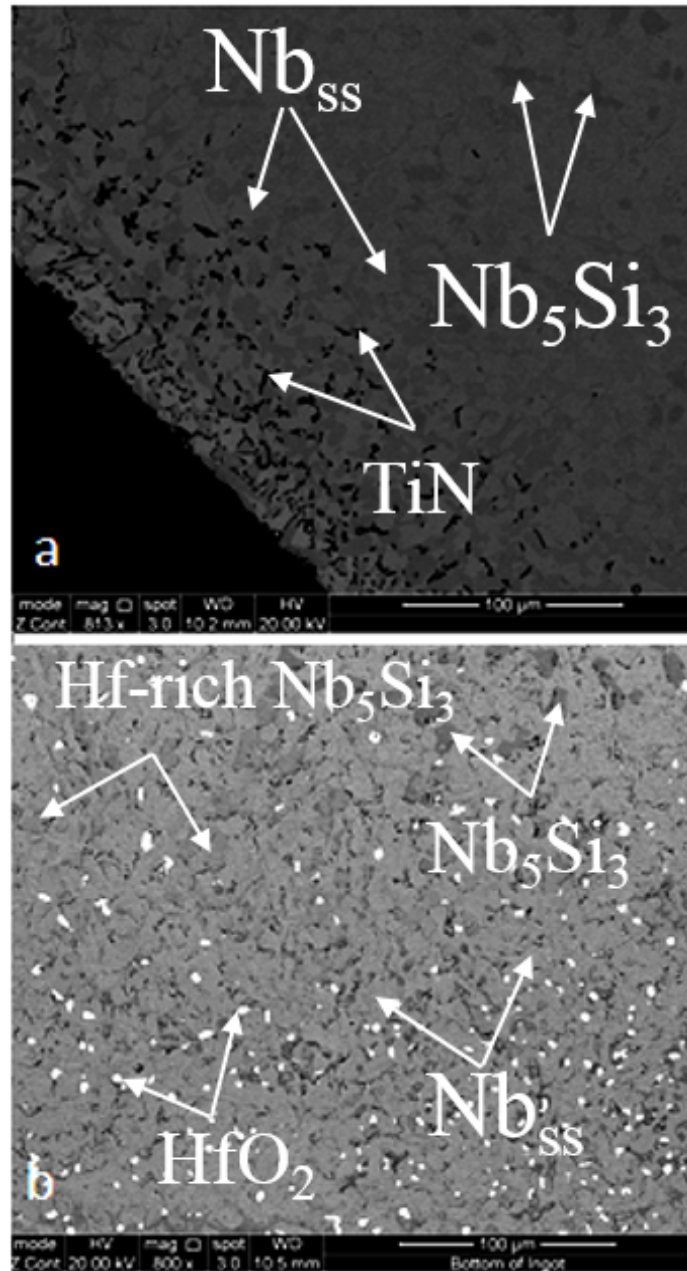


Figure 37: BSE image taken from the top (a) and the bottom (b) of the ingot.

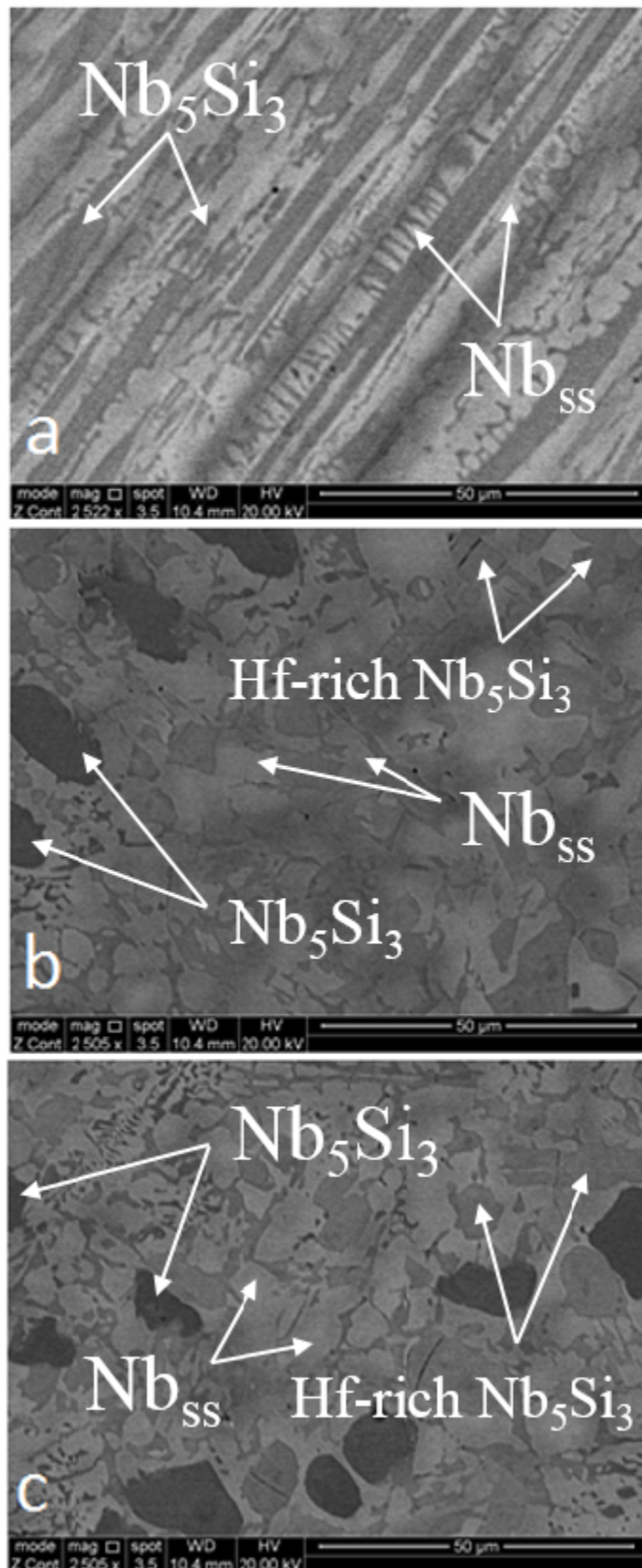


Figure 38: BSE images taken from different areas of the heat treated specimen of the alloy MG1 at high magnification: (a) top, (b) centre and (c) bottom

3.1.3 Oxidation behaviour

3.1.3.1 Isothermal oxidation at 800 °C for 100 h

The oxidation behaviour of the alloy MG1 was studied at 800 °C using TGA. The TGA data is shown in figure 39 and the oxidized specimen in figure 40. The oxidation rate constants (K_l and K_p) were calculated using the equations:

$$\frac{\Delta M}{A} = K_l t \quad (1)$$

$$\left(\frac{\Delta M}{A}\right)^2 = K_p t \quad (2)$$

where ΔM is the weight change of the specimen, t is the exposure time and A is the surface area of the specimen.

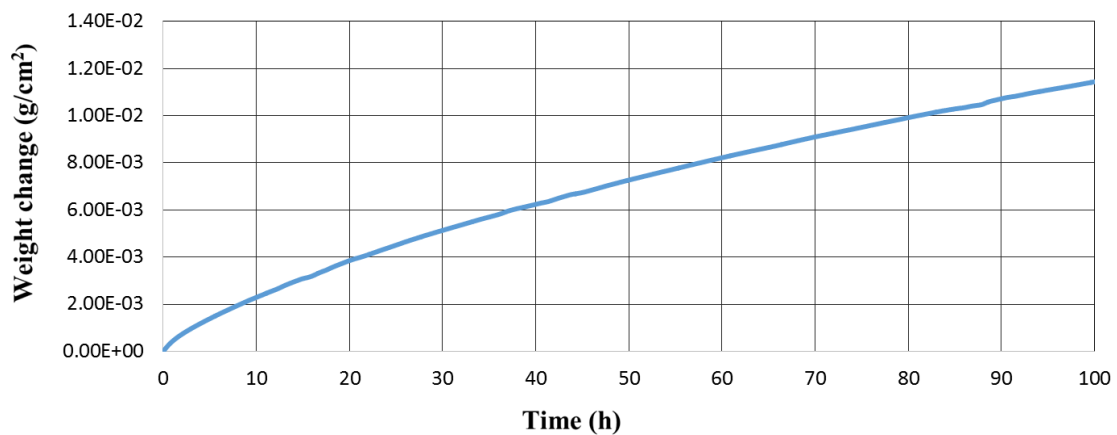


Figure 39: TGA data of the alloy MG1 at 800 °C

Equation 1 was used for the linear oxidation rate constant and equation 2 was used for the parabolic oxidation rate constant. The oxidation data is summarised in table 10.

Figure 40 shows the oxidized specimen after TGA at 800 °C for 100 h. As can be seen, the alloy did not pest nor showed any scale spallation. However, there was evidence of

scale detachment from one edge of the oxidized cubic specimen. At 800°C the alloy MG1 followed parabolic oxidation with oxidation rate constant $K_p = 4 \cdot 10^{-10} \text{ g}^2\text{cm}^{-4}\text{s}^{-1}$. The colour of the oxidized specimen was attributed to TiNb_2O_7 (titanium niobate), which has been reported to be an oxidation product formed on alloys with large Ti concentration (Felten, 1969, Harlen, 1960, Geng et al, 2006 and 2007, Mathieu et al, 2012). As we shall discuss later on in this thesis, the scale formed at 800 °C on the alloys MG5 and MG6 had the same colour.

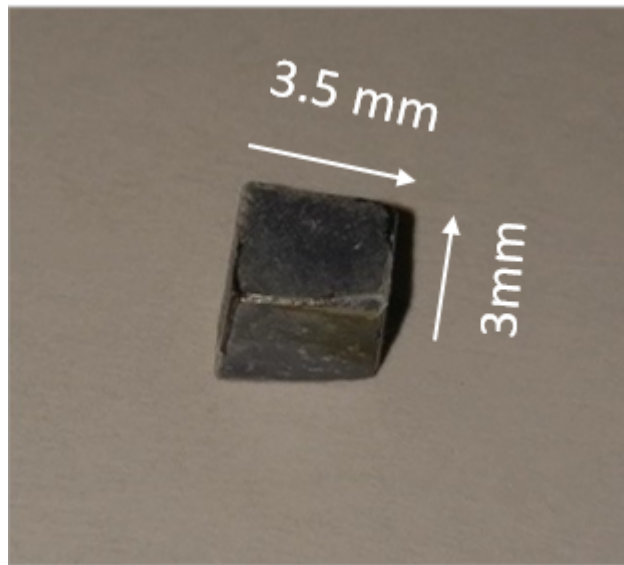


Figure 40: The specimen of the alloy MG1 after TGA at 800°C

Table 10: Oxidation rate constants and weight gains of the alloy MG1 at 800 °C and 1200 °C

Alloy	800 °C		1200 °C		
	$K_p \text{ (g}^2 \text{ cm}^{-4} \text{ s}^{-1}\text{)}$	Weight gain (g/cm^2)	$K_l \text{ (g cm}^{-2} \text{ s}^{-1}\text{)}$	$K_p \text{ (g}^2 \text{ cm}^{-4} \text{ s}^{-1}\text{)}$	Weight gain (g/cm^2)
MG1	4×10^{-10}	1.14×10^{-2}	(> 20h) 1×10^{-9}	(< 20h) 6×10^{-8}	2.6×10^{-2}

3.1.3.2 Isothermal oxidation at 1200 °C for 100 h

A specimen of the alloy MG1 after isothermal oxidation at 1200 °C for 100 h is shown in figure 41 and figure 42 and the TGA data is shown in figure 43. The oxidation rate constants are shown in table 10. Figure 42 shows that spallation of the scale had occurred. The spallation of the scale most likely occurred during the cooling stage, see figure 41.

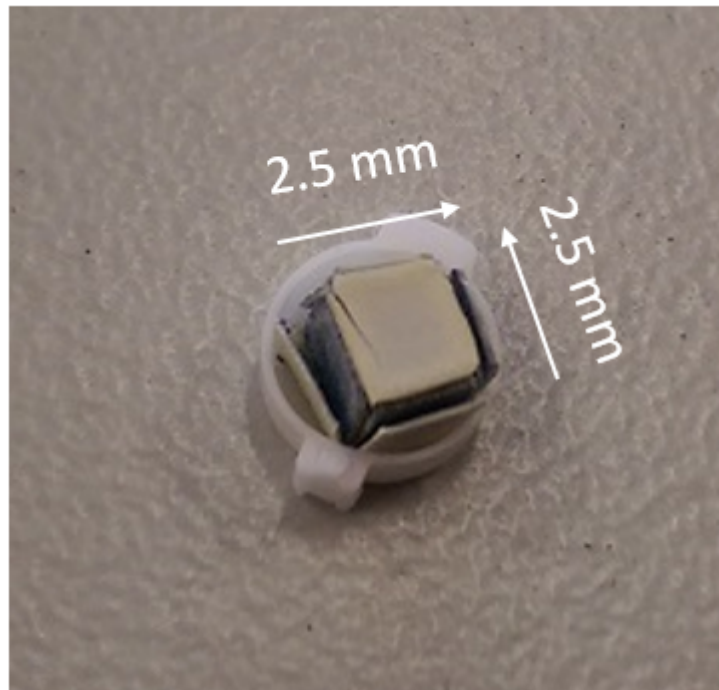


Figure 41: Oxidized specimen of the alloy MG1 in the sample holder (alumina crucible)

The spalled scale consisted of 12 oxide layers uniformly separated after the oxidation. Given that the sample was a cube, two oxide layers had spalled off from each side of the cube. The layers disintegrated easily after removal of the specimen from the sample holder.



Figure 42: Oxidized specimen of the alloy MG1 at 1200 °C, after its removal from the sample holder

The alloy MG1 followed parabolic oxidation in the early stage of oxidation, which was succeeded by linear oxidation, see table 10.

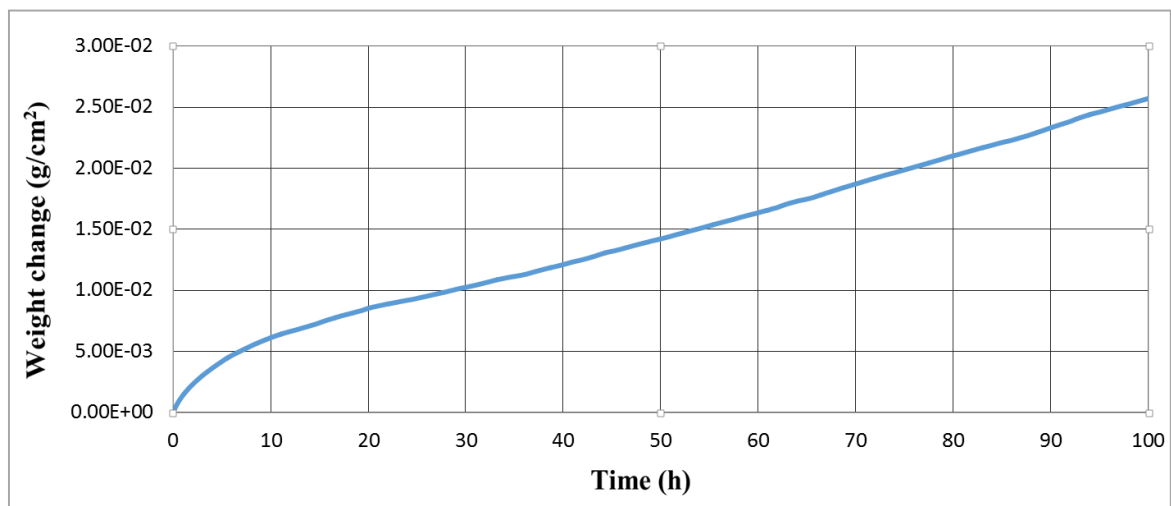


Figure 43: TGA data of the alloy MG1 at 1200 °C

3.1.3.3 Microstructure of oxidised MG1

The near the surface and bulk microstructures of oxidised specimens of the alloy MG1 at 800 and 1200 °C are shown in figure 44 and figure 45. Data about the contamination of phases by oxygen from the edge towards the bulk of the specimen is shown in table 11 and table 12, respectively for 800 and 1200 °C. It should be noted that scale spallation occurred at 1200 °C, with 12 layers (i.e., two per cube face) spalled off, and therefore the data in table 12 is from the remaining cube shape specimen without the scale.

Figure 44 shows the thick layer adherent scale structure formed at 800 °C with cracks in the substrate parallel to the surface, which is typical of the oxidation of Nb silicide based alloys. The data in table 11 shows that both phases, namely the solid solution and the 5-3 silicide, were contaminated by oxygen, the former more severely than the latter with the contamination becoming less with depth below the scale.

Figure 45 shows remnants of the scale just above the substrate. The near the surface area was heavily oxidised with high volume fraction of hafnia forming there. The data in table 12 shows contamination of both phases by oxygen near the surface and in the bulk, with more severe contamination of the solid solution compared with the 5-3 silicide as was the case at 800 °C. The lower oxygen contamination of both phases near the top of the substrate is attributed to the spallation of the scale, meaning that it is likely that the second (inner) spalled off layer removed part of the substrate. The higher contamination of the solid solution and 5-3 silicide in the bulk of the oxidised specimen, compared with the specimen oxidised at 800 °C is attributed to the higher oxidation temperature.

Figure 46 shows the XRD data for the oxidised alloy. Figure 46a is the glancing angle XRD for the alloy oxidised at 800 °C and suggests the presence of Ti niobates, hafnia, Nb₂O₅, TiO₂ and SiO₂. Figure 46b is the powder XRD data taken from the spalled off scale that formed on the alloy at 1200 °C and suggests the presence of the same oxides as at 800 °C plus tetragonal and hexagonal 5-3 silicide, which supports the conclusion that part of the spalled off material included heavily contaminated substrate below the actual alloy scale.

Table 11: Analysis data (at%) for Nb₅Si₃ and Nb_{ss} at 800 °C

Area and Phase analysis		Element					
Nb ₅ Si ₃							
↓		O	Nb	Si	Ti	Al	Hf
	Edge	9.8	40	30.9	13.1	2.7	3.3
		9.1	40.2	31.4	13.2	2.8	3.3
	Bulk	9.8	38.9	31.3	13.4	3.2	3.4
		8.4	39.7	31.8	14	3.1	3
		1.5	43.5	33.9	14.8	2.9	3.3
Nb _{ss}							
↓	Edge	46.9	31.8	1.4	14.5	3.3	2.1
		44.5	36.1	1.3	12.8	3.4	1.8
	Bulk	8.9	50.7	4.1	27.3	5.3	3.7
		5.8	54.7	2.8	27	5.9	3.8

Table 12: Analysis data (at%) for Nb₅Si₃ and Nb_{ss} at 1200 °C

Area and Phase analysis		Element					
Nb ₅ Si ₃							
↓		O	Nb	Si	Ti	Al	Hf
	Edge	6.9	37.5	33.5	14.3	2.7	5.1
		6.1	36.4	34.6	14.7	2.3	5.8
		5.4	41.4	33.3	13.7	2.5	3.6
	Bulk	5.5	30.4	34.4	19.8	2.9	6.9
		4.2	37.1	35.5	14.6	2.6	6
		4.1	37.4	34.8	15.3	2.4	6
		2.7	37.4	36	15.1	2.5	6.3
Nb _{ss}							
↓	edge	13.1	71.1	0.1	10.8	4.5	0.4
	Bulk	11.4	59.8	0.6	21	5.6	1.6
		10.1	55.7	4.3	21.8	5.8	2.3

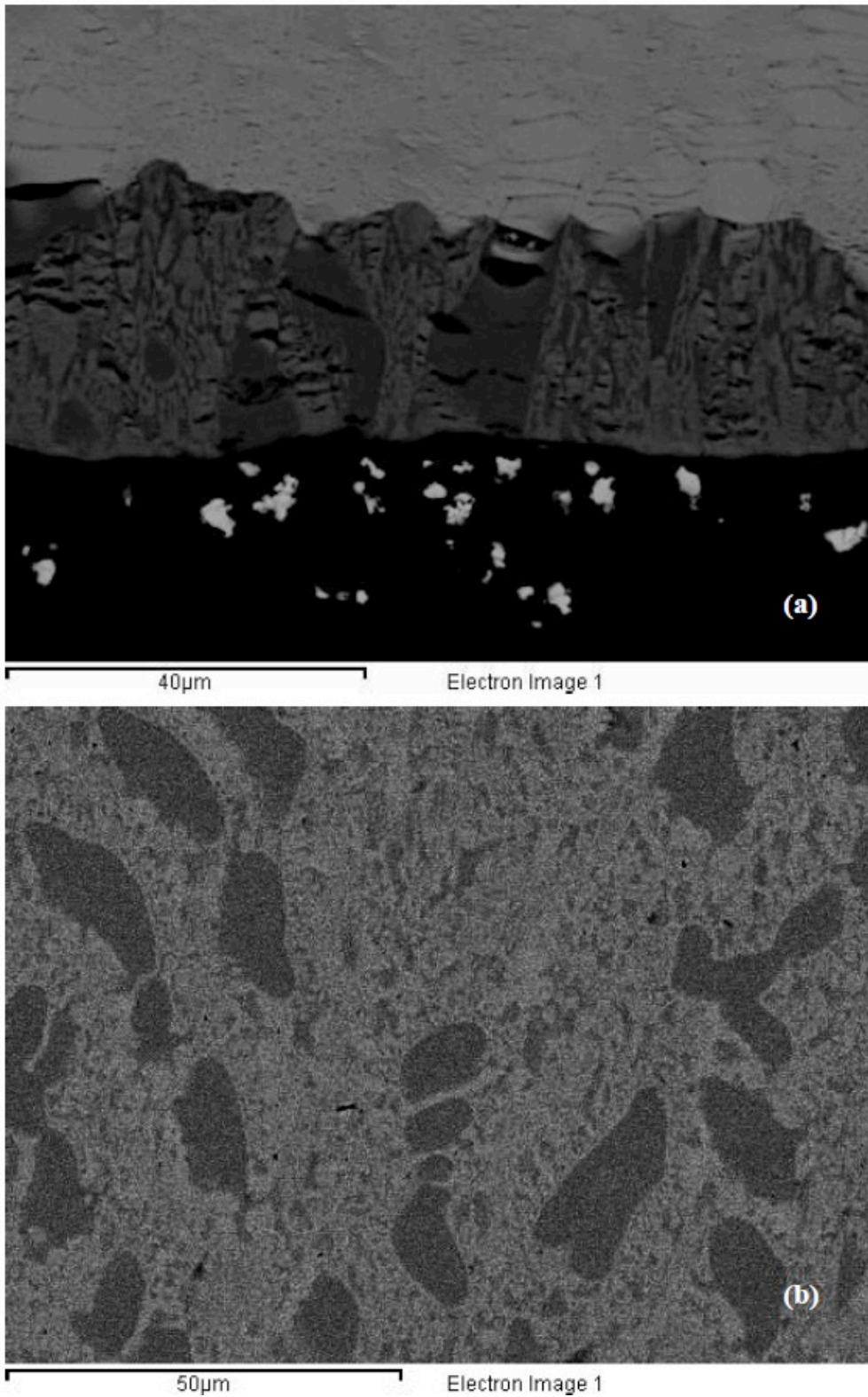


Figure 44: BSE images of oxidised MG1 at 800 °C (a) below scale and (b) bulk

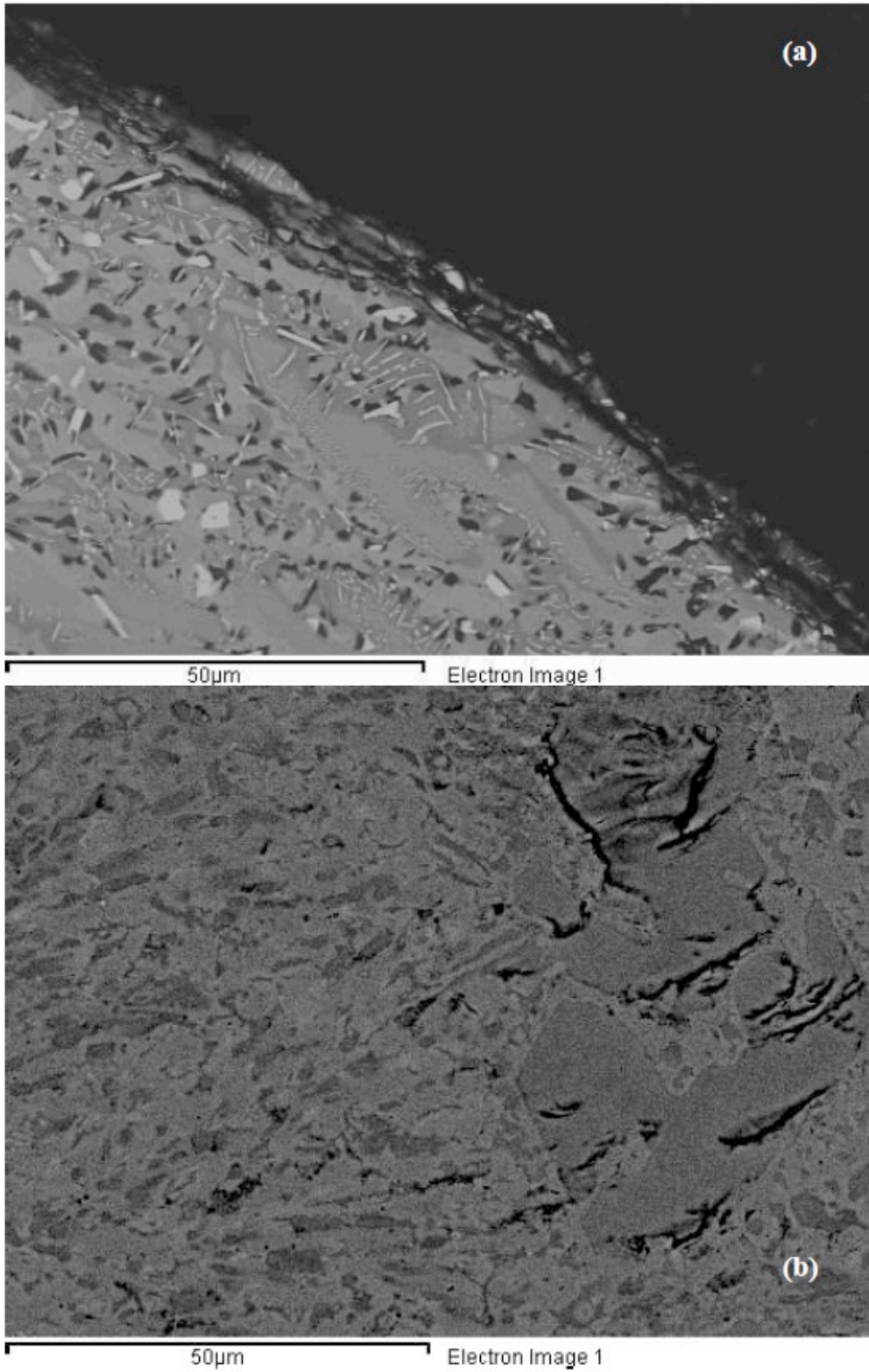


Figure 45: BSE images of oxidised MG1 at 1200 °C (a) below scale and (b) bulk

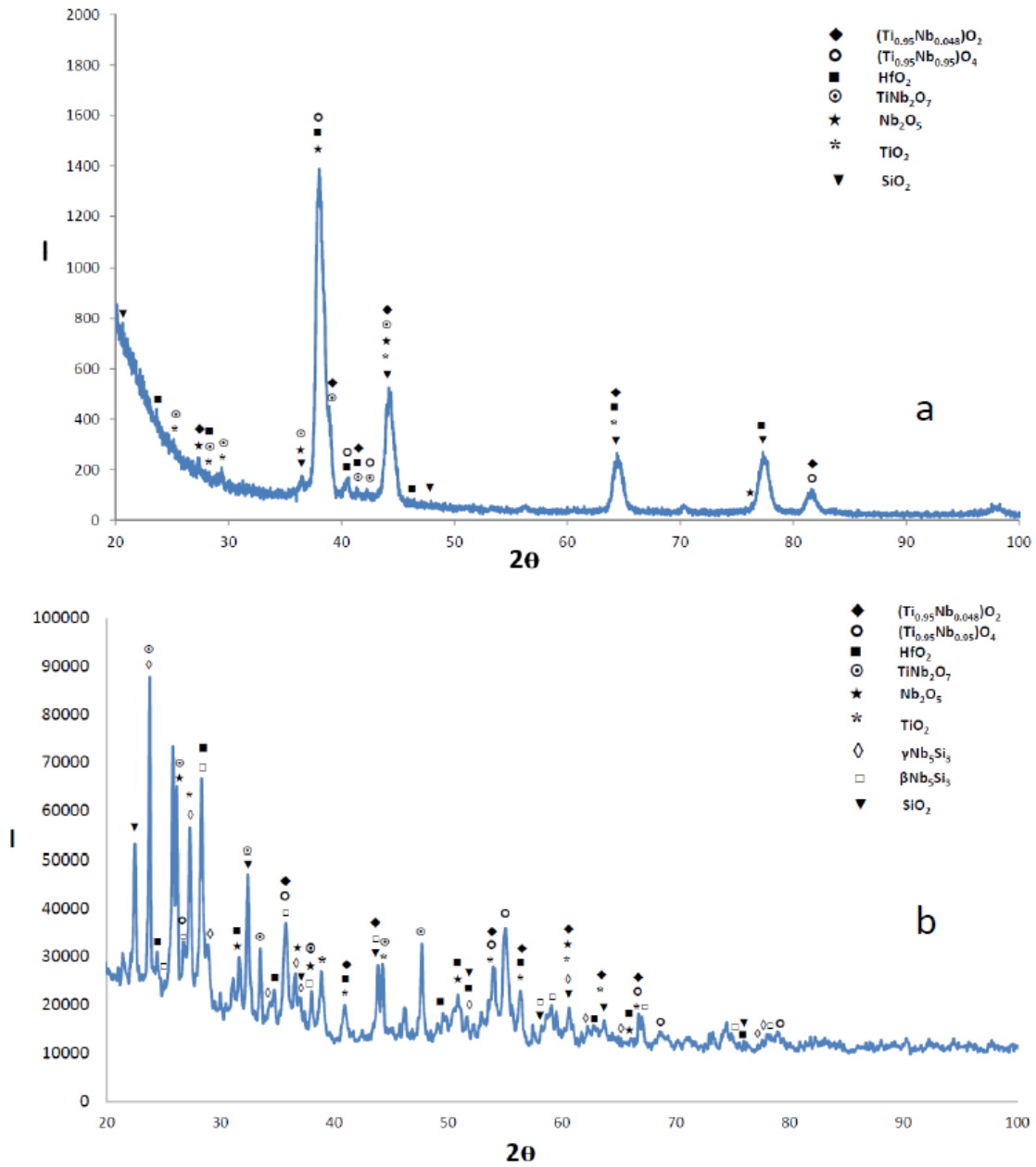


Figure 46: XRD data for the alloy MG1 (a) glancing angle ($\theta = 5^\circ$) for the oxidized specimen at 800 °C (b) powder XRD data taken from the spalled off scale of the oxidized specimen at 1200 °C

3.1.4 Discussion

The alloy MG1 can be compared with the alloys KZ7 (nominal composition Nb-24Ti-18Si-5Al, Zelenitsas and Tsakirooulos, 2005) and YG3 (nominal composition Nb-24Ti-18Si-5Hf, Grammenos and Tsakirooulos, 2010) to help us understand how the addition of Hf in the alloy MG1 (and thus the synergy of Hf with Ti and Al) affect phase stability.

Macrosegregation of Si will be discussed first before we focus on phase selection and stability. The alloy MG1-AC exhibited severe macrosegregation of Si with $C_{\max}^{\text{Si}} - C_{\min}^{\text{Si}} = 7.4$ at% Si, which is attributed to the synergy of Al and Hf. Indeed, the macrosegregation of Si was 1.6 at% Si in the alloy KZ3 (nominal composition Nb-24Ti-18Si, Zelenitsas and Tsakirooulos, 2005), the addition of Al in the alloy KZ7 increased it to 2.3 at% while the addition of Hf in the alloy YG3 increased it to 3.3 at%. In other words, alloying with Al or Hf individually increases the macrosegregation of Si and the latter increases further when Al and Hf are present simultaneously in the alloy, the case of MG1.

The average Si macrosegregation calculated for the overall actual composition of MG1-AC using the alloy design methodology developed by our group (not published because of confidentiality) gave $C_{\max}^{\text{Si}} - C_{\min}^{\text{Si}} = 7.05$ at% Si and also indicated that the parameters $\Delta H_m^{\text{sd}}/\Delta H_m^{\text{sp}}$ and $T_m^{\text{sd}}/T_m^{\text{sp}}$ were the most important ones (Tsakirooulos, 2014).

The actual composition of the alloy KZ7-AC differed from its nominal composition as it had $25 < \text{Ti} < 27$ at%, $15 < \text{Si} < 17.5$ at% and $4.9 < \text{Al} < 5.5$ at%. Considering only

its Si content, the alloy KZ7 could be considered as hypo-eutectic, in which case, given that $\beta\text{Nb}_5\text{Si}_3$ was the primary phase (Zelenitsas and Tsakirooulos, 2005), it could be suggested that the addition of Al “pushed” the eutectic composition (≈ 17.5 at% Si in the Nb-Si system, Schlesinger et al, 1993) to lower values. It is now, however, known that Al and Si substitute each other in the eutectics observed in Nb silicide based alloys, in which case the alloy KZ7 could be considered as hyper-eutectic ($19.9 \text{ at\%} < (\text{Si} + \text{Al}) < 23 \text{ at\%}$, i.e., its Si + Al content is above 19.5 at% Si in the Nb-Si binary (Schlesinger et al, 1993, peritectic reaction $\text{L} (19.5 \text{ at\% Si}) + \beta\text{Nb}_5\text{Si}_3 (35 \text{ at\% Si}) \rightarrow \text{Nb}_3\text{Si} (25 \text{ at\% Si})$), which would explain the formation of $\beta\text{Nb}_5\text{Si}_3$ as the primary phase in KZ7.

The Nb_3Si was not formed in KZ7-AC but since it was formed in the alloy KZ3 (nominal composition Nb-24Ti-18Si, Zelenitsas and Tsakirooulos, 2005), its suppression in KZ7-AC was attributed to the addition of Al. In the ingot of the latter alloy the microstructure consisted of $\beta\text{Nb}_5\text{Si}_3$ next to which formed either the Nb_{ss} or the $\text{Nb}_{\text{ss}} + \beta\text{Nb}_5\text{Si}_3$ eutectic or the Nb_{ss} and then the $\text{Nb}_{\text{ss}} + \beta\text{Nb}_5\text{Si}_3$ eutectic. In the $\beta\text{Nb}_5\text{Si}_3$ there was microsegregation of Ti, in other words Ti rich $\beta\text{Nb}_5\text{Si}_3$ was also present in the microstructure together with “normal” $\beta\text{Nb}_5\text{Si}_3$. However, it should be noted that in the alloy KZ7 the Ti rich $\beta\text{Nb}_5\text{Si}_3$ was observed at interfaces with Nb_{ss} grains, meaning no individual Ti rich $\beta\text{Nb}_5\text{Si}_3$ grains were observed.

The actual composition of the alloy YG3-AC differed from its nominal composition as it had $21.4 < \text{Ti} < 25 \text{ at\%}$, $17 < \text{Si} < 20.4 \text{ at\%}$, $4.5 < \text{Hf} < 5.4 \text{ at\%}$. The Si content of this alloy was in the range 17.5 to 19.5 at% of the Nb-Si binary where Nb_3Si can form

as the primary phase (Schlesinger et al 1993) and indeed this silicide was observed in the cast microstructure together with a very low volume fraction of Nb_5Si_3 . According to the XRD data no hexagonal Nb_5Si_3 was formed and both $\beta\text{Nb}_5\text{Si}_3$ and $\alpha\text{Nb}_5\text{Si}_3$ were present in YG3-AC, which implies that some $\beta\text{Nb}_5\text{Si}_3 \rightarrow \alpha\text{Nb}_5\text{Si}_3$ transformation occurred during solid state cooling. The EPMA analysis did not confirm Ti and Hf rich Nb_5Si_3 but only the microsegregation of Ti in Nb_{ss} , in other words there was Ti rich Nb_{ss} in YG3-AC. Furthermore, in the microstructure there were two eutectics, namely $\text{Nb}_{\text{ss}} + \text{Nb}_3\text{Si}$ and $\text{Nb}_{\text{ss}} + \text{Nb}_5\text{Si}_3$, the former is the stable eutectic in the equilibrium Nb-Si binary phase diagram and the latter is a metastable eutectic in the Nb-Si binary, which was reported to form in Nb-Si near eutectic (i.e., with Si content near that of the $L \rightarrow \text{Nb}_{\text{ss}} + \text{Nb}_3\text{Si}$ eutectic) binary alloys under rapid solidification conditions and to have $\text{Si} \approx 20.5 \text{ at\%}$, but this value depends very much on the version of the Nb-Si binary phase diagram used. The composition of the metastable eutectic in YG3-AC was 34.3Nb–36.8Ti –21Si –7.9Hf (at%).

The alloy MG1 was hypereutectic ($\text{Si}+\text{Al} > 22.3 \text{ at\%}$), thus the 5-3 silicide formed as the primary phase and the microstructure of MG1-AC was essentially the same as that of KZ7-AC, meaning that the addition of Hf had no effect of the “architecture” of the microstructure. However, the microstructure of MG1-AC was distinctly different than that of the alloy YG3-AC owing to the suppression of Nb_3Si formation in the former.

Considering the 5-3 silicide in MG1-AC, there was segregation of Hf and Ti in the 5-3 silicide in the very bottom of the MG1-AC ingot and “normal” Nb_5Si_3 in the “transition zone” from the bottom to the bulk and in the bulk and top of the ingot. Furthermore, in

contrast with KZ7-AC and YG3-AC, under BSE imaging conditions there were no Ti rich areas observed in the Nb_{ss}. The Ti and Hf rich Nb₅Si₃ formed as distinct grains as did the “normal” Nb₅Si₃, but in the very bottom of MG1-AC the Nb_{ss} was leaner in Hf and Ti compared with the Nb_{ss} in the bulk and top, which would suggest that, owing to the high cooling rate at the very bottom of MG1-AC and the presence of both Hf and Al in the alloy MG1 (compared with KZ7 (no Hf) and YG3 (no Al)), there was not enough time for equilibrium solute partitioning of Hf and Ti to occur between Nb₅Si₃ and the melt. In some 5-3 grains the concentration of Hf + Ti was high enough to give Nb/(Ti+Hf) < 1, which is consistent with the XRD data suggesting the presence of hexagonal 5-3 silicide (i.e., γ Nb₅Si₃). The presence of β Nb₅Si₃ and no α Nb₅Si₃ in MG1-AC is consistent with Al stabilising the former silicide in the cast microstructure and comparison with YG3-AC would suggest that the synergy of Hf with Al did not promote the β Nb₅Si₃ \rightarrow α Nb₅Si₃ transformation during solid state cooling in MG1-AC.

The suppression of the stable (i.e., the $L \rightarrow \text{Nb}_{ss} + \text{Nb}_3\text{Si}$) eutectic is consistent with the absence of Nb₃Si in MG1-AC and the composition of the metastable $L \rightarrow \text{Nb}_{ss} + \text{Nb}_5\text{Si}_3$ eutectic with average Si + Al \approx 20.6 at% is consistent with the literature and the data for YG3-AC. However, the lower Hf and Ti concentrations in the metastable eutectic in MG1-AC compared with YG3-AC (see above) and the absence of the metastable eutectic in the bottom of MG1-AC would suggest that its formation depended not only on solidification conditions but also on the partitioning of solutes, which must have been influenced by the synergy of Al with Hf and Ti.

Considering the above discussion, as the 5-3 silicide formed in the very bottom of MG1-AC the surrounding melt became lean in Si and Hf and rich in Ti and Al. In this melt formed the Nb_{ss} and the melt became rich in Si and Hf, poor in Al and its Ti concentration did not change. As the cooling rate decreased, in the latter melt formed “normal” 5-3 silicide, the surrounding melt became lean in Si but now Ti and Hf had more time to partition to the melt which thus became richer in Al, Hf and Ti. From this melt formed Nb_{ss} (slightly richer in Ti and Hf compared with the Nb_{ss} formed in the bottom (see table 8) and as this Nb_{ss} formed the melt became rich in Si, Hf and poor in Al. When the Si + Al composition of the melt approached that of the metastable eutectic the latter formed either in-between Nb_{ss} grains or from the Nb_{ss} that was formed on 5-3 silicide grains (figure 35b). Thus, from the observed microstructure in MG1-AC it is suggested that in the bulk of MG1-AC the solidification path was $L \rightarrow L + \beta\text{Nb}_5\text{Si}_3 \rightarrow L + \beta\text{Nb}_5\text{Si}_3 + \text{Nb}_{\text{ss}} \rightarrow \beta\text{Nb}_5\text{Si}_3 + \text{Nb}_{\text{ss}} + (\beta\text{Nb}_5\text{Si}_3 + \text{Nb}_{\text{ss}})_{\text{eutectic}}$.

The solidification path was calculated using the Pandat software for the actual alloy composition. The calculated path is $L \rightarrow L + \text{Nb}_5\text{Si}_3 \rightarrow L + \text{Nb}_5\text{Si}_3 + \text{Nb}_{\text{ss}} \rightarrow L + \text{Nb}_{\text{ss}} + \text{Ti}_5\text{Si}_3 \rightarrow \text{Nb}_{\text{ss}} + \text{Ti}_5\text{Si}_3$. In the Pandat software the type of Nb₅Si₃ (meaning β or α) is not specified. The calculated path predicts a final microstructure consisting of Nb_{ss} and the hexagonal 5-3 silicide (the prototype of γNb₅Si₃ is Mn₅Si₃, the same as for Ti₅Si₃).

The actual composition of KZ7-HT (1500 °C/100 h) differed from the nominal alloy composition (24.4 < Ti < 25.5 at%, 15.3 < Si < 18.1 at%, 4.6 < Al < 5 at%) and was also slightly leaner in Ti compared with the cast alloy. The microstructure consisted of αNb₅Si₃, Nb_{ss} with Ti rich areas still persisting in the αNb₅Si₃, precipitation of Nb_{ss} in

$\alpha\text{Nb}_5\text{Si}_3$, no Ti rich areas in the solid solution and no prior eutectic. Precipitation of Nb_{ss} in $\alpha\text{Nb}_5\text{Si}_3$ has been observed in the $\beta\text{Nb}_5\text{Si}_3 \rightarrow \alpha\text{Nb}_5\text{Si}_3$ transformation in Nb silicide based alloys by many members of our research group.

The actual composition of YG3-HT (1500 °C/100 h) also differed from the nominal one but was essentially similar to that of the cast alloy. In the microstructure of YG3-HT the hexagonal 5-3 silicide (i.e., the $\gamma\text{Nb}_5\text{Si}_3$) was stabilised together with the $\beta\text{Nb}_5\text{Si}_3$ and $\alpha\text{Nb}_5\text{Si}_3$ that were in the cast alloy. However, it was not clear whether the volume fractions of the latter two silicides were changed significantly after the heat treatment (one would expect the $\beta\text{Nb}_5\text{Si}_3 \rightarrow \alpha\text{Nb}_5\text{Si}_3$ transformation to have proceeded to the right after 100 h at 1500 °C). The Nb_3Si was also stable in YG3-HT as well as the Nb_{ss} . The concentrations of Hf and Ti in the 5-3 silicide had increased compared with YG3-AC and there were Hf rich Nb_5Si_3 grains. No prior eutectics were observed.

The microstructure of MG1-HT (1300 °C/100 h) consisted of $\beta\text{Nb}_5\text{Si}_3$ and $\gamma\text{Nb}_5\text{Si}_3$ (the latter being rich in Hf and Ti), Nb_{ss} and coarsened prior eutectic. Comparison with KZ7 and YG3 would suggest respectively that the addition of Hf stabilised the $\beta\text{Nb}_5\text{Si}_3$ and the synergy of Al with Hf and Ti promoted the stability of $\gamma\text{Nb}_5\text{Si}_3$. The latter is also supported by the results in another PhD project in the group (Nelson, 2015). No Nb_{ss} precipitates were observed in the 5-3 silicide in MG1-HT, which is consistent with the now accepted view that precipitation of Nb_{ss} in $\alpha\text{Nb}_5\text{Si}_3$ is often observed in the $\beta\text{Nb}_5\text{Si}_3 \rightarrow \alpha\text{Nb}_5\text{Si}_3$ transformation in Nb silicide based alloys (McCaughey, 2017). The presence of coarsened prior eutectic in MG1-HT compared with its absence in KZ7-HT and YG3-HT can be explained by the lower homologous temperature of the

MG1 heat treatment (the higher Si concentration in MG1-HT ($16.3 < \text{Si} < 25.4$ at%, compared with $15.3 < \text{Si} < 18.1$ at% and $17.3 < \text{Si} < 19.8$ at%, respectively for KZ7-HT and YG3-HT) implies higher $T_{\text{liquidus}}^{\text{MG1}}$ than $T_{\text{liquidus}}^{\text{KZ7}}$ and $T_{\text{liquidus}}^{\text{YG3}}$ and the heat treatment temperature of MG1 was lower than those of KZ7 and YG3).

The available phase equilibria data cannot account for the presence of bcc Nb_{ss} , $\beta\text{Nb}_5\text{Si}_3$ and hexagonal $\gamma\text{Nb}_5\text{Si}_3$. If we were to consider the alloy MG1-HT as (Nb,Ti,Hf)-Si-Al then in the isothermal Nb-Si-Al sections at 1400 °C by Raghavan (2006) and 1300 °C by Batzner, see figure 47a and figure 47b, the alloy is in the $\text{Nb}_{\text{ss}} + \alpha\text{Nb}_5\text{Si}_3$ two phase area. If we were to consider the alloys MG1-HT as (Ti,Nb,Hf)-Si-Al then in the isothermal Ti-Al-Si sections at 1200 °C by Schob and 1270 °C by Bulanova, see figure 47c and figure 47d, the alloy falls in the bcc Ti_{ss} and Ti_5Si_3 two phase area. This suggests that the elements Hf and Ti that form hexagonal 5-3 silicides with Mn_5Si_3 prototype (the same as hexagonal $\gamma\text{Nb}_5\text{Si}_3$), as expected, promote the stability of $\gamma\text{Nb}_5\text{Si}_3$. The phase equilibria data cannot account for the stability of $\beta\text{Nb}_5\text{Si}_3$ at 1300 °C.

The oxidation behaviour of the alloy MG1 can be compared with that of the alloys KZ7 and YG3. In the case of the former alloy the specimens used for the TGA experiments had been heat treated at 1500 °C for 100 h, but the oxidation specimens of the latter alloy and MG1 were selected from the cast alloy ingots.

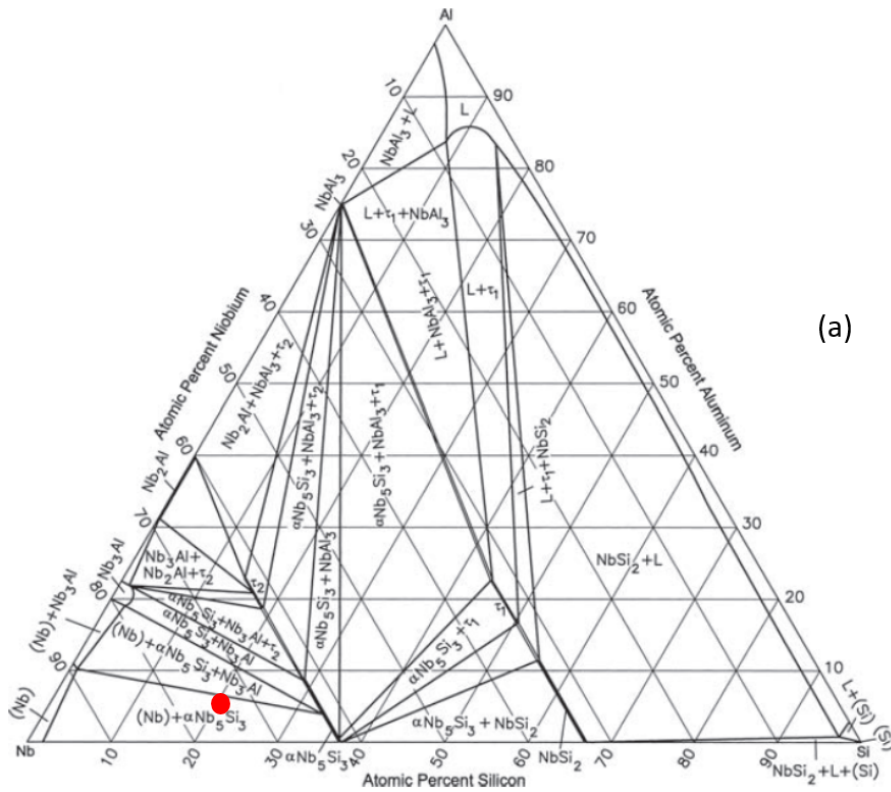
At 800 °C the alloy YG3 exhibited pest oxidation. It followed linear oxidation kinetics and after 18h, when the TGA experiment was stopped because of pesting, it had gained 52 mg/cm². The alloy KZ7 also followed linear oxidation kinetics but did not pest,

gained 25 mg/cm^2 and the scale did not spall off. The alloy MG1 gained 11.4 mg/cm^2 , but followed parabolic oxidation kinetics and like KZ7 did not pest and retained the scale. This would suggest (i) that the synergy of Hf and Ti was not able to “stop” the fast diffusion of oxygen to the bulk of YG3, (ii) that the synergies of Al and Ti and Al with Hf and Ti were beneficial for oxidation at $800 \text{ }^\circ\text{C}$, which is in the pest regime, (iii) that the former synergy improved the adhesion of the scale and slowed down oxidation and (iv) that the latter synergy slowed down further the diffusion of oxygen, which is consistent with Ghosh and Olson (2007) and also promoted parabolic oxidation. The average weight gain calculated using the alloy design methodology developed in the group gives weight gain of 13.3 mg/cm^2 at $800 \text{ }^\circ\text{C}$ for the alloy MG1.

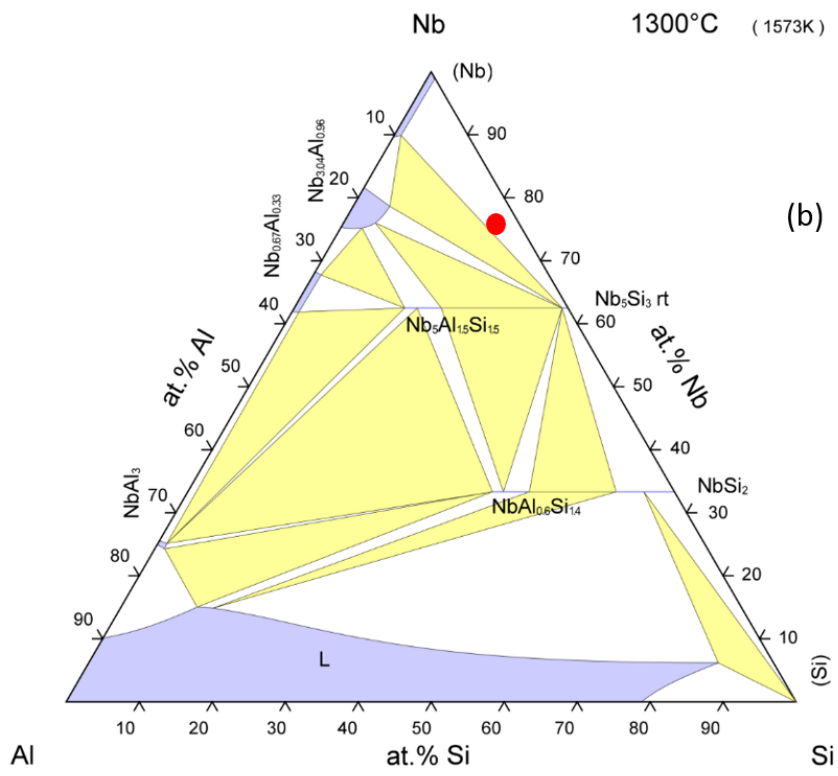
At $1200 \text{ }^\circ\text{C}$, the scale formed on the alloy YG3 spalled off, like the scales formed on the oxidised specimens of the alloys KZ7 and MG1. The weight gains of YG3, KZ7 and MG1 after 100 h at $1200 \text{ }^\circ\text{C}$ were 180, 135 and 26 mg/cm^2 . All alloys started following parabolic oxidation kinetics which then changed to linear kinetics. Comparison of the data shows a steady improvement in terms of reducing weight gain with changes in alloying additions, from high weight gain from the synergy of Hf and Ti to lower weight gain from the synergy of Al and Ti and then to even lower weight gain from the synergy of Al with Hf and Ti, which is consistent with slower diffusion of oxygen towards the bulk (Ghosh and Olson, 2007). The spallation of the scale formed on all three alloys however shows that the latter synergy was not capable of improving adhesion. It is likely that Ti with Hf play the key role in this phenomenon. The formation of hafnia in MG1 is consistent with the data for the alloy YG3. The average weight gain at $1200 \text{ }^\circ\text{C}$ calculated using the alloy design methodology developed in the group was 48 mg/cm^2 for the alloy MG1.

Contamination of both phases by oxygen and the more severe contamination of the solid solution compared with the 5-3 silicide is consistent with the results for other Nb silicide based alloys studied in our group. The synergy of Al with Hf and Ti was able to slow down but not to stop the diffusion of oxygen to the bulk of MG1 at 800 and 1200 °C.

The oxides forming the scale on the alloy MG1 at 800 and 1200 °C can be compared with the oxidised alloy KZ7 (Zelenitsas and Tsakirooulos, 2006) and literature about other oxidised Nb silicide based alloys. Compared with the alloy KZ7 oxidised at 800 °C, where Nb₂O₅ and Ti niobates were suggested by Bragg-Brentano XRD (i.e., GXR was not done on KZ7), on the alloy MG1, hafnia, TiO₂ and SiO₂ were also suggested by the GXR but not the aluminium niobate AlNbO₄ that was suggested for KZ7. The aforementioned oxides excluding hafnia and the aluminium niobate were suggested by Bragg-Brentano XRD for the oxidised alloy JG3 (=Nb-24Ti-18Si-5Al-5Cr-2Mo) at 800 °C (Geng et al, 2006) and the same oxides including hafnia but not AlNbO₄ for the oxidised alloy JG3 (see above) and JG4 (=Nb-24Ti-18Si-5Al-5Cr-5Hf-2Mo) at 1200 °C (Geng et al, 2006). The implications of the formation of Ti niobates and TiO₂ in the scale of the alloys studied in this work will be discussed later on, after the results for the alloy MG6 are considered in the chapter 6.



(a)



(b)

Continued

Continued

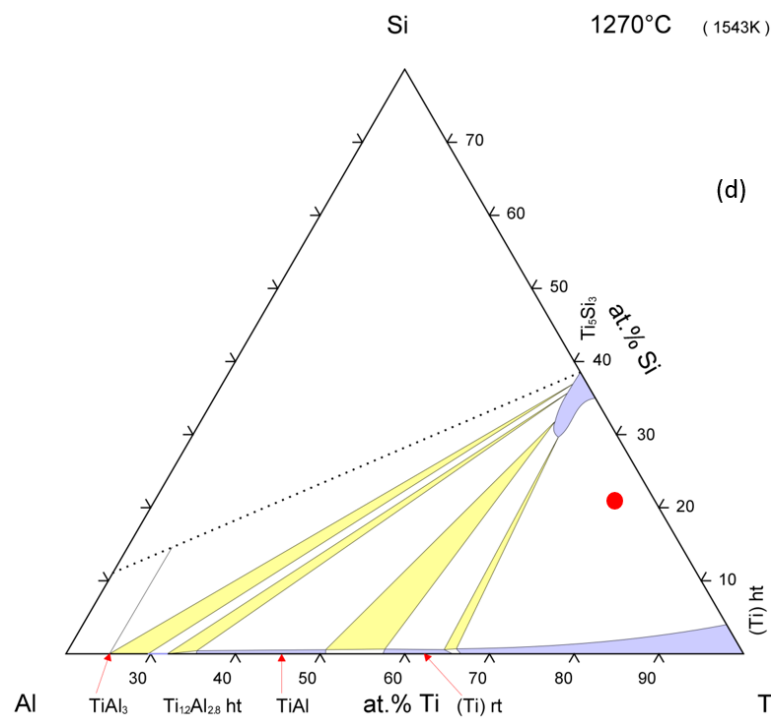
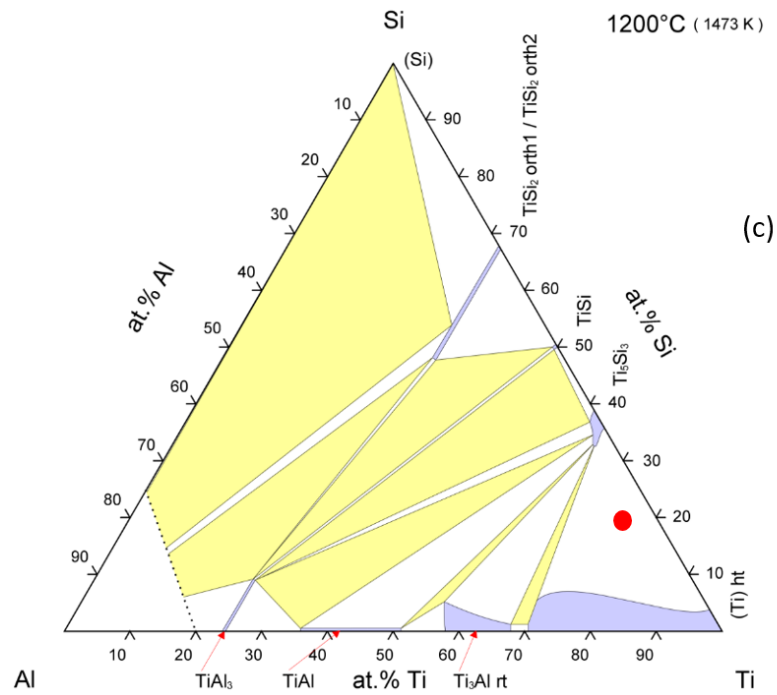


Figure 47: Isothermal sections of Nb-Al-Si and Ti-Al-Si systems, (a) 1400 °C, Raghavan 2006, (b) 1300 °C, Batzner et al 1993, (c) 1200 °C, Schob et al 1962, and (d) 1270 °C, Bulanova et al, 2004

3.1.5 Summary

The alloy MG1 was selected to study how the synergy of Ti with Al and Hf affects phase stability and oxidation. It was already known from previous research in the group that Al or Hf individually increase the macrosegregation of Si. This work showed that the latter increases further when Al and Hf are present simultaneously in the alloy. There was also macrosegregation of Ti in the alloy MG1. The addition of Hf did not have any effect on the architecture of the cast microstructure, which consisted of Nb_{ss}, β Nb₅Si₃ and γ Nb₅Si₃ and Nb_{ss} + β Nb₅Si₃ eutectic, did not lead to the formation of Ti rich Nb_{ss}, encouraged the formation of distinct (separate) Ti and Hf rich Nb₅Si₃ and normal Nb₅Si₃ and did not promote the β Nb₅Si₃ → α Nb₅Si₃ during solid state cooling. The Al + Si content of the eutectic was in agreement with the literature.

Chemical inhomogeneity persisted after the heat treatment at 1300 °C for 100 h, during which there was contamination of the near the top and bottom areas but not of the bulk, meaning that the synergy of Ti with Al and Hf was effective in controlling contamination of the alloy. The α Nb₅Si₃ was not observed and the evidence pointed to increased stability of the γ Nb₅Si₃.

The alloy MG1 did not pest at 800 °C and exhibited parabolic oxidation. The synergy of Al and Hf reduced further the weight gain at 800 °C and 1200 °C. There was no spallation of the thick layered scale that formed at 800 °C but spallation occurred at 1200 °C and the spalled off scale consisted of 12 layers, two layers from each cube surface. The Nb_{ss} and Nb₅Si₃ were contaminated by oxygen, the former more severely than the latter and the contamination of both phases became less severe with increasing

depth below the scale. At both temperatures Nb_2O_5 , TiO_2 , SiO_2 , HfO_2 and Ti niobates formed in the scale but not Al niobates.

Chapter 4: The alloy Nb-24 Ti-22Si-30Al-5Hf

4.1 Alloy Nb-24Ti-22Si-30Al-5Hf (MG2)

4.1.1 As cast

The nominal composition of the alloy MG2 is shown in table 13. The actual composition was determined by EDS and was Nb-23.4Ti-22.8Si-29.7Al-4.8Hf. This was the average composition of all EDS analysis data from the top, centre and bottom of the ingot, the data of which is given in table 14. The standard deviations for all elements in the average alloy composition were large owing to the macrosegregation of all elements. Indeed, the difference between the maximum and minimum analyses values were 12.8, 16, 17 and 4 at%, respectively for Si, Ti, Al and Hf. For Si, Ti and Hf the strongest macrosegregation was observed in the centre (bulk) of the ingot. There was strong chemical inhomogeneity for Nb, with the lowest concentration in the bottom of the ingot owing to the severe macrosegregation of all alloying elements. Furthermore, the highest average Al+Si concentration was in the bottom of the ingot.

Table 13: Nominal composition (at%) of the alloy MG2-AC

Alloy	Nb	Si	Ti	Al	Hf
MG2	19	22	24	30	5

The microstructure of MG2-AC is shown in figure 48. In all parts of the ingot there were large (bulky) faceted grains of a light contrast phase surrounded by a darker contrast microstructure in which there were fine second phase(s). The formation of the latter microstructure was significantly reduced in the bottom of the ingot.

The XRD data for the alloy MG2-AC is shown in figure 49 and indicated the presence of silicides and Tm_xAl_y intermetallics. In the X-ray diffractogram there were peaks that corresponded only to hexagonal 5-3 silicide γNb_5Si_3 , βNb_5Si_3 , $TiAl_3$, while the peak for $TiAl$ coincided with those of other phases. The outline of some of the large lighter contrast grains in figure 48 suggested hexagonal symmetry, which is consistent with the crystal structure of γNb_5Si_3 . The XRD data suggested the presence of Ti_5Si_4 and $TiSi$. Peaks for the latter silicide coincided with peaks for other phases. As we shall see in subsequent chapters the Ti_5Si_4 forms as thin layers on 5-3 silicide and the $TiSi$ has similar contrast with Ti_5Si_4 . Careful study of MG2-AC using EDS did not confirm the existence of Ti_5Si_4 and $TiSi$.

The EDS analysis data for the large lighter contrast grains identified them as 5-3 silicide. The data for the silicide is summarized in table 14. High magnification BSE images of the microstructure in the centre and top are shown in figure 50 and figure 51. In the centre of the ingot (figure 50) there was segregation (partitioning) of Ti and Hf in the 5-3 silicide with some being Ti-rich with $Nb/(Ti+Hf) \approx 0.6$ and others Ti+Hf rich with $Nb/(Ti+Hf) \approx 1$ which would indicate γNb_5Si_3 according to the empirical Bewlay rule (Bewlay and Jackson, 2003), while others were Hf-rich with the $Nb/(Ti+Hf) > 1$, which would correspond to tetragonal Nb_5Si_3 according to the same rule. This is consistent with the outline of the microstructure of silicide in figure 50, some of which clearly show hexagonal symmetry.

In the top of the ingot (Figure 51a Figure 50a) the concentration of Al in 5-3 silicide grains was decreased. There were Hf-rich and Al-rich but with $Nb/(Ti+Hf)$ ratio greater

than 1. In the bottom of the ingot Ti rich Nb_5Si_3 was formed with $\text{Nb}/(\text{Ti}+\text{Hf}) = 0.56$. Thus, the complimentary techniques of XRD and EDS confirmed the presence of $\gamma\text{Nb}_5\text{Si}_3$ and tetragonal $\beta\text{Nb}_5\text{Si}_3$. The 5-3 silicide had $38.2 < \text{Si}+\text{Al} < 41.6$ at%, which is consistent with the binary phase diagram assuming that Si atoms are substituted by Al atoms in the crystal structure.

The microstructure surrounding the 5-3 silicide grains exhibited dark contrast but within the “dark” contrast areas there was also a slight variation in contrast that is not possible to show in the printed image, for example see figure 50. The EDS analyses confirmed different Al+Si concentration in these areas some of which were Ti rich, and others Ti and Nb rich. With the “guidance” of the XRD data (figure 49) and Dezellus et al, (2014), Bulanova et al, (2004) and Perrot, (2009) these were identified to be aluminides, in particular Al_3Ti and $\text{Al}_3(\text{Ti},\text{Nb})$ in the bottom of the ingot, TiAl , Ti_2Al_5 and $\text{TM}_{2.35}\text{Al}_{1.65}\text{Si}$ in the centre and TiAl and $\text{TM}_{3.7}\text{Al}_3\text{Si}$ in the top of the ingot. In the latter the $\text{TM}_{3.7}\text{Al}_3\text{Si}$ had the same Al+Si content but different Al/Si ratio than that in the bulk with similar compositions that have not been reported in the literature. Thus, it was assumed that these were metastable phases that formed because of the strong chemical inhomogeneity in the MG2-AC ingot. The results of the heat treated alloy (see below) supported this assumption. Finally, in the top of the ingot some of the microstructure in the dark contrast area would correspond to a eutectic. Large area analyses of the area are summarized in table 14. The Si and Al contents are in agreement with a eutectic between the 5-3 silicide and TiAl aluminides, as reported in Bulanova et al, (2004) and Perrot, (2009).

Table 14: EDS analysis data (at%) of the alloy MG2-AC

Area and phase analysis		Element					Al+Si	
		Nb	Si	Ti	Al	Hf		
Large area analyses	Top	23.8±0.4 23.3-24.4	18.2±1.1 16.8-19.5	20.3±0.3 20-20.7	31.9±1.6 29.8-33.7	5.7±0.2 5.3-5.9	50.1	
	Bulk	21.8±5.1 15.9-30.6	24±3.6 15.7-28.5	22.7±5.2 14.6-30.6	25.6±3.4 21-32.6	5.1±1.1 2.8-6.8	49.6	
	Bottom	13.7±0.7 12.9-15	23±1.3 21.3-25.5	25.6±0.7 24-26.5	33.3±2.8 32.3-38	4±0.2 3.8-4.4	56.3	
	Average	18.9±5.4 12.0-30.6	22.8±3.2 15.7-28.5	23.4±3.9 14.6-30.6	29.7±4.7 21-38	4.8±1 2.8-6.8	52.5	
Phase (spot) analysis			Aluminides					
	top	TM _{3.7} Al ₃ Si	18.7±0.9 18-19.3	12.9±2 11.4-14.3	20.4±0 20.4-20.5	39.2±2 37.8-40.7	8.8±0.8 8.1-9.4	52.1
		TiAl	15.9±2.4 14.5-18.7	6.7±3.4 2.8-9.4	17.3±2.3 15.6-19.9	49±5.1 43.8-54.1	10.9±2.5 8.1-12.9	55.8
		TiAl	18.9±0.8 17.6-19.9	0.8±0.2 0.6-1.1	19.4±0.7 18.8-20.7	57.8±0.8 56.4-58.8	3.1±0.6 2.4-4.2	58.6
		TiAl	18.8±0.6 18.3-19.7	3.5±0.8 2.3-4.1	19.7±0.5 19.3-20.4	53.3±1.4 52.2-55.1	4.6±0.8 3.5-5.4	56.9
	bulk	Ti ₂ Al ₅	16±0.5 15.2-16.5	1.1±0.5 0.5-1.9	10.8±1.2 9.1-12.4	70.8±1.8 67.8-72.4	1.4±0.2 1.1-1.9	72
		TiAl	16.2±1.4 14.8-18.5	0.9±0.6 0.4-2.3	20.3±1.9 18-22.4	58.2±1 57.7-59.4	4.2±0.9 2.8-5.2	59
		TiAl	9.9±1 8.4-11	1.2±0.4 0.8-1.9	23.7±2.4 19.6-25.6	62.4±2.6 60.9-66.7	2.8±0.3 2.2-3.1	63.6
		TM _{2.35} Al _{1.65} Si	13±2.6 10.1-15.8	19.8±4.4 16-26.4	26.5±3.3 23.1-32.3	33.3±6.7 23.1-40.6	7.1±1.6 4.8-9.2	52.6
	bottom	Al ₃ (Ti,Nb)	6.51±0.4 3.5-8.2	2.1±0.6 1.6-3.4	17.5±1.8 15.6-19.9	72.1±1 70.8-73.5	1.6±0.3 1.4-2.2	74.2
		Al ₃ (Ti,Nb)	12±1.1 10.2-13.2	1.4±0.1 1.3-1.6	12.7±1 11.2-13.7	72.5±0.4 72-73.3	1.2±0.1 1.1-1.4	73.9
		Al ₃ Ti	1.4±0.4 0.9-1.8	2.7±0.7 1.8-3.4	22±1.1 21.2-23.7	71.9±0.2 71.6-72.1	1.4±0.4 1.8-2	74.6
			5-3 silicide					
	top	Hf-rich Nb ₅ Si ₃	32.4±2.8 29.4-40.1	35.9±1.1 34.1-36.8	18.5±4 7.4-23.2	4.8±1 2.2-6.3	8.4±1.2 7.3-11.9	40.7
		Nb ₅ Si ₃	36.6±1 36.6-36.7	30.2±1.1 29.5-31.1	19±0.1 19-19.2	9.5±1.4 8.5-10.5	4.5±0.1 4.4-4.5	39.8
	bulk	Ti-rich Nb ₅ Si ₃	21.9±1.4 18.7-24.2	38±1.2 34.1-39	31.2±1.5 28.7-34.4	3±0.8 2.3-5.3	5.8±0.6 5.3-7.4	41
		Hf and Ti-rich Nb ₅ Si ₃	29.4±1.8 7.1-8.4	37±1.4 35.4-38	21.7±2.5 18.8-23.6	4.2±1.5 3.3-5.9	7.7±0.7 7.1-8.4	41.2
		Hf-rich Nb ₅ Si ₃	37.4±0.6 34.6-35.8	33.3±1 32.9-34.9	13.2±1.2 12.4-14.6	6.2±0.6 5.2-6.4	9.9±0.8 10.6-12.1	39.7
		Nb ₅ Si	43.1±1.3 42.2-44.1	31.2±0.6 30.8-31.6	12.8±1.8 11.5-14.2	7±0.1 6.9-7.1	5.7±0 5.7-5.8	38.2

	Bottom	Ti-rich Nb ₅ Si ₃	21.1±0.5 20.5-21.7	38.6±0.3 38.1-39	32±0.6 31.4-33.3	2.7±0.3 2.5-3.6	5.4±0.5 4.6-6	41.6
Large area	Top	Eutectic	19.8±0.8	6.1±1.9	20.2±0.5	49.4±3.1	4.5±0.5	55.5

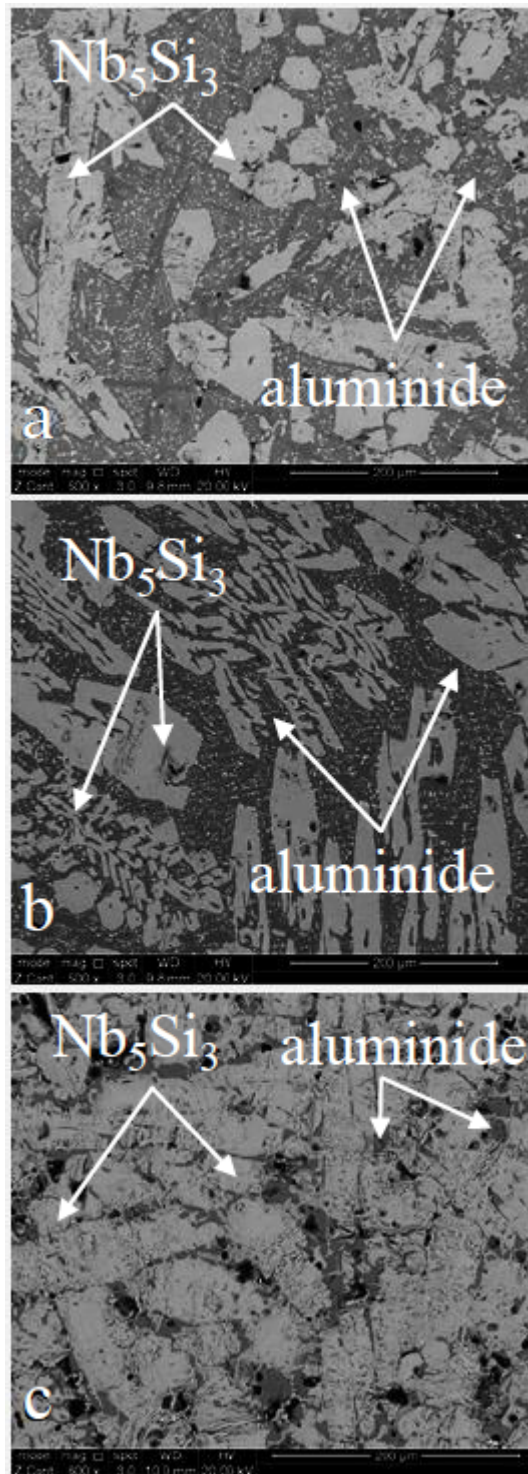


Figure 48: SEM backscatter electron images of the microstructure of the alloy MG2-AC (a) top, (b) centre and (c) the bottom of the ingot

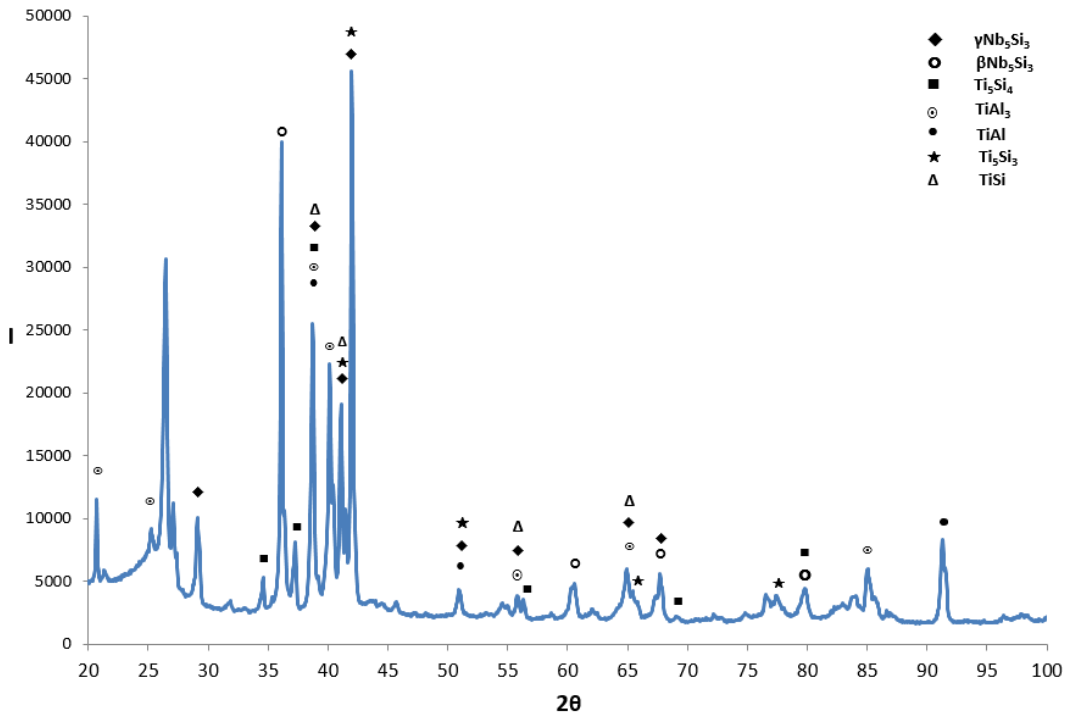


Figure 49: X-ray diffractogram of the alloy MG2-AC

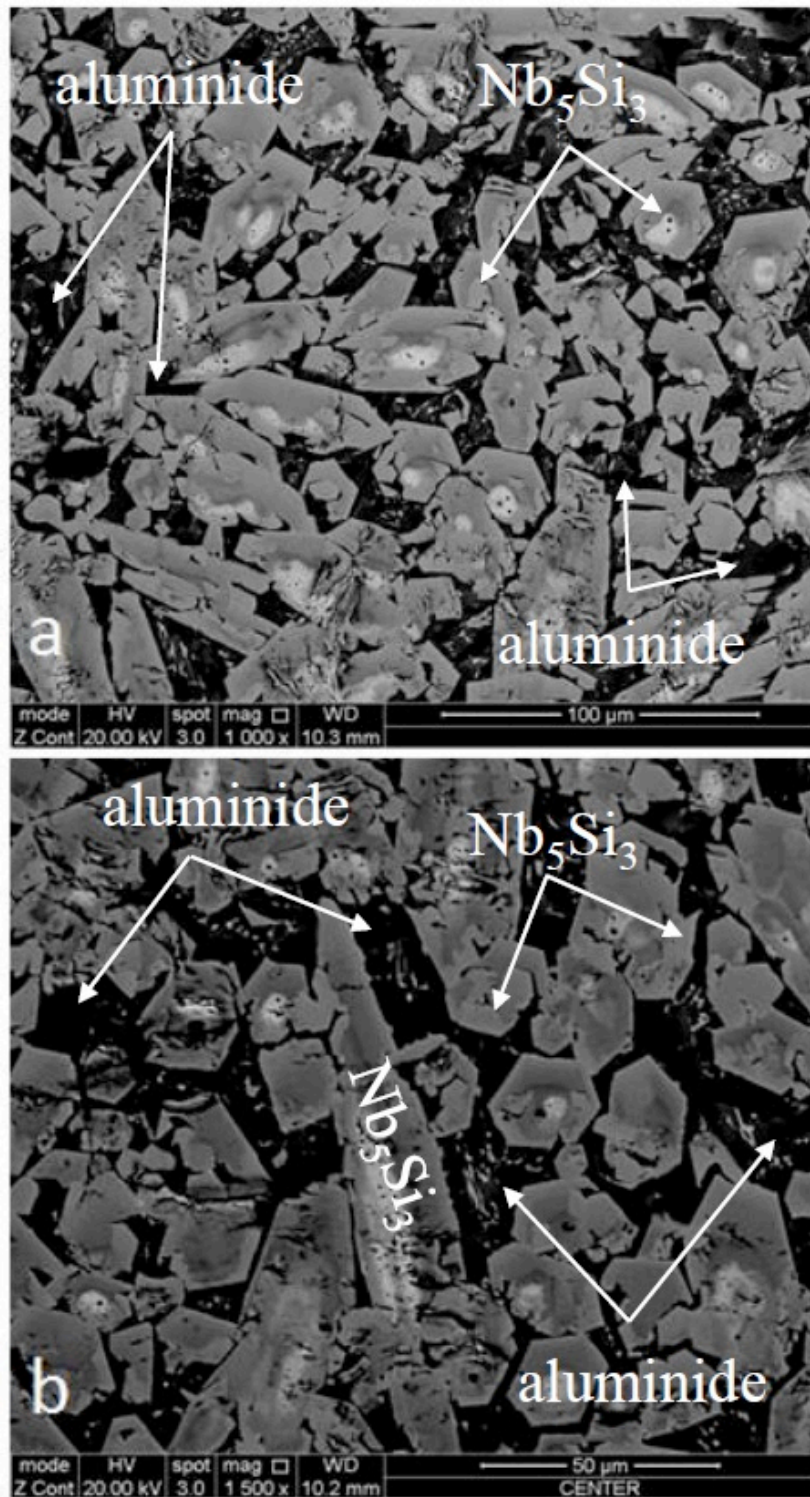


Figure 50: SEM backscatter electron images of the microstructure of the centre of the ingot of MG2-AC. (a) microstructure of the centre near the top, (b) microstructure of the bulk near the bottom

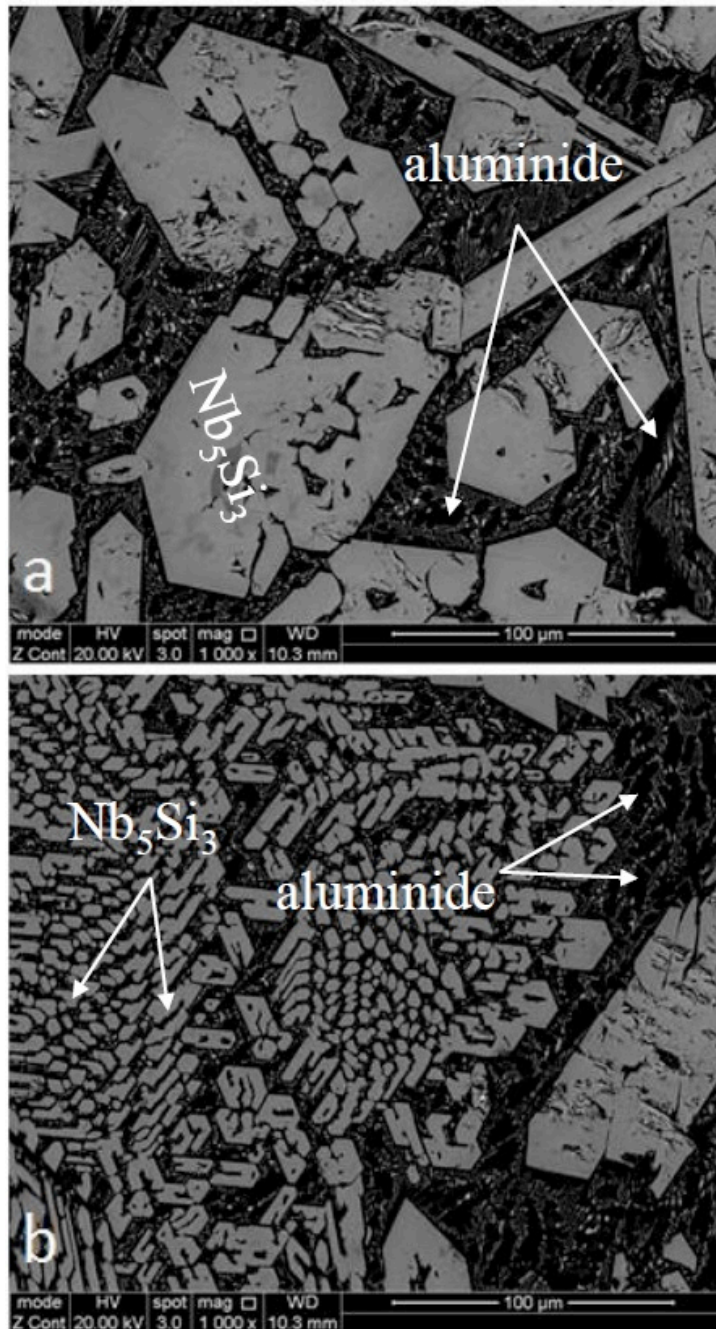


Figure 51: SEM backscatter electron images of the microstructure in the top of the alloy MG2-AC, (a) top of the alloy, (b) very top near the surface of the ingot

4.1.2 Heat treated

The alloy MG2 was heat treated at 1300 °C for 100 h. The choice of the heat treatment temperature was based on the DSC trace (figure 52), the microstructure of MG2-AC, which showed the presence of aluminides, and the TiAl and Nb-Al binary phase diagrams. The latter show that aluminides can be in equilibrium with the liquid above 1400 °C. The DSC trace did not show any melting up to 1500 °C but there was weak evidence of transformation around 1000 °C where there are solid state transformations in the Ti-Al binary.

Low magnification BSE images of the microstructure of MG2-HT are shown in figure 53, and higher magnification images in figure 53 to figure 57. The XRD data is shown in figure 58 and the EDS data in table 15. The average composition of MG2-HT was close to that of MG2-AC and the Al+Si content was the same. The standard deviations of the elements were large with the exception of Hf, owing to the prevailing large scale chemical inhomogeneity after the heat treatment, which was most severe in the bulk for Si, Ti and Al, as was the case in MG2-AC.

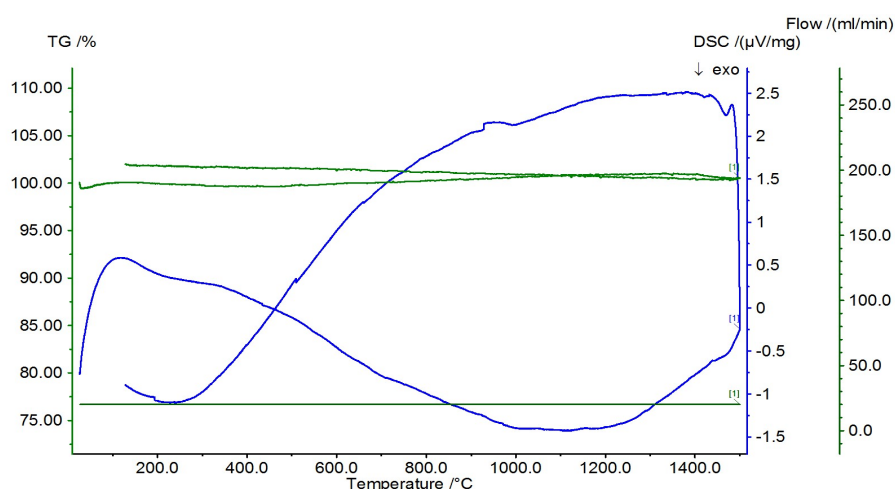


Figure 52: DSC trace of the alloy MG2

The microstructure in the bottom of the heat treated ingot, figure 53b, was very similar to that of the as cast alloy. It consisted of two phases namely the Nb_5Si_3 and TMAl_3 . The EDS data of the former showed that it was Ti-rich with $\text{Nb}/(\text{Ti}+\text{Hf}) = 0.5$, which would suggest hexagonal silicide according to the empirical rule of Bewlay (Bewlay and Jackson, 2003). The latter had Si slightly lower than the same phase in the cast alloy because of a smaller reduction in the concentration of Si. The aforementioned phases were also corroborated by the XRD data of the MG2-HT, see figure 58, which indicated hexagonal 5-3 silicide and Al_3Ti aluminide.

The microstructure in the bulk (centre) of MG2-HT, figure 53b, figure 54a, figure 55, consisted of hexagonal Nb_5Si_3 with $\text{Nb}/(\text{Ti}+\text{Hf}) = 0.8$ and TiAl and Al_3TM aluminides. The TM_xAl_y that was observed in the cast alloy was absent, confirming that it was a metastable phase and the Ti_2Al_5 had transformed to Al_3TM owing to the slight increase in the Al concentration. These phases were also consistent with the XRD data, figure 58.

Moreover, in the top the microstructure (Figure 53a, Figure 55a, Figure 56 and Figure 57) consisted of tetragonal Nb_5Si_3 with $\text{Nb}/(\text{Ti}+\text{Hf}) = 1$ and TiAl and Ti_2Al_5 aluminides. The $\text{TM}_{3.7}\text{Al}_3\text{Si}$ was absent, confirming its metastable nature. Instead, Ti_2Al_5 was observed, this was not observed in the top of the cast alloy. Therefore, the microstructure of MG2-HT would suggest that the stable aluminides in the alloy MG2 were the TiAl , Al_3TM and probably Ti_2Al_5 with differentiation between the two being difficult with EDS data. However, the XRD data suggested the presence of TiAl and Al_3TM . The XRD data also indicated stability of β and $\gamma\text{Nb}_5\text{Si}_3$ but according to the EDS data the $\text{Nb}/(\text{Ti}+\text{Hf})$ ratio was reduced to ≤ 1 after the heat treatment, which

suggests that the hexagonal 5-3 silicide is most likely the stable 5-3 silicide in the microstructure of the alloy MG2. There was no evidence of the prior eutectic seen in the top of the cast alloy. However, the microstructure surrounding the bulky 5-3 silicide grains exhibited light contrast particles in the dark contrast matrix, a microstructure that is consistent with coarsened $\text{Nb}_5\text{Si}_3 + \text{TiAl}$ prior eutectic. According to the XRD data the Ti_5Si_4 and TiSi silicides were also present. Careful study using EDS did not confirm their existence, meaning no analysis corresponded to these phases. However, one image, figure 56b shows slightly different contrast at the edge of Nb_5Si_3 , i.e., in the areas where Ti_5Si_4 forms. This contrast is similar to that of Ti rich areas in Nb_5Si_3 and as table 15 shows there was Ti rich Nb_5Si_3 in MG2-HT. Thus it was confirmed that the Ti_5Si_4 and TiSi were not present in MG2-HT.

Table 15: EDS analysis data (at%) for the alloy MG2-HT (1300 °C/100 h)

Area and phase analysis		Element					Al+Si	
		Nb	Si	Ti	Al	Hf		
Large area	Top	23±1.2 20.5-24.6	19.1±3.4 14.8-26.3	21.5±1.1 20.6-24.2	31.4±5.2 20.3-33.7	5±0.3 4.4-5.3	50.5	
	Bulk	19.3±2.4 17.2-24.1	22.5±4.8 18.4-31.2	24.3±3.1 20.8-30.5	29.5±6.9 14.7-36.9	4.4±0.5 3.7-5.3	52	
	Bottom	14.8±1.8 13-19	24.7±2.8 20.4-28.7	26.5±1 24.8-28.6	30.1±5.6 21.1-38.6	3.9±0.4 3.2-4.6	54.8	
	Average	18.8±3.8 13-24.6	22.3±4.3 14.8-31.2	24.3±2.8 20.6-30.5	30.2±5.8 14.7-38.6	4.4±0.6 3.2-5.3	52.5	
Phase (spot) analysis			Aluminides					
	Top	TiAl	18.7±1.2 16.7-21	1.8±3 0.2-9.6	20.8±1.6 15.9-23	56.3±2.5 49.3-59.8	2.3±0.5 1.6-2.8	58.2
		Ti ₂ Al ₅	20.7±0.4 20.5-21.7	0.6±0.8 0.1-2.7	7.3±0.7 6.7-8.7	70.2±2.1 65-71.3	1±0.3 0.8-1.8	70.8
	Bulk	TiAl	12.9±0.3 12.5-13.1	0.3±0.1 0.2-0.4	26±0.3 25.6-26.3	58.9±0.1 58.7-58.9	2±0.1 1.9-2.1	59.1
		Al ₃ (Ti,Nb)	17.7±0.1 17.6-17.8	0.1±0 0-0.1	9.6±0.2 9.5-9.8	71.7±0.2 71.5-72	1±0.1 0.9-1	71.8
	Bottom	Al ₃ (Ti,Nb)	16.2±1.3 13.3-17.2	0.9±1 0.2-2.9	10.2±3.2 8-17.1	72±2.5 67.8-73.9	0.7±0.1 0.6-1	72.9
			5-3 silicide					
	Top	Nb ₅ Si ₃	29.9±0.7 28.7-31	36.6±0.6 35.8-37.6	22.1±1.2 20.4-23.9	4±0.5 3.3-4.6	7.4±3 7-7.9	40.6
	Bulk	γNb ₅ Si ₃	26.6±2.2 23.3-28.3	36.4±1.3 35-37.6	26±2.2 23.4-29	4.2±1.1 3-5.7	6.8±0.2 6.5-7	40.6
	Bottom	Ti-rich Nb ₅ Si ₃	20.7±3.5 16.4-25.4	36.6±3.5 31.4-39	35.1±7.5 27.4-45.4	2.6±0.6 2.2-3.5	5.1±0.5 4.5-5.5	39.2

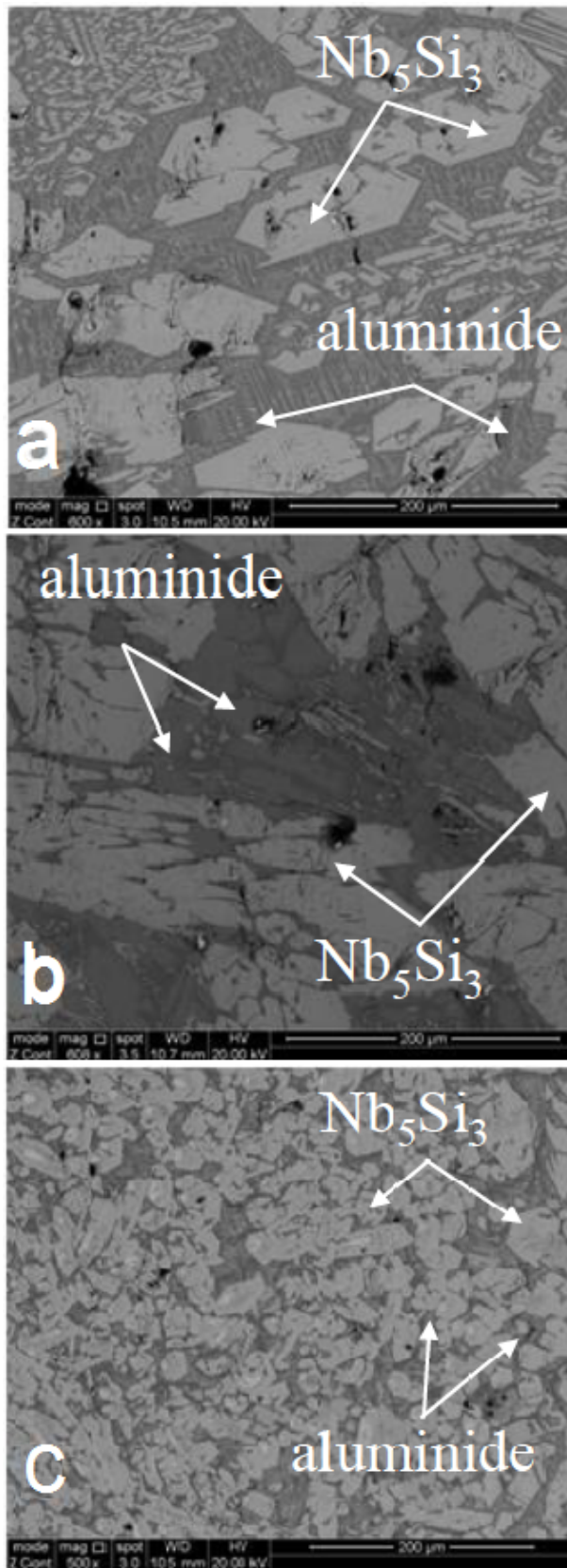


Figure 53: SEM backscatter electron images of the alloy MG2-HT, (a) top, (b) centre and (c) bottom of the heat treated alloy

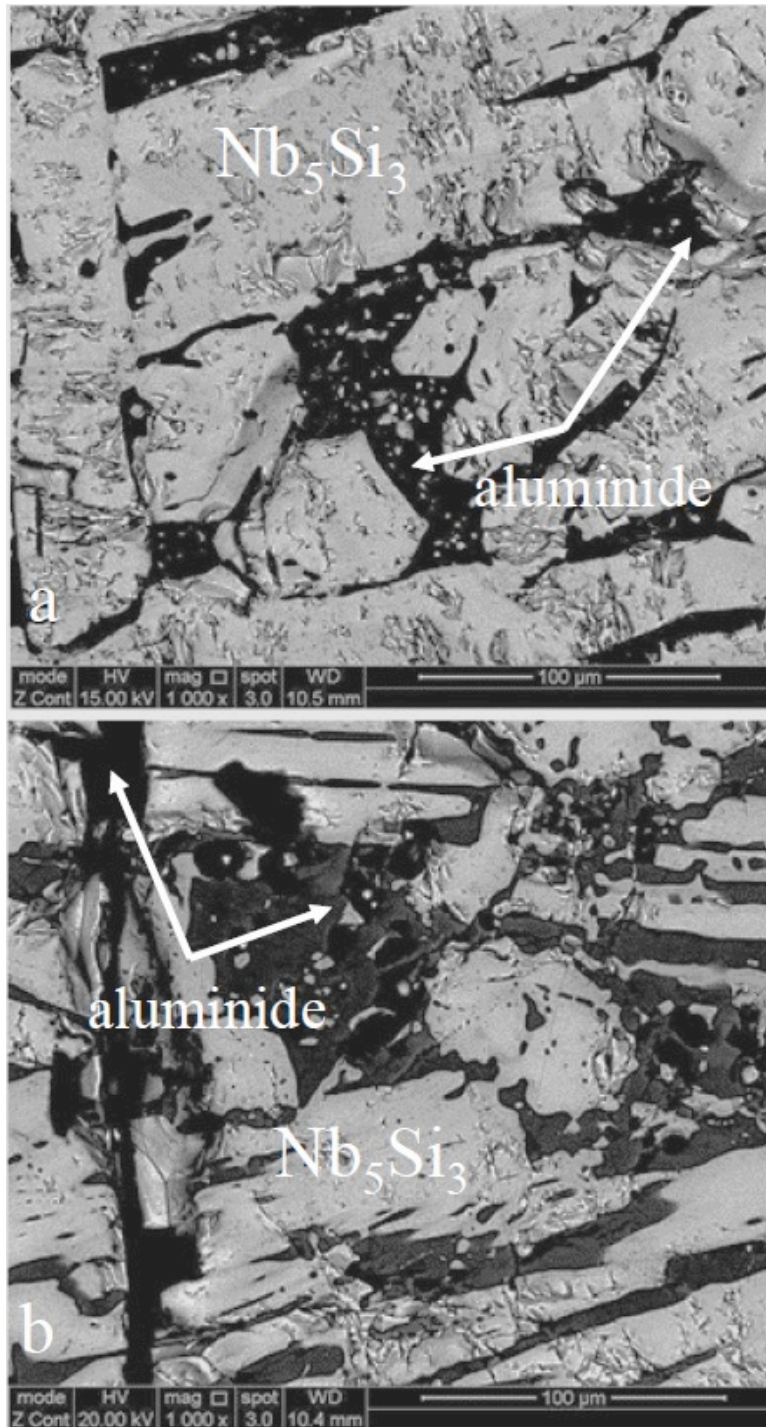


Figure 54: SEM backscatter electron images taken from the bottom of MG2-HT (a) bottom near the centre, (b) bottom

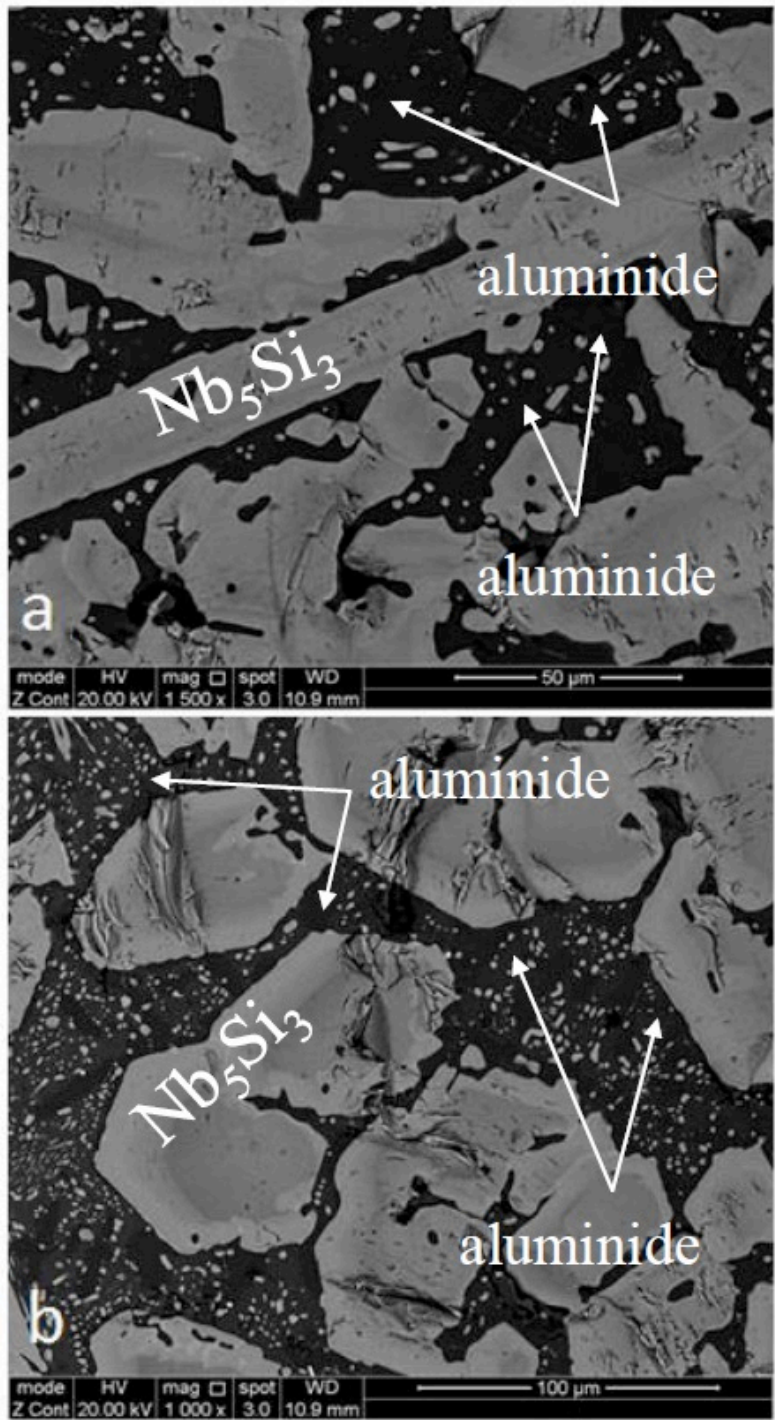


Figure 55: SEM backscatter electron images of the microstructure in the centre of MG2-HT, (a) centre near the bottom, (b) centre near the top

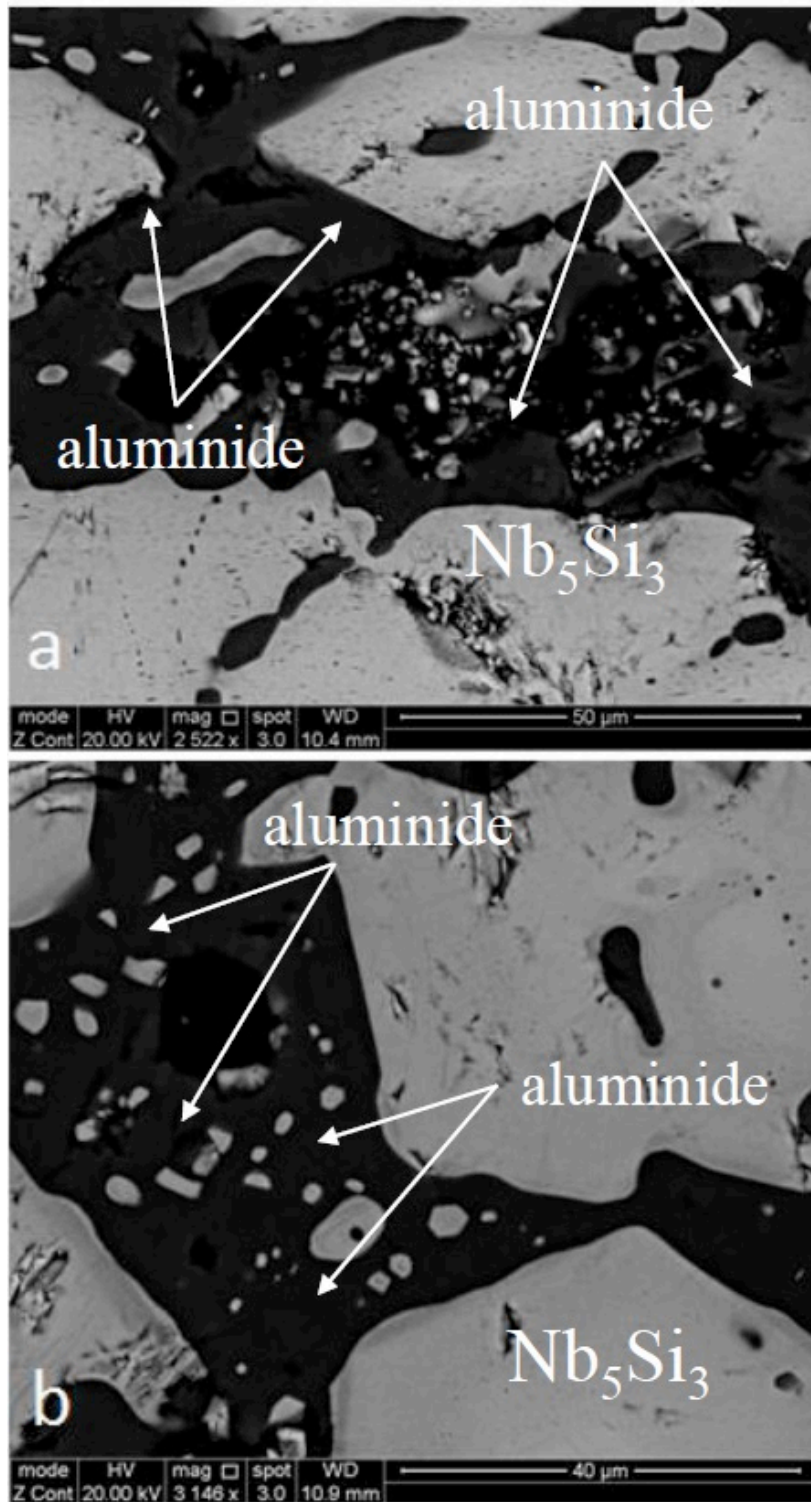


Figure 56: High magnification SEM backscatter electron images of the alloy MG2-HT taken (a) from the top of the heat treated specimen and (b) from the very top near the surface

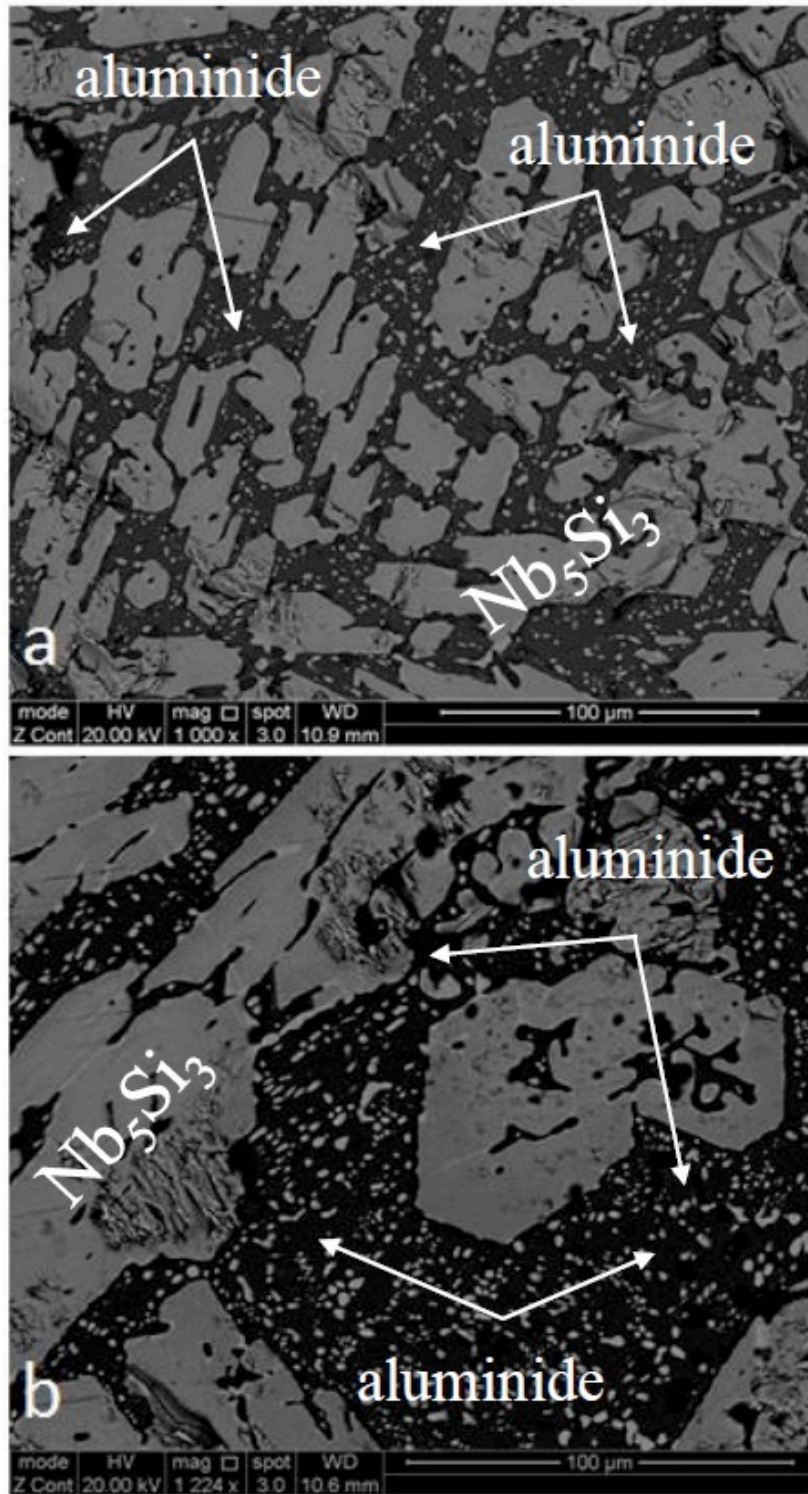


Figure 57: Microstructure of the top of the heat treated MG2 alloy taken in backscattered electron mode. The gray contrast is Nb_5Si_3 phase and the dark areas are considered to be TM_xAl_y type and TMA_3 aluminides which had been found in the top of the as cast sample

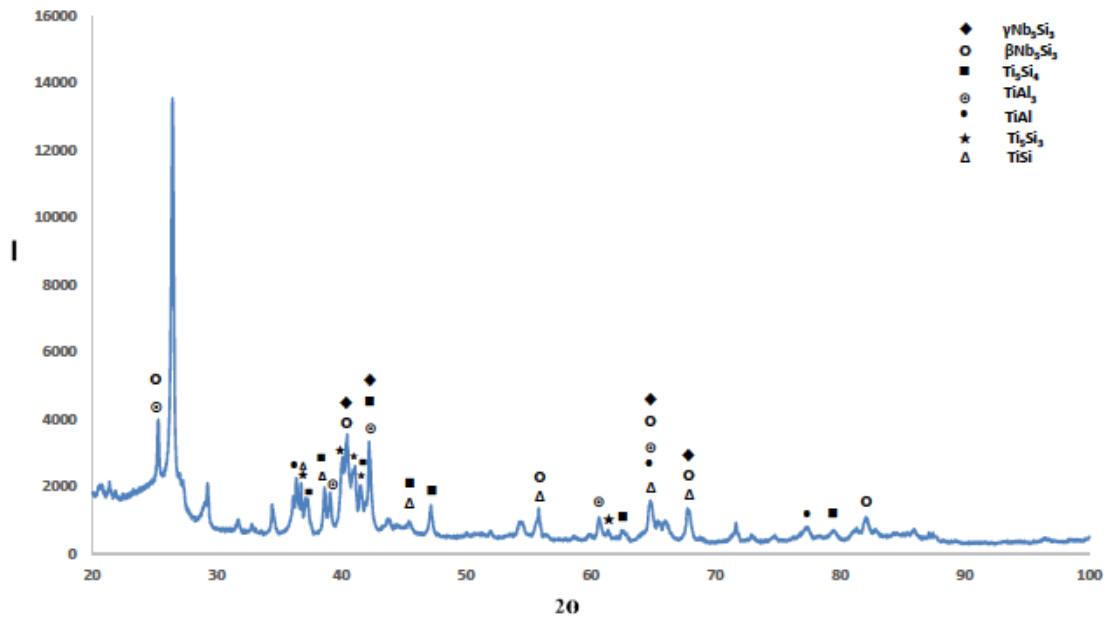


Figure 58: X-ray diffractogram of the alloy MG2-HT (1300 °C/100 h)

4.1.3 Oxidation behaviour

The alloy MG2 was the first Nb-Si based alloy with high Al concentration studied in our group. We anticipated good oxidation behaviour given that its microstructure was free of bcc Nb_{ss} and with high volume fractions of Si rich silicides and Al rich aluminides. The ingot of MG2-AC was severely cracked. It was decided to evaluate first its oxidation behaviour by oxidising “crack free” specimens in air in a muffle furnace at 800 °C and 1200 °C for 100 h. The oxidised specimens are shown in figure 59. At 800 °C the alloy did not pest, and at 1200 °C it did not exhibit spallation of the scale, which appeared to be thin. Unfortunately, at 1200 °C upon removal from the furnace the oxidised specimen broke in three pieces, see figure 59b, but did not disintegrate into powder. Perhaps the sample had contained cracks through which the oxidation had been severely accelerated. Given the promising results from the muffle furnace oxidation tests, it was then decided to proceed to evaluate the oxidation of MG2 using TGA. The TGA specimens were analysed using SEM and XRD.

4.1.3.1 Isothermal oxidation using TGA

The oxidation behaviour of MG2 was studied at 800 °C and 1200 °C using TGA. The oxidised specimens after 100 h isothermal oxidation at each temperature are shown in figure 60 and figure 61. The TGA data is shown in figure 62 and figure 63 and the oxidation rate constants are given in table 16. The alloy MG2 followed parabolic oxidation kinetics at 800 °C with rate constant $k_p = 2 \times 10^{-12} \text{ g}^2\text{cm}^{-4}\text{s}^{-1}$. At 1200 °C all the data gave parabolic oxidation with parabolic rate constant $k_p = 2 \times 10^{-10} \text{ g}^2\text{cm}^{-4}\text{s}^{-1}$ and the weight gain was 8.5 mg/cm^2 . However, there were changes in weight gain after 14 and 41 h and when the data was considered for each time section the oxidation was parabolic with $k_p = 6 \times 10^{-11} \text{ g}^2\text{cm}^{-4}\text{s}^{-1}$ for the first 14 h at 1200 °C and then linear, see table 16.

The microstructures of the oxidised specimen just below the scale and in the bulk are shown in figure 64 and figure 65, respectively for 800 °C and 1200 °C. Analysis data for phases in the oxidised specimens just below the scale and in the bulk are given in table 17 and table 18. Figure 64a shows remnants of the thin scale attached to the substrate. Figure 65a shows more severe attack (as should be expected) of the microstructure below the scale. Table 17 and table 18 show less contamination of the tri-aluminide compared with TiAl both below the scale and in the bulk, and worse contamination of the 5-3 silicide compared with the aluminides at both temperatures and more severe contamination at 1200 °C.

Figure 66 shows the GXR data for the TGA specimens of the oxidised alloy. Figure 66a is the GXR for the alloy oxidised at 800 °C and suggests the presence of Ti niobates, Nb_2O_5 , HfO_2 , TiO_2 , TiAl_2O_5 and SiO_2 . Figure 66b is the GXR data of the

alloy oxidised at 1200 °C and suggests the presence of the same oxides as at 800 °C plus $\alpha\text{Al}_2\text{O}_3$.

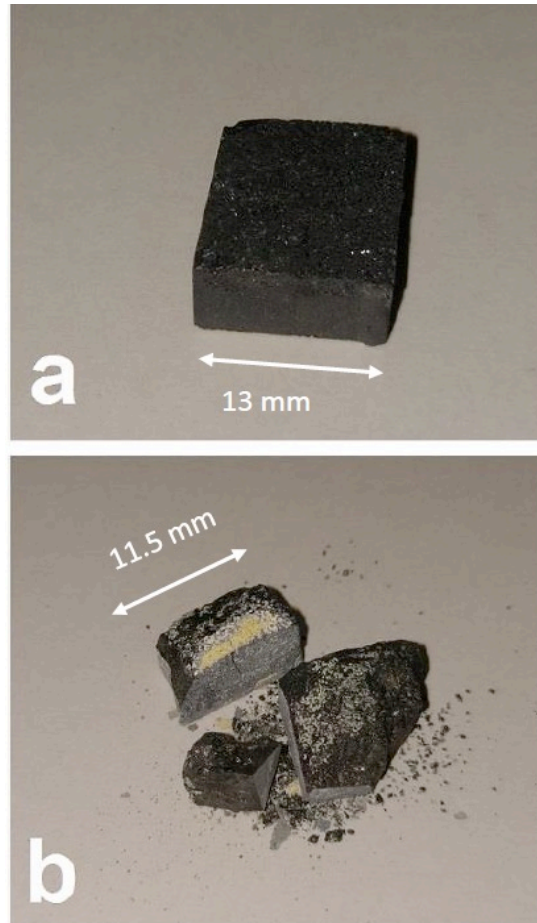


Figure 59: Specimen of oxidized alloy MG2 in muffle furnace for 100 h: a) 800 °C, b) 1200 °C for 100h

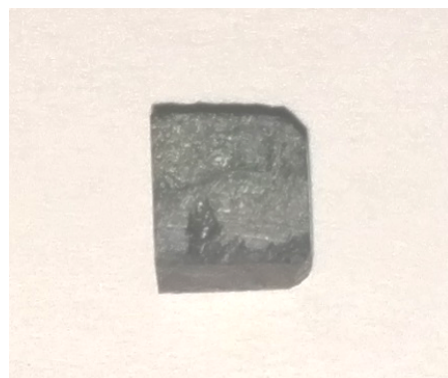


Figure 60: The specimen of the alloy MG2 after TGA at 800 °C

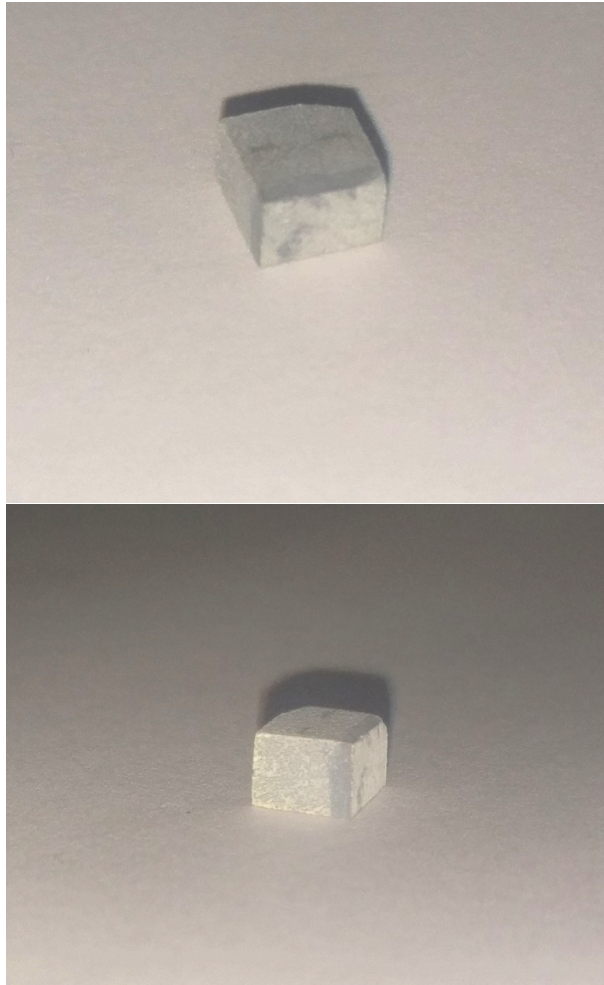


Figure 61: The specimen of the alloy MG2 after TGA at 1200 °C

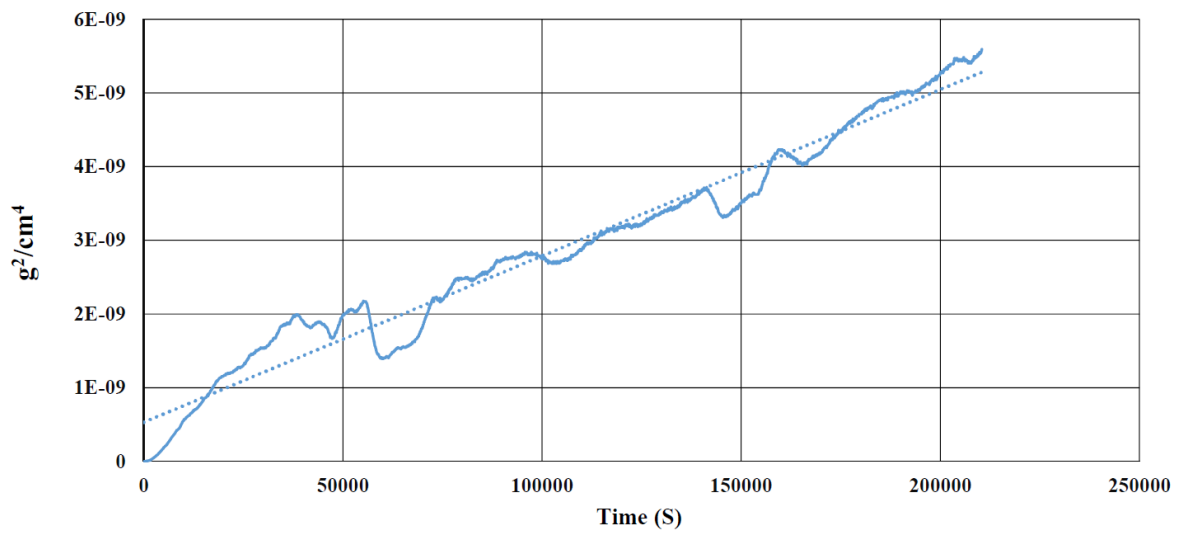


Figure 62: Fit of TGA data of MG2 oxidised at 800 °C to parabolic oxidation, $R^2 = 0.9663$

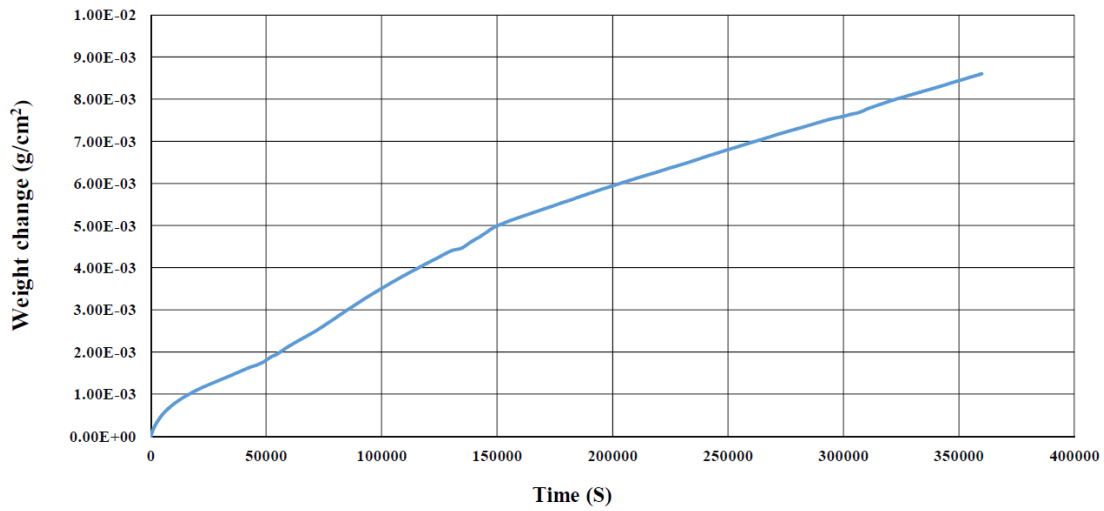


Figure 63: TGA data for MG2 oxidised at 1200 °C

Table 16: Oxidation rate constants of the alloy MG2 after TGA at 800 °C and 1200 °C

Alloy	800 °C	1200 °C		
	K_p ($\text{g}^2 \text{cm}^{-4} \text{s}^{-1}$)	K_p ($\text{g}^2 \text{cm}^{-4} \text{s}^{-1}$)	K_l ($\text{g cm}^{-2} \text{s}^{-1}$)	K_l ($\text{g cm}^{-2} \text{s}^{-1}$)
MG2	2×10^{-12}	All data ($t \leq 100 \text{ h}$) 2×10^{-10}	$14\text{h} < t < 41\text{h}$ 3×10^{-8}	$(t > 41\text{h})$ 2×10^{-8}
		$(t < 14\text{h})$ 6×10^{-11}		

Table 17: Analysis data (at%) for Nb_5Si_3 , TiAl and Al_3Ti at 800 °C

Area and Phase analysis		Element					
Nb_5Si_3							
↓	Edge	O	Nb	Si	Ti	Al	Hf
		6.4	25.2	34.6	24.3	4	5.4
		6.3	26.4	35.3	22.6	3.3	6.1
		5.4	26.9	35.3	22.6	3.3	6.1
	Bulk	5.1	25.8	35.6	24.1	3.9	5.5
		5.7	24.8	34.8	25.1	3.9	5.8
TiAl							
		5.3	26.2	35.4	23.7	3.5	5.9

↓		O	Nb	Si	Ti	Al	Hf
	Edge	5.9	12.6	1.4	22.6	55.3	2.1
		4.8	9.3	1.4	23.9	57	3.5
		4.2	9.7	3.4	24.9	54	3.7
	Bulk	4.8	13	0.7	23	56.3	2.2
TiAl ₃							
↓		O	Nb	Si	Ti	Al	Hf
	Edge	4.5	17.3	0.5	9.8	66.9	1.1
		3.8	16.9	0.4	10.1	67.7	1
	Bulk	3.9	16.9	0.5	9.8	67.8	1.1
		2.6	17.5	0.3	9.8	68.6	1.2

Table 18: Analysis data (at%) for Nb₅Si₃, TiAl and Al₃Ti at 1200 °C

Area and Phase analysis		Element					
Nb ₅ Si ₃							
↓		O	Nb	Si	Ti	Al	Hf
	Edge	14.6	23.5	31.6	21.6	3	5.7
		12.6	23.3	32.8	22.9	3.1	5.3
		11.8	23.7	33.2	22.6	3.4	5.3
		9.6	23.3	32.7	25.3	4	5.1
		7.3	25	35.1	23.7	3	5.8
	Bulk	8.5	24.9	34.7	23	3.2	5.7
		7.2	25.4	34.4	23.9	3.4	5.7
		6.8	24.8	35.1	24.4	3.2	5.7
		5.4	25.7	35.3	25	3.1	5.6
4.5		25.7	35.3	25	3.9	5.6	

TiAl							
↓	Edge	4.8	13.6	0.6	26.9	52.9	1.2
		3.8	15.8	0.6	24.7	54	1.1
	Bulk	3.4	10.9	10.5	27.4	43.1	4.6
		3.1	16.8	6.6	15	56.3	2
TiAl3							
↓	Bulk	4.1	16	0.3	10	68.4	1.2
		3.5	15.8	0.7	10.7	67.7	1.4
		3.3	15.8	0.5	11.6	67.6	1.2
		2.7	16	0.3	10.1	69.6	1.3
		2.3	16.5	0.02	10.1	69.7	1.4
		2	16.4	0.01	10.4	69.9	1.3
		0.8	16.9	0.3	10.4	70.2	1.3

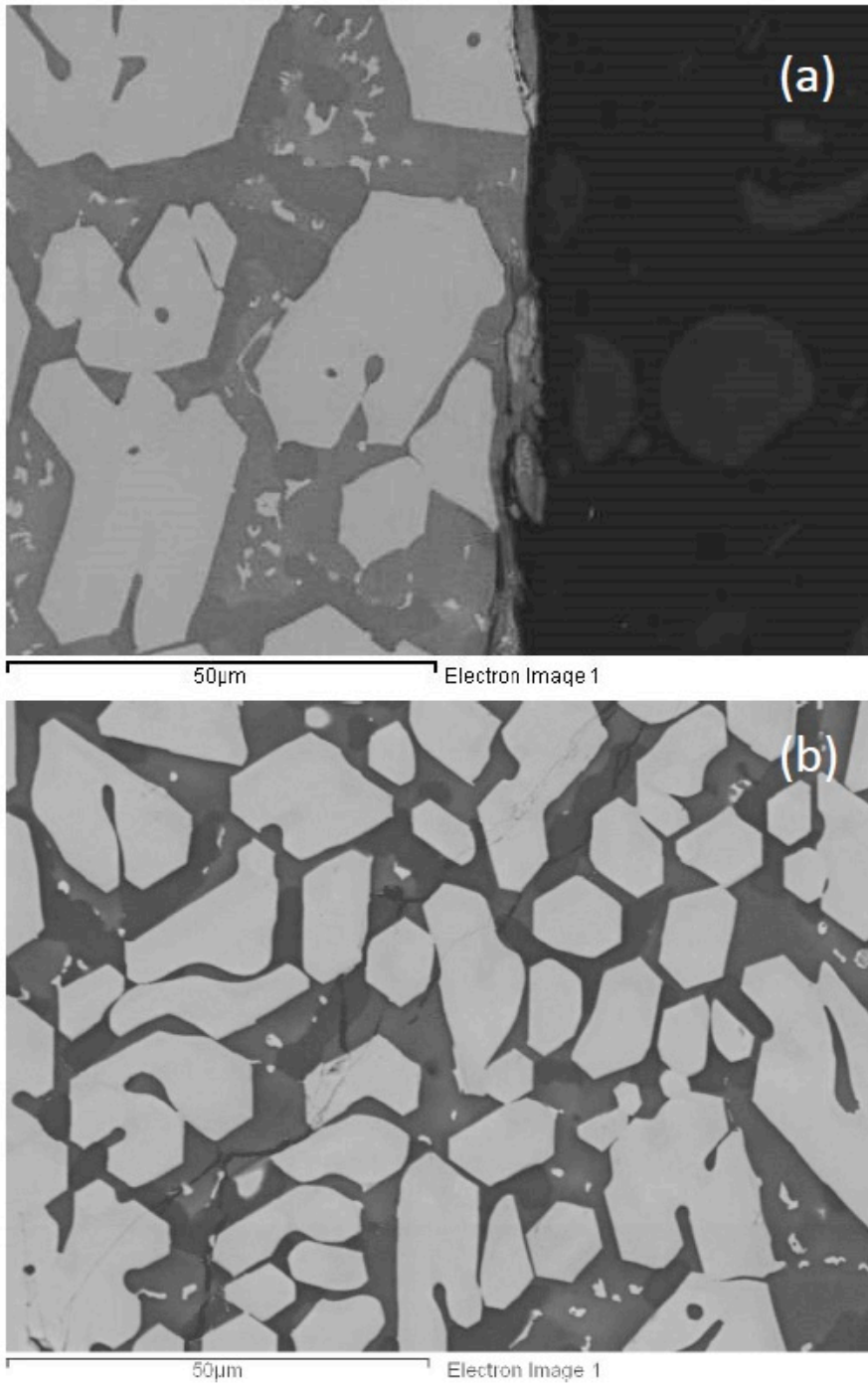


Figure 64: BSE images of oxidised MG2 at 800 °C (a) on the top and (b) in the bottom

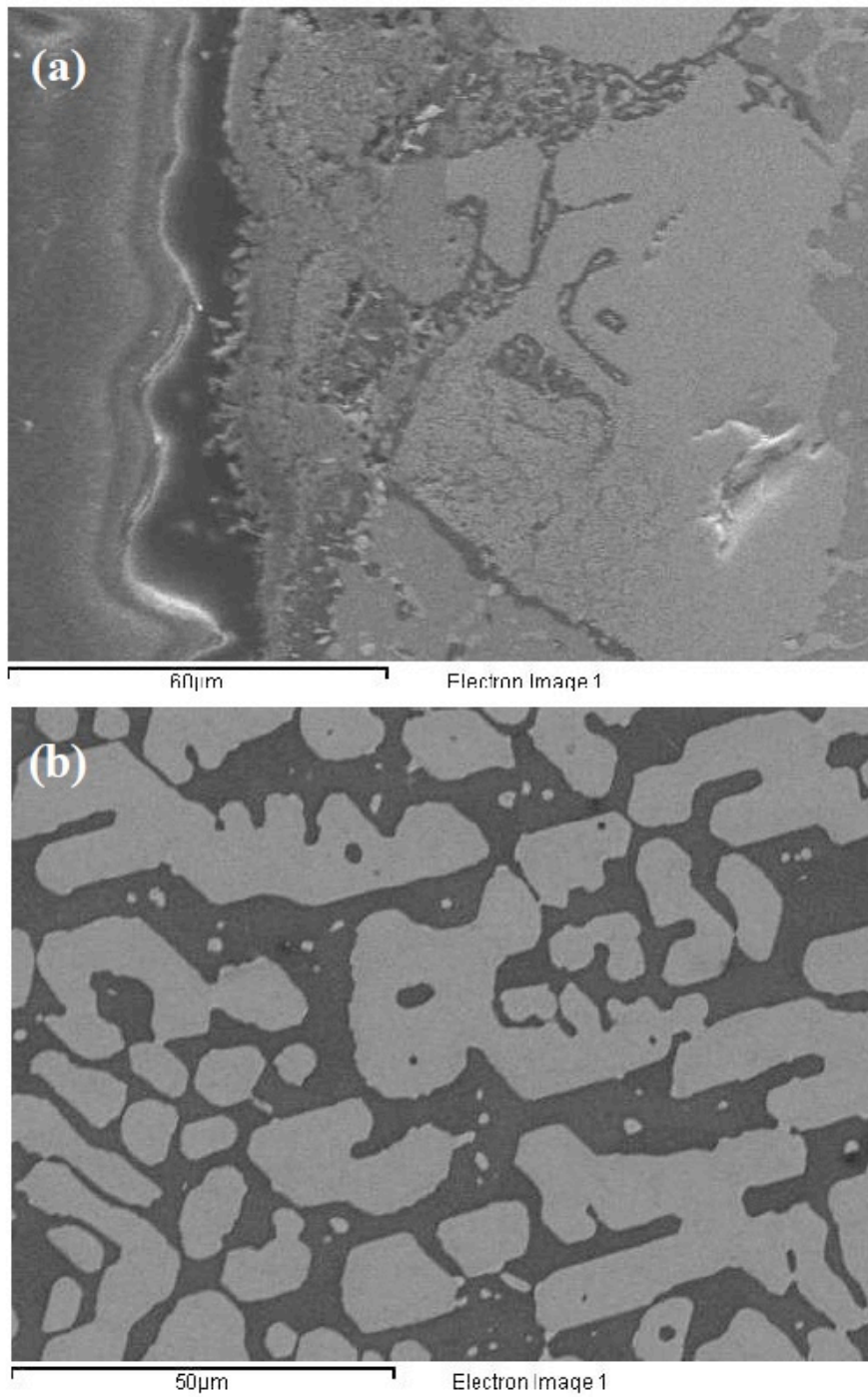


Figure 65: BSE images of oxidised MG2 at 1200 °C (a) below scale and (b) bulk

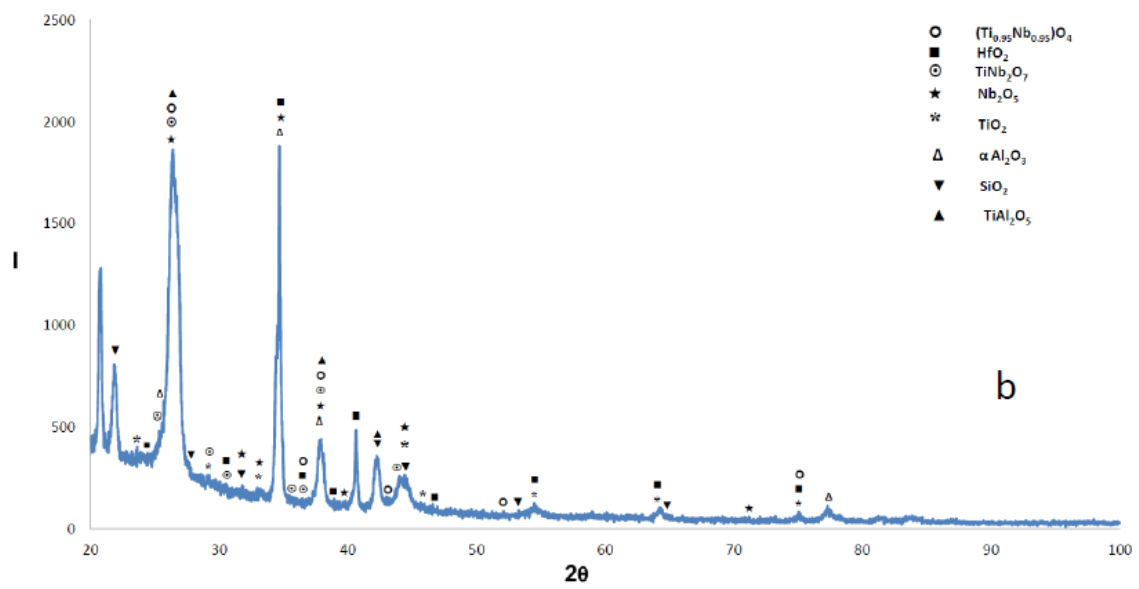
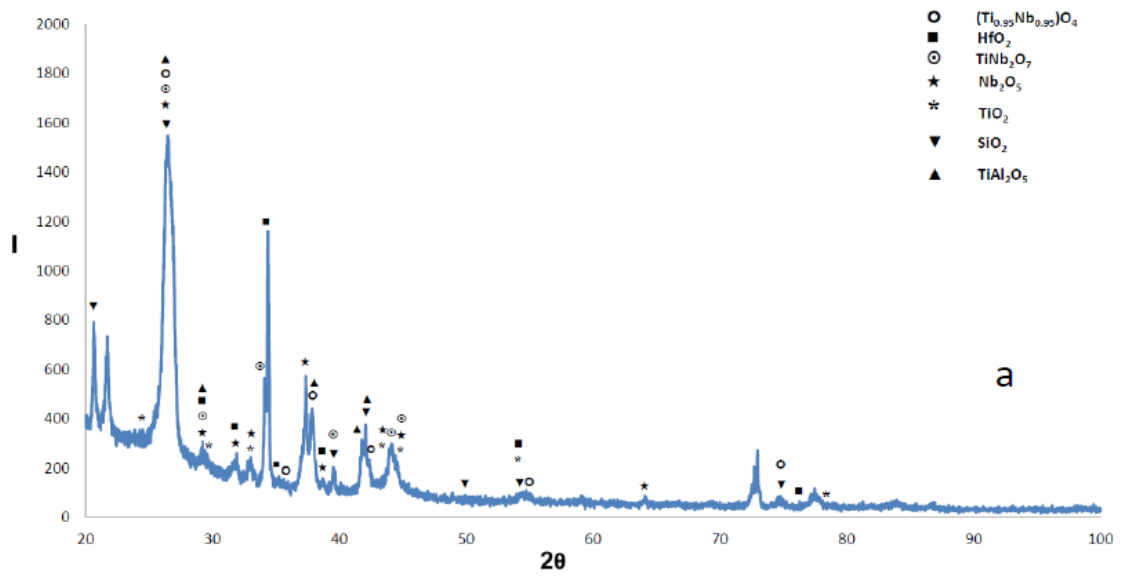


Figure 66: XRD data (glancing angle ($\theta=5^\circ$)) for the alloy MG2 (a) oxidized at 800 °C (b) oxidized at 1200 °C

4.1.4 Discussion

The alloy MG2-AC exhibited severe macrosegregation of Si, more severe than the alloy MG1-AC. The high macrosegregation of Si ($C_{\max}^{\text{Si}} - C_{\min}^{\text{Si}} = 12.8 \text{ at\% Si}$) was attributed to the synergy of Al and Hf, as was the case in the alloy MG1. However, since the Ti and Si concentrations in the alloy MG2 were not different than those in the alloy MG1, and (as discussed in section 3.1.4) individually Al and Hf increase the macrosegregation of Si, the data for the alloy MG2 would suggest that when Al and Hf are present simultaneously in the alloy, it is Al that plays the “key role” regarding the macrosegregation of Si.

The microstructure in the bottom of MG2-AC consisted of hexagonal Ti rich Nb_5Si_3 and tri-aluminide Al_3TM , see table 14. As the Ti rich 5-3 silicide formed the melt became lean in Si, Ti, Hf and Nb and rich in Al. As the solidification proceeded towards the bulk of MG2-AC, from the aforementioned melt formed the tri-aluminides shown in table 14, with different TM content depending on the local melt chemistry. As the tri-aluminides formed in the bottom, the melt became lean in Al and rich in Si and Nb while the concentration of Ti in the melt either increased or did not change depending on the chemistry of the tri-aluminide. In the melt formed Ti and/or Hf rich Nb_5Si_3 and the melt near the silicide became lean in Si, Hf and Nb, rich in Al and either lean or rich in Ti depending on the chemistry of Nb_5Si_3 , see table 14. In this melt formed TiAl and then the melt became lean in Al, rich in Si, Hf and Nb with no significant change in Ti concentration, see table 14. In this Si rich melt formed $\text{TM}_x\text{Al}_y\text{Si}_z$ aluminide and then Ti_2Al_5 and thus the melt became rich in Ti, Nb, Hf and Si and lean in Al. As the solidification proceeded towards the top of MG2-AC, from the latter melt formed Nb_5Si_3 and the surrounding melt became lean in Si, Hf and Nb and rich in Al and Ti,

then the TiAl formed and the the melt became lean in Al, rich in Si, Hf and Nb with no significant change in Ti concentration, see table 14 and in this Si rich melt formed $TM_xAl_ySi_z$ aluminide.

The solidification sequence discussed above indicates hexagonal 5-3 as the primary phase. If the alloy MG2 is considered as (Ti,Nb,Hf)-Al-Si, the above conclusion is in agreement with the liquidus projection of the Ti-Al-Si system, see figure 67(a), which shows that the overall average alloy composition as well as the average compositions in the bottom, bulk and top are in the Ti_5Si_3 primary phase area. The formation of the tri-aluminide from the melt surrounding the hexagonal 5-3 silicide is in agreement with the solidus projection in figure 67(b). Formation of the other aluminides shown in table 14 is in agreement with figure 67(b). The Ti_5Si_4 should be expected to form in the bottom, this however was not found in the microstructure of MG2-AC after careful study using EDS in the SEM. It is interesting to notice that the isothermal section at 1200 °C (figure 67(c)) would also suggest the Ti_5Si_4 in the bottom but not the section at 1250 °C (figure 67(d)). As discussed in the sections 4.1.1 and 4.1.2, it was concluded that the 5-4 silicide was not stable in the alloy MG2. The eutectic between TiAl and 5-3 silicide is in agreement with Perrot (2009).

Thus, based on the experimental results and the above discussion it is suggested that the solidification path in the bottom of MG2 was $L \rightarrow L + \gamma Nb_5Si_3 \rightarrow L + \gamma Nb_5Si_3 + Al_3TM$, in the bulk $L + \gamma Nb_5Si_3 + \beta Nb_5Si_3 \rightarrow L + \gamma Nb_5Si_3 + \beta Nb_5Si_3 + TiAl + TM_xAl_y + Ti_2Al_5$ and in the top $L + \beta Nb_5Si_3 \rightarrow L + \beta Nb_5Si_3 + TiAl + TM_xAl_y + (\beta Nb_5Si_3 + TiAl)_{eutectic}$.

The Pandat software was used to calculate the solidification path for the overall average composition of MG2-AC. The following path was calculated: Solidification starts at 2050 °C with $L \rightarrow L + \text{Ti}_5\text{Si}_3$, then $L \rightarrow \text{Ti}_5\text{Si}_3 + \text{Nb}_5\text{Si}_3$ at 1827 °C, then $L \rightarrow \text{Nb}_5\text{Si}_3$ at 1669 °C, then $L \rightarrow \text{Nb}_5\text{Si}_3 + \text{DO22-Al}_3\text{X}$ at 1513 °C, then $L + \text{Nb}_5\text{Si}_3 \rightarrow \text{DO22-Al}_3\text{X} + \text{Ti}_5\text{Si}_3$ at 1508 °C, then $L + \text{Ti}_5\text{Si}_3 \rightarrow \text{DO22-Al}_3\text{X} + \text{HfSi}$ at 1374 °C, then $L + \text{HfSi} \rightarrow \text{DO22-Al}_3\text{X}$ at 1200 °C, then $L \rightarrow \text{DO22-Al}_3\text{X} + \text{Ti}_3\text{Al}_2\text{Si}_5$ at 1104 °C, and $L \rightarrow \text{DO22-Al}_3\text{X} + \text{Ti}_3\text{Al}_2\text{Si}_5 + \text{fcc-Al}$ at 663 °C. The calculation gave hexagonal silicide as the primary phase, in agreement with the above discussion, did not specify the type of tetragonal Nb_5Si_3 (the inability of the Pandat software to distinguish between $\alpha\text{Nb}_5\text{Si}_3$ and $\beta\text{Nb}_5\text{Si}_3$ is well known) and correctly predicted the formation of tri-aluminide. The HfSi (isomorphous with TiSi), $\text{Ti}_3\text{Al}_2\text{Si}_5$ and fcc Al predicted by Pandat were not observed and formation of TiAl was not given in the calculated solidification path.

The alloy MG2 exhibited severe macrosegregation and the average compositions in the bottom, bulk and top were different, see table 14. Thus, it was decided to calculate the solidification path using the Pandat software for each part of the MG2-AC ingot, using the average compositions given in table 14.

The following path was calculated for the bottom of MG2. Solidification starts at 2050 °C with $L \rightarrow L + \text{Ti}_5\text{Si}_3$, then $L \rightarrow \text{Ti}_5\text{Si}_3 + \text{Nb}_5\text{Si}_3$ at 1716 °C, then $L \rightarrow \text{Nb}_5\text{Si}_3$ at 1552 °C, then $L \rightarrow \text{Nb}_5\text{Si}_3 + \text{DO22-Al}_3\text{X}$ at 1447 °C, then $L + \text{Nb}_5\text{Si}_3 \rightarrow \text{DO22-Al}_3\text{X} + \text{Ti}_5\text{Si}_3$ at 1441 °C, then $L + \text{Ti}_5\text{Si}_3 \rightarrow \text{DO22-Al}_3\text{X} + \text{HfSi}$ at 1334 °C, then $L \rightarrow \text{DO22-Al}_3\text{X}$ at 1156 °C, then $L \rightarrow \text{DO22-Al}_3\text{X} + \text{Ti}_3\text{Al}_2\text{Si}_5$ at 1118 °C, and $L \rightarrow \text{DO22-Al}_3\text{X} + \text{Ti}_3\text{Al}_2\text{Si}_5 + \text{fcc-Al}$ at 663 °C. The calculated solidification path for the bottom was

essentially the same as the path calculated using the overall actual alloy composition, with the exception that the HfSi did not form, which implies that formation of the latter silicide is very sensitive to the composition of the melt. The calculation gave hexagonal silicide as the primary phase, in agreement with the experimental observation for the bottom of MG2-AC and correctly predicted the formation of tri-aluminide in this area of the ingot. The $Ti_3Al_2Si_5$ and fcc Al predicted by Pandat were not observed. The calculation was also in agreement with the experimental observation regarding the absence of TiAl in the bottom of MG2-AC.

The calculated solidification path for the bulk of MG2-AC was as follows: Solidification starts at 2065 °C with $L \rightarrow L + Ti_5Si_3$ then $L \rightarrow Ti_5Si_3 + Nb_5Si_3$ at 1896 °C, then $L \rightarrow Nb_5Si_3$ at 1681 °C, then $L \rightarrow Nb_5Si_3 + DO22-Al_3X$ at 1517 °C, then $L + Nb_5Si_3 \rightarrow Ti_5Si_3 + DO22-Al_3X$ at 1512.69 °C, then $L \rightarrow DO22-Al_3X + Ti_5Si_3$ at 1512.68 °C, then $L \rightarrow DO22-Al_3X + Ti_5Si_3 + TiAl$ at 1447 °C, then $L + DO22-Al_3X \rightarrow Ti_2Al_5 + Ti_5Si_3 + TiAl$ at 1436 °C, then $L \rightarrow Ti_2Al_5 + Ti_5Si_3 + TiAl$ at 1406 °C. The calculated microstructure in the bulk of MG2-AC was in agreement with the experimental results regarding the Ti_2Al_5 and TiAl aluminides and the hexagonal 5-3 silicide.

The calculated solidification path for the top of MG2-AC was as follows: Solidification starts at 2041 °C with $L \rightarrow L + Ti_5Si_3$, then $L \rightarrow L + Ti_5Si_3 + Nb_5Si_3$ at 1780 °C, then $L + Nb_5Si_3 \rightarrow Ti_5Si_3 + DO22-Al_3X$ at 1484 °C, then $L \rightarrow Ti_5Si_3 + DO22-Al_3X$ at 1484 °C, then $L \rightarrow Ti_5Si_3 + DO22-Al_3X + TiAl$ at 1459 °C, then $L + Ti_5Si_3 \rightarrow DO22-Al_3X + Hf_2Si + TiAl$ at 1410 °C, then $L \rightarrow DO22-Al_3X + Hf_2Si + TiAl + bcc-A2$ at 1385 °C, then $L \rightarrow DO22-Al_3X + Hf_2Si + bcc-A2$ at 1371 °C, then $L + bcc-A2 \rightarrow DO22-Al_3X$

+ Hf₂Si + hcp-A3 at 1323 °C, then L → DO22-Al₃X + Hf₂Si + hcp-A3 at 903 °C. The calculation showed formation of both TiAl and tri-aluminide, the latter was not observed in the top of MG2, and a final microstructure that did not agree with the experimental observations. Furthermore, the calculated path gave formation of Hf₂Si and Ti_{ss}, both of which were not observed experimentally.

The “best” agreement between calculation and experiment was only for the bulk of MG2-AC, which had solidified under lower cooling rates compared with the bottom and top of the ingot. The calculations also highlighted the sensitivity of phase selection/solidification path on melt chemistry, as discussed above. The phases present in the microstructure of MG2-HT that were confirmed by both the XRD and EDS data were tetragonal (β) Nb₅Si₃, hexagonal (γ) Nb₅Si₃, Al₃TM, TiAl and Ti₂Al₅. This is in agreement with the 1250 °C isothermal section of Ti-Al-Si, see figure 67(d). The TM_xAl_ySi_z intermetallics were not stable at 1300 °C, which confirmed that they were metastable phases formed during solidification owing to the partitioning of solutes and the prevailing solidification conditions. The composition of the 5-3 silicide had changed towards lower Nb/(Ti+Hf) ratios (≤ 1 compared with ≤ 2.3 for MG2-AC) which would suggest that the hexagonal 5-3 silicide is likely the stable 5-3 silicide in this alloy. In the aluminides the Si concentration was reduced to very low levels, which is in agreement with the literature.

The oxidation behaviour of MG2 specimens at 800 and 1200 °C was significantly better than that of Nb silicide based alloys studied to date. The microstructure of the alloy MG2 of course was different compared with that of Nb silicide based alloys as it consisted of tetragonal and hexagonal 5-3 silicides and aluminides, i.e., Si and Al rich

phases that could act as reservoirs for Al and Si for oxidation purposes, and no bcc Nb solid solution, while the latter alloys usually have bcc Nb solid solution, 5-3 silicide(s) and other intermetallics such as Nb₃Si, A15 phases and C14 Laves phases. High Al concentrations in Nb silicide based alloys are known to have a strong adverse effect on toughness, thus the alloy MG2 is of interest as a candidate material for a coating system for Nb silicide based alloys, particularly as it forms alumina scales.

In the case of Nb silicide based alloys, at 800 °C very thin scale formation and no pest oxidation is achieved when Al, Cr, Hf and Ti are present simultaneously in the alloy with addition(s) of B, Ge or Sn individually or simultaneously. However, at 1200 °C thicker scales are formed compared with those at 800 °C and their adherence (if any) to the substrate is very poor, with scale spallation being the rule rather than the exception.

The oxidation of the alloy MG2 presented a very significant improvement when compared with Nb silicide based alloys. No pest oxidation at 800 °C, no scale spallation at 1200 °C and very thin oxides were formed at both temperatures. Indeed, compared with the “best” Nb silicide based alloys the oxidation of which was tested at the same temperatures using specimens from the cast ingot (i.e., not heat treated specimens) the ratios of parabolic rate constants given below confirm the exceptional oxidation of MG2 at both temperatures.

$$k_p^{MG2-800}/k_p^{JG6-800} = 0.2, k_p^{MG2-800}/k_p^{OHS1-800} = 0.1,$$

$$k_p^{MG2-800}/k_p^{ZF9-800} = 2.5, k_p^{MG2-800}/k_p^{CMSX4-800} = 50$$

and

$$k_p^{MG2-1200}/k_p^{JG6-1200} = 0.06^*, k_p^{MG2-1200}/k_p^{OHS1-1200} = 0.12^*,$$

$$k_p^{MG2-1200}/k_p^{ZF9-1200} = 0.03^*, k_p^{MG2-1200}/k_p^{TT7-1200} = 0.3, k_p^{MG2-1200}/k_p^{CMSX4-1200} = 20.$$

In the above ratios the asterisk (*) indicates parabolic rates for early stages of oxidation. The nominal compositions (at%) of the polycrystalline Nb silicide based alloys were JG6 = Nb-24Ti-18Si-5Al-5Cr-5Hf-5Sn-2Mo (Geng et al, 2007), OHS1 = Nb-24Ti-18Si-5Al-5Cr-5Sn-5Ge (Hernandez, 2017), ZF9 = Nb-24Ti-18Si-5Al-5Cr-5Hf-5Ge (Li, 2012), TT7 = Nb-24Ti-18Si-5Al-5Cr-5Hf-6B (Thandorn, 2009) and CMSX-4 is single crystal Ni based superalloy that is used as reference for comparison purposes with developmental ultra-high temperature alloys.

The improved oxidation behaviour of MG2 compared with MG1 ($k_p^{MG2-800}/k_p^{MG1-800} = 0.005$, and $k_p^{MG2-1200}/k_p^{MG1-1200} = 0.001^*$) is attributed to the absence of bcc Nb solid solution and the presence of aluminides in the former. In both alloys the Nb₅Si₃ was contaminated by oxygen at both temperatures and more severely at 800 °C. Comparison with the data for Nb₅Si₃ for 1200 °C is not easy because in the alloy MG1 that was oxidised at 1200 °C the spalled scale consisted of 12 pieces, meaning that it is likely that some of the substrate below the scale also spalled off (see section 3.1.4). In the alloy MG2, at both temperatures the aluminides were also contaminated by oxygen, with less severe contamination of the Al rich tri-aluminide. Thus, if one were to compare the microstructures of the two alloys regarding the phases surrounding the 5-3 silicide, i.e., the Nb_{ss} (MG1) and aluminides (MG2), the better oxidation of the alloy MG2 could be attributed to the less severe contamination of (mainly the) aluminides and 5-3 silicides compared with the severe contamination of the solid solution.

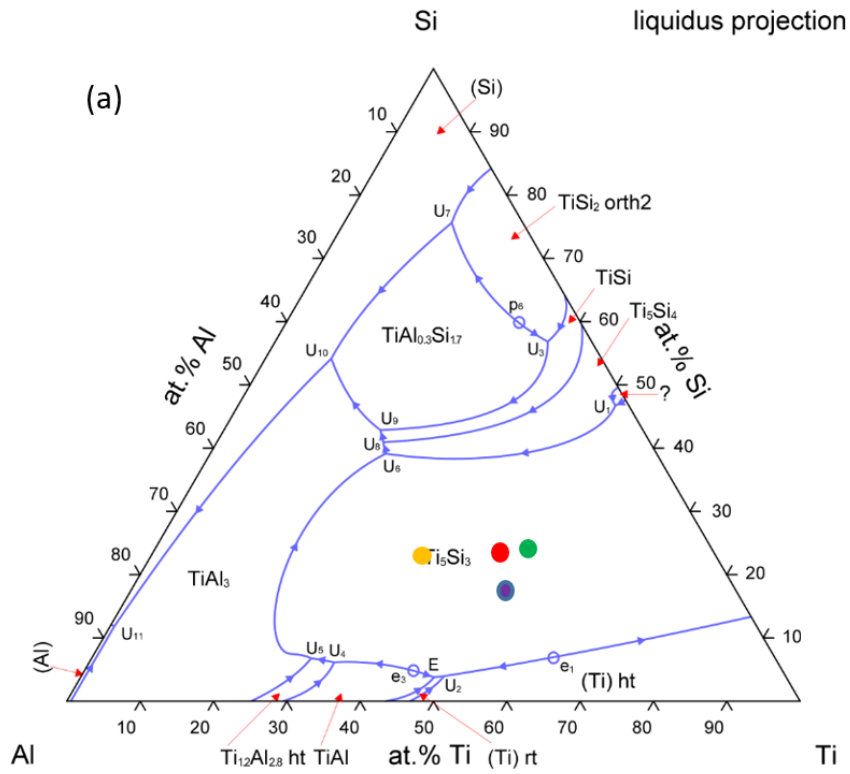
The oxides forming the scale on the alloy MG2 at 800 °C and 1200 °C can be compared with the literature about other oxidised Nb silicide based alloys. Compared with the literature on Nb silicide based alloys oxidised at 800 °C, where in almost all cases

Bragg-Brentano XRD (i.e., no GXRD) was used, the same oxides formed on MG2 plus TiAl_2O_5 , e.g., see Geng et al (2006). Compared with the literature on Nb silicide based alloys oxidised at 1200 °C, the same oxides formed, e.g., see Geng et al (2006), plus TiAl_2O_5 and $\alpha\text{Al}_2\text{O}_3$. The exciting discovery from the oxidation of the alloy MG2 was that the increased Al concentration (activity) in the alloy contributed to the formation of TiAl_2O_5 at 800 °C and TiAl_2O_5 plus $\alpha\text{Al}_2\text{O}_3$ in the scale formed at 1200 °C. The $\alpha\text{Al}_2\text{O}_3$ was confirmed by GXRD.

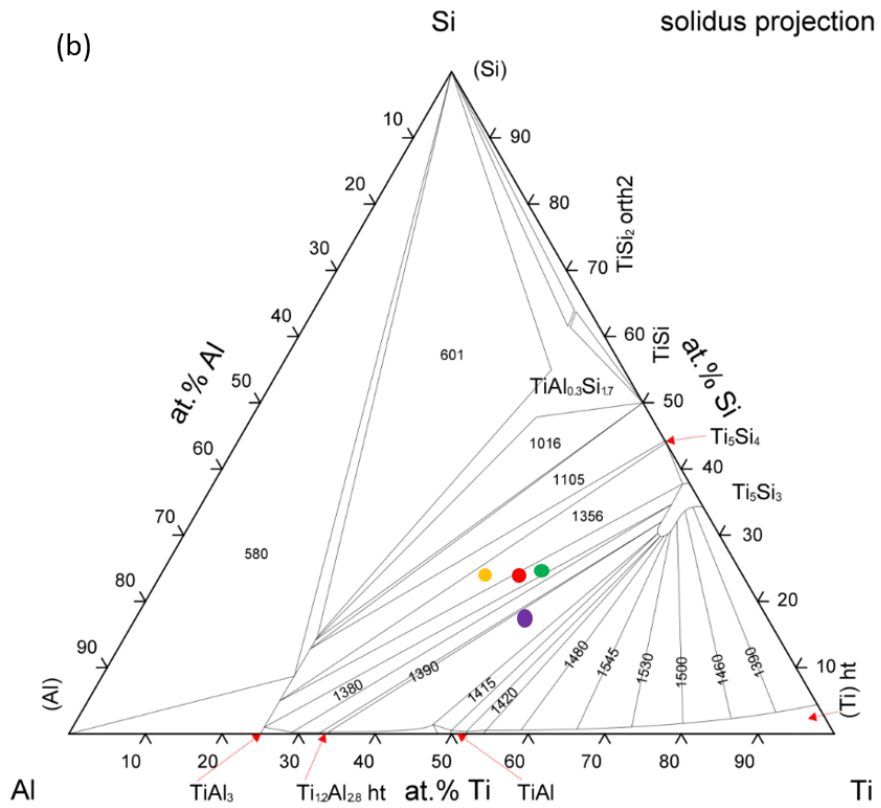
The aluminides that were present in MG2-AC (table 14) can be in equilibrium with alumina (see also section 5.1.4 in the next chapter). Furthermore, in the Ti-Al-O system at 700 and 900 °C the stable oxide changes from TiO_2 to Al_2O_3 for Al rich aluminides such as TiAl and Al_3Ti (Rahmel and Spencer, 1991) and according to the same authors the ternary oxide TiAl_2O_5 becomes stable around 1010 °C. The GXRD suggested only the presence of TiO_2 but not of Al_2O_3 , which would suggest that the activity of Al in the alloy was not enough to ensure the formation of Al_2O_3 .

The GXRD also suggested SiO_2 and TiO_2 in the scale formed at 800 °C (figure 66a). Rahmel and Spencer (1991) reported that in the Ti-Si-O system a change from Ti-oxide to SiO_2 occurs at 800 °C for Si rich silicides with Si > 39.5 at%, i.e., for silicides to the right of Ti_5Si_3 in the Ti-Si binary, while for Si < 39.5 at% (i.e., between Ti and Ti_5Si_3 in the Ti-Si binary) the TiO is the stable oxide. It is also known that the TiO oxidises rapidly to form TiO_2 . The presence (according to GXRD) of SiO_2 in the scale of MG2 at 800 °C was attributed to the fact that only 5-3 silicides were present in the microstructure MG2-AC and these silicides had Si+Al < 41.6 at%.

In the Ti-Al-O system at 1100 °C the stable oxide changes from TiO₂ to Al₂O₃ for Al rich aluminides such as TiAl, Ti₂Al₅ and TiAl₃. The GXRD suggested the presence of αAl₂O₃, which would suggest that the activity of Al in the alloy was enough to stabilise alumina in the scale. Rahmel and Spencer (1991) reported that in the Ti-Si-O system at 1300 °C a change from Ti-oxide to SiO₂ occurs for Si rich silicides to the right of Ti₅Si₃ (see above). The presence (according to GXRD) of SiO₂ and TiO₂ in the scale of MG2 at 1200 °C would suggest that the activity of Si in the alloy MG2 was not high enough to stabilise the SiO₂. As discussed above, this can be attributed to the presence of only 5-3 silicides in the microstructure.



© ASM International 2007. Diagram No. 200367



© ASM International 2007. Diagram No. 200368

Continued

Continued

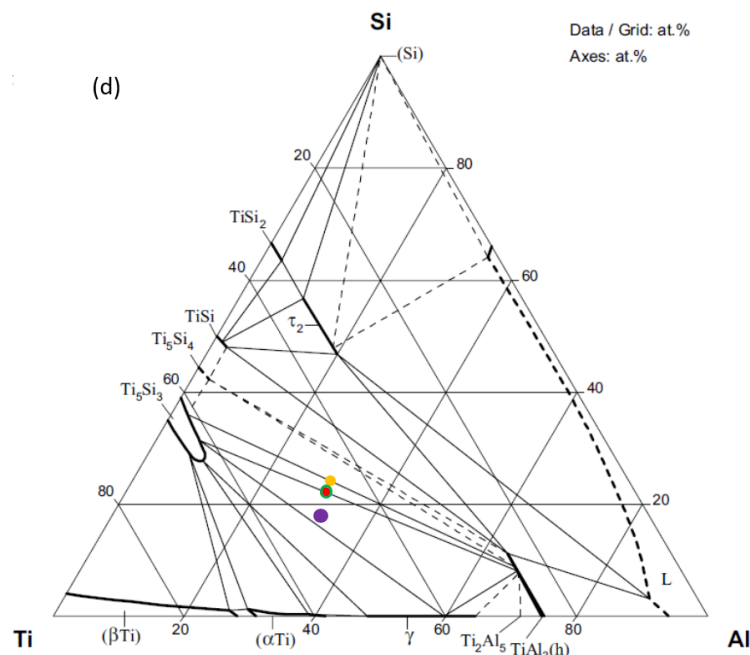
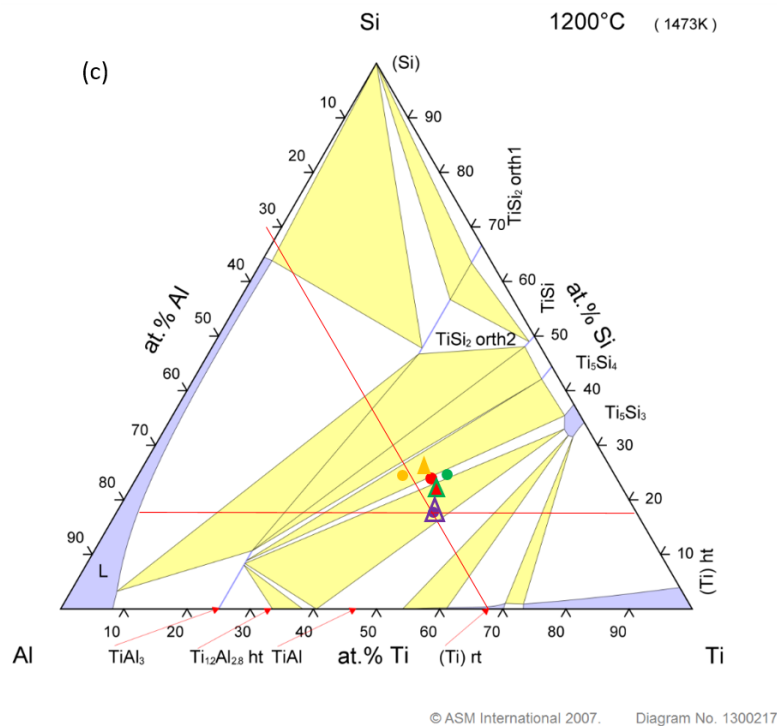


Figure 67: (a) Liquidus and (b) solidus projection and isothermal sections (c) for 1200 °C and (d) 1250 °C of Ti-Al-Si. (a) and (b) from Bulanova (2004) and (c) from Perrot [ASM alloy phase diagram database] and (d) from Perrot (2009). Colours correspond to average MG2-AC or MG2-HT compositions as follows: red-overall average, **orange - bottom**, green - bulk, purple - top. (a) and (b) for MG2-AC, (d) for MG2-HT. In (c) circles are for MG2-AC and triangles for MG2-HT.

4.1.5 Summary

The Al rich alloy MG2 was selected to study phase stability, oxidation behaviour and in particular whether alumina scale could form at 800 °C and/or 1200 °C, owing to the higher Al activity in the alloy. There was macrosegregation of Al, Hf, Si and Ti in the alloy MG2. The higher Al concentration in this alloy was responsible for the more severe macrosegregation of Si compared with the alloy MG1. Owing to the strong macrosegregation the solidification paths in different parts of the ingot were very sensitive to melt composition. The ingot was severely cracked owing to the absence of Nb_{ss} and large volume fractions of silicides and aluminides in the cast microstructure.

The cast microstructure consisted of the $\beta\text{Nb}_5\text{Si}_3$ and $\gamma\text{Nb}_5\text{Si}_3$ (primary phase), Al_3TM , TiAl , Ti_2Al_5 intermetallics and metastable $\text{TM}_{3.7}\text{Al}_3\text{Si}$ and $\text{TM}_{2.35}\text{Al}_{1.65}\text{Si}$ intermetallics. There was strong partitioning of Hf and Ti in the 5-3 silicide, particularly in the bulk of the ingot. There were differences in the microstructure in different parts of the ingot, in particular no tetragonal Nb_5Si_3 , metastable intermetallics, Ti_2Al_5 and TiAl were observed in the bottom and no eutectic in the bottom and bulk.

Chemical inhomogeneity of Al, Si and Ti persisted after the heat treatment at 1300 °C for 100 h. The microstructure consisted of $\beta\text{Nb}_5\text{Si}_3$ and $\gamma\text{Nb}_5\text{Si}_3$, Al_3TM , TiAl , and Ti_2Al_5 . The Ti_5Si_4 and TiSi silicides and the Nb_{ss} were not stable in the alloy MG2. The evidence would suggest that the $\gamma\text{Nb}_5\text{Si}_3$ is the stable 5-3 silicide, as was the case in the alloy MG1.

The alloy MG2 did not pest at 800 °C and at 1200 °C formed a thin $\alpha\text{Al}_2\text{O}_3$ containing scale that did not spall off and at both temperatures followed parabolic oxidation kinetics. All phases were contaminated by oxygen, the contamination of 5-3 silicide

grains was more severe than TiAl and Al₃TM, with the latter exhibiting less contamination. At both temperatures Nb₂O₅, TiO₂, SiO₂, HfO₂, TiAl₂O₅ and Ti niobates were detected by GXRD in the scale plus α Al₂O₃ at 1200 °C.

Chapter 5: The alloy Nb-23Ti-25Si-30Al-4Hf

5.1 Alloy Nb-23Ti-25Si-30Al-4Hf (MG5)

5.1.1 As cast

The nominal composition of the alloy MG5 is shown in table 19. The actual composition was determined using EDS. The average composition of the alloy MG5 was Nb-24.2Ti-26.7Si-30.6Al-3.4Hf. This was the average of all the analyses taken from the top, bulk and bottom of the ingot of MG5-AC. Even though the average concentration of the solutes were close to the nominal ones, the standard deviations for Al, Si and Ti were large, owing to the macrosegregation of these elements.

Table 19: Nominal composition (at%) of the alloy MG5

Alloy	Nb	Si	Ti	Al	Hf
MG5	18	25	23	30	4

Indeed, there was very strong macrosegregation of Al the concentration of which varied from 18.5 at% in the bottom to 40.4 at% in the top giving $C_{\max}^{\text{Al}} - C_{\min}^{\text{Al}} = 21.9$ at% with the strongest chemical inhomogeneity in the bulk. The Si concentration varied from 22.2 at% in the top to 32.1 at% in the bottom giving $C_{\max}^{\text{Si}} - C_{\min}^{\text{Si}} = 9.9$ at% with the strongest inhomogeneity in the bulk. The concentration of Ti varied between 21.2 at% in the bottom to 28.2 at% in the top of the ingot giving $C_{\max}^{\text{Ti}} - C_{\min}^{\text{Ti}} = 7$ at% with the strongest inhomogeneity in the bottom. The macrosegregation of Al and Si resulted in different Al+Si concentration in the top, bulk and bottom of MG5-AC, see Table 20. The above macrosegregation of Al, Si and Ti resulted in inhomogeneity in the concentration of Nb, which varied between 12.9 at% and 17.3 at% in the centre of the ingot.

The microstructures in the top, bulk and bottom of the ingot are shown in Figure 68, and the XRD data is shown in Figure 69. According to the latter, four phases were present in the microstructure, namely the TMAI_3 , Nb_5Si_3 , TiSi and Ti_5Si_4 intermetallics. These phases were confirmed by the EDS analyses, see Table 20. The identification of Al_3TM in Table 20 was done as discussed in the previous chapter. The identification of TiSi and Ti_5Si_4 in the same table was done with the help of the Ti-Si binary phase diagram and the data in Perrot (2009). The latter shows very small solubility of Al in Ti_5Si_4 and higher solubility of Al in TiSi . It is noted that the Si+Al content of the 5-4 silicide is slightly higher than the stoichiometric composition. This is attributed (i) to difficulties in EDS analyses because this phase was formed as thin layers around the 5-3 silicide and (ii) to the high Hf concentration of this phase, which might introduce error in the Si measurement by EDS. It is of course also possible that in the presence of Nb and Hf this 5-4 silicide exhibited a solubility range (homogeneity range), i.e., it is no more a line compound. The Si+Al concentration of the 5-3 silicide was within the ranges of values expected from the Nb-Si binary. However, the 5-3 silicide was Ti and Hf rich with $\text{Nb}/(\text{Ti}+\text{Hf}) = 0.67$, which should indicate $\gamma\text{Nb}_5\text{Si}_3$ according to the empirical Bewlay rule (Bewlay and Jackson, 2003). It should be noted that the XRD also indicated $\gamma\text{Nb}_5\text{Si}_3$ (Figure 69). The 5-3 and 5-4 silicides exhibited cracks in both the bottom and top of the ingot.

Figure 68c shows that the scale of the microstructure in the bottom of the as cast ingot was different from that in the top and bulk of the ingot. The same phases were observed in all three parts of the ingot. The 5-3 and 5-4 silicides exhibited almost the same contrast. Their contrasts were grey and brighter grey, respectively. The similar contrast made their visual identification using SEM with BSE impossible in some parts of the

alloy. Thus, their identification was based on spot analyses that allowed the 5-3 and 5-4 silicides to be identified from their Al+Si concentration and the higher Si and lower Al contents of the latter.

The 5-3 and 5-4 silicides were surrounded by a darker contrast microstructure where the two intermetallics, namely TiSi and TMAI₃ were observed. The latter exhibited very dark contrast and the former a light dark one, see Figure 68a and b. In order to show all four phases, the contrast in Figure 68 was slightly changed. As can be seen, the dark and very dark contrasts correspond to the TiSi and TMAI₃ intermetallics, respectively. The difference in contrast between these two phases arises from their different Si and Al concentration: an increase in Si makes the contrast brighter and an increase in Al makes the contrast darker.

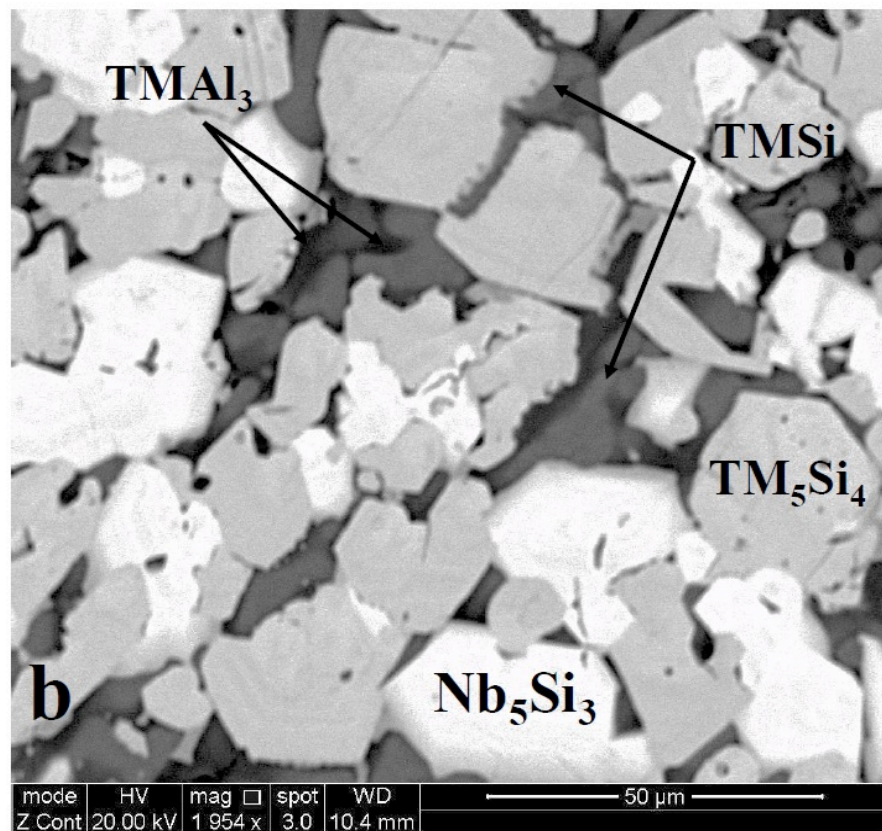
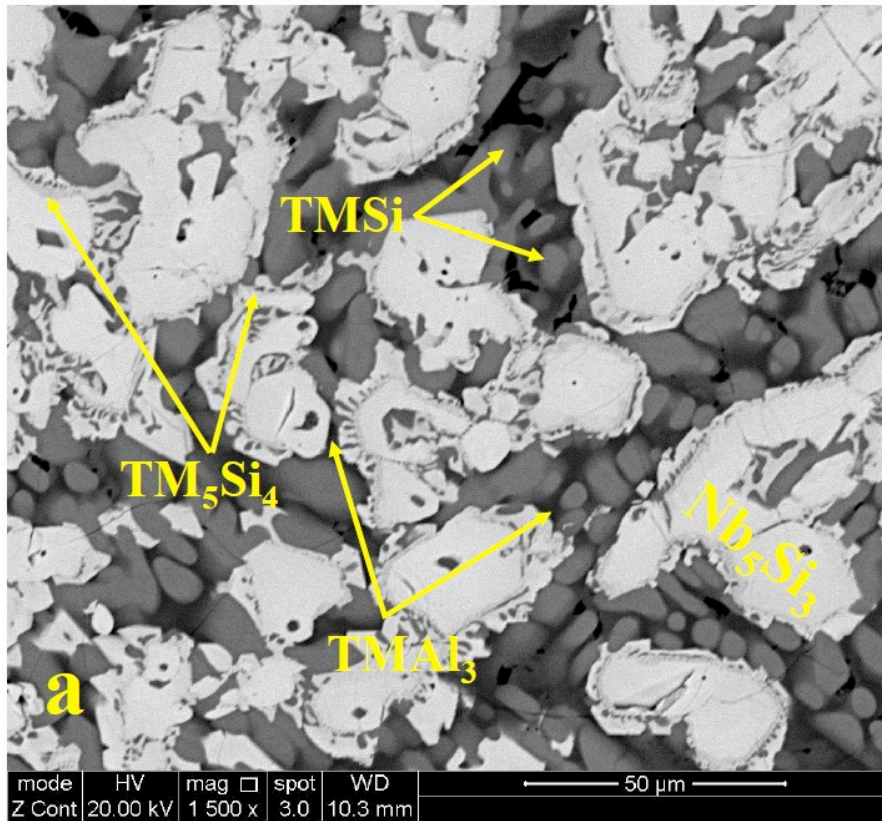
Compared with the top and bulk of the ingot the microstructure in the bottom of MG5-AC was fine. In the microstructure the visual identification of the 5-3 and 5-4 silicides was not possible and was done using EDS spot analyses, as discussed earlier. The coarse microstructure in the bulk of MG5-AC is shown in Figure 68b. The bright contrast grains of Nb₅Si₃ are seen to exhibit darker contrast near their surfaces. This contrast is similar to that of the 5-4 silicide, but could also be attributed to the partitioning of Ti, i.e., to Ti-rich grains. This will be re-visited in the discussion.

Figure 68a shows the microstructure in the top of the ingot of MG5-AC. The volume fraction of TMAI₃ was higher in the top compared with the bottom and bulk of the ingot. The volume fractions of the 5-3 and 5-4 silicides were higher in the bulk of MG5-AC. In the top, the 5-3 silicide grains exhibited darker contrasts, similar to that of the

5-4 silicide, at their surfaces where also two phases, one forming bright contrast “lamellae”, were observed. EDS spot analyses on “large” enough lamellae indicated that they were 5-4 silicide. This microstructure will be re-visited in the discussion.

Table 20: EDS analysis data (at%) of the cast alloy MG5

Area and phase analysis		Elements					Al+Si
		Nb	Si	Ti	Al	Hf	
Large area	Top	14.3±1.17 13.4-16.7	24.5±2.3 22.2-30.9	22.8±1.7 21.2-26.4	35.2±6.1 22-40.4	3.2±0.4 2.8-4	59.7
	Bulk	15.7±1.6 12.9-17.3	28.9±3.4 22.4-31.7	25.4±1.8 21.8-26.8	26.3±7 20.9-39.9	3.6±0.3 2.9-3.9	55.2
	Bottom	15.3±1.1 14.1-17.1	27.2±3.2 24-32.1	24.7±2.3 22.3-28.2	29.2±7 18.5-36.3	3.6±0.3 3.2-4.1	56.4
	Average	15.1±1.5 12.9-17.3	26.7±3.7 22.2-32.1	24.2±2.2 21.2-28.2	30.6±7.7 18.5-40.4	3.4±0.4 2.8-4.1	57.3
Phase (spot) analysis		Aluminide and silicides					
	Al ₃ TM	10.6±3.5 9.7-12.9	3.2±0.7 2.6-4.4	14.4±3.4 11.9-15.4	70.7±1.3 67.5-71.8	1.1±0.2 0.9-1.3	73.9
	Ti ₅ Si ₄	17.4±0.3 17.1-17.7	46±0.4 45.3-46.3	29.3±1.2 24.3-26.8	2±0.3 1.8-2.5	9.3±0.8 8.2-9.9	48
	TiSi	15.5±1.8 13.7-17.3	39.6±3.4 36-42.8	28.1±1.6 26.8-30	10.7±4.4 6.6-15.4	6±1.3 4.5-6.9	50.3
		5-3 silicide					
	γNb ₅ Si ₃	23.5±1 21.2-24.8	38.6±0.7 37.2-39.4	29.6±1.1 28.3-32.1	3±0.8 2.4-5	5.3±0.2 5.1-5.6	41.5



Continued

Continued

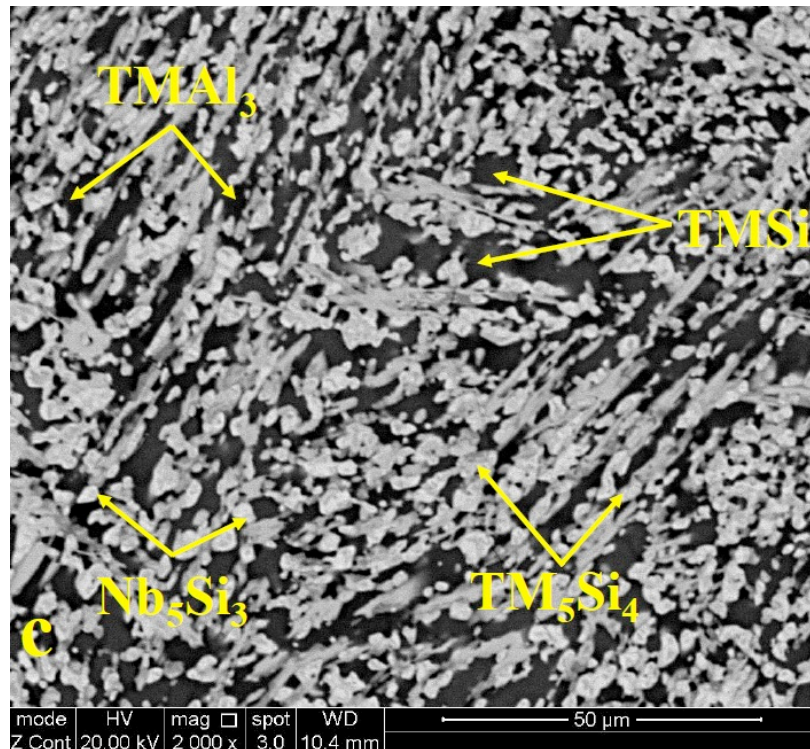


Figure 68: SEM backscatter electron image of the microstructure of the alloy MG5-AC taken from (a) the top, (b) bulk and (c) bottom of the ingot

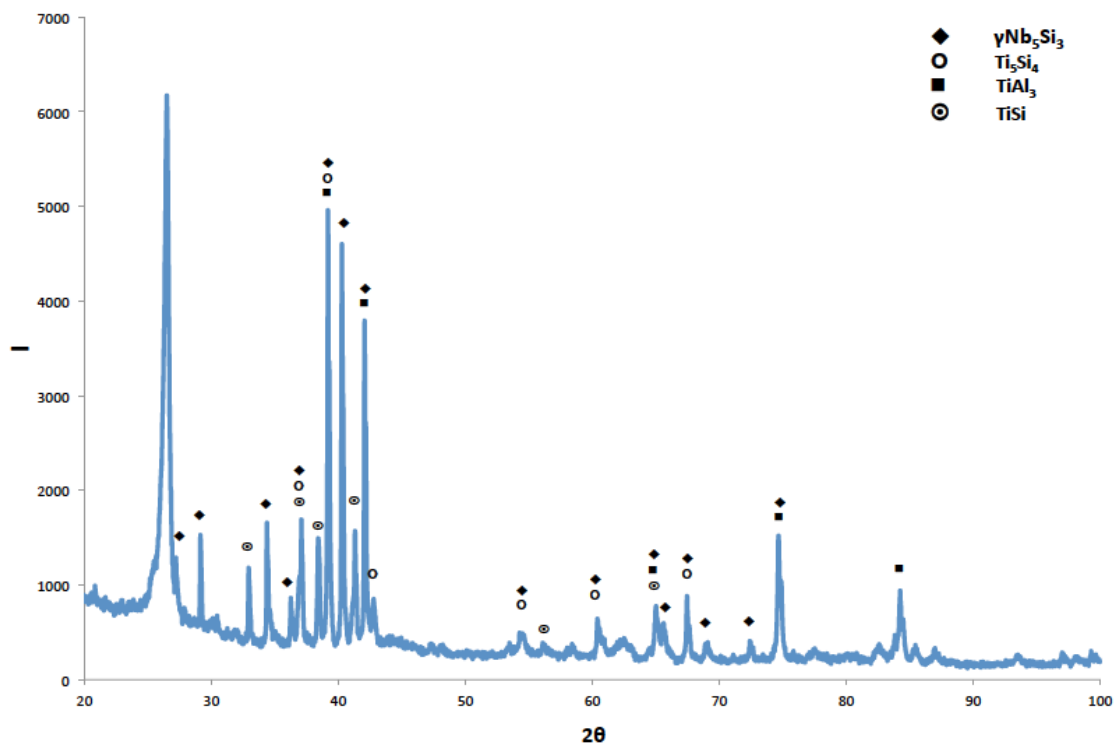


Figure 69: X-ray diffractogram of the alloy MG5-AC

5.1.2 Heat treated

5.1.2.1 Heat treatment at 800 °C

The alloy MG5 was heat treated following the procedure discussed in chapter 2. Two heat treatment temperatures were chosen, namely 800 °C and 1200 °C, the same as the temperatures where the oxidation behaviour of this alloy was studied (see chapter 5.1.3). The DSC trace of this alloy did not show any endothermic reactions.

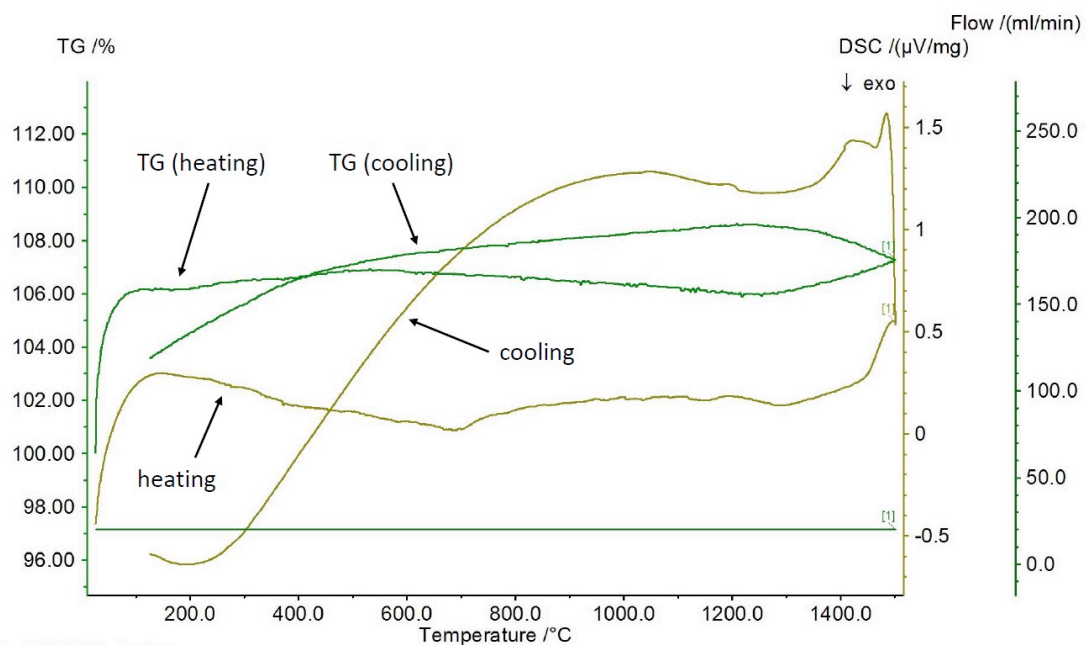


Figure 70: DSC trace of the alloy MG5

The average composition of the heat treated specimen (MG5-HT800) was Nb-22.6 Ti-24.7Si-26.8Al-3.3Hf (see Table 21). Compared with the cast alloy, the MG5-HT800 was poorer in Al, Si and Ti. However, the average composition of MG5-HT800 was very close to the nominal one (Table 19) for Si and Ti but lower for Al.

Table 21: EDS analysis data (at%) of the alloy MG5 heat treated at 800 °C for 100 h

Area and phase analysis		Element					Al+Si
		Nb	Si	Ti	Al	Hf	
Large area	Top	16.6±1.3 14.5-18.7	30.2±2.1 26.8-32.8	26.4±1.1 24.6-28.3	22.7±4.6 17.6-30.2	4±0.2 3.8-4.5	52.9
	Bulk	12.5±1.1 11.4-14.1	25.8±2.8 22.2-30.2	24.8±1.1 23.7-26.2	33.6±5.4 25.3-40.1	3.4±0.5 2.7-4.2	59.4
	Bottom	13.7±0.9 12.5-14.9	25±3.5 21.5-30.8	23.4±2 21.8-26.9	34.4±6.8 23.1-41.2	3.4±0.5 3-4.3	59.4
	Average	13.1±4.5 11.4-18.7	24.7±8.3 21.5-32.8	22.6±7.6 21.8-28.3	26.8±10.3 17.6-41.2	3.3±1.1 2.7-4.5	51.5
Phase (spot) analysis		Aluminides and silicides					
	TiAl	4±1.8 0.4-5.4	5.2±0.4 6.1-7.2	18.7±0.8 21-23.5	61.5±1.7 64.4-69	0.9±0.1 0.8-1.2	66.7
	Al ₃ TM	11.9±1.2 8.6-13	3.1±0.7 2.4-5	12.6±1.4 11.5-15.6	71.2±0.8 69-71.8	1.2±0.1 1-1.4	74.3
	Ti ₅ Si ₄	14±2.8 11.1-18.4	45.9±0.7 44.5-46.6	32.1±3.2 27.2-36.1	1.8±0.2 1.4-2	6.1±0.6 5.2-6.8	47.7
	TiSi	8.2±2.4 6.5-9.9	34.2±3 32.1-36.4	38.5±4.1 35.6-41.4	16.7±1.5 15-17.1	2.9±0.1 2.9-3	50.9
		5-3 silicide					
	γNb ₅ Si ₃	23.9±2 20.2-26.2	38.8±0.3 38.5-39.1	29.4±1.9 27.3-32.9	2.4±0.3 2.1-3.1	5.4±0.4 4.7-6	41.2

The standard deviations of these elements were higher than the MG5-AC, confirming the very strong macrosegregation of these elements in the cast alloy. The strongest chemical inhomogeneity for Al, Si and Ti was observed in the bottom of MG5-HT 800 where the Al content was high. Furthermore, the average Al+Si concentration in the MG5-HT800 was lower than that in the MG5-AC.

The microstructure of MG5-HT+800 and the XRD data are shown in Figure 71 and Figure 72, respectively. In the X-ray diffractogram two peaks correspond only to TiAl_{2.92}Si_{0.08}. This phase has the same stoichiometry as TiAl₃. Compared with the microstructure of MG5-AC (Figure 68) very subtle changes had occurred after 100 h at 800 °C. The brighter white contrast phase is representative of the Nb₅Si₃ silicide and

according to EDS spot analysis the darker white contrast represents the 5-4 silicide. Two other contrasts, namely grey and black are representative of the TiSi and TiAl₃ intermetallics, respectively. There was no change in the composition of γ Nb₅Si₃. However, the 5-4 silicide became richer in Ti. More significantly were the changes in the TiSi, which became richer in Al and Ti and poorer in Si and Hf. The composition of the tri-aluminide Al₃TM was essentially unchanged with a very slight decrease in the Ti concentration compared with MG5-AC. In the dark contrast (Al-rich) areas surrounding the 5-3 and 5-4 silicides i.e, the areas where the Al₃TM was observed, some analyses corresponded to TiAl, see Table 21. There was weak evidence for this aluminide in the XRD data, Figure 72, where two weak peaks correspond only to this aluminide. Thus, the main difference in the microstructure of MG5-HT800 compared with the cast alloy was the formation of TiAl, which would suggest that this intermetallic might be stable in the alloy MG5. This hypothesis was tested in the higher temperature heat treatment, which is considered in the next section.

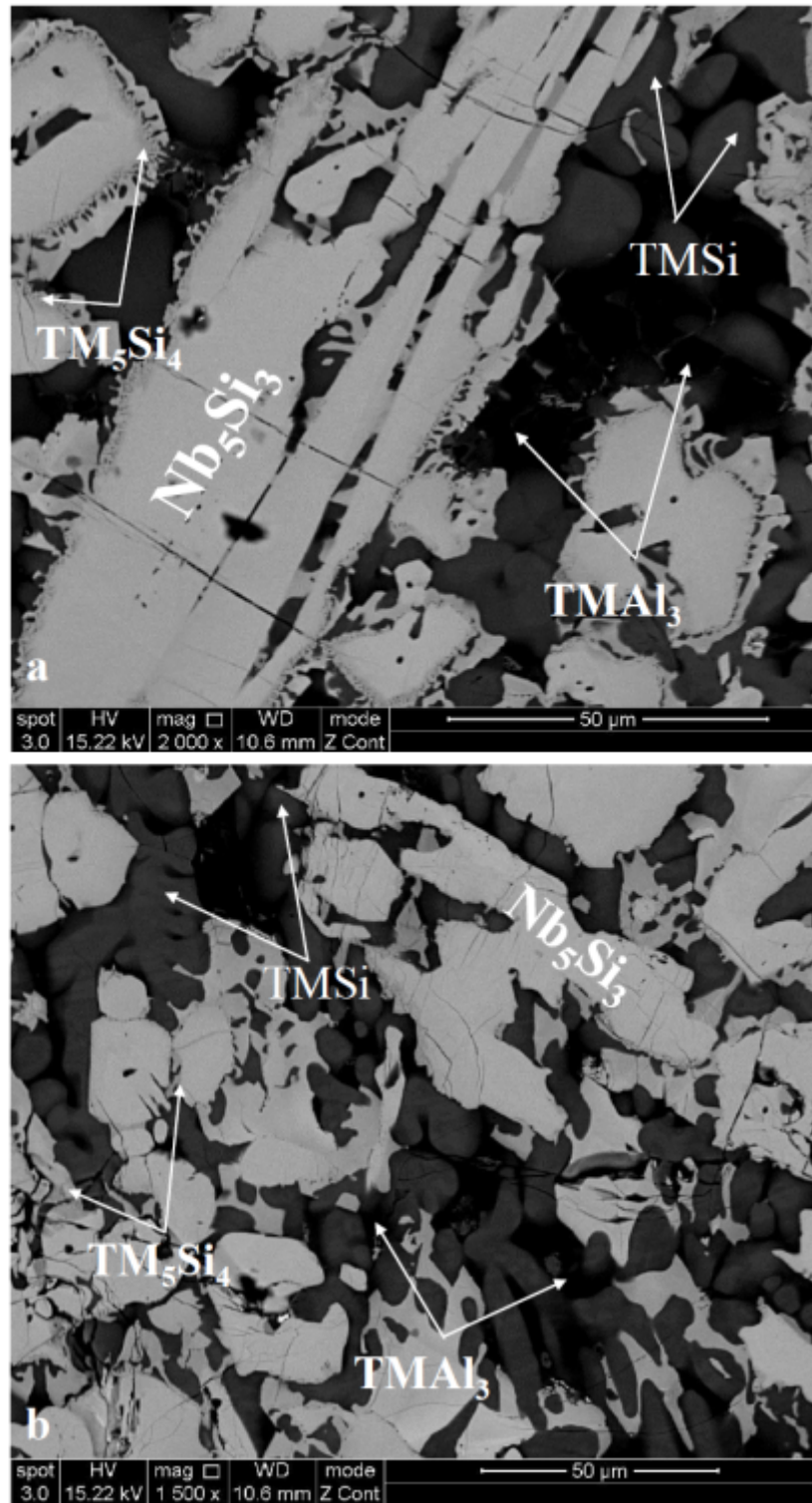


Figure 71: SEM backscatter electron images of MG5-HT800 taken from (a) the top and (b) the bulk of the heat treated alloy.

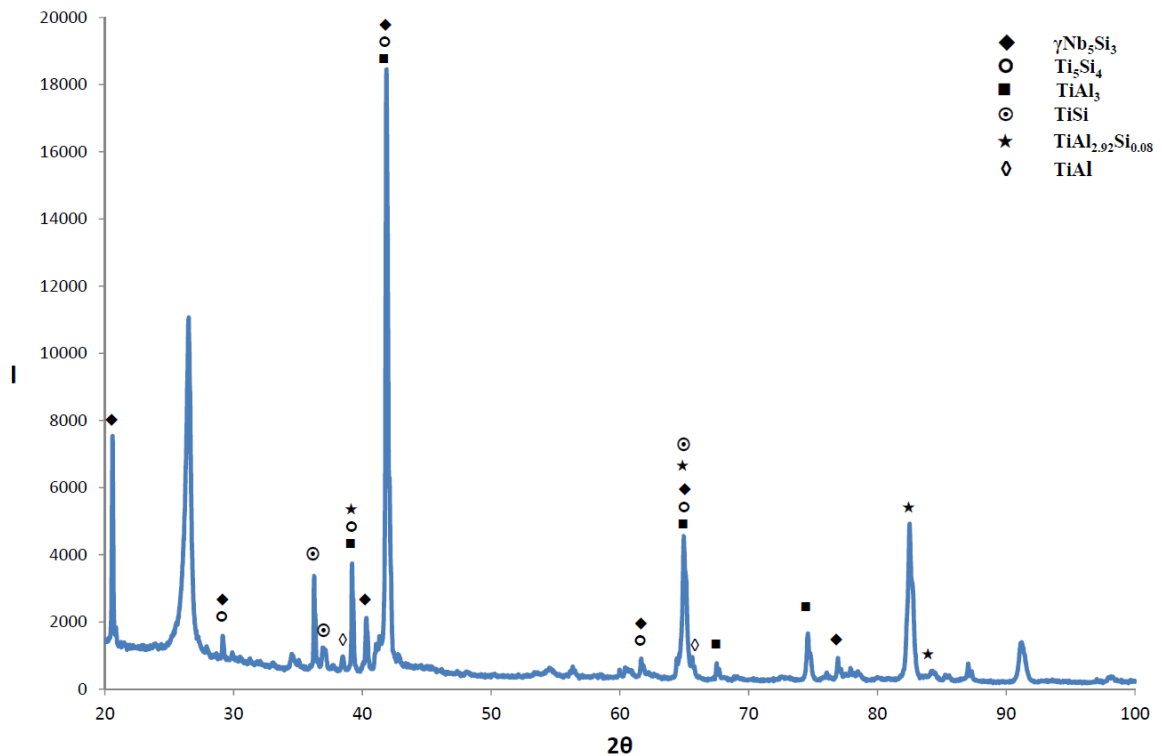


Figure 72: X-ray diffractogram of MG5-HT800

5.1.2.2 Heat treatment at 1200 °C

The average composition of MG5-HT1200 is shown in Table 22 and was determined by EDS. It was close to the nominal composition (Table 19) but the standard deviations of Al, Si and Ti were still high confirming the strong macrosegregation in the cast alloy and that there was very little (if any) homogenization at 1200 °C. The strongest chemical inhomogeneity was observed in the bulk of MG5-HT1200, where the Al+Si concentration was the highest (58.1 at%) compared with that in the alloy (52.8 at%). The latter was close to that in MG5-HT800 (Table 21). The microstructure and the XRD data of MG5-HT1200 are shown in Figure 73 and Figure 74, respectively. The XRD indicated that five different phases were present after the heat treatment at 1200 °C namely: TiAl₃, TiSi, Ti₅Si₄, TiAl and hexagonal Nb₅Si₃.

Table 22: EDS analysis data (at %) of the alloy MG5 heat treated at 1200 °C for 100 h

Area and phase analysis		Elements					Al+Si
		Nb	Si	Ti	Al	Hf	
Large area	Top	14.2±1.1 13.4-16.4	25.9±2.2 22.6-29.4	24.2±1 22.4-25.6	32±4.4 24.4-38.2	3.7±0.3 3.1-4.1	57.9
	Bulk	14.5±1.6 12.9-17.5	25.4±2.8 21.4-29.7	23.9±1.5 21.7-25.3	32.7±5.8 23.4-40.5	3.6±0.4 2.9-4.1	58.1
	Bottom	14.9±1.6 13.4-17.8	26.8±2.3 22.5-30.4	24.3±1 22.3-25.7	30±4.9 21.8-38.6	3.9±0.4 3.1-4.3	56.8
	Average	13.3±4.1 12.9-17.8	23.7±7.3 21.4-30.4	21.9±6.8 21.7-25.7	29.1±9.1 21.8-40.5	3.4±1 2.9-4.3	52.8
Phase (spot) analysis		Aluminides and silicides					
	Al ₃ TM	12.6±0.5 11.6-13.3	1.5±1.2 0.6-5.3	13.3±0.8 12.2-15.4	71.9±2.1 65.5-73.7	0.6±0.2 0.4-1	73.4
	TiSi	14.2±4.5 12.6-20.7	37.8±2.5 35-40.9	30.9±5.1 25.5-39.2	12.2±1.6 10.5-14.4	4.8±1.5 2.4-6.1	50
	Ti ₅ Si ₄	14.6±2.9 11-17.7	46±0.7 45.2-47.3	30±2.3 27.1-33.5	1.8±0.3 1.3-2.2	7.5±0.5 6.5-8.1	47.8
	TiAl	3.8±0.9 3.1-4.8	7.3±1 6.1-8	41.8±3.9 38-45.9	45.2±3 43.3-48.6	1.8±2.1 0.6-4.3	52.5
		5-3 silicide					
	γNb ₅ Si ₃	22±1.5 20.4-24.2	38.3±0.2 38-38.6	31.5±1.4 29.8-33.4	2.6±0.3 2.4-3.1	5.6±0.2 4.3-5.9	40.9

Compared with MG5-AC and MG5-HT800, changes were observed of the morphologies of the 5-3 and 5-4 silicides. The Nb₅Si₃ had become slightly richer in Ti and thus the Nb/(Ti+Hf) ratio was reduced from 0.67 in the cast alloy to 0.59 in MG5-HT1200. The TiAl was observed in the microstructure, but compared with MG5-HT800 it was richer in Ti and poorer in Al with Al+Si = 52.5 at%. The presence of this intermetallic was confirmed by the XRD (Figure 74). The 5-4 silicide had become richer in Ti compared with the MG5-AC, with principally no changes in the Al+Si concentration. This shift towards higher Ti concentration would suggest that the 5-4 silicide is stable in MG5. An increase in the Ti concentration was observed in the TiSi phase, where the Al+Si content had shifted to 50 at%. There were hardly any changes in the chemical composition of Al₃TM, compared with MG5-AC. Thus, the XRD data was corroborated by the identification of phases using EDS.

The microstructure of MG5-HT1200 is shown in Figure 73 where the aforementioned phases are indicated. In Figure 73a the dark and dim-gray (brighter dark) contrasts represent the TiAl_3 and TiAl intermetallic phases, respectively. The dark grey, bright gray and white contrasts represent the TiSi , Ti_5Si_4 and Nb_5Si_3 intermetallic phases, respectively. It should be noted that the phases that exhibited bright contrasts could not be easily distinguished with the exception of Nb_5Si_3 whose associated contrast was somewhat different from that of the other two phases. The TiSi and Ti_5Si_4 silicides exhibited almost the same contrast but the identification of the latter was easier owing to the places where it formed. Indeed, the Ti_5Si_4 was seen to surround Nb_5Si_3 grains, see also Figure 68 and Figure 71.

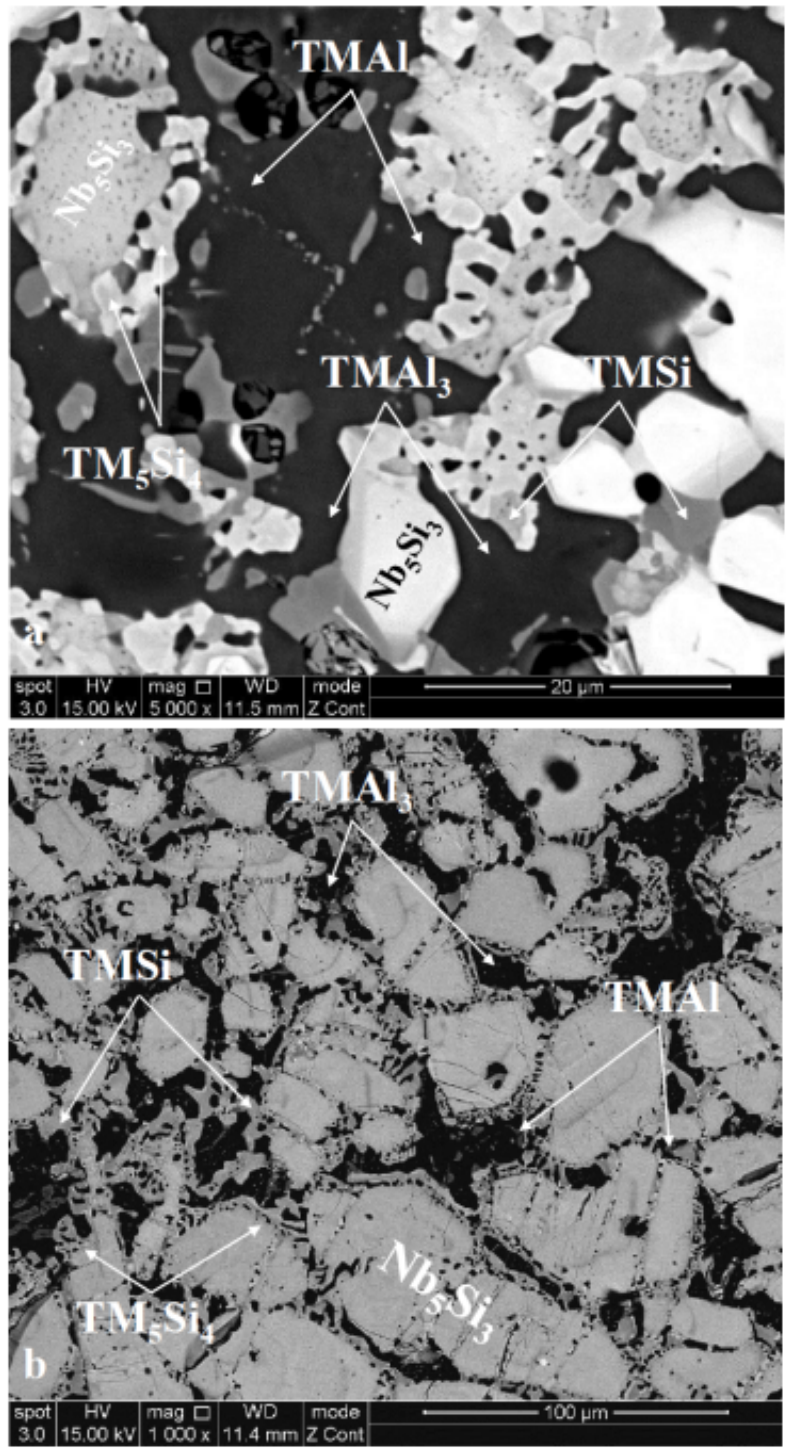


Figure 73: SEM backscatter electron images of the heat treated alloy MG5 at 1200 °C taken from (a) near the surface and (b) the bulk of the specimen

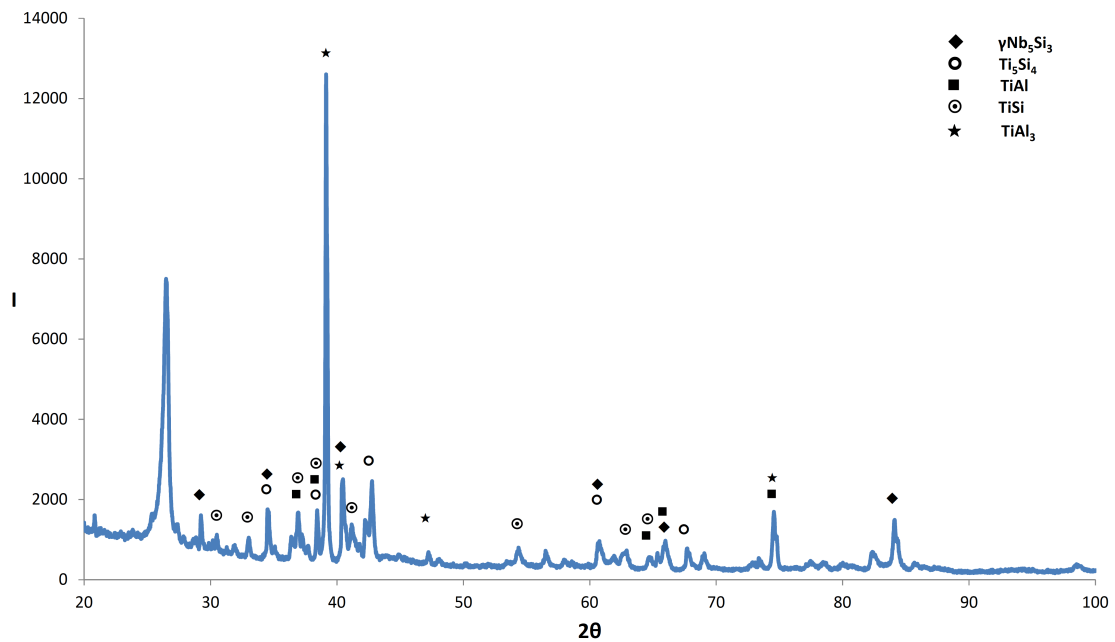


Figure 74: X-ray diffractogram of MG5-HT1200

5.1.3 Isothermal oxidation

The oxidation behaviour of the alloy MG5 was studied at 800 and 1200 °C. Muffle furnaces were used for this study because it was not possible to cut crack free cube specimens for TG experiments owing to the brittle nature of the cast alloy.

5.1.3.1 Oxidation at 800 °C

The oxidised specimen after 100 h at 800 °C is shown in figure 75. The alloy did not pest and formed a very thin scale, see figure 76a, b. The average composition of the alloy was 14.4Nb-25.7Si-24.6Ti-32Al-3.3Hf or 13.4Nb-23.9Si-23Ti-30.2Al-3.1Hf-6.9O, the latter analysis includes oxygen as hafnia was formed in the alloy, see figure 77a.

The XRD data is shown in figure 77, where the glancing angle diffractogram (GXRD) is given in figure 77b. The EDS data for the phases in the bulk of the specimen (figure 76c) is shown in table 23. The EDS analyses confirmed the presence of tri-aluminide

Al_3TM , hexagonal Nb_5Si_3 , the TiSi and Ti_5Si_4 silicides and $\text{Ti}(\text{Al},\text{Si})_2$ [$(\text{Ti}(\text{Al}_x\text{Si}_{1-x})_2$ and metastable TiAl_2 are isomorphous (oC12), Perrot 2009)], see table 23 and figure 77a, and also suggested the presence of $\text{TM}_2\text{Si}_{1.5}\text{Al}$ and $\text{TM}_8\text{Al}_{11}\text{Si}_3$, the composition of the latter being close to $\text{TM}_4(\text{Al},\text{Si})_7$ and $\text{Ti}_5\text{Al}_{11}$ (Perrot, 2009). However, the TiAl aluminide that was suggested by XRD (figure 77a) was not confirmed by EDS.

The microstructure near the surface of the oxidised specimen is shown in figure 78a and the EDS data in table 24. Figure 78b and c show a line scan and associated data. The line scan (figure 78b) was taken from the surface towards the bulk of the oxidised specimen. Spectra 1 to 5 in figure 78a indicate that the thin scale (see also figure 76) was Al rich (Table 24), probably alumina. However, there were no peaks corresponding to alumina in the glancing angle XRD (figure 77b). The latter confirmed the presence of Ti niobates as well as monoclinic Nb_2O_5 , rutile, TiAl_2O_5 and hafnia. Below the scale the Ti_5Si_4 silicide (spectra 7 and 8) and aluminides (spectra 8 and 9) were contaminated by oxygen, the latter more severely than the former, see also line scan in Figure 78.

5.1.3.2 Oxidation at 1200 °C

The oxidised specimen after 100 h at 1200 °C is shown in figure 79. The alloy did not suffer catastrophic oxidation and formed a thin continuous scale with no evidence of scale spallation, see figure 80a, b. The average composition of the alloy was 16.9Nb-27.8Si-24.6Ti-27.3Al-3.4Hf or 15.3Nb-25.3Si-22.5Ti-25.3Al-3.1Hf-8.5O, the latter analysis includes oxygen as hafnia was formed in the alloy, see figure 81a (in figure 81a the peaks for SiO_2 coincide with peaks of other phases but there are peaks that correspond only to hafnia).

The XRD data is shown in figure 81, where the GXRD is given in figure 81b. The microstructure of the oxidised specimen is shown in figure 82. The EDS data for the phases in the bulk of the specimen (figure 82b) is shown in table 25. The EDS analyses confirmed the presence of Al rich aluminide, hexagonal Nb₅Si₃, and the TiSi and Ti₅Si₄ silicides, see table 25 and figure 81a but not the aluminides TiAl and TiAl₂, and also suggested the presence of TM₂Si_{1.5}Al. In the X-ray diffractogram (figure 81) there were also peaks corresponding to Hf₁₀(Si₃,Al₃), which is isomorphous with Hf₅Si₄ and Ti₅Si₄ (both have the tP36 structure). The Hf₁₀(Si₃,Al₃) also confirms that there is solubility of Al in the 5-4 silicide, as suggested by the EDS analysis data presented in this thesis. In all areas of the oxidised alloy MG5 the microstructure exhibited similar characteristics around and near the 5-3 silicide grains (figure 82) as observed in the heat treated alloy at 1200 °C (figure 73).

The microstructure near the surface of the oxidised specimen is shown in figure 80 and figure 83a, and the EDS data for the latter figure is given in table 26. Figure 83b and c show a line scan and associated data. The line scan (figure 83b) was taken from the surface towards the bulk of the oxidised specimen. Spectra 1 to 4 in figure 83a indicate that the thin scale (see also figure 80) was Al rich (table 26), probably alumina. This is supported by peaks corresponding to alumina in the glancing angle XRD (figure 81b). The latter confirmed the presence of Ti niobates as well as monoclinic Nb₂O₅, rutile, hafnia, TiAl₂O₅, TiO and SiO₂. Below the scale the Ti₅Si₄ (spectrum 9) and 5-3 (spectrum 6) silicides and aluminides (spectra 5, 8 and 11) were contaminated by oxygen.

Table 23: EDS analysis data (at%) of the alloy MG5 oxidized at 800 °C

Area and phase analysis		Elements						Al+Si
		O	Nb	Si	Ti	Al	Hf	
Large area	Average		14.4±2.7 10.7-18	25.7±5.7 14.5-32.5	24.6±2.8 20.5-28.9	32±11.4 16.9-52.2	3.3±0.7 2-4.3	57.7
	Average	6.9±2.4 2.1-11.1	13.4±2.3 9.8-16.5	23.9±5.2 13.4-30.7	23.1±2.7 18.9-27.4	30.2±11 16.1-48.6	3.1±0.6 1.8-4.1	54.1
Phase (spot) analysis		Aluminide and silicides						
	Al ₃ TM		11.2±2.5 8.4-14	2.9±0.8 1.9-5	13.5±2.4 10.7-17.7	71.3±1 68.9-72.4	1±0.3 0.6-1.4	74.2
	Ti ₂ Al ₅		6.1±5.8 0.7-14.5	6.5±1.2 4.7-7.6	19.5±4.2 13.2-23	66.4±2.5 63.9-70	1.3±0.2 1-1.6	73
	Ti ₅ Si ₄		20.6±2.7 16.8-24.6	41.4±3.8 37.3-46.7	28.4±1.4 26.5-30.2	3.7±2 1.7-7	5.9±1.1 4.9-7.4	45.2
	TiSi		17.8±2.1 14.7-19.2	38±2.9 34.4-41.6	26.1±1.6 14.7-19.2	13.4±4.2 7.8-18.1	4.7±0.5 4-5	51.4
	Ti(Al,Si) ₂		13.7±1.9 11-15.2	20.3±7.1 10.4-26.6	20.6±0.4 20.3-21.2	42.2±8.5 33.3-53.8	3.1±0.9 1.9-3.8	62.6
	TM ₂ Si _{1.5} Al		14.3±1.9 3.9-5.3	31.2±4.6 26.3-38	27.2±1.7 25.3-29.6	23±3.8 17.1-26.3	4.3±0.6 3.9-5.3	54.2
	TM ₈ Al ₁₁ Si ₃		9.2±2.1 6-11.7	14.8±3 10.6-18.4	20.3±1.9 18.4-22.8	54±4.2 48.8-60	1.6±0.5 1.2-2.4	68.8
		5-3 silicide						
	γNb ₅ Si ₃		21.5±3.1 15.2-25.7	37.9±3.8 27.6-39.6	32±3.6 28-40.4	3.6±3.5 1.9-13	5±0.5 3.7-5.5	41.4

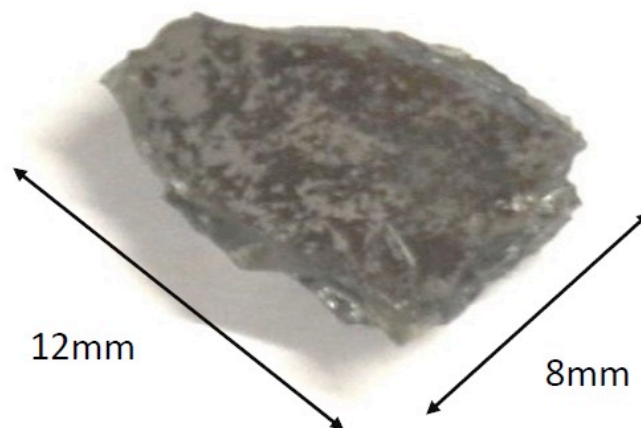


Figure 75: Specimen of the alloy MG5 oxidized in muffle furnace at 800 °C

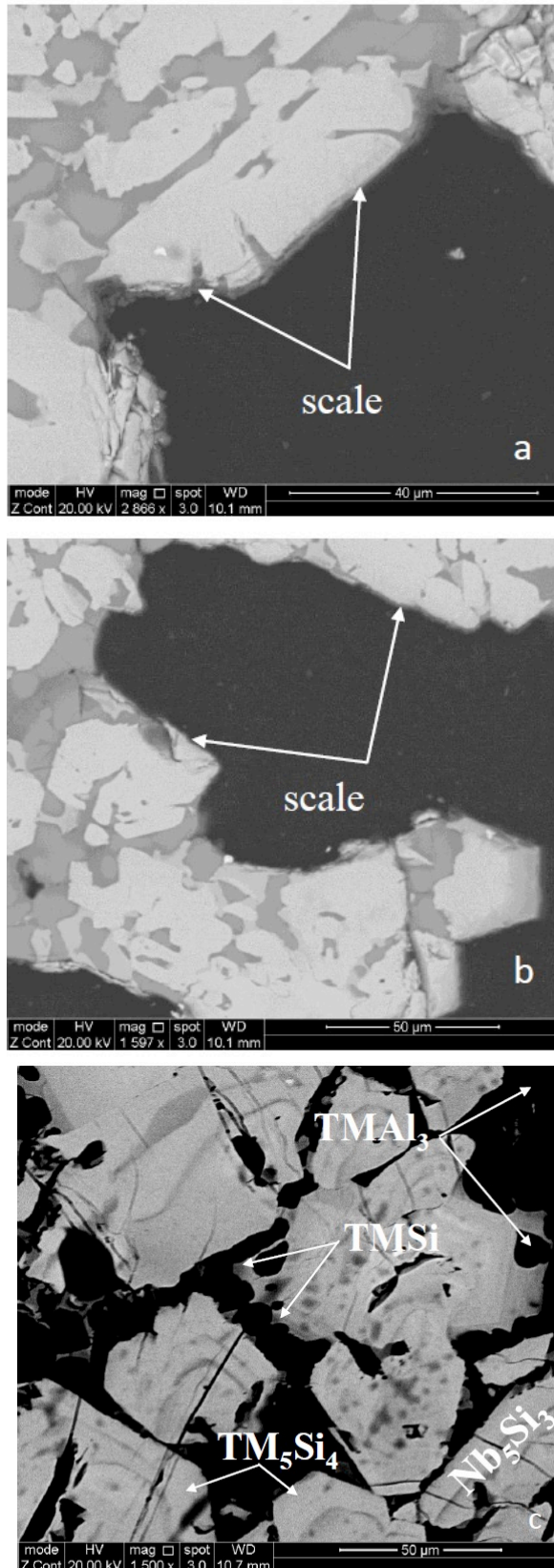


Figure 76: BSE images showing (a), (b) the near surface microstructure of cross section of the alloy MG5 oxidized at 800 °C in muffle furnace and (c) the bulk microstructure

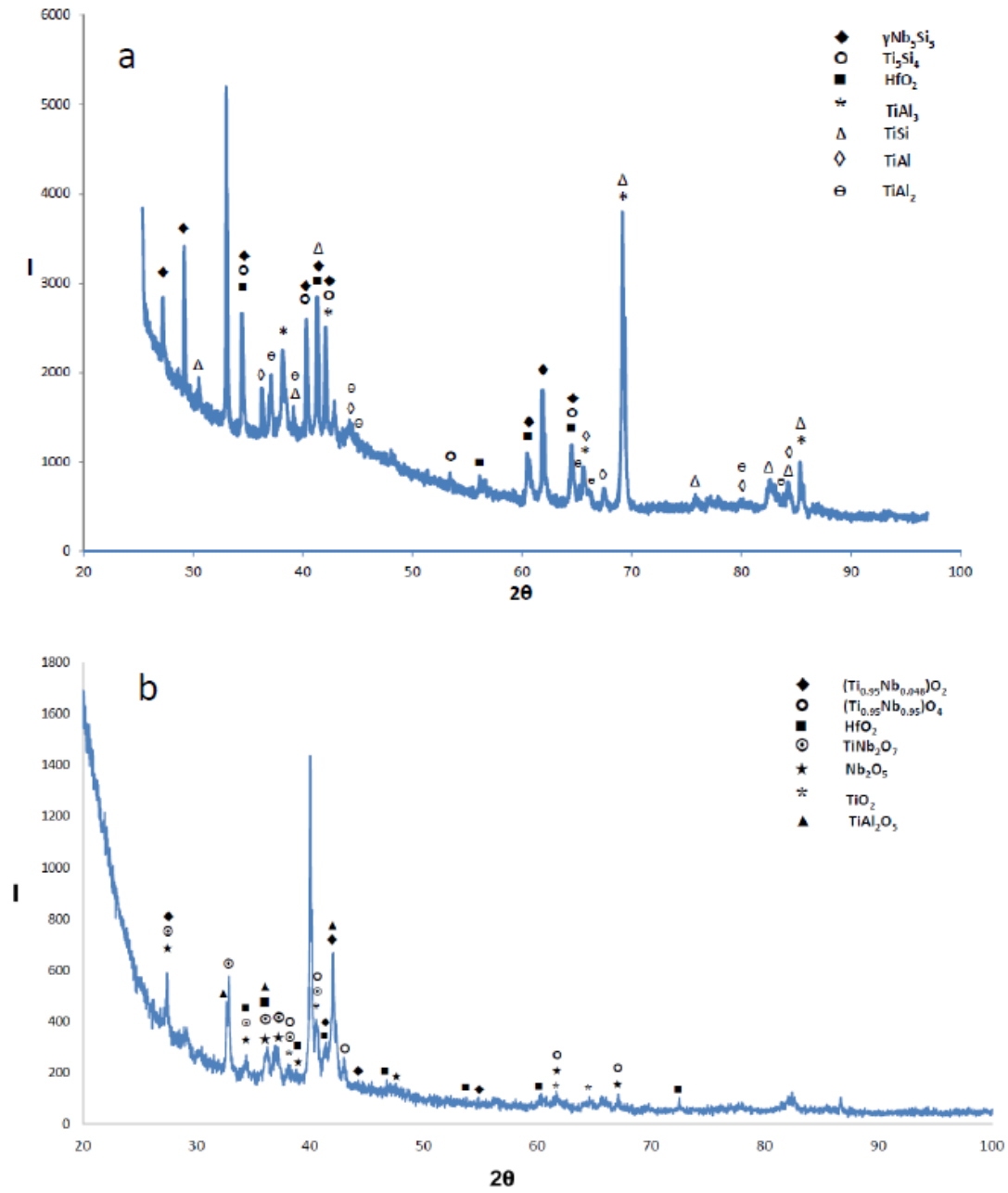
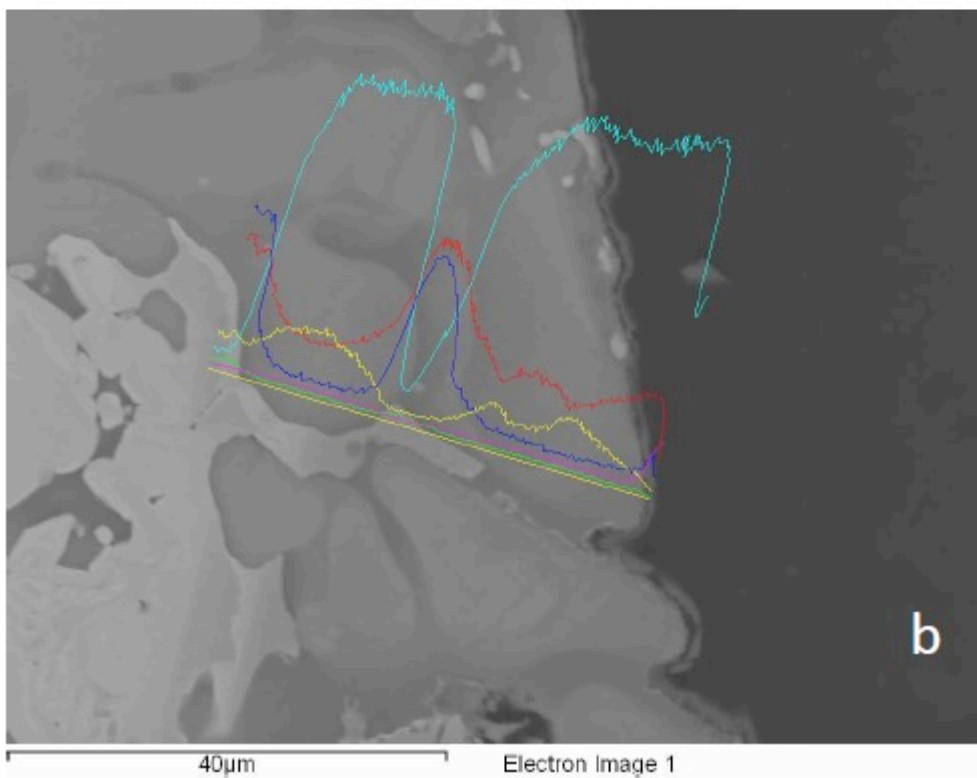
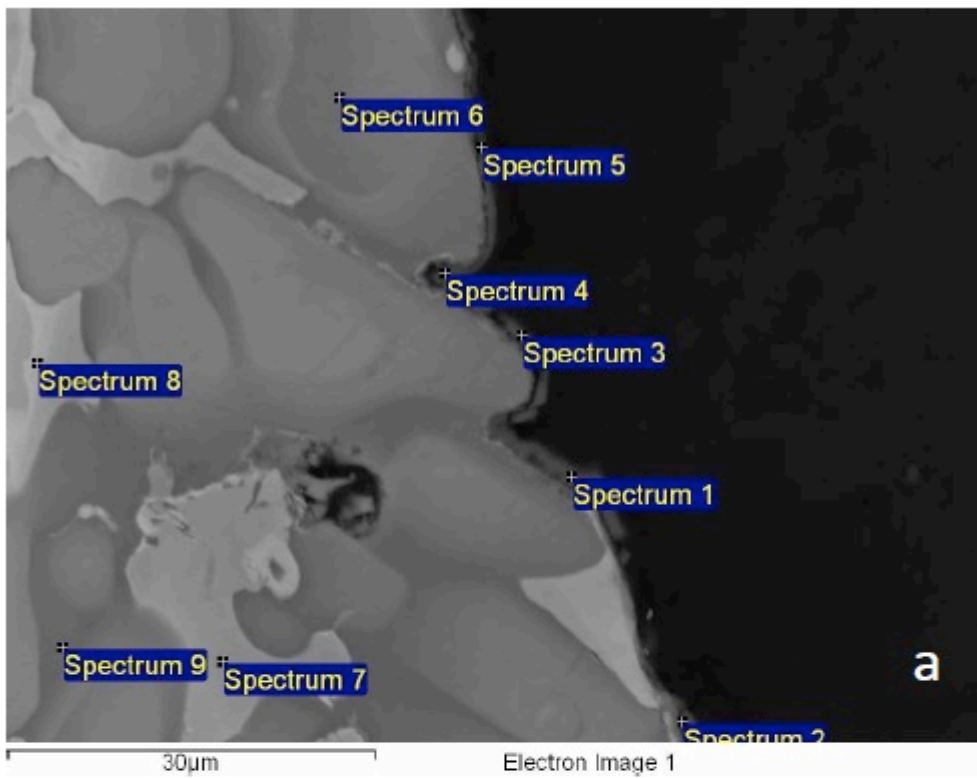


Figure 77: XRD data for the oxidized specimen of alloy MG5 at 800 °C. (a) Bragg-Brentano and (b) glancing angle ($\theta = 5^\circ$)

Table 24: EDS analysis data (at%) of the near surface microstructure of the oxidized specimen at 800 °C

Spectra	Phase	Element					
		O	Nb	Si	Ti	Al	Hf
Spectrum 1	Al ₂ O ₃	70.1	0.04	2.2	3.6	23.9	0.09
Spectrum 2	Al ₂ O ₃	69	0.3	5.3	5.1	19.7	0.5
Spectrum 3	Al ₂ O ₃	66.1	0.05	1.5	2.5	29.7	0.06
Spectrum 4	Al ₂ O ₃	70	0.2	3.1	5.8	20.8	0.1
Spectrum 5	Al ₂ O ₃	61.6	0.2	1.4	3.1	33.6	0.06
Spectrum 6	Ti ₂ A ₅	8	5.9	2.8	17.2	65.3	0.8
Spectrum 7	Ti ₅ Si ₄	1.1	3.4	46.4	44.5	1.1	3.4
Spectrum 8	Ti ₅ Si ₄	1	9.8	46.6	35.9	1.4	5.3
Spectrum 9	Ti ₂ Al ₅	4.6	1.6	5.6	21.9	65.5	0.8



Continued

Continued

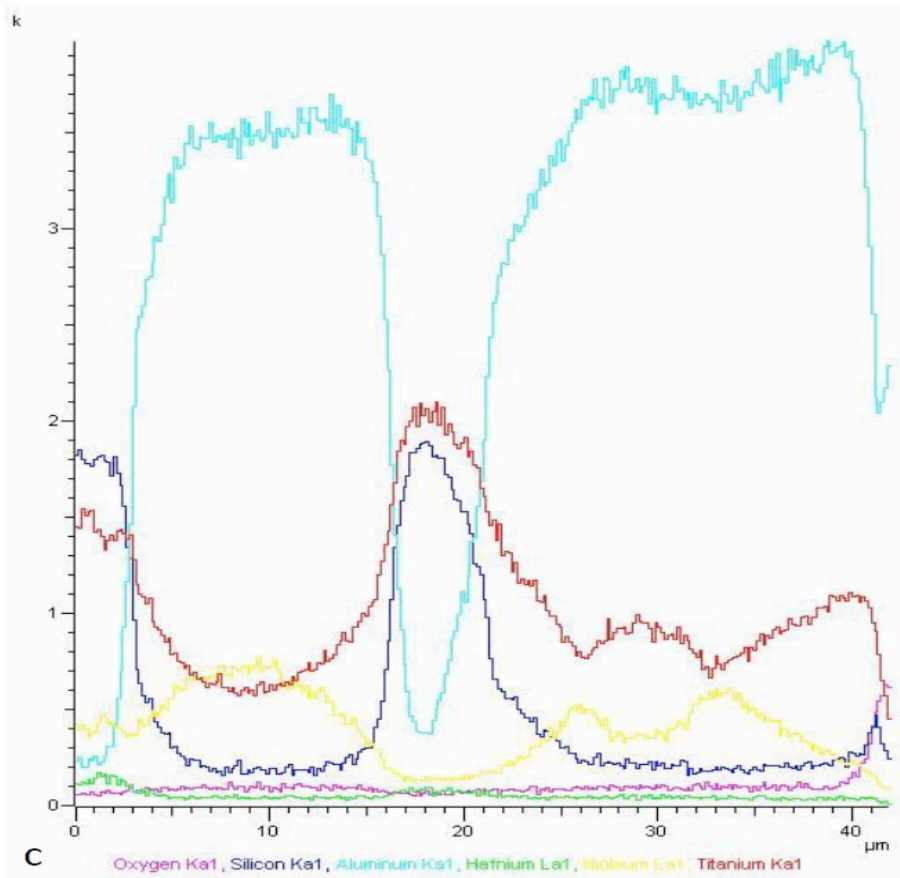


Figure 78: BSE image showing (a) the near surface microstructure of cross section of the alloy MG5 oxidized at 800 °C in muffle furnace, (b) line scan and (c) the associated data

Table 25: EDS analysis data (at%) of the MG5 alloy oxidized at 1200 °C

Area and phase analysis		Elements						Al+Si
		O	Nb	Si	Ti	Al	Hf	
Large area	Average		16.8±2.4 12.5-21.7	27.8±3.5 24.2-33.6	24.6±1.7 21.8-27.3	27.3±7.7 13.6-41.7	3.4±0.5 2.4-4.2	55.1
	Average	8.5±3.7 2.8-16.6	15.3±2 11.3-18.9	25.3±2.9 18.8-29.5	22.5±1.6 20.5-26	25.3±7.4 12.1-33.7	3.1±0.4 2.2-3.7	50.6
Phase (spot) analysis	Aluminide and silicides							
	TM ₂ Al ₅		12.7±1.2 11.8-14.5	1.5±0.7 0.8-2.5	15.3±1.8 13.1-16.7	69.8±2 67.5-72.4	0.6±0.1 0.5-0.8	71.3
	Ti ₅ Si ₄		14±3.7 11.5-18.2	42.2±5.2 36.2-45.7	33.1±4.5 28.6-37.7	4.5±3.9 2.1-8.9	6.2±0.5 6.2-0.5	46.7
	TM ₂ Al _{1.5} Si		11.6±2.9 7.4-14.1	22.4±2.1 19.2-25.2	28.8±8.4 20.7-38.3	34.2±3.4 30-39.2	2.8±1.1 1.5-4.1	56.7
	TiSi		8.2±2.4 6.5-9.9	34.2±3 32.1-36.4	38.5±4.1 35.6-41.4	16.1±1.4 15-17.1	2.9±0.1 2.9-3	50.3
	5-3 silicides							
	γ(Nb,Ti) ₅ Si ₃		21.2±0.5 19.7-22	34.1±0.9 33.4-36	37.3±1.6 35-39.3	2.2±0.3 1.9-2.7	5.2±0.3 4.8-5.9	36.3
	(Ti,Nb) ₅ Si ₃		9.2±0.5 8.2-9.8	38.8±0.6 37.7-39.6	44.4±0.5 43.9-45.1	2.3±0.8 1.3-3.7	5.3±0.2 5-5.5	41.1

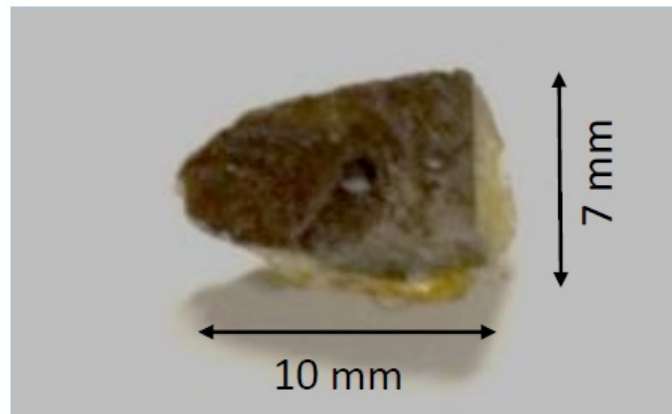


Figure 79: Specimen of the alloy MG5 oxidized in muffle furnace at 1200 °C

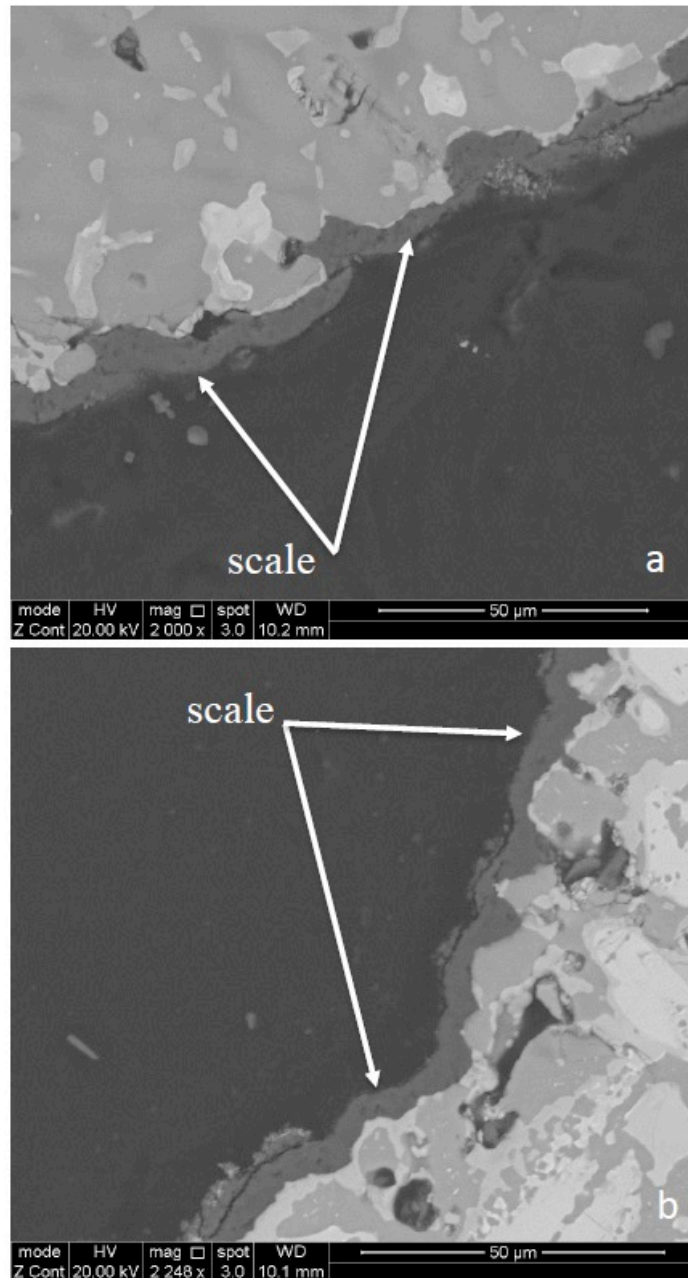


Figure 80: Backscatter electron images taken from the edge of the oxidized alloy MG5 at 1200 °C

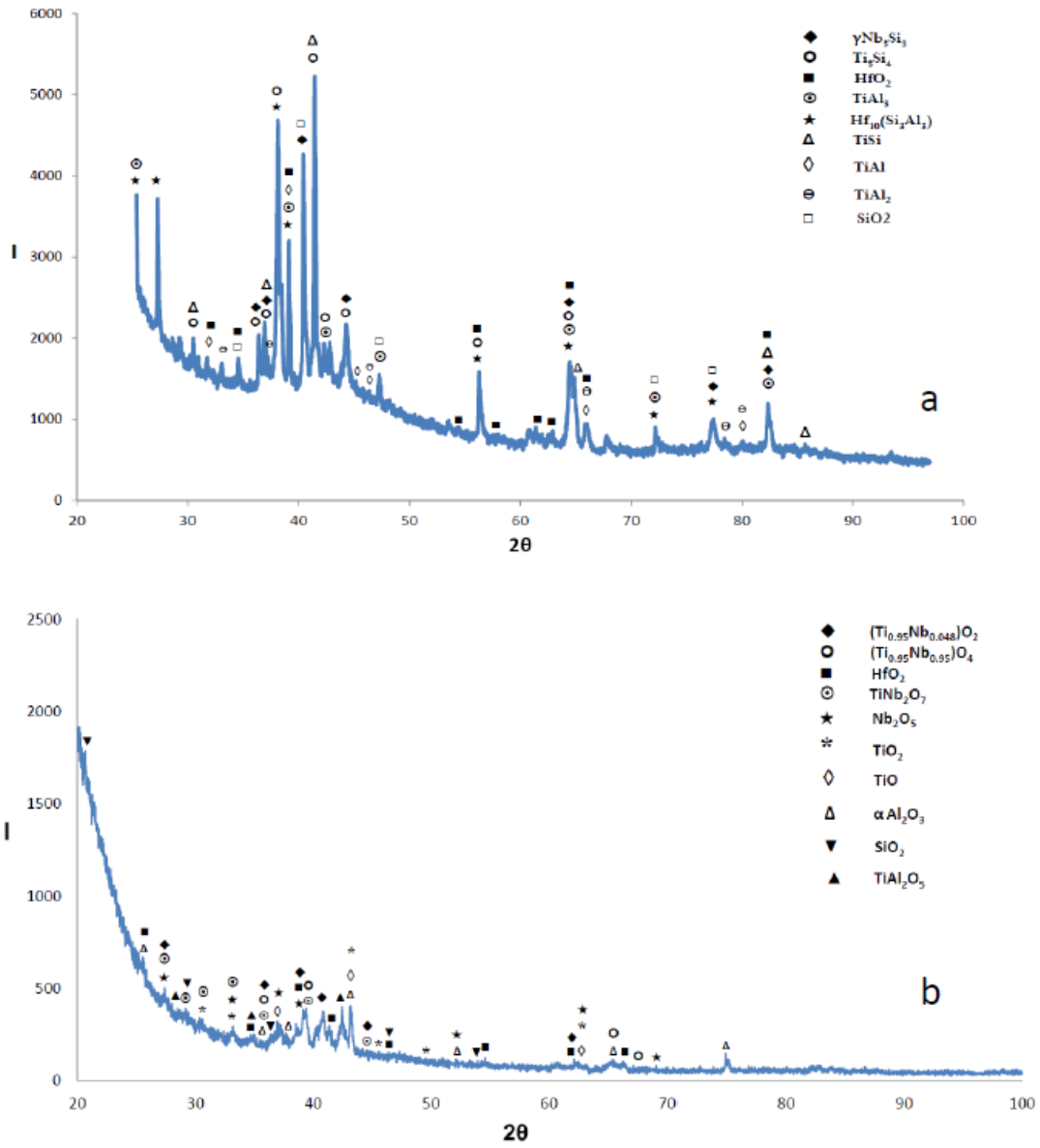
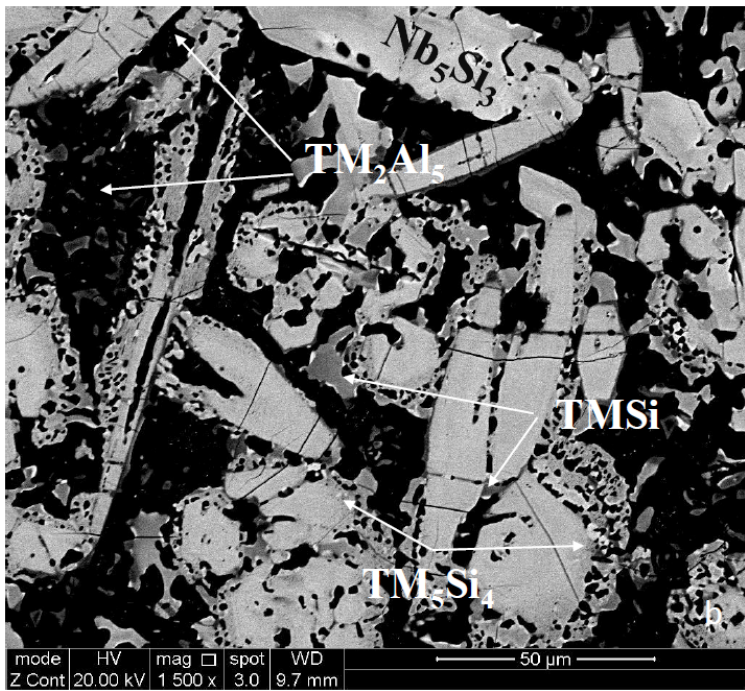
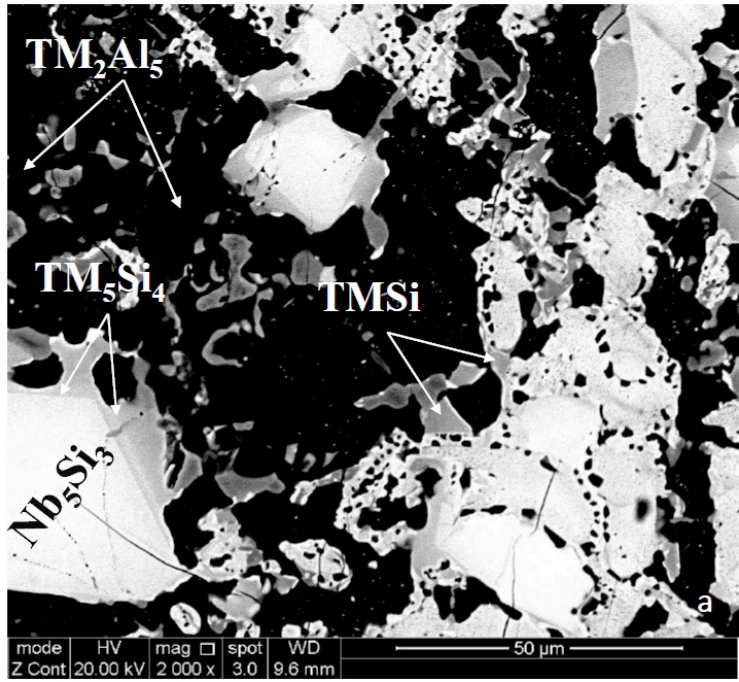


Figure 81: XRD data for the specimen of the alloy MG5 oxidized at 1200 °C for 100 h in muffle furnace (a) Bragg-Brentano and (b) glancing angle ($\theta = 5^\circ$)



Continued

Continued

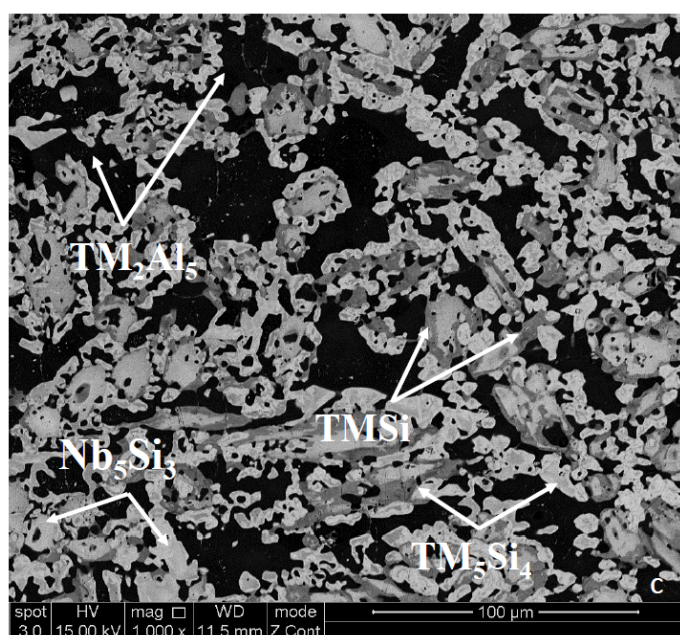
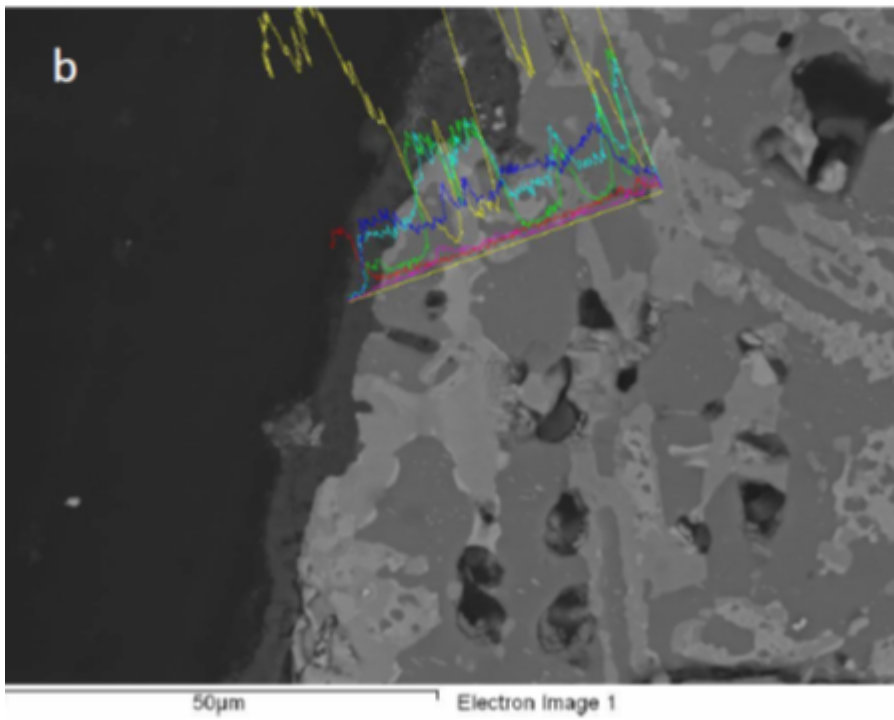
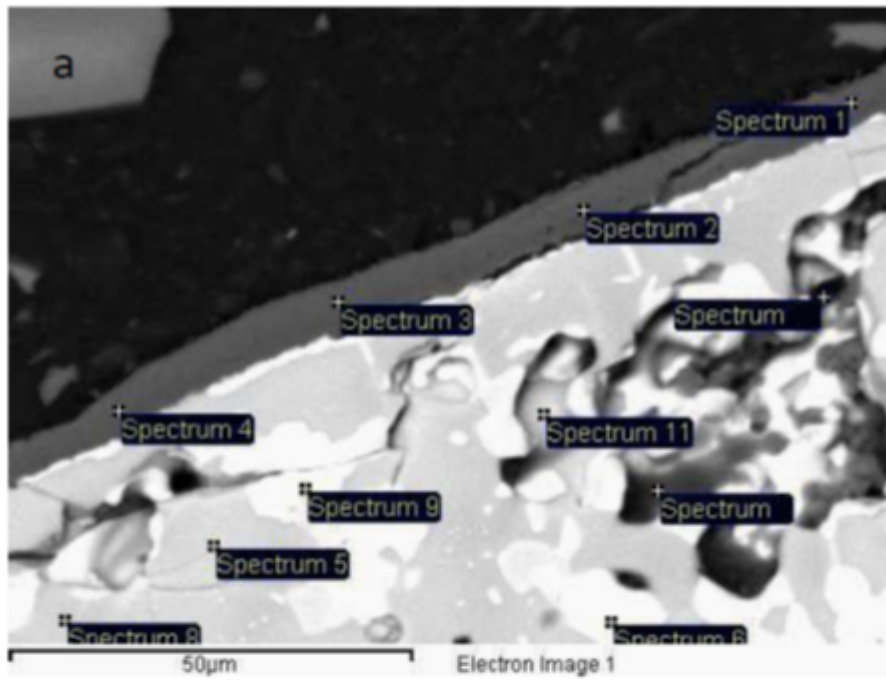


Figure 82: BSE images of the microstructure of the oxidized alloy MG5 at 1200 °C, (a) top, (b) bulk and (c) bottom of the oxidized specimen

Table 26: EDS analysis data (at%) of the near surface microstructure of the oxidized specimen at 1200 °C

Spectra	Phase	Element					
		O	Nb	Si	Ti	Al	Hf
Spectrum 1	Al ₂ O ₃	62.8	0.01	0.03	0.05	37.1	0
Spectrum 2	Al ₂ O ₃	62.6	0.1	0.09	0.1	37.2	0
Spectrum 3	Al ₂ O ₃	62.8	0	0	0.04	37.2	0
Spectrum 4	Al ₂ O ₃	62.1	0.02	0.02	0.03	37.9	0
Spectrum 5	Al ₂ O ₃	4.1	11.5	1	12.7	69.8	0.7
Spectrum 6	Ti ₂ A ₅	6.2	6.4	37.6	45	0.8	4
Spectrum 8	Ti ₅ Si ₄	3.8	9.7	0.9	14.1	70.6	0.8
Spectrum 9	Ti ₅ Si ₄	3.8	16	43.7	28.9	1.8	5.7
Spectrum 11	Ti ₂ Al ₅	9.5	6	6.4	39	38	1



Continued

Continued

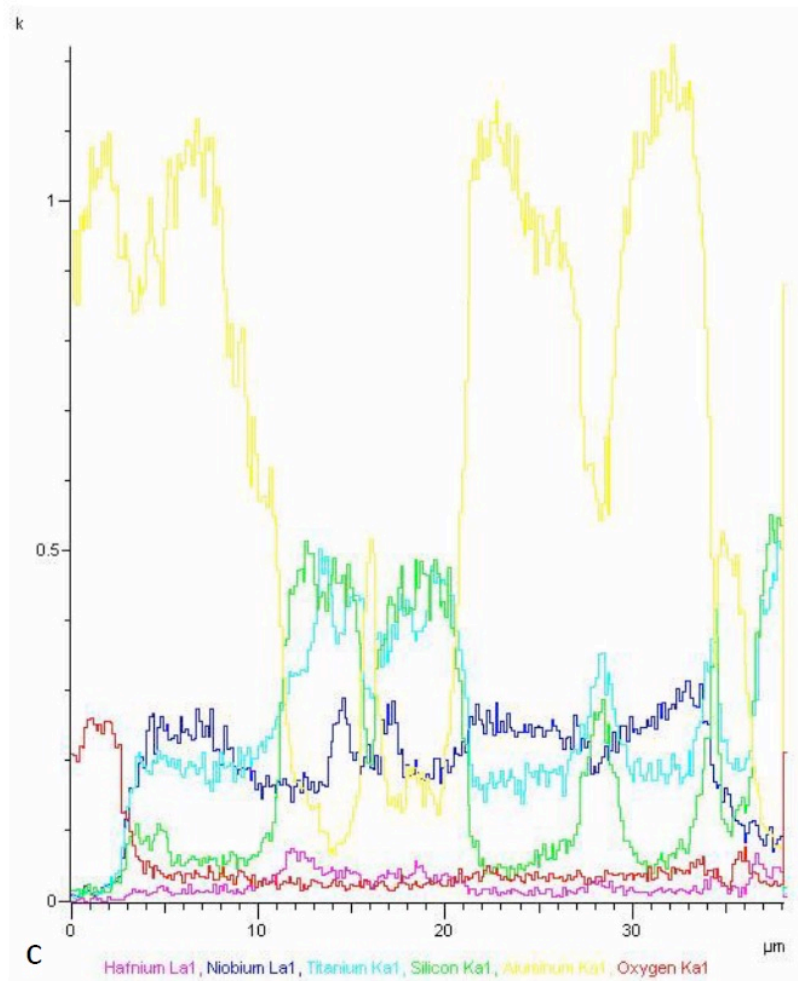


Figure 83: BSE image showing (a) the near surface microstructure of cross section of the alloy MG5 oxidized at 1200 °C in muffle furnace, (b) line scan and (c) the associated data

5.1.4 Discussion

The alloy MG5-AC exhibited macrosegregation of Al, Si and Ti. Compared with the alloy MG2-AC, the macrosegregation of Si and Ti was reduced respectively by about 22% and 56%, but the macrosegregation of Al had increased by about 29%. The actual compositions of the alloys MG5-AC and MG2-AC differed only regarding the Ti/Si ratio, which was less than one in the former. This would suggest that in Al rich alloys the latter ratio plays an important role in the development of chemical inhomogeneity

in the alloy microstructure. This tentative conclusion was tested in the alloy MG6, which will be considered in the following chapter.

The same phases were present in all parts of the ingot of MG5-AC, namely hexagonal $\gamma(\text{Nb,Ti})_5\text{Si}_3$ (isomorphous with Ti_5Si_3), $(\text{Ti,Nb})_5\text{Si}_4$, $(\text{Ti,Nb})\text{Si}$ and Al_3TM tri-aluminide. The microstructure was finer in the bottom of the ingot, owing to the higher cooling rate(s) prevailing there during solidification.

We need to consider the Ti-Si binary phase diagram (see figure 84) in order to understand the microstructures in the alloy MG5. In Si rich melts where the Ti_5Si_3 is the primary phase there is a “cascade” of peritectic reactions, namely $\text{L} + \text{Ti}_5\text{Si}_3 \rightarrow \text{Ti}_5\text{Si}_4$, then $\text{L} + \text{Ti}_5\text{Si}_4 \rightarrow \text{TiSi}$, and the resulting microstructure would consist of Ti_5Si_3 (primary) core “surrounded” by Ti_5Si_4 (first peritectic) and then Ti_5Si_4 “surrounded” by TiSi (second peritectic). This was observed in MG5-AC in all parts of the ingot but the TiSi also formed independently (meaning not on the 5-4 silicide). In very rich Si melts it is possible for the primary phase to be the 5-4 silicide in which case the latter can form as individual grains. This was observed in the bulk of MG5-AC (see figure 68b), which incidentally was richer in Si than the bottom and top.

The melting temperatures of binary intermetallics of interest that can help us to understand the microstructure of the cast alloy MG5 are as follows: $\beta\text{Nb}_5\text{Si}_3 - 2515\text{ }^\circ\text{C}$, hexagonal 5-3 silicides $\text{Hf}_5\text{Si}_3 - 2357\text{ }^\circ\text{C}$ and $\text{Ti}_5\text{Si}_3 - 2130\text{ }^\circ\text{C}$, tP36 (prototype Zr_5Si_4) silicides $\text{Hf}_5\text{Si}_4 - 2313\text{ }^\circ\text{C}$ and $\text{Ti}_5\text{Si}_4 - 1920\text{ }^\circ\text{C}$, B27 (prototype FeB) silicides $\text{HfSi} - 2133\text{ }^\circ\text{C}$ and $\text{TiSi} - 1570\text{ }^\circ\text{C}$, and DO22- Al_3X intermetallics with $\text{X} = \text{Nb}$ ($\text{Al}_3\text{Nb} - 1680\text{ }^\circ\text{C}$), Hf ($\text{Al}_3\text{X} - 1590\text{ }^\circ\text{C}$) and Ti ($\text{Al}_3\text{Ti} - 1387\text{ }^\circ\text{C}$). The alloyed hexagonal $\gamma\text{Nb}_5\text{Si}_3$ is

expected to have a melting temperature higher than that of the alloyed 5-4 silicide. The alloying of the Ti based tri-aluminide with Nb and Hf should increase the melting temperature, and the same should be the case for the alloyed TiSi.

In the microstructures of MG5-AC the tri-aluminide formed in the areas between the “composite” silicide grains (composite here means 5-3 core surrounded by 5-4 silicide, surrounded by TMSi), i.e., in the last melt to solidify, but also TMSi grains were observed in the same areas (meaning between the “composite” grains without TMSi on the 5-4 silicide). Thus, it was deduced that in MG5 the melting temperatures of the 5-3 silicide and 5-4 silicide were higher than those of the tri-aluminide Al_3TM and TMSi silicide.

As the primary 5-3 silicide formed the surrounding melt became poor in Hf, Nb, Si and Ti and rich in Al, from this melt the 5-4 silicide formed on the 5-3 silicide via a peritectic reaction and the melt became poor in Hf, Si, Ti and richer in Al and Nb and then (depending on the composition of the melt) from Al rich and Si and Hf poor melt formed the Al_3X and the surrounding melt became rich in Hf, Nb, Si, Ti and poor in Al and TMSi formed OR from Si rich melt (around the 5-4 silicide) resulted the peritectic reaction $L + Ti_5Si_4 \rightarrow TiSi$ giving TMSi on 5-4 silicide.

It is suggested that the solidification path of MG5-AC was $L \rightarrow L + \text{hexagonal } Nb_5Si_3$ then $L + \text{hexagonal } Nb_5Si_3 \rightarrow TM_5Si_4$, then $L + \text{hexagonal } Nb_5Si_3 \rightarrow TM_5Si_4 + Al_3TM$ $\rightarrow \text{hexagonal } Nb_5Si_3 + TM_5Si_4 + Al_3TM + TMSi$ or $L \rightarrow L + \text{hexagonal } Nb_5Si_3$ then $L + \text{hexagonal } Nb_5Si_3 \rightarrow TM_5Si_4$, then $L + TM_5Si_4 \rightarrow TMSi \rightarrow \text{hexagonal } Nb_5Si_3 + TM_5Si_4 + TMSi + Al_3TM$.

If the alloy MG5 is considered as (Ti,Nb,Hf)-Si-Al, primary hexagonal 5-3 silicide is in agreement with the results reported by Bulanova et al (2004) and the same is the case for the reaction $L + \text{hexagonal Nb}_5\text{Si}_3 \rightarrow \text{Ti}_5\text{Si}_4 + \text{Al}_3\text{TM}$. However, Bulanova et al (2004) did not observe TiSi in the cast microstructures of Ti-Si-Al alloys of compositions similar to those of MG5, when the latter is considered as (Ti,Nb,Hf)-Si-Al.

If the alloy MG5 is considered as (Nb,Hf) - Ti - (Si,Al) then according to Bulanova and Fartushna (2010) the class II (transition reaction - U₂) $L + (\text{Ti,Nb})_5\text{Si}_3 \rightarrow \beta(\text{Nb,Ti})_5\text{Si}_3 + (\text{Ti,Nb})_5\text{Si}_4$ occurs at $T < 1815 \text{ }^\circ\text{C}$ and then via $L + \beta(\text{Nb,Ti})_5\text{Si}_3 \rightarrow (\text{Ti,Nb})_5\text{Si}_4 + (\text{Nb,Ti})\text{Si}_2$ and $L + (\text{Ti,Nb})_5\text{Si}_4 \rightarrow (\text{Nb,Ti})\text{Si}_2 + (\text{Ti,Nb})\text{Si}$ the TMSi is formed below $1570 \text{ }^\circ\text{C}$.

The above discussion based on Bulanova et al (2004) and Bulanova and Fartushna (2010) would suggest that in the alloy MG5 the formation of DO22-Al₃TM tri-aluminide was “controlled” by the Ti-Al-Si phase equilibria and that of TMSi by the Nb-Ti-Si phase equilibria.

The Pandat software was used to calculate the solidification path for the overall average composition of MG5-AC (the average composition in the bottom of the ingot was essentially the same as the overall average alloy composition). The following path was calculated: Solidification starts at $2009 \text{ }^\circ\text{C}$ with $L \rightarrow L + \text{Ti}_5\text{Si}_3$, then $L \rightarrow \text{Ti}_5\text{Si}_3 + \text{Nb}_5\text{Si}_3$ at $1744 \text{ }^\circ\text{C}$, then $L + \text{Ti}_5\text{Si}_3 \rightarrow \text{Nb}_5\text{Si}_3 + \text{HfSi}$ at $1547 \text{ }^\circ\text{C}$, then $L + \text{HfSi} \rightarrow \text{Nb}_5\text{Si}_3 + \text{Ti}_3\text{Al}_2\text{Si}_5$ at $1443 \text{ }^\circ\text{C}$, then $L + \text{Nb}_5\text{Si}_3 \rightarrow \text{Ti}_3\text{Al}_2\text{Si}_5 + \text{TiSi}_2$ at $1187 \text{ }^\circ\text{C}$, then $L \rightarrow$

$\text{Ti}_3\text{Al}_2\text{Si}_5 + \text{TiSi}_2 + \text{DO22-Al}_3\text{X}$ at 995 °C, then $\text{L} \rightarrow \text{Ti}_3\text{Al}_2\text{Si}_5 + \text{TiSi}_2$ at 940 °C, then $\text{L} + \text{TiSi}_2 \rightarrow \text{Ti}_3\text{Al}_2\text{Si}_5 + \text{NbSi}_2$ at 896 °C, then $\text{L} + \text{Ti}_3\text{Al}_2\text{Si}_5 \rightarrow \text{NbSi}_2 + \text{Ti}_7\text{Al}_5\text{Si}_{14}$ at 864 °C, then $\text{L} \rightarrow \text{NbSi}_2 + \text{Ti}_7\text{Al}_5\text{Si}_{14}$ at 863.99 °C, with the last step in the solidification path $\text{NbSi}_2 + \text{Ti}_7\text{Al}_5\text{Si}_{14}$ at 635 °C. The calculations agreed with the experimental observations regarding the primary phase, the DO22- Al_3TM tri-aluminide and TiSi (isomorphous with HfSi) but could not account for the formation of the TM_5Si_4 .

The following path was calculated for the bulk of MG5. Solidification starts at 2024 °C with $\text{L} \rightarrow \text{L} + \text{Ti}_5\text{Si}_3$, then $\text{L} \rightarrow \text{Ti}_5\text{Si}_3 + \text{Nb}_5\text{Si}_3$ at 1773 °C, then $\text{L} + \text{Ti}_5\text{Si}_3 \rightarrow \text{Nb}_5\text{Si}_3 + \text{HfSi}$ at 1562 °C, then $\text{L} + \text{HfSi} \rightarrow \text{Nb}_5\text{Si}_3 + \text{Ti}_3\text{Al}_2\text{Si}_5$ at 1467 °C, then $\text{L} + \text{Nb}_5\text{Si}_3 \rightarrow \text{Ti}_3\text{Al}_2\text{Si}_5 + \text{TiSi}_2$ at 1278 °C, then $\text{L} \rightarrow \text{Ti}_3\text{Al}_2\text{Si}_5 + \text{TiSi}_2$ at 1277.7 °C, then $\text{L} + \text{Ti}_3\text{Al}_2\text{Si}_5 \rightarrow \text{TiSi}_2 + \text{Ti}_7\text{Al}_5\text{Si}_{14}$ at 996.13 °C, then $\text{L} \rightarrow \text{TiSi}_2 + \text{Ti}_7\text{Al}_5\text{Si}_{14}$ at 996.12 °C, then $\text{L} + \text{TiSi}_2 \rightarrow \text{Ti}_7\text{Al}_5\text{Si}_{14} + \text{NbSi}_2$ at 978 °C, with the last step in the solidification path $\text{NbSi}_2 + \text{Ti}_7\text{Al}_5\text{Si}_{14}$ at 892 °C. The calculations agreed with the experimental observations regarding the primary phase (TiSi isomorphous with HfSi) but could not account for the formation of the TM_5Si_4 and DO22- Al_3TM tri-aluminide.

The following path was calculated for the top of MG5: Solidification starts at 1998 °C with $\text{L} \rightarrow \text{L} + \text{Ti}_5\text{Si}_3$, then $\text{L} \rightarrow \text{Ti}_5\text{Si}_3 + \text{Nb}_5\text{Si}_3$ at 1761 °C, then $\text{L} + \text{Ti}_5\text{Si}_3 \rightarrow \text{Nb}_5\text{Si}_3 + \text{HfSi}$ at 1456 °C, then $\text{L} + \text{HfSi} \rightarrow \text{Nb}_5\text{Si}_3 + \text{Ti}_3\text{Al}_2\text{Si}_5$ at 1299.88 °C, then $\text{L} \rightarrow \text{Nb}_5\text{Si}_3 + \text{Ti}_3\text{Al}_2\text{Si}_5$ at 1299.87 °C, then $\text{L} + \text{Nb}_5\text{Si}_3 \rightarrow \text{Ti}_3\text{Al}_2\text{Si}_5 + \text{DO22-Al}_3\text{X}$ at 1189 °C, then $\text{L} + \text{DO22-Al}_3\text{X} \rightarrow \text{Ti}_3\text{Al}_2\text{Si}_5 + \text{fcc-Al}$ at 663.4 °C, then $\text{L} \rightarrow \text{fcc-Al}$ at 663.38 °C, with the last step in the solidification path fcc-Al at 657 °C. The calculations agreed with the experimental observations regarding the primary phase, TiSi and the DO22- Al_3TM tri-aluminide but could not account for the formation of the TM_5Si_4 phase.

The calculated solidification paths would suggest that the cast microstructure of the alloy MG5 was very sensitive to melt composition, even though there were not very large differences in Al+Si and Si/Ti between the different parts of the ingot. This was not supported by the experimental results.

The microstructure of MG5-HT800 consisted of the hexagonal $\gamma\text{Nb}_5\text{Si}_3$, the aluminides TiAl and Al_3TM and the silicides Ti_5Si_4 and TiSi. Compared with the cast alloy, the TiAl was the new phase to form, which would suggest that the latter is stable in MG5. The solubilities of Si and Al respectively in TiAl and Ti_5Si_4 were in agreement with the literature (Bulanova et al, 2004, Park et al, 2007) but the solubility of Al in TiSi was higher than that reported in Park et al (2007). The solubilities of Al, Hf and Ti in the 5-3 silicide were in agreement with the literature.

Figure 85 shows the positions of the average MG5-HT800 compositions in two Ti-Si-Al isothermal sections at 700 °C, the closest available to 800 °C. In figure 85a the overall average alloy composition is in the two phase Ti_5Si_3 and Al_3Ti area and in figure 85b is near the three phase Ti_5Si_3 , Al_3Ti and $\text{Al}_{28}\text{Ti}_{12}$ area. For the average compositions in the top, bulk and bottom in both parts of figure 85 the alloy falls in the three phase Ti_5Si_3 , Ti_5Si_4 and Al_3Ti area.

The microstructure of MG5-HT1200 consisted of the hexagonal $\gamma\text{Nb}_5\text{Si}_3$, the aluminides TiAl and Al_3TM and the silicides Ti_5Si_4 and TiSi. Compared with the cast alloy, the TiAl was the new phase to form, and considering the results for MG5-HT800 it was concluded that the TiAl indeed is stable in MG5. This conclusion is supported by the 1200 °C isothermal section for Ti-Al-Si in figure 86a, which shows that the

overall average alloy composition falls in the three phase Ti_5Si_3 , $TiAl$ and Al_3Ti area and is close to the area of the same three phases in figure 86b. Equilibrium between Ti_5Si_3 , $TiSi$ and Al_3Ti is shown in figure 86a for top and bulk compositions and for the same compositions between Ti_5Si_3 , Ti_5Si_4 and Al_3Ti in figure 86b. The Al and Si concentrations respectively in Ti_5Si_4 and $TiSi$ and $TiAl$ were closer with those reported in the literature.

A characteristic feature of the microstructures of the alloy MG5 observed in the cast, heat treated and oxidised conditions was the fibrous nature (structure) of Ti_5Si_4 , see figure 68a, figure 71b, figure 73b and figure 83. Similar structure for Ti_5Si_4 has been reported by Gupta (2003) and Park et al (2007). Gupta also described it as “wool like” and observed it in Ti-Al-Si diffusion couples air cooled after annealing at 800 °C or 900 °C for 3 or 6 h. In the couples studied by Gupta the fibrous Ti_5Si_4 “grew” towards (“was over”, “formed in a matrix of”) Al_3Ti and was on top of (“sitting on”) Ti_5Si_3 that exhibited a brighter contrast than Ti_5Si_4 . The average Al concentration in Ti_5Si_4 given by Gupta (2003) was approximately 7.5 to 8 at%, and is higher than the average Al concentrations analysed in this research, see table 20, table 21, table 22, table 23, table 25 (in the oxidised MG5 specimens at 800 and 1200 °C the maximum Al values, respectively were 7 and 8.9 at%).

Park et al (2007) also reported about the formation of Ti_5Si_4 in diffusion couples annealed at 1100 °C for ≥ 200 h. They studied two couple types, one between $TiAl$ and $TiSi_2$ (type A, our notification) and the other $TiAl/Ti/TiSi_2$ (type B, our notification). The type A and type B couples were referred to by Park et al (2007) respectively as “direct interface reaction” and “biased interface reaction” couples. In the type A couple

the sequence of phases was TiAl/TiAl₂/Ti₂Al₅/TiAl₃+Ti₅Si₄/Ti₅Si₄/TiSi/TiSi₂, i.e., the Ti₅Si₃ silicide did not form. The Ti₅Si₄ formed its own irregular “thick porous” layer and in the Ti₅Si₄ the solubility of Al was < 2 at%. It should be noted that in this work the average Al concentrations in the Ti₅Si₄ in the cast and heat treated (800 and 1200 °C) alloy were ≤ 2 at% (see table 20, table 21 and table 22). The Ti₅Si₄ also grew a columnar (fibrous in Gupta’s terminology) morphology through TiAl₃ (see sequence given above) and for this growth morphology, according to Park et al (2007), the rate-limiting component was Ti ($D_{Ti(Al_3Ti)} < D_{Si(Ti_5Si_4)}$), where D_i is diffusivity of species i (= Si, Ti) in the indicated intermetallic).

In the type B couple the porous Ti₅Si₄ did not develop but the Ti₅Si₃ silicide formed. The sequence of phases was TiAl/Ti₃Al/Ti/Ti₃Si/Ti₅Si₃/Ti₅Si₄/TiSi/TiSi₂. In the Ti₅Si₃ the Al concentration was about 5 at%, double the average Al concentrations measured in this work in hexagonal 5-3 silicide in the cast, heat treated and oxidised alloy, see table 20, table 21, table 22, table 23 and table 25. The Al concentration in Ti₅Si₄ was the same as in the type A couple. Park et al (2007) suggested that in type A the Ti flux was not enough for the formation of Ti₅Si₃.

In this work in the alloy MG5 the Ti₅Si₄ was observed in the cast, heat treated and oxidised alloy to be in contact with Ti₅Si₃ (also observed by Gupta, 2003), with TiSi (also observed by Park et al (2007) in their type A couple), and with TiAl₃ (also observed by both Gupta and Park et al) in which it formed a fibrous (columnar, wool like) structure (also observed by both Gupta and Park et al). The formation of Ti₅Si₄ and the other phases was accompanied by partitioning of solute during solidification (see above) and solid state cooling of the ingot, during heat treatment and during the

oxidation experiments. Porosity was not observed in any of the microstructures. Thus, on the basis of the results of this work and their comparison with those of Gupta (2003) and Park et al (2007), it is concluded that in the alloy MG5 the Ti_5Si_4 formed and grew with a fibrous (columnar, wool like) morphology towards Al_3TM and that its growth was not accompanied by the formation of porosity.

In the 5-3 silicide cracks were observed growing from one side of a grain to the other and often these cracks were parallel to each other, see figure 68a, figure 71a and figure 71b. In the cracked 5-3 silicide grains “lines” (sometimes curved) of darker contrast were observed after the heat treatment at 800 °C (figure 4b) and 1200 °C (figure 73b). In the heat treated microstructure at 1200 °C the growth of 5-4 towards Al_3TM was noticeable (see above discussion, also Park et al reported that the growth rate of Ti_5Si_4 is higher than that of $TiSi$, Al_3Ti and Al_2Ti (decreasing growth rate sequence) with Ti_2Al_5 having the lowest growth rate from the aforementioned intermetallics) and the 5-3 silicide grains were also “partitioned” in separate (sub?) grains with a structure that resembled the fibrous structure of Ti_5Si_4 . Furthermore, inside the 5-3 grains there was evidence of precipitation of a second (mostly) equiaxed phase(s?) (figure 73a) that exhibited a dark contrast.

In the alloy MG5 oxidised at 800 °C (see figure 76c) cracks were observed in 5-3 grains growing from one side to the other and parallel to each other, and “lines” of darker contrast that were thicker than the lines observed in the heat treated specimen, as well as second (mostly) equiaxed phase(s?) that exhibited a dark contrast. In the alloy oxidised at 1200 °C the same observations were made plus the “partitioning” of 5-3 grains in separate (sub?) grains with a structure the resembled the fibrous structure of

Ti_5Si_4 and the growth of the fibrous Ti_5Si_4 was more pronounced than at 800 °C and the heat treated alloy (see figure 82b). The structures inside the 5-3 silicide grains that resembled the fibrous structure of Ti_5Si_4 were parallel to each other.

In all conditions the cracking of 5-3 silicides was attributed (a) to the enhanced anisotropy of coefficient of thermal expansion with partitioning of Ti in the 5-3 silicide (Papadimitriou et al, 2017) and (b) to the large volume changes at the interfaces where the Ti_5Si_4 was formed (Park et al, 2007). The precipitation of second equiaxed phase(s?) in 5-3 grains could be attributed to their contamination by oxygen, based on the results of Tweddle (2015) and Bywater (2017). The “partitioning” of 5-3 grains by Ti_5Si_4 like growths is more difficult to explain. The dark contrast in between the fibrous Ti_5Si_4 was the same as that exhibited by the tri-aluminide, but owing to the size of the grown features the latter could not be confirmed. Considering the fact that the latter (i.e., Ti_5Si_4 like features) had 5-3 silicide on either side, that Ti_5Si_3 , Ti_5Si_4 and Al_3Ti can be at equilibrium at 700 °C (figure 85) and 1200 °C (figure 86b), that the darker contrast of the lines observed inside 5-3 grains would arise from Ti rich (most likely) and/or Al rich areas (formed owing to partitioning of aforementioned solutes in 5-3 silicides, formation of $(Ti,Nb)_5Si_3$ in the oxidised alloy at 1200 °C, see table 25) and that Ti rich areas would have increased the Ti flux in the diffusive phenomena occurring at the two temperatures (conditions resembling (?) those in the type B couple of Park et al, 2007) it is suggested that the Ti_5Si_4 like growths formed in Ti rich areas inside the 5-3 silicide. The parallel nature of these growths could be attributed to some kind of prior subgrain formation (polygonisation(?)) in 5-3 grains caused by recovery mechanisms linked with the strain energy from the enhancement of anisotropy with the partitioning of Ti in 5-3

grains (see above) with the enhanced diffusion along the sub-grain walls promoting the three phase equilibria (see above).

Agreement and/or disagreement with the literature regarding the Al concentration in Ti_5Si_4 and 5-3 silicides was discussed above. The solubility of Si in Al_3TM (less than 3 at% in the cast alloys MG2, see previous chapter, and MG5, see table 20, and even lower in the heat treated alloys MG2 (less than 1 at%, see previous chapter), and MG5 (less than 3 at%) and oxidised MG5 at 800 °C (less than 3 at%) is in agreement with Bulanova et al (2004), lower than range reported by Park et al (up to 7 at%) and significantly lower than the values reported by Gupta (9.2 to 14.3 at%). There are no reports about the solubility of Al in TiSi in higher order systems than the ternary Ti-Al-Si where it is suggested to be very low or negligible (Bulanova et al, 2004, Park et al 2007). However, the 700 °C and 1200 °C isothermal sections for the Ti-Al-Si system by Perrot show solubility of Al in TiSi (about 10-12 at% at 700 °C and about 5-7 at% at 1200 °C). In this work, the solubility of Al in the intermetallic that has been identified as TiSi on the basis of the XRD (figure 69, figure 72, figure 74, figure 81a) and EDS data (table 20, table 21, table 22, table 23, table 25) was not negligible and was about 16.7 at% at 800 °C (table 21) and 12.2 at% at 1200 °C (table 22).

The oxidation behaviour of the alloy MG5 at 800 and 1200 °C was exceptional. The alloy did not pest at 800 °C, it did not oxidise catastrophically at 1200 °C, in both temperatures it formed a thin and adherent scale which did not spall off at all at 1200 °C and during subsequent handling of the oxidised specimen, and alumina scale was formed in both temperatures.

The alloy MG5 was rich in Al, Si and Ti and thus we were interested to find out whether alumina and/or silica can form and what role is played by Ti oxide(s). It was anticipated, on the basis of earlier research on the oxidation of “typical” Nb silicide based alloys (meaning alloys like Nb-24Ti-18Si-5Al-5Cr-5Hf with/out refractory metal additions, Zelenitsas and Tsakirooulos, 2006, Geng et al., 2006) that scale(s) containing Ti niobates and possibly silica will form.

Formation of a dense and continuous scale of alumina or silica on an alloy requires (necessary but not sufficient condition) the oxide to be the most stable of all possible oxides. Figure 87 shows that for the Ti/TiO and Al/Al₂O₃ oxygen equilibrium pressures are very close and that the former is several orders lower than the oxygen equilibrium pressure for Si/SiO₂, meaning that SiO₂ can be reduced by Ti (unity activities, as shown in the figure) and not form a stable protective scale.

The microstructure of the alloy oxidised at 800 °C consisted of the same phases as MG5-HT800, namely hexagonal γ Nb₅Si₃, the tri-aluminide Al₃TM and the silicides Ti₅Si₄ and TiSi, and the new phases Ti₂Al₅, Ti(Al,Si)₂, TM₂Si_{1.5}Al and TM₈Al₁₁Si₃. The latter four (new) phases and the absence of TiAl are attributed to changes in phase equilibria due to contamination by oxygen during the oxidation experiment (Hf scavenged oxygen to form HfO₂) and the consumption of Al to form alumina scale (the aluminides in the microstructure of MG5 can be in equilibrium with alumina, see figure 88), the latter supported by the formation of Ti₂Al₅, an aluminide slightly leaner in Al than the tri-aluminide.

The oxides formed on MG5 at 800 °C, namely Ti niobates, TiO₂, Nb₂O₅, TiAl₂O₅ and HfO₂ (see figure 77b, figure 78 and table 24), are consistent with the literature on Nb silicide based alloys (Zelenitsas and Tsakirooulos, 2006, Geng et al., 2006) and the oxidation of alloys of the Ti-Al system, given that in the Ti-Al-O system at 700 and 900 °C the stable oxide changes from TiO₂ to Al₂O₃ for Al rich aluminides such as TiAl and Al₃Ti (Rahmel and Spencer, 1991). The possible presence of TiAl₂O₅, suggested by the glancing angle XRD, contradicts Rahmel and Spencer (1991), who reported that this ternary oxide becomes stable around 1010 °C. Figure 88b shows that this oxide can be in equilibrium with TiO₂ at 945 °C.

No silica was observed in the scale formed on MG5 at 800 °C (figure 77b, figure 78). According to Rahmel and Spencer (1991), in the Ti-Si-O system a comparable (with the Ti-Al-O system) change from Ti-oxide to SiO₂ occurs at 800 °C for Si rich silicides from the right of Ti₅Si₃ to Si in the Ti-Si binary, i.e., in the areas Ti₅Si₃ - Ti₅Si₄, Ti₅Si₄-TiSi, TiSi-TiSi₂, TiSi₂-Si), while for Ti₅Si₃ and lower Si concentrations (Ti₅Si₃ (this silicide has a solubility range), Ti₅Si₃-Ti₃Si, Ti₃Si-Ti) the TiO is the stable oxide. TiO, Ti₂O₅ and the Ti_xO_{2x-1} Magnelli phases oxidise rapidly to form TiO₂. The fact that no SiO₂ was observed in the scale of MG5 at 800 °C would suggest that in the Nb-Ti-Si-Al-Hf-O system the stability of TiO₂ over SiO₂ was increased, probably because the Ti₅Si₄ and TiSi were present in the microstructure at a lower volume fraction than the hexagonal 5-3 silicide.

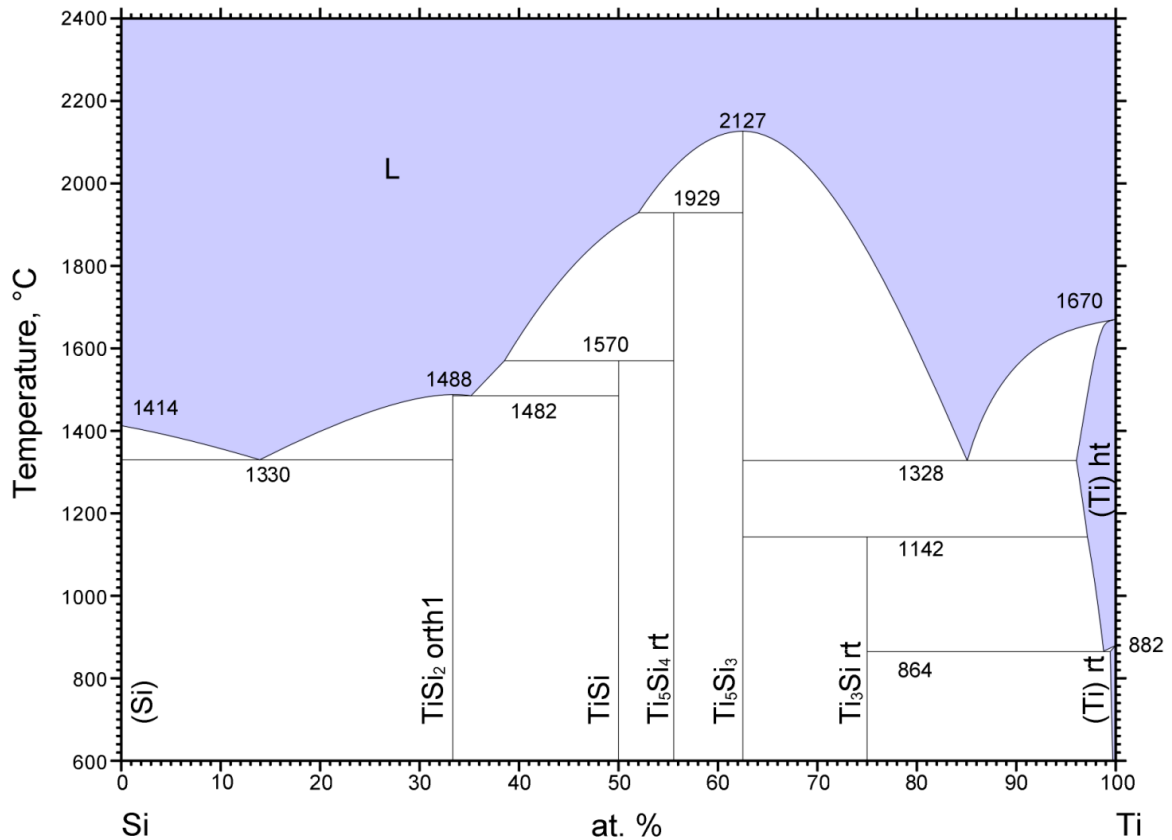


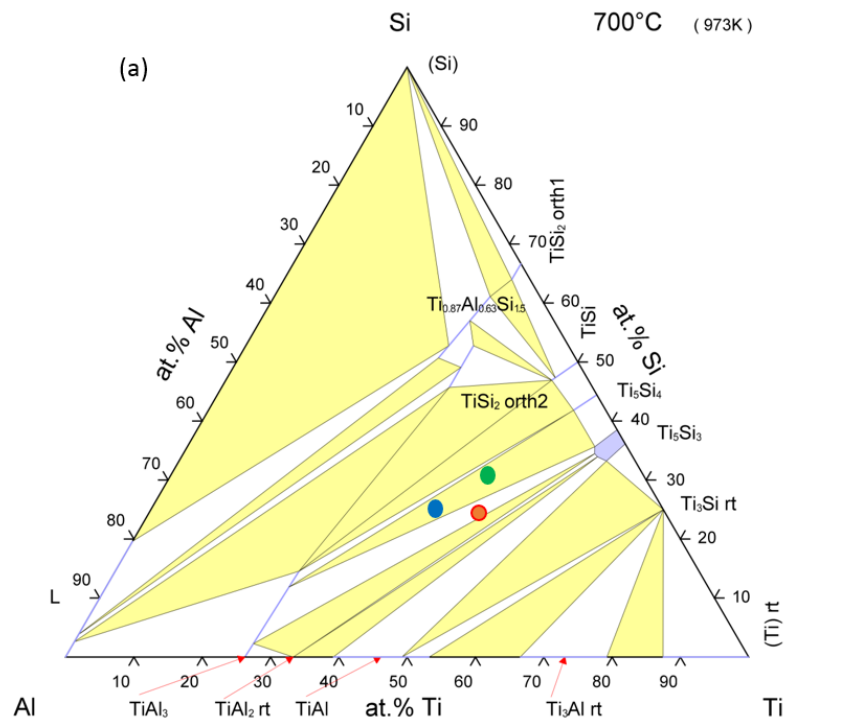
Figure 84: Ti-Si binary system (Yang et al, 2007)

The microstructure of the alloy oxidised at 1200 °C consisted of the same phases as MG5-HT1200, namely hexagonal $\gamma(\text{Nb,Ti})_5\text{Si}_3$, the tri-aluminide Al_3TM and the silicides Ti_5Si_4 and TiSi , and the new phases hexagonal $(\text{Ti,Nb})_5\text{Si}_3$, Ti_2Al_5 and $\text{TM}_2\text{Si}_{1.5}\text{Al}$. The TiAl that was observed in MG5-HT1200 was not confirmed by EDS analyses in the oxidised specimen but there were peaks corresponding to TiAl in the XRD data of the latter, see figure 81. The XRD also indicated the presence of Al_2Ti and Al_3Ti , which was not confirmed by EDS, but the EDS suggested the Ti_2Al_5 (table 25) which was not observed by XRD (figure 81). Careful consideration of the data in table 25, however, shows a high standard deviation for Al in the phase with average composition Ti_2Al_5 , an aluminide very close to Al_2Ti and Al_3Ti and it is possible that some of the Al lean analyses correspond to Al_2Ti and some of the rich ones to Al_3Ti . The new phases in the microstructure of MG5 oxidised at 1200 °C were attributed to

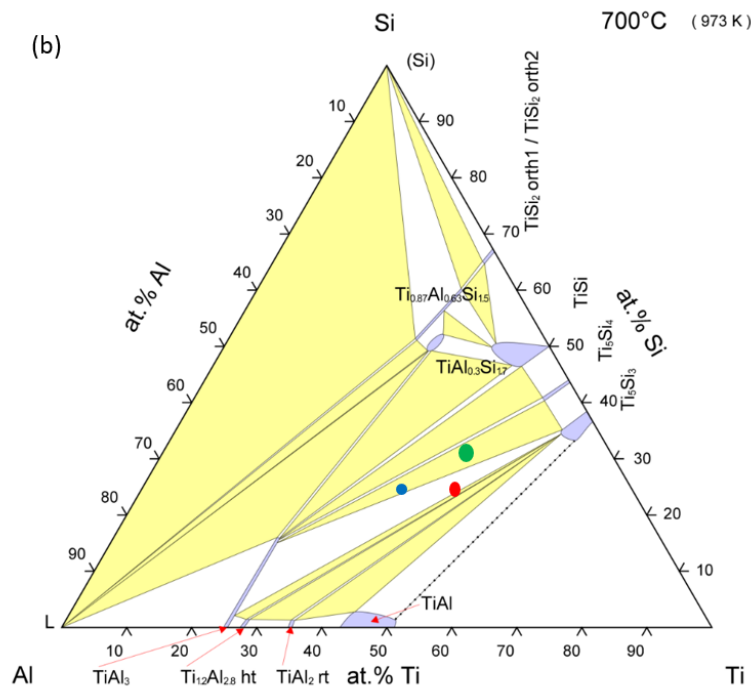
changes in phase equilibria due to contamination by oxygen during the oxidation experiment (Hf scavenged oxygen to form HfO_2) and the consumption of Al to form alumina scale (the aluminides in the microstructure of MG5 can be in equilibrium with alumina), the latter supported by the formation of Ti_2Al_5 (also observed in MG5 oxidised at 800 °C, an aluminide slightly leaner in Al than the tri-aluminide).

The oxides formed on MG5 at 1200 °C, namely Ti niobates, TiO_2 , Nb_2O_5 and HfO_2 , and SiO_2 , $\alpha\text{Al}_2\text{O}_3$, TiAl_2O_5 and TiO (see figure 81b, figure 83 and table 26), are consistent with the literature on Nb silicide based alloys (Zelenitsas and Tsakirooulos, 2006, Geng et al., 2006) and the oxidation of alloys of the Ti-Al and Ti-Si binary systems. Indeed, in the Ti-Al-O system at 1100 °C the stable oxide changes from TiO_2 to Al_2O_3 for Al rich aluminides such as TiAl, TiAl_2 , Ti_2Al_5 and TiAl_3 and in the Ti-Si-O system at 1300 °C a change from Ti-oxide to SiO_2 occurs for Si rich silicides to the right of Ti_5Si_3 in the Ti-Si binary (see above) (Rahmel and Spencer, 1991). In the microstructure of MG5 oxidised at 1200 °C the volume fraction of TiSi was higher compared with the cast alloy, the heat treated alloy at 1200 °C and the alloy oxidised at 800 °C and the Si+Al content of the $(\text{Ti,Nb})_5\text{Si}_3$ (new phase) was higher than that of the $(\text{Nb,Ti})_5\text{Si}_3$ silicide (respectively 41.1 and 36.3). There was “significant” $(\text{Ti,Nb})_5\text{Si}_3$ (new phase) in the microstructure, but owing to contrast difficulties it was not possible to differentiate between the fractions of this phase and $(\text{Nb,Ti})_5\text{Si}_3$. Considering that the solubility range of Ti_5Si_3 is 35.5 to 39.5 at%Si, the $(\text{Ti,Nb})_5\text{Si}_3$ (new phase) falls to the right of the 5-3 silicide (in the Ti_5Si_3 - Ti_5Si_4 area) and thus according to Rahmel and Spencer should be expected to form SiO_2 . The fact that TiO_2 , TiO and SiO_2 were observed in the scale of MG5 at 1200 °C would suggest that in this alloy the TiO_2 and TiO were still stable at 1200 °C. The glancing angle XRD also suggested the presence

of TiAl_2O_5 . According to Rahmel and Spencer, this ternary oxide is stable above 1010 °C.

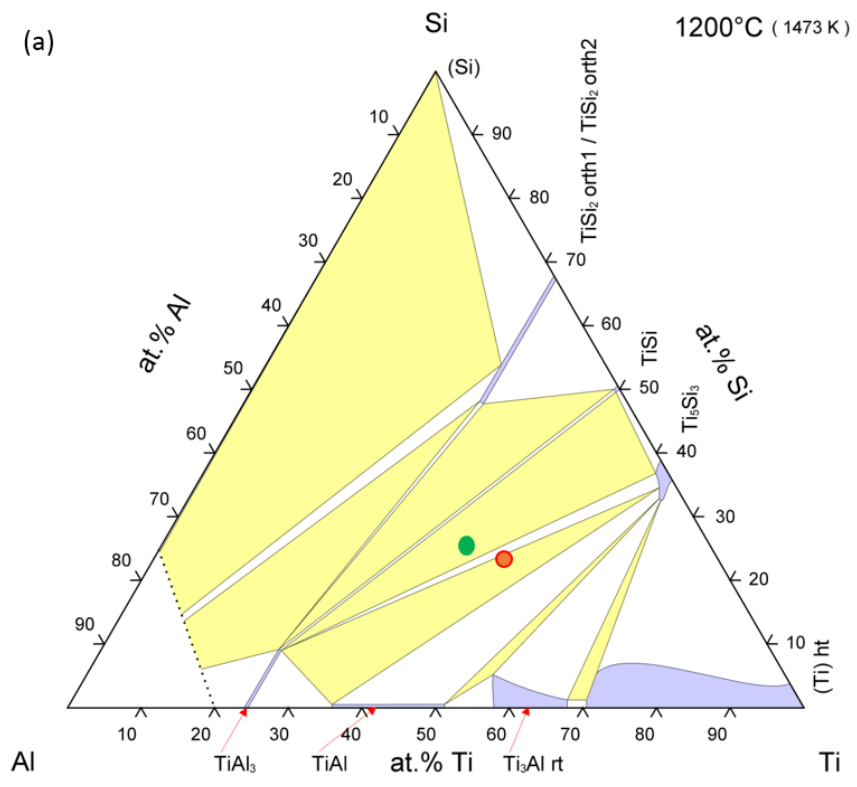


© ASM International 2007. Diagram No. 1300218

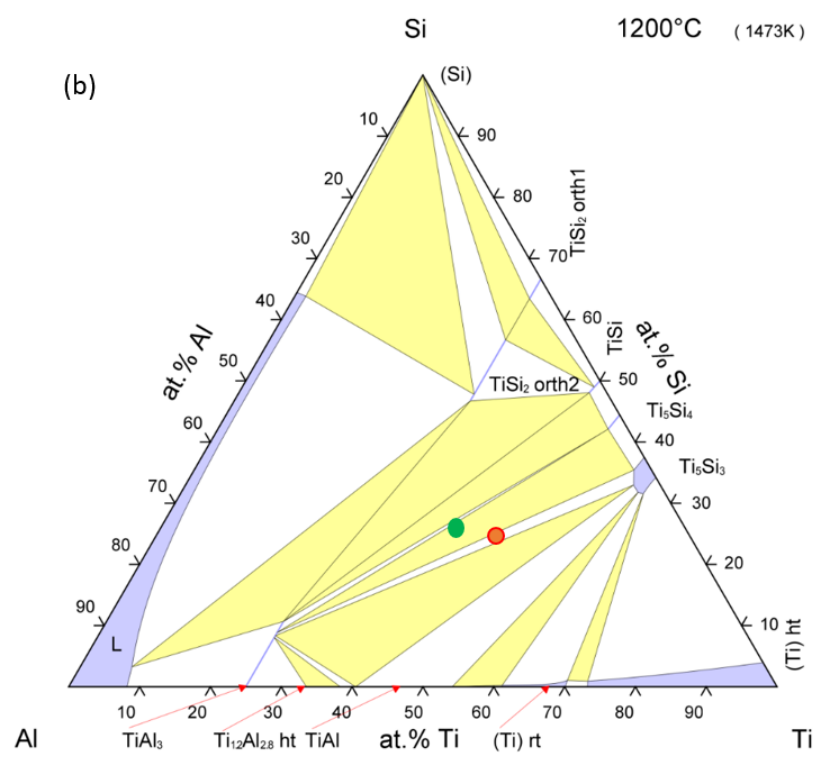


© ASM International 2006. Diagram No. 976532

Figure 85: Ti-Al-Si isothermal sections at 700 °C from (a) Perrot, (b) Raman, Red is for the overall average alloy composition, green is for that in the top, and blue for the bottom and bulk



© ASM International 2006. Diagram No. 976531



© ASM International 2007. Diagram No. 1300217

Figure 86: Ti-Al-Si isothermal sections at 1200 °C from (a) Schob, (b) Perrot, red for overall and bottom compositions, green for top and bulk

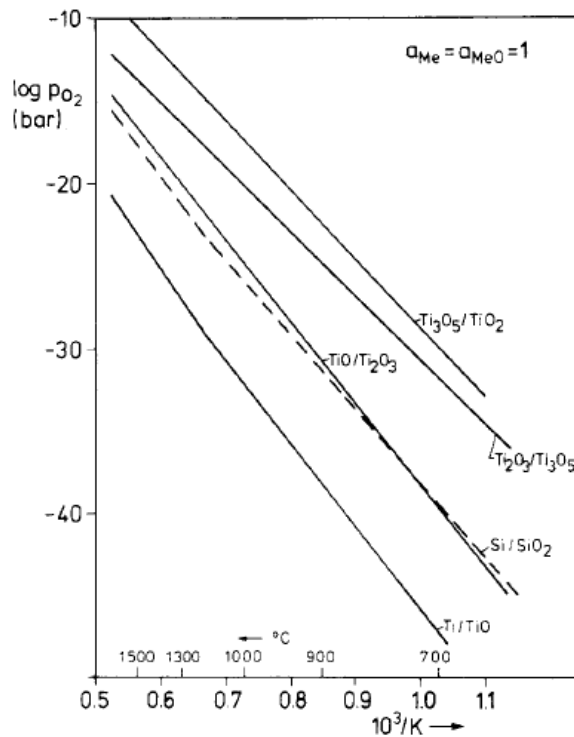
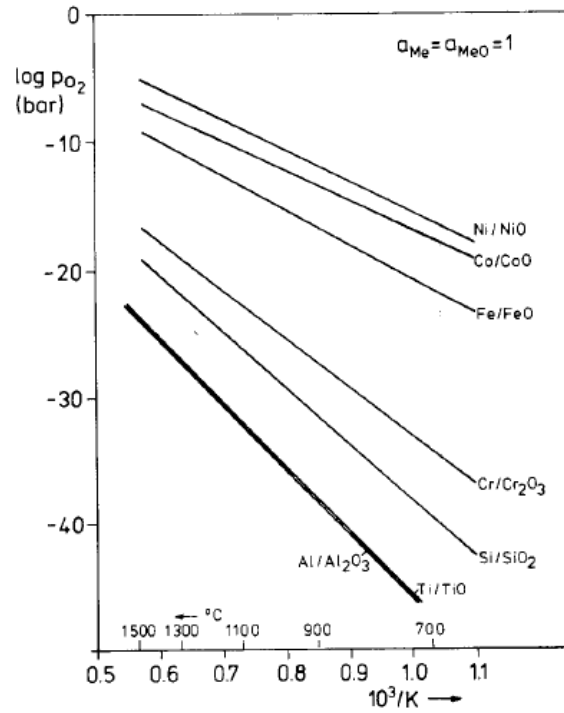


Figure 87: Oxygen equilibrium pressures (a) of pure metal X/oxide systems (X=Al, Co, Cr, Fe, Ni, Si, Ti) and (b) the Si-O and Ti-O systems (Rahmel and Spencer, 1991).

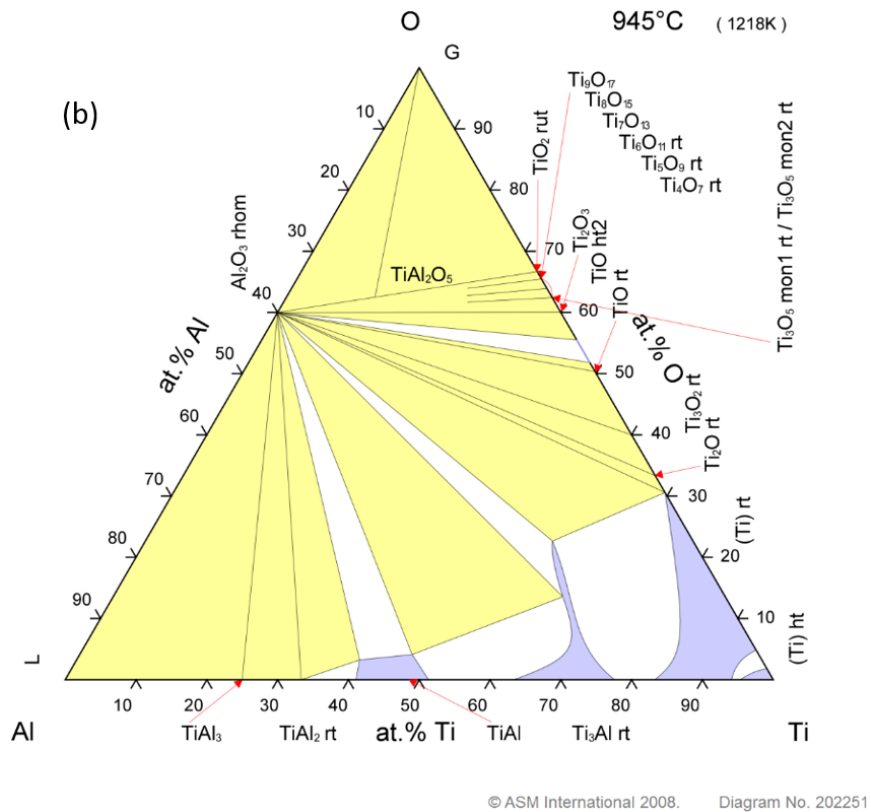
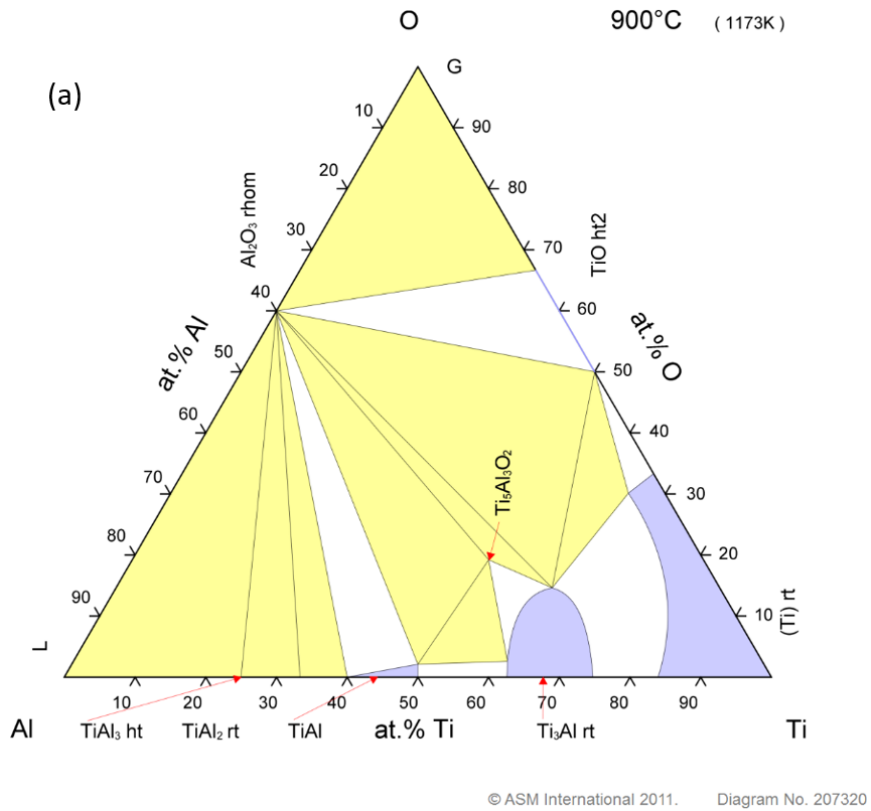


Figure 88: Isothermal sections of Ti-Al-O (a) at 900 °C by Zeng (1995), (b) 945 °C by Kelkar (1995). In (b) Magnelli phases in equilibrium with alumina are indicated

5.1.5 Summary

There was macrosegregation of Al, Si and Ti in the alloy MG5, with more severe macrosegregation of Al compared with the alloy MG2. The ingot of the alloy MG5 was very brittle. The same phases were present in all parts of MG5-AC, namely $\gamma\text{Nb}_5\text{Si}_3$ (primary phase), Ti_5Si_4 , TiSi and Al_3TM tri-aluminide. The microstructure was finer in the bottom of the ingot. The volume fraction of Al_3TM was higher in the top and the volume fractions of the 5-3 and 5-4 silicides were higher in the bulk of MG5-AC, owing to the strong macrosegregation.

The microstructures of the heat treated alloy at 800 °C and 1200 °C, MG5-HT800 and MG5-HT1200, exhibited chemical inhomogeneity for Al, Si and Ti and consisted of the hexagonal $\gamma\text{Nb}_5\text{Si}_3$, the aluminides TiAl and Al_3TM and the silicides Ti_5Si_4 and TiSi . The 5-4 silicide formed a fibrous (wool like) structure growing towards Al_3TM . The TiAl was a stable phase in MG5 but not the Nb_{ss} .

The oxidation behaviour of the alloy MG5 at 800 and 1200 °C was exceptional. The alloy did not pest at 800 °C, it did not oxidise catastrophically at 1200 °C, in both temperatures it formed a thin and adherent scale which did not spall off at all at 1200 °C and during subsequent handling of the oxidised specimen, and alumina scale was formed in both temperatures.

The microstructure of the alloy oxidised at 800 °C consisted of the same phases as MG5-HT800, namely hexagonal $\gamma\text{Nb}_5\text{Si}_3$, the tri-aluminide Al_3TM and the silicides Ti_5Si_4 and TiSi , and the new phases Ti_2Al_5 , $\text{Ti}(\text{Al},\text{Si})_2$, $\text{TM}_2\text{Si}_{1.5}\text{Al}$ and $\text{TM}_8\text{Al}_{11}\text{Si}_3$.

The oxides formed on MG5 at 800 °C were Ti niobates, TiO₂, SiO₂, Nb₂O₅, TiAl₂O₅ and HfO₂.

The microstructure of the alloy oxidised at 1200 °C consisted of the same phases as MG5-HT1200, namely hexagonal $\gamma(\text{Nb,Ti})_5\text{Si}_3$, the tri-aluminide Al₃TM and the silicides Ti₅Si₄ and TiSi, and the new phases hexagonal (Ti,Nb)₅Si₃, Ti₂Al₅ and TM₂Si_{1.5}Al. The oxides formed on MG5 at 1200 °C were Ti niobates, TiO₂, Nb₂O₅ and HfO₂, and SiO₂, $\alpha\text{Al}_2\text{O}_3$, TiAl₂O₅ and TiO.

At both oxidation temperatures there was contamination of the phases with the contamination of the 5-4 silicide being less severe than the Ti₂Al₅ aluminide. There was precipitation of second phase in contaminated 5-3 silicide grains. In the oxidised alloy at 1200 °C, a structure resembling fibrous Ti₅Si₄ formed inside 5-3 grains.

Chapter 6: The alloy Nb-23Ti-23Si-38Al-5Hf

6.1 Alloy Nb-23Ti-23Si-38Al-5Hf (MG6)

6.1.1 As cast

The nominal composition of this alloy is shown in table 27. The actual composition was determined by EDS and was Nb-22.7Ti-23.3Si-37.7Al-3.6Hf. This was the average of all EDS analyses taken from different parts of the ingot, see table 28. Even though the average concentration of the elements and the Al+Si sum were close to the nominal ones, the standard deviations were large, particularly for Ti, Al and Si, owing to the macrosegregation in the ingot.

Table 27: Nominal composition (at%) of alloy MG6-AC

Alloy	Nb	Si	Ti	Al	Hf
MG5	12	23	23	38	4

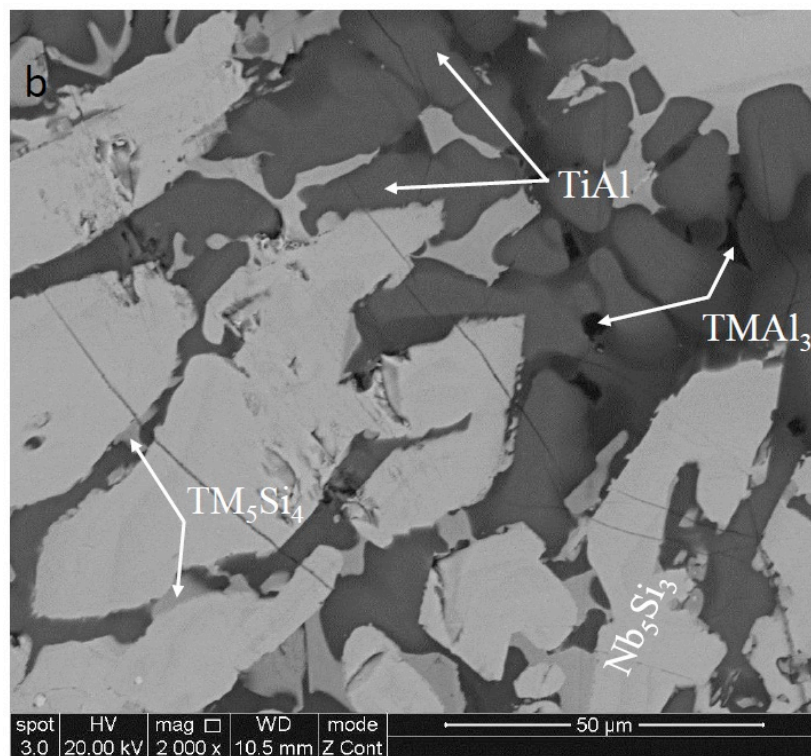
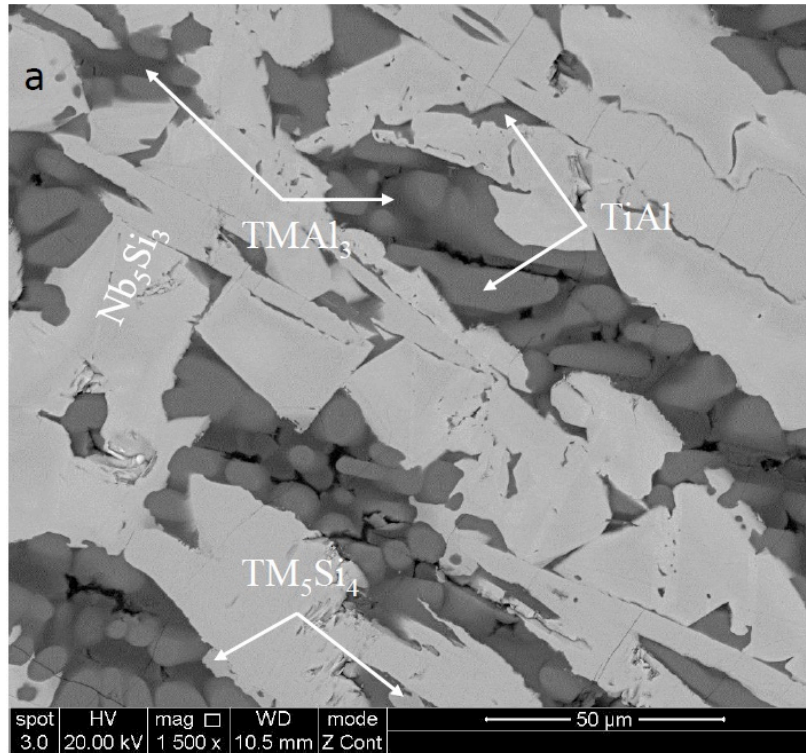
Indeed, the minimum and maximum concentration of Al, Si and Ti were 30.7 and 49.8 at% Al, 16.6 and 27.3 at% Si and 20.7 and 24.7 at% Ti, with the maximum and C_i^{Max} - C_i^{Min} difference in the bulk of the ingot, see table 28. This also resulted in significant variation in the concentration of Nb in the bulk of the ingot. The Al+Si concentration was lowest at the top, and highest in the bottom of the ingot, with the Al+Si content in the bulk essentially the same as in the nominal alloy composition. The same microstructure was observed in the top, bulk and bottom of MG6-AC. Typical microstructures are shown in figure 89. The white contrast phase is representative of the Nb₅Si₃ silicide type phase similarly to other alloys of this work. The darker white contrast or silver contrast phase is indicative of the Ti₅Si₄ silicide.

Table 28: EDS analysis data (at%) of the alloy MG6-AC

Area and phase analysis		Elements					
		Nb	Si	Ti	Al	Hf	Al+Si
Large area	Top	13.2±0.5 12.7-14.1	24.9±1.3 23.8-26.8	22.9±0.3 22.5-23.4	34.6±2 31.5-36.7	4.3±0.3 4-4.9	59.5
	Bulk	12.6±1.3 10.6-14.4	22.9±3.2 16.5-27.3	22.8±1.1 20.7-24.7	38.3±5.8 30.7-49.8	3.3±0.5 2.4-4	61.2
	Bottom	12.3±0.9 11.2-14.2	22.5±2 20.2-26	22.4±0.8 21.3-23.7	39.4±3.2 32.2-44	3.4±0.2 3-3.9	61.9
	Average	12.7±1 10.6-14.4	23.3±2.5 16.5-27.3	22.7±0.8 20.7-24.7	37.7±4.7 30.7-49.8	3.6±0.5 2.4-4.9	61
Phase (spot) analysis		Aluminides and silicide					
	Al ₃ TM	8.1±6.7 0.7-13.4	4.4±3 2.2-8	16.4±6.1 11.8-23.3	70.3±2.5 67.3-72.3	0.8±0 0.7-0.8	74.7
	Ti ₅ Si ₄	18.6	46.3	23.1	2	10	48.3
	TiAl	2.1	6.2	36.5	54.2	1	60.5
		5-3 silicide					
	γNb ₅ Si ₃	21.7±0.2 21.5-22	38.9±0.6 38.1-39.2	31.3±0.9 29.9-31.9	2.6±0.4 2.3-3.1	5.5±0.5 5-6.1	41.5

The dark contrast and the brighter dark or gray contrast are indicative of the TiAl₃ and TiAl type aluminides. It should be noted that the TiAl and TiAl₃ phases were extremely difficult to distinguish in the SEM using associated contrasts. The latter were almost similar to each other under backscatter imaging conditions. This was attributed to the fact that the TMAI₃ phase analyzed in this alloy has significant standard deviations for the Al, Nb, Si and Ti concentrations, see table 28. Thus, the identification of TiAl using EDS analysis was frustrated from the aforementioned complication. Based on the contrast exhibited by the microstructure in the SEM, four phases were identified. Owing to almost same contrasts exhibited by two of them, only one analysis was possible for each phase, as shown in table 28. The XRD data for the cast alloy is shown in figure 90. The XRD data indicated the presence of hexagonal Nb₅Si₃, tri-aluminide, TiAl, Ti₅Si₄ and TiSi. The EDS analysis confirmed the former four phases, but not the TiSi.

As we shall see when the heat treated microstructure will be discussed, the Ti_5Si_4 exhibited almost the same contrast as $TiSi$. Our search using EDS to find the latter silicide in MG6-AC did not manage to confirm its presence in the ingot. Thus, it was concluded that the microstructure of MG6-AC consisted of large bulky γNb_5Si_3 and the aluminides $TiAl$, Al_3TM , in between the 5-3 silicide grains. The Ti_5Si_4 formed on γNb_5Si_3 grains as thin layers, see figure 89. The EDS analysis data confirmed the XRD data according to which the Nb_5Si_3 phase was the hexagonal 5-3 silicide. According to the empirical Bewlay rule (Bewlay and Jackson, 2003), the $Nb/(Ti+Hf)$ ratio, which was below one, indicated the formation of hexagonal Nb_5Si_3 . Furthermore, the content of the 5-3 silicide was within the acceptable range reported for Nb_5Si_3 (Schlesinger et al, 1993).



Continued

Continued

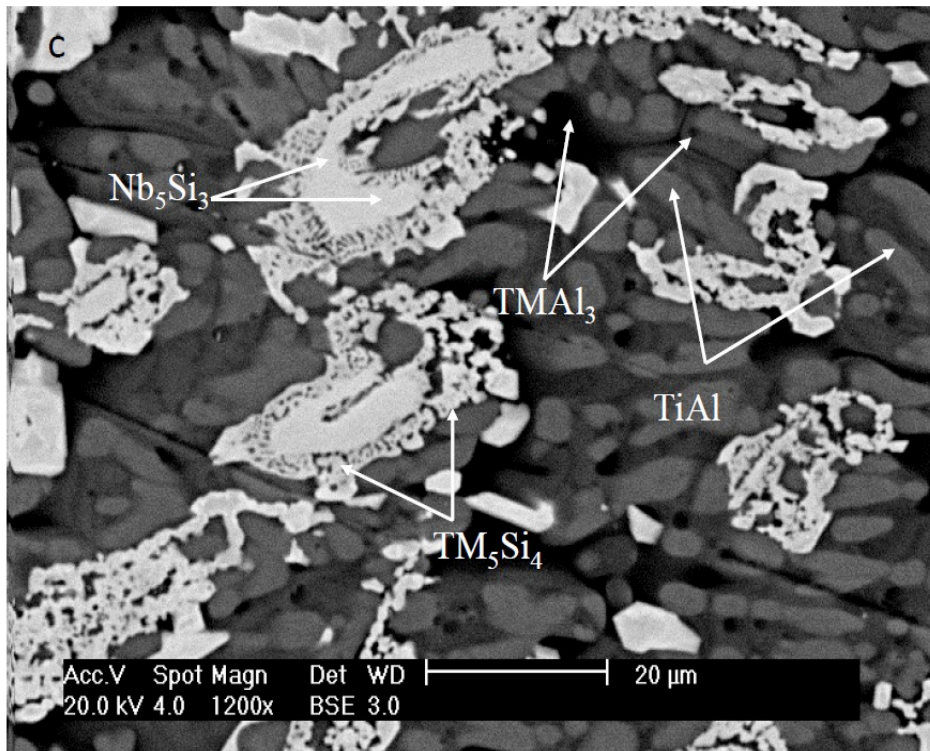


Figure 89: Backscatter electron images of the as cast alloy MG6 from (a) top, (b) bulk and (c) bottom

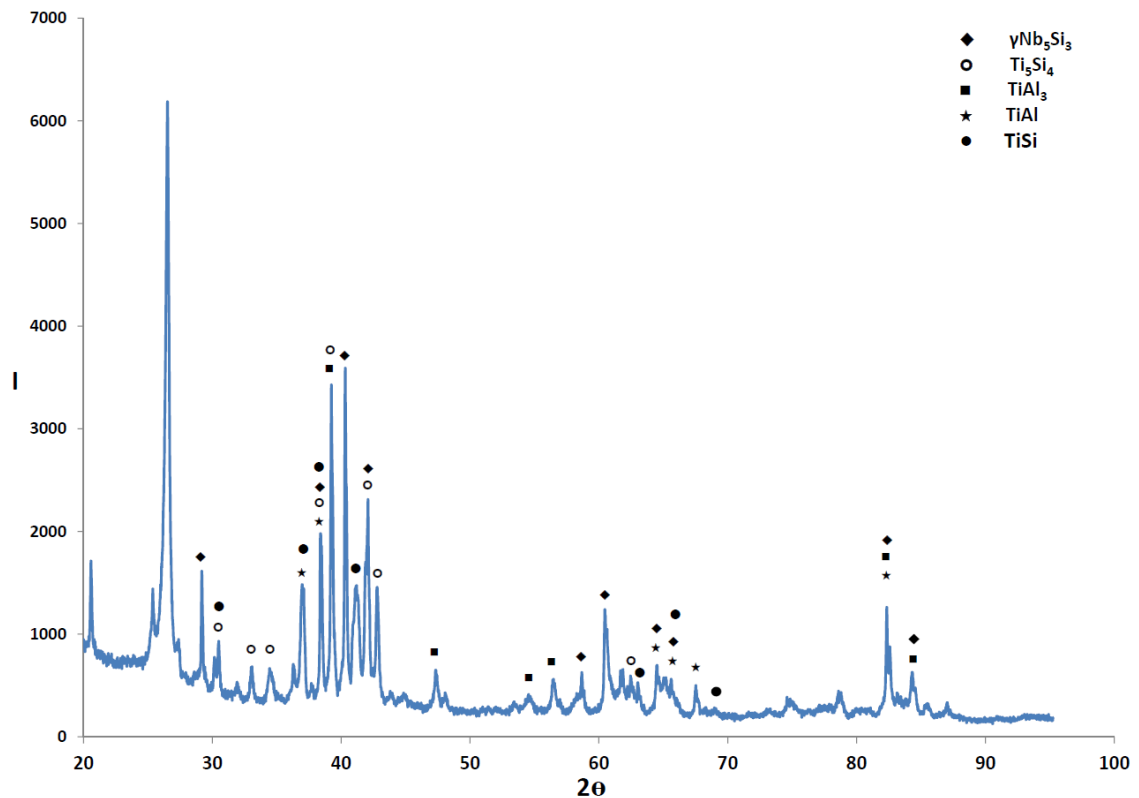


Figure 90: X-ray diffractogram of the alloy MG6-AC

6.1.2 Heat treated

The DSC trace for the alloy MG6 is shown in figure 91. The DSC trace on heating showed an exothermic reaction (transformation) at about 700 °C, which is accompanied by a small weight gain in the TG trace. Thus, the heat treatment at 800 °C, apart from considering the microstructure at a typical oxidation temperature, also aimed to establish of any new phase (s) formed in the microstructure. It should be accentuated that the heat treatment samples were wrapped in tantalum foil to avoid oxidation, and heat treated in a tube furnace, whereas the oxidation experiments were done in a muffle furnace without any protection in order for the samples to be oxidised. Oxidation experiments were also performed using TGA in order for the oxidation rate constant to be calculated - these have been discussed in section 6.1.3.

6.1.2.1 Heat treated at 800 °C

The alloy MG6 was heat treated at 800 °C for 100 h. The average composition of MG6-HT800 was Nb-22.9Ti-23.6Si-36.8Al-3.7Hf, see table 29. This was essentially the same (within experimental error) with that of MG6-AC and not significantly different than the nominal alloy composition. However, there was still significant chemical inhomogeneity in the microstructure, as shown by the standard deviations of Al, Nb, Si and Ti, see table 29.

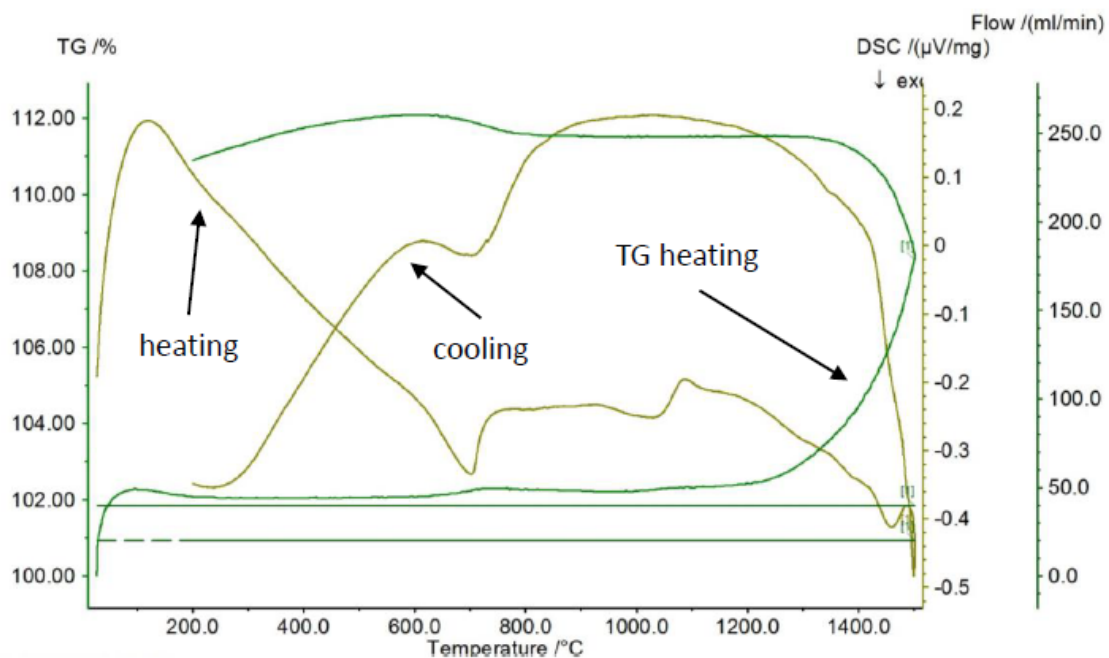


Figure 91: DSC trace of the alloy MG6

The microstructure of the MG6-HT800 is shown in Figure 92. Four different contrast phases can be seen, as was the case in MG6-AC, namely white, silver, grey and dark grey. The white contrast is indicative of the Nb₅Si₃ silicide and the silver contrast represents the Ti₅Si₄. The other two phases, meaning the dark and dark grey contrast ones, were in between the large bulky 5-3 silicide grains. The XRD data for the alloy is shown in figure 93. According to the XRD, the phases Ti₅Si₄, TiAl, TiAl₃, TiSi and

$\gamma\text{Nb}_5\text{Si}_3$ were present in the heat treated microstructure, the same as in the XRD of MG6-AC, see figure 90. The EDS analysis of phases had the same difficulties as in the cast alloy, owing to the similarities in contrast between the phases. The phases in MG6-HT800 according to the EDS data are given in table 29. The EDS analysis confirmed the presence of $\gamma\text{Nb}_5\text{Si}_3$ and the aluminides TiAl and Al_3TM and the silicide Ti_5Si_4 . One analysis with $\text{Al}+\text{Si} \approx 52$ at% is indicated as TiSi in table 29. It should be noted that the composition of this phase is similar to that identified as TiSi in the alloy MG5, and that the Al concentration is in agreement with that in the 700 °C isothermal section of Ti-Al-Si given by Perrot (2006). As we shall see in the next section, the TiSi was observed next to the Ti_5Si_4 and like the latter it was thin and not continuous. It is thus possible that there is analysis error in the Al concentration for TiSi in table 29. The EDS analyses taken from the microstructure between the large Nb_5Si_3 grains, i.e., the microstructures with dark and dark grey contrast, provided data that did not correspond to any of the phases indicated by XRD. This data is attributed to $\text{TM}_9\text{Si}_7\text{Al}_4$ intermetallic with $\text{Al}+\text{Si} \approx 55$ %. It is possible that some of the un-identified peaks in figure 93 correspond to this phase and that the exothermic reaction in the DSC trace at about 700 °C was due to its formation.

Table 29: EDS analysis data (at%) of the alloy MG6-HT (800 °C / 100 h)

Area and phase analysis		Elements					Al+Si
		Nb	Si	Ti	Al	Hf	
Large area	Top	12.6±2.7 6.6-16.1	23.4±3.2 17.5-28.5	23±0.9 22.4-25.1	37.2±6.7 25.8-49.8	3.7±0.5 2.6-4.5	60.6
	Bulk	13.3±1.4 10.8-15.1	23.9±3.2 17.4-27.6	22.7±1.1 20.5-24	36.2±6.1 28.7-48.3	3.8±0.5 2.9-4.5	60.1
	Bottom	13±2.1 10.9-16.8	23.6±4.5 19.3-31.8	22.8±1.9 21.3-26.6	36.9±9 20.1-45.2	3.7±0.5 3.2-4.7	60.5
	Average	13±2.1 6.6-16.8	23.6±3.4 17.4-31.8	22.9±1.3 20.5-26.6	36.8±6.9 20.1-49.8	3.7±0.5 2.6-4.7	60.4
Phase (spot) analysis		Aluminides and silicides					
	Al ₃ TM	8.1±4.6 0.5-13	3.9±1.8 2.3-9.6	16.7±4.9 11.2-25.1	70.3±2.2 62.8-71.8	1.1±0.3 0.6-1.5	74.2
	Ti ₅ Si ₄	10.8±6.6 2.7-18.8	44.1±3.8 38.4-46.3	35.7±5.3 31.3-42.9	3.2±2.2 1.4-6.5	6.1±1.8 3.9-8.1	47.4
	TiAl	0.7±0.7 0.2-1.3	3.2±0.9 2.5-3.8	34.2±3.5 31.8-36.7	61±1.3 60.1-61.9	0.8±0.6 0.4-1.2	64.2
	TM ₉ Si ₇ Al ₄	10.7±3.8 8.4-15	35±2.6 32.1-37.1	30.3±1.6 29.2-32.1	20.2±5.5 15.2-26.1	3.8±0.3 3.4-4.1	55.2
	TiSi	13.6	40.8	28.6	11	5.9	51.8
		5-3 silicide					
	γNb ₅ Si ₃	21.9±1.1 19.2-23	39.4±0.3 39.1-40.2	30.4±1 29.6-32.6	2.5±0.1 2.4-2.7	5.8±0.2 5.5-6.2	41.9

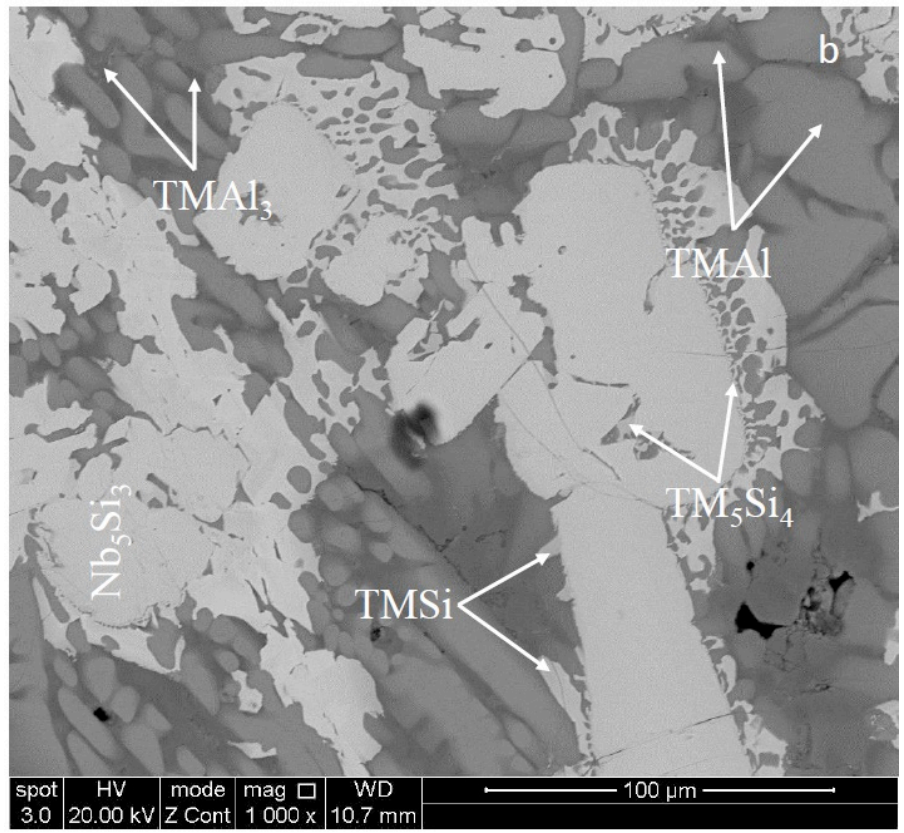
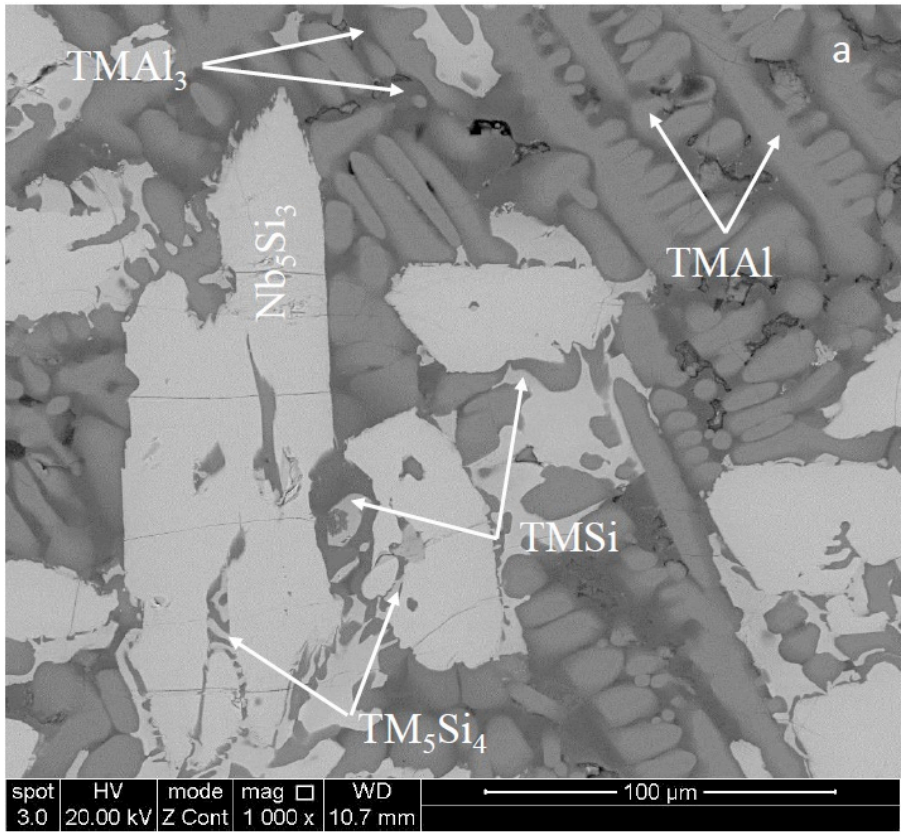


Figure 92: Backscatter electron images of the alloy MG6-HT800

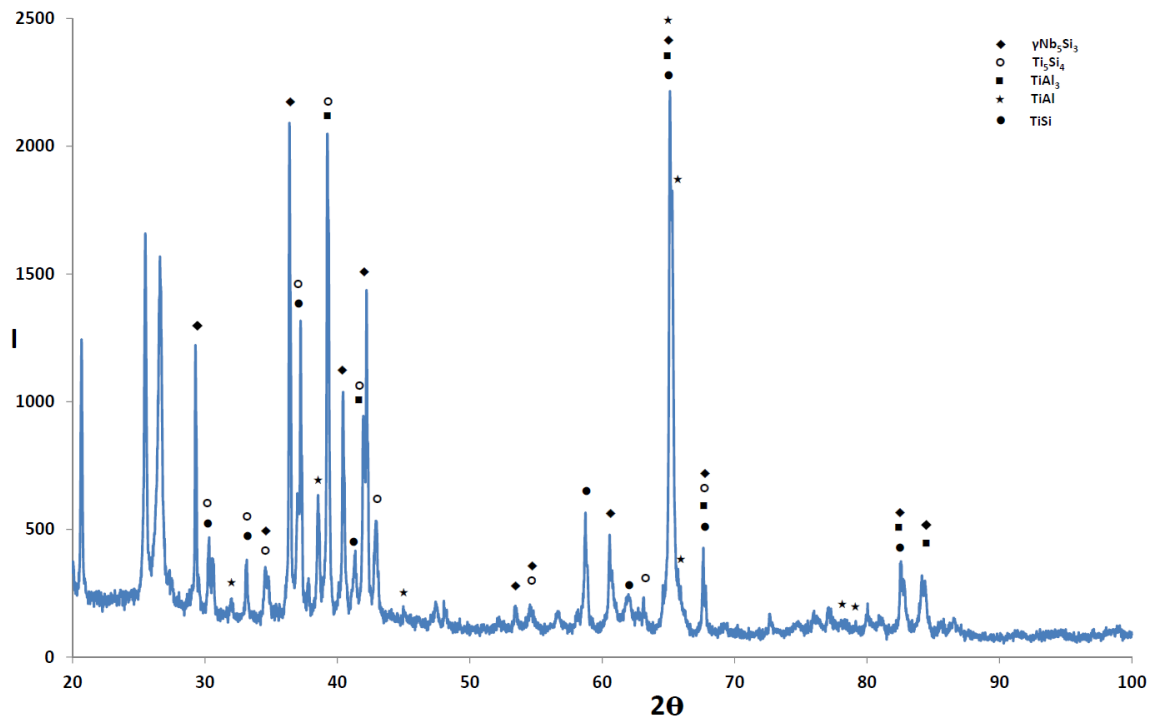


Figure 93: X-ray diffractogram of MG6-HT800

6.1.2.2 Heat treated at 1200 °C

The DSC trace of the alloy MG6 is shown in figure 91. There was an endothermic reaction at around 1100 °C and the corresponding TG trace indicated rapid weight gain after this temperature. There was no exothermic peak on the cooling peak of the DSC trace and the DSC specimen had retained the shape meaning it was not possible to confirm melting looking at the specimen. It was decided to heat treat the alloy at 1200 °C not only because this heat treatment would be at a temperature of interest for oxidation behaviour, but also to find out what (if any) microstructure changes had occurred.

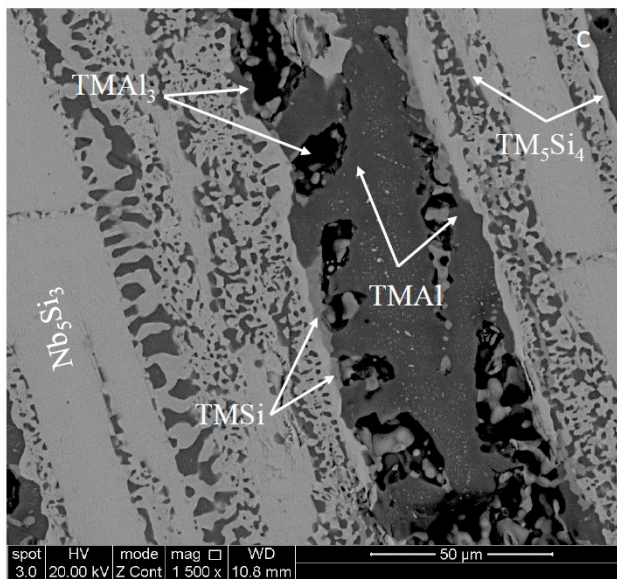
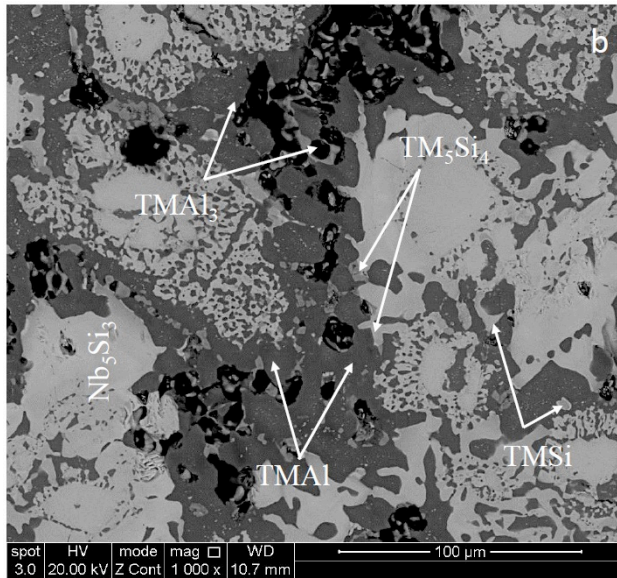
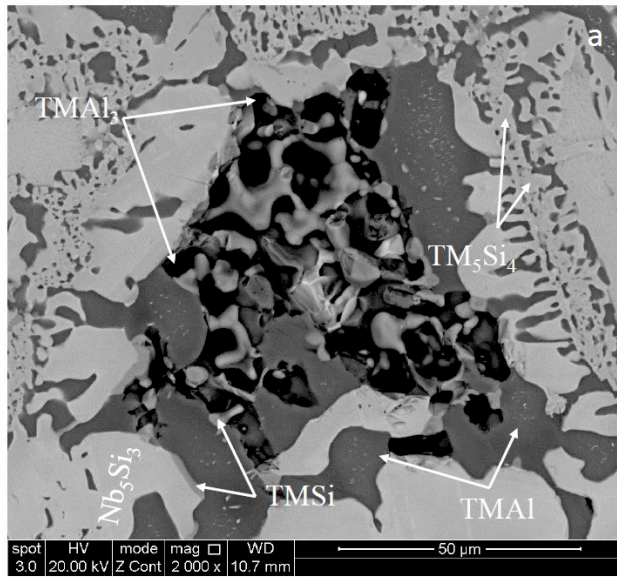
The alloy MG6 was heat treated at 1200 °C for 100 h. The actual composition of MG-HT1200 was Nb-23Ti-23.2Si-37.1Al-3.5Hf and was very close to the nominal alloy composition and the actual composition of MG6-AC and MG6-HT800, see table 27 to table 30. There was still chemical inhomogeneity for Al and Si but not for Ti and Nb.

The Al+Si concentration was essentially the same in all parts of the heat treated alloy. The microstructure of MG6-HT1200 is shown in figure 94. In all parts of the heat treated alloy there was evidence of localized melting. In these areas that were formed in between the bulky 5-3 silicide grains, there was a very dark contrast phase (Al_3TM) and brighter contrast phase. Considering the latter, the grey contrast phase had fine precipitates of a brighter contrast phase inside it and the light grey contrast phase appeared to have similar contrast with the TiAl seen in the alloys of this work as well as Ti_5Si_4 and TiSi. To summarise, in the areas of localized melting the following phases precipitated: Ti_5Si_4 , TiSi, Al_3TM , TiAl. These phases were surrounded by 5-3 silicide grains. The X-ray diffractogram of the alloy MG6-HT1200 is shown in figure 95. The XRD data suggested that $TiAl_3$, Ti_5Si_4 , TiSi and γNb_5Si_3 were in the microstructure.

The EDS analysis data is shown in table 30. The analyses confirmed the presence of hexagonal 5-3 silicide, tri-aluminide and the Ti_5Si_4 and TiSi silicides. In other words, the EDS confirmed the phases suggested by XRD. In the SEM under BSE conditions it was easy to distinguish the tri-aluminide owing to its very strong contrast, but separation of the other phases in the areas of localized melting was very difficult using their contrast. In figure 94 the contrast has been manipulated so that all phases can be seen. Analysis of the grey contrast phase (i.e., the one with second phase particles in it) was possible once and this phase was identified as TiAl, see table 30. Compared with the data for composition of TiAl in other alloys of this work, the Si concentration in TiAl in MG6-HT1200 was high, probably because the analysis included some of the second phase particles that exhibited similar contrast with the silicide. One analysis from this area corresponded to Ti_3Al , see table 30.

Table 30: EDS analysis data (at%) of the alloy MG6-HT(1200 °C/100 h)

Area and phase analysis		Elements					Al+Si
		Nb	Si	Ti	Al	Hf	
Large area	Top	13.1±0.4 12.8-13.8	23.5±1.4 22.3-26	23±0.3 22.1-23.4	36.9±2.4 32.6-38.4	3.5±0.4 3.1-4.1	60.4
	Bulk	13.1±0.4 12.6-13.5	22.8±1.1 21.3-23.9	23±0.3 22.5-23.4	37.7±1.9 35.6-40.4	3.4±0.2 3.2-3.7	60.5
	Bottom	13.4±0.7 12.5-14.4	23.3±1.4 21.2-24.8	23±0.5 22.4-23.6	36.7±2.6 33.4-40.4	3.5±0.2 3.2-3.8	60
	Average	13.2±0.5 12.5-14.4	23.2±1.3 21.2-26	23±0.4 22.1-23.6	37.1±2.2 32.6-40.4	3.5±0.3 3.1-4.1	60.3
Phase (spot) analysis		Aluminides and silicides					
	Al ₃ TM	12.1±1 10-13.1	0.8±1 0-2.4	13.6±0.7 12.2-14.5	72.8±1.4 70.9-74.6	0.6±0.3 0-0.9	73.7
	Ti ₅ Si ₄	11.7±1.9 10.1-15.3	46.2±1.5 43.4-47.5	32.9±1.4 31.6-34.7	1.8±0.5 1.2-2.8	7.4±1.1 6.2-8.8	48
	TiSi	8.9±1.1 8-10.1	35.9±5.9 32.1-42.8	37.7±4.3 33-41.5	13.3±4.2 8.5-16	4.1±1.3 2.9-5.5	49.3
	Ti ₃ Al	3.3	5.8	60.6	19.1	11.1	24.9
	TiAl	11.6	18.4	21.6	45.9	2.5	64.3
		5-3 silicide					
	γNb ₅ Si ₃	21.4±1.8 19.8-23.5	37.3±1.5 35.9-39.3	30.4±1.2 29.2-31.7	5.4±2.9 2.3-8.6	5.4±0.6 4.7-6	42.7



Continued

Continued

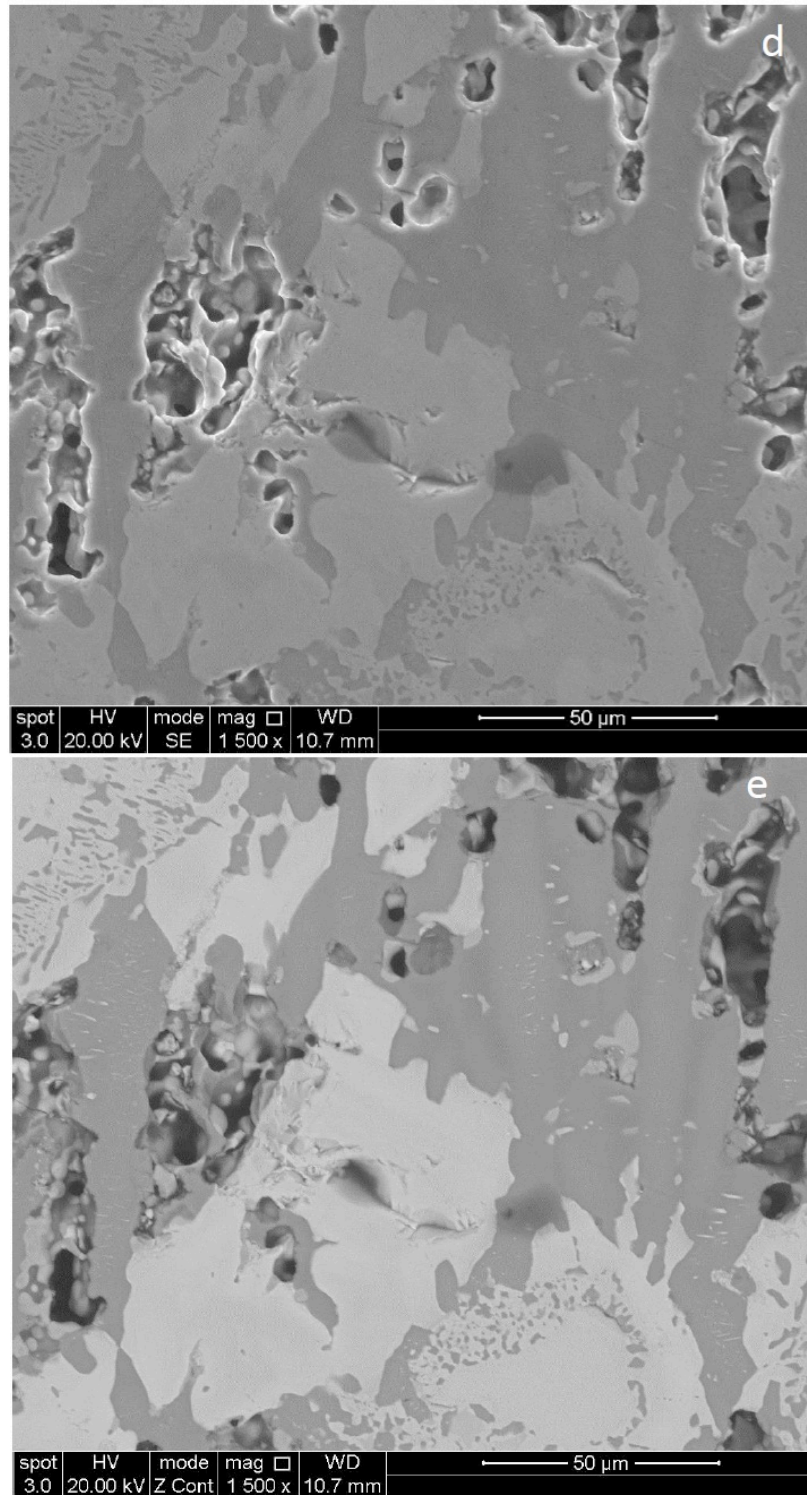


Figure 94: BSE images showing the microstructure of MG6-HT1200 at (a) top, (b) bulk, (c) bottom of the heat treated specimen. (d) secondary electron image, (e) BSE image of areas where it is suggested that localized melting had occurred

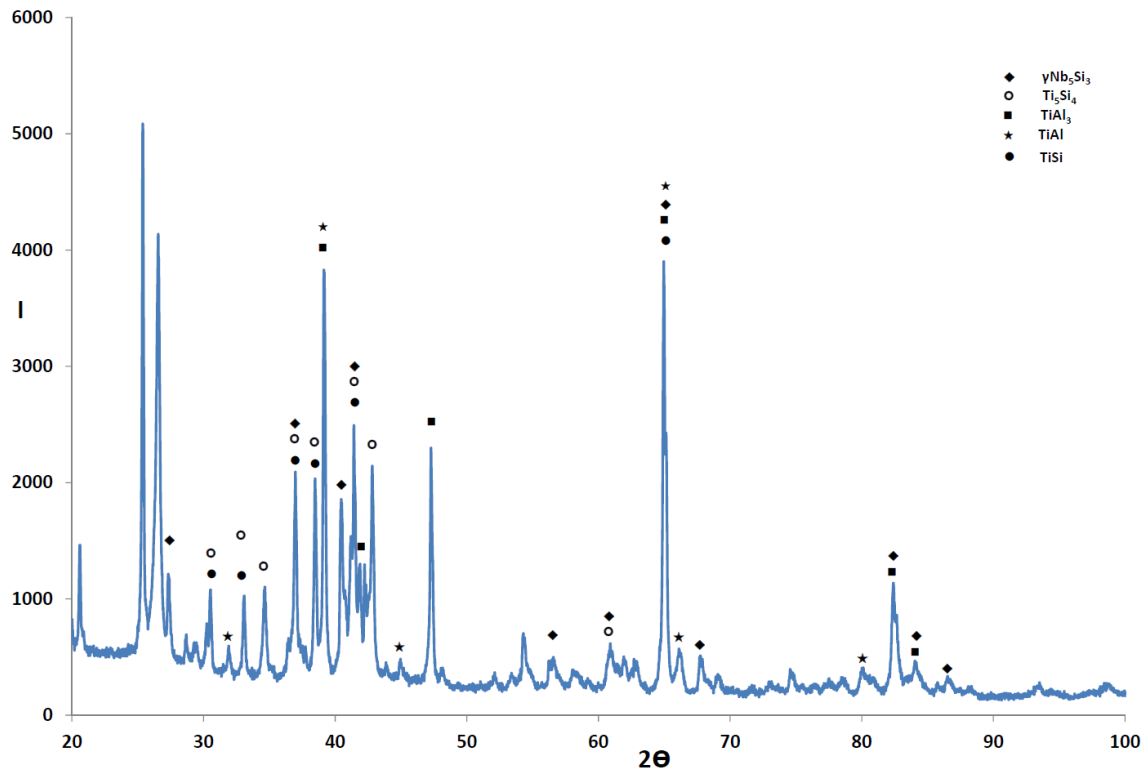


Figure 95: X-ray diffractogram of the alloy MG6-HT1200

6.1.3 Oxidation behaviour

The oxidation of the alloy MG6 was studied at 800 and 1200 °C. The first set of experiments was done using TG. The alloy did not pest at 800 °C and the scale was adherent at 1200 °C. As there was evidence for formation of alumina scale, it was decided to perform a second set of experiments that involved isothermal oxidation in air in a muffle furnace at 800 °C or 1200 °C of large specimens so that the composition of the scale would be studied. Both sets of experiments are discussed in this section.

6.1.3.1 Thermogravimetry

6.1.3.1.1 Isothermal oxidation at 800 °C for 100 h

The oxidized specimen is shown in figure 96a. The weight gain data is shown in figure 97 and the oxidation rate constant is shown in table 31. The alloy MG6 did not pest at 800 °C and no Maltese-cross scale was formed. There was some porosity on the top of

the sample but no cracks were seen. The GXRD data is shown in figure 98 and shows that the oxide scale consisted of TiO₂, Nb₂O₅, Ti niobates, HfO₂, SiO₂ and TiAl₂O₅. The colour of the scale was attributed to TiNb₂O₇. The alloy MG6 exhibited linear oxidation with linear oxidation rate constant $k_l = 9 \times 10^{-10} \text{ g cm}^{-2} \text{ s}^{-1}$.

Table 31: The oxidation rate constants of the alloy MG6 at 800 °C and 1200 °C

Alloy	800 °C		1200 °C			Weight gain (mg/cm ²)
	K _l (g cm ⁻² s ⁻¹)	Weight gain (mg/cm ²)	K _p (g ² cm ⁻⁴ s ⁻¹)			
MG6	9 x 10 ⁻¹⁰	0.37	t < 12.47 h	t > 12.47 h	overall	2.3
			1 x 10 ⁻⁷	1 x 10 ⁻⁸	3 x 10 ⁻¹³	

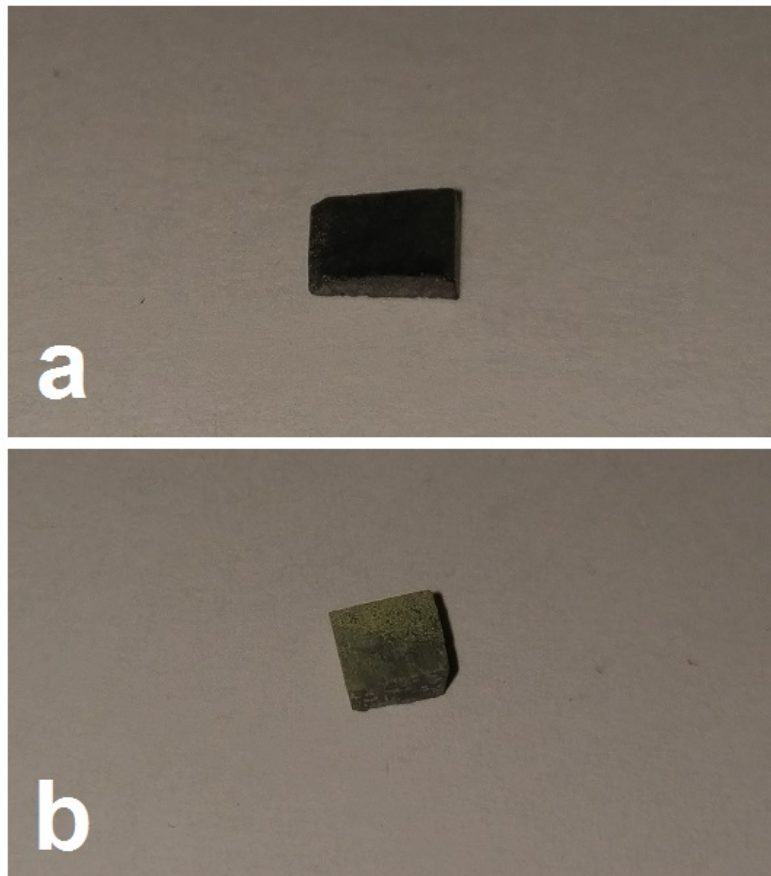


Figure 96: TGA samples after exposure, (a) at 800 °C, (b) at 1200 °C

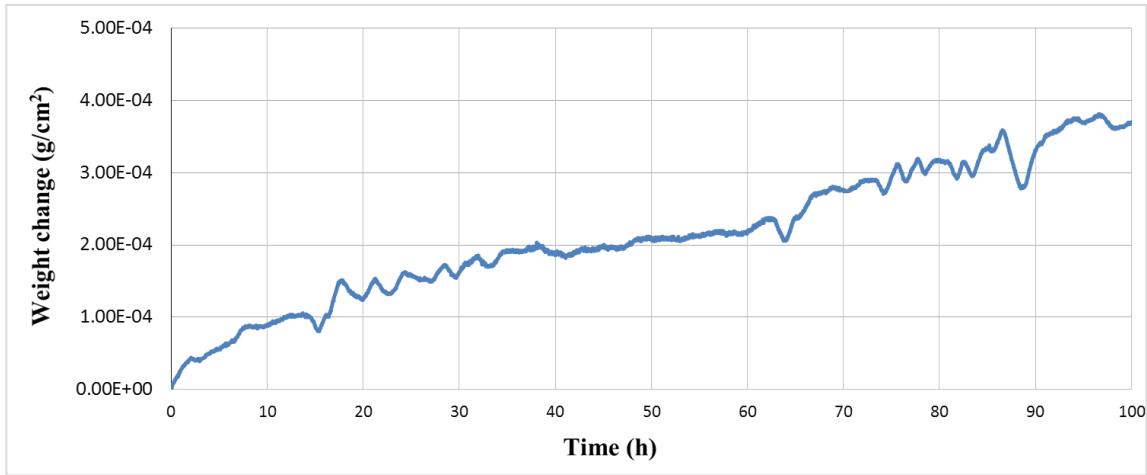


Figure 97: TGA data of the alloy MG6 at 800 °C for 100 h

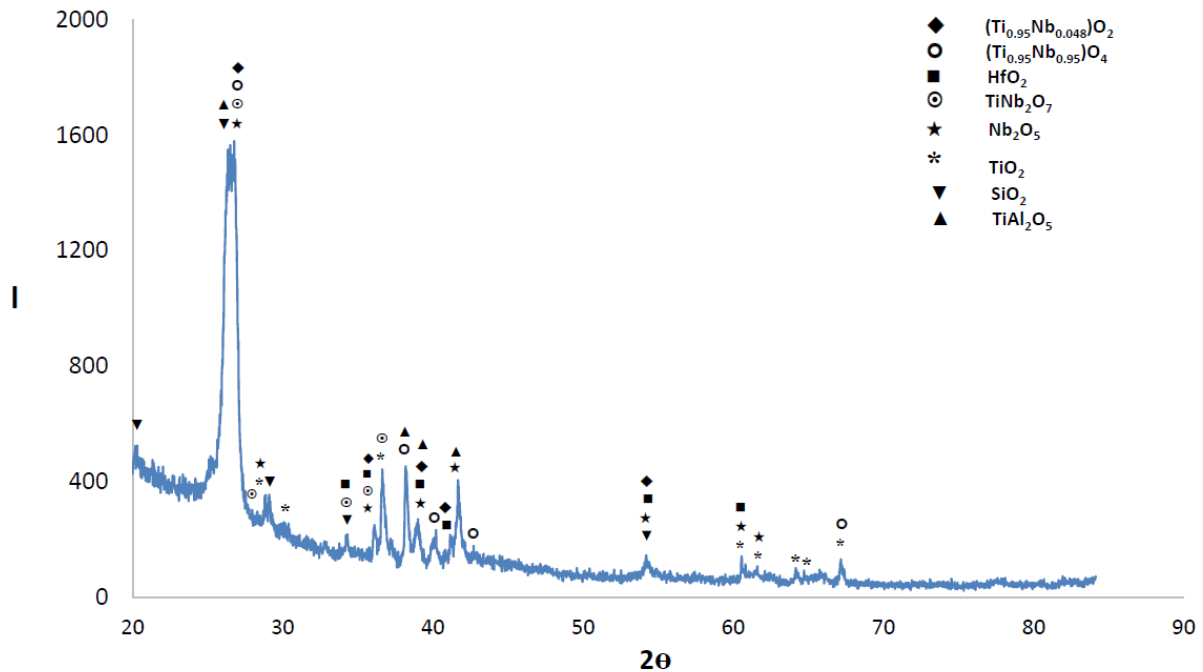


Figure 98: GXR D data (glancing angle ($\theta= 5^\circ$)) of the alloy MG6 oxidized at 800 °C

6.1.3.1.2 Isothermal oxidation at 1200 °C for 100 h

The oxidized specimen is shown in figure 96b, the weight gain data is shown in figure 99, the oxidation rate constant is shown in table 31 and the GXR D data is shown in figure 100. The alloy did not suffer catastrophic oxidation. The same oxides were determined in the scale as at 800 °C plus α -Al₂O₃. In contrast with the TGA sample at 800 °C, the colour of the scale was not dark but rather bright. The change in the colour

of the scale would suggest that there was enough $\alpha\text{-Al}_2\text{O}_3$ to cause this change. The alloy MG6 followed parabolic oxidation kinetics at 1200 °C which is consistent with alumina scale formation. The parabolic rate constant was $k_p = 3 \cdot 10^{-13} \text{ g}^2 \text{ cm}^{-4} \text{ s}^{-1}$.

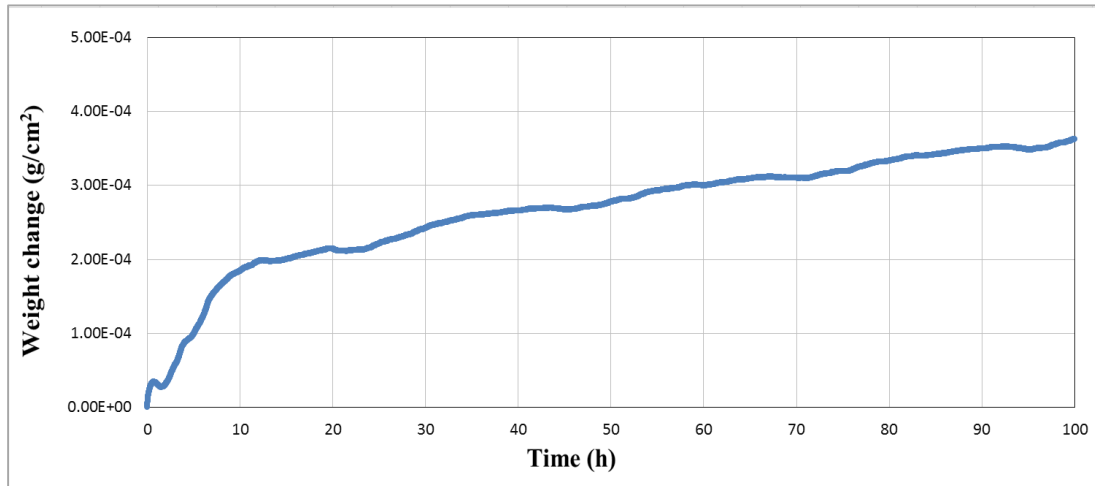


Figure 99: TGA data of the alloy MG6 at 1200 °C for 100 h

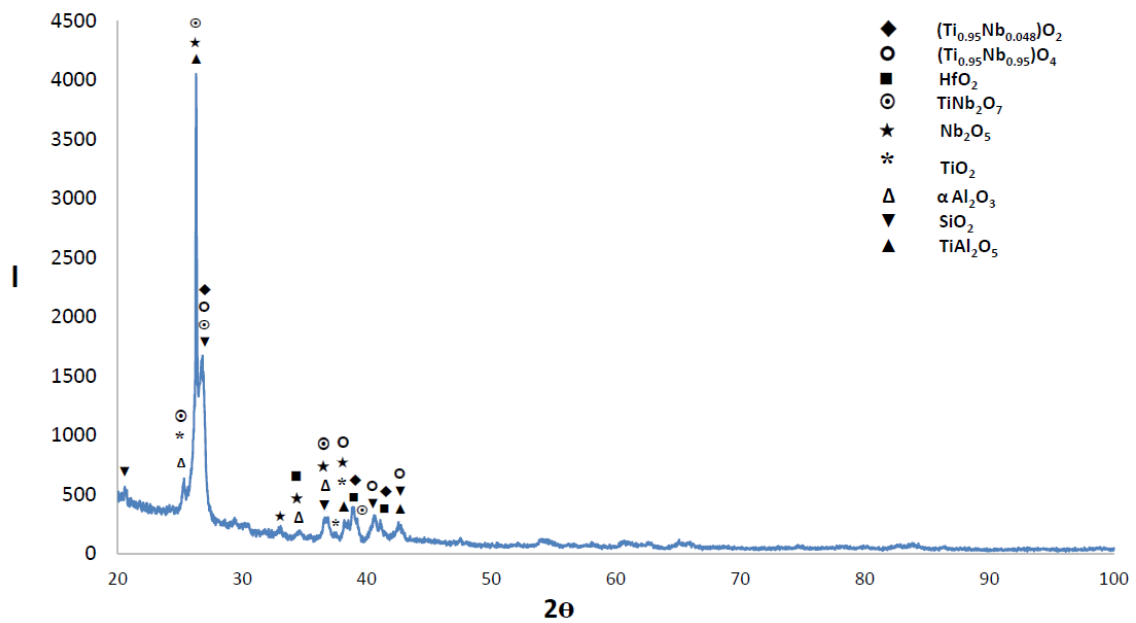


Figure 100: GXRD data (glancing angle ($\theta = 5^\circ$)) of the alloy MG6 oxidized at 1200 °C

6.1.3.2 Muffle furnace oxidation experiments

6.1.3.2.1 Isothermal oxidation at 800 °C

The bulk microstructure of the oxidized specimen is shown in figure 101, the Bragg-Brentano XRD data is shown in figure 102 and the thin scale formed at 800 °C is shown in figure 103. The specimen did not pest, as expected from the TG experiment.

The EDS analysis data of the bulk of the oxidized sample at 800 °C is given in table 32. The average composition was essentially the same as that of MG6-HT800, see table 29. The XRD data suggested that five phases were present in the microstructure, namely hexagonal Nb_5Si_3 , Ti_5Si_4 , Al_3TM , TiAl_2 and TiSi . These phases were confirmed by EDS, see table 32, which also provided evidence for TiAl . As one can realize from the microstructure shown in figure 101, there were similarities in the contrast of the phases surrounding the bulky 5-3 silicide grains. It is for this reason, as was discussed previously, that one analysis is given for the Ti_5Si_4 , TiAl_2 , TiSi and TiAl phases in table 32. Given that TiAl was present in the microstructure of MG6-HT800, it is likely that this aluminide was indeed present in-between the 5-3 grains and its non-detection by XRD might be attributed to it having acted as the reservoir of Al to form alumina in the scale. Evidence for the latter is provided in figure 103b, figure 104 and table 33. The data in the latter suggested that the silicides and aluminides below the thin scale were contaminated by oxygen, the contamination of Nb_5Si_3 was more severe than that of Ti_5Si_4 (richer in Si) but the contamination of Al_3TM and Ti_2Al_5 was essentially the same.

Table 32: EDS analysis data (at %) of the bulk of the alloy MG6 oxidized at 800°C for 100 h

Area and phase analysis		Elements					Al+Si
		Nb	Si	Ti	Al	Hf	
Large area	Bulk	13±1.4 10.2-14.7	23.7±2.8 16.2-26.2	22.9±1.1 20.6-24.3	36.6±5.5 31-50.2	3.7±0.4 2.7-4.4	60.3
Phase (spot) analysis		Aluminides and silicides					
	Al ₃ TM	8.7±4.9 0.5-13.8	4±3.2 1.8-14.1	15.4±4.5 11.2-23.2	70.8±1.9 65.6-72.5	1±0.1 0.9-1.1	74.8
	Ti ₅ Si ₄	18.1	45.4	27.6	2.1	6.8	47.5
	TiAl ₂	5.5	7.4	13.7	60.5	12.8	67.9
	TiAl	7	9	20.4	41.9	21.7	50.8
	TiSi	7.8	37.9	32.9	16.6	4.7	54.5
		5-3 silicide					
	γNb ₅ Si ₃	19.6±2.9 14.2-21.9	39.1±1.1 36.9-39.9	33.1±3.1 30.5-38.7	2.6±0.2 2.3-2.8	5.5±0.7 4.9-6.7	41.7

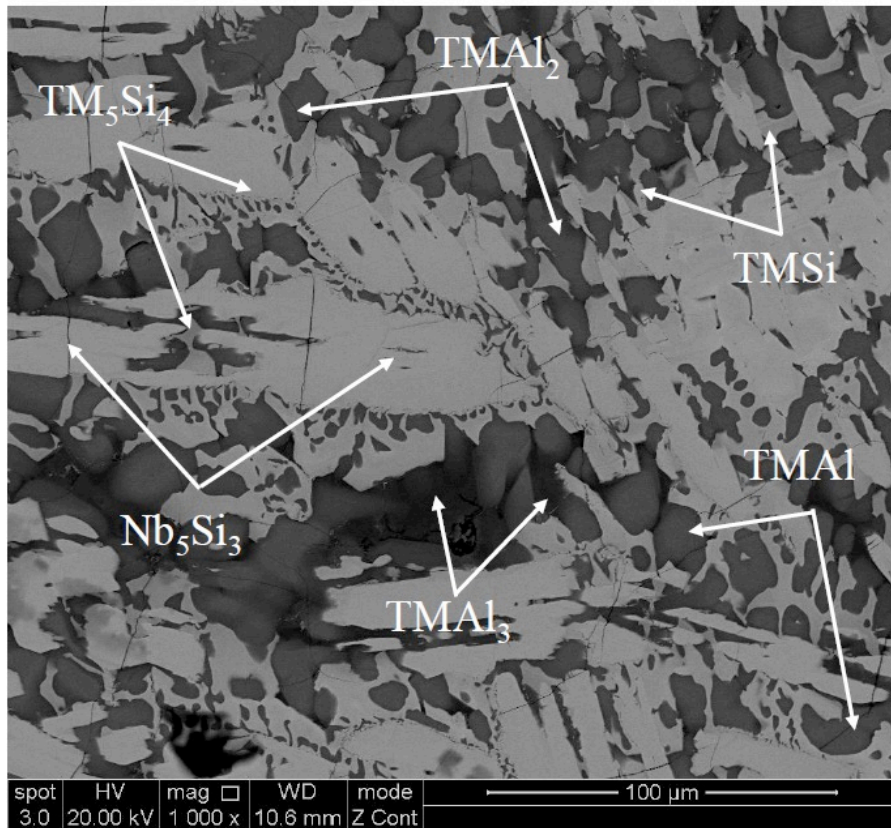


Figure 101: BSE image of the bulk microstructure of the oxidized alloy MG6 at 800 °C

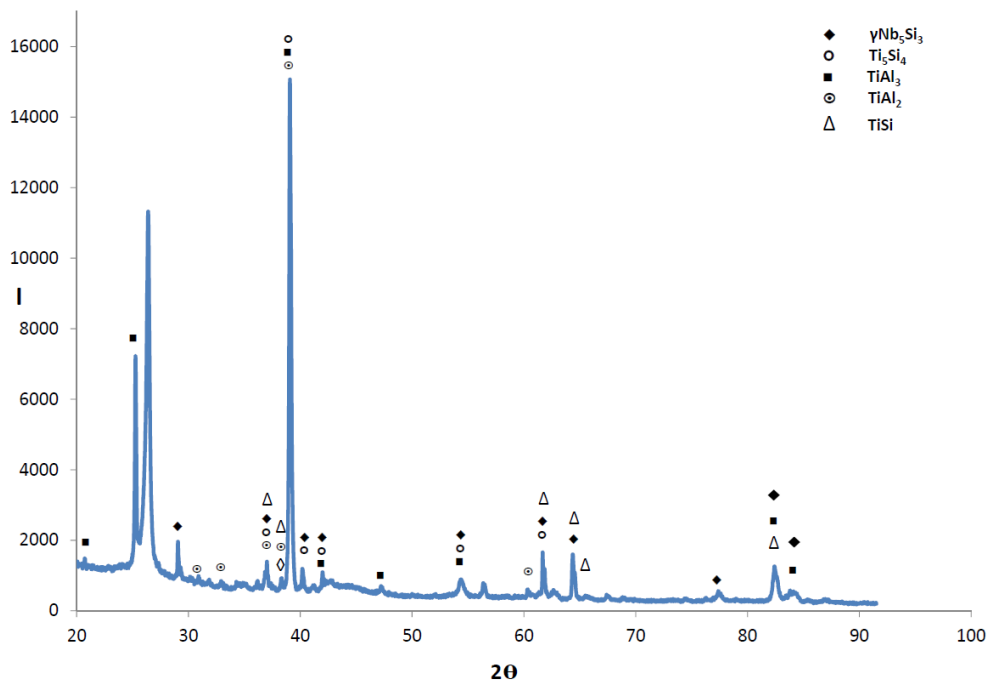


Figure 102: XRD diffractogram of the alloy MG6 oxidized at 800 °C for 100 h in muffle furnace

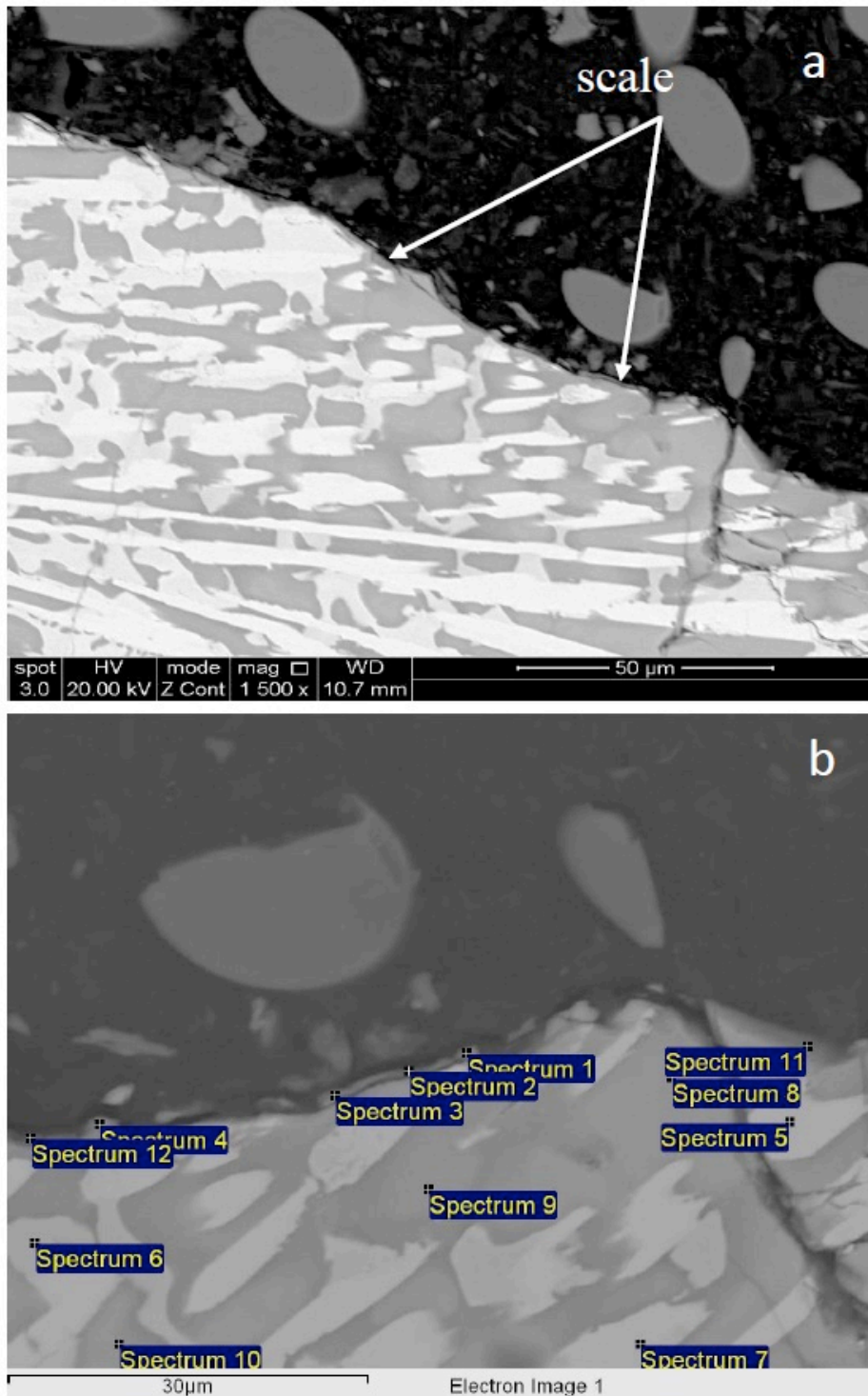


Figure 103: BSE images of the microstructure of the oxidized alloy MG6 at 800 °C (a) near the surface, (b) high magnification image showing where point analyses data were collected from, see table 33

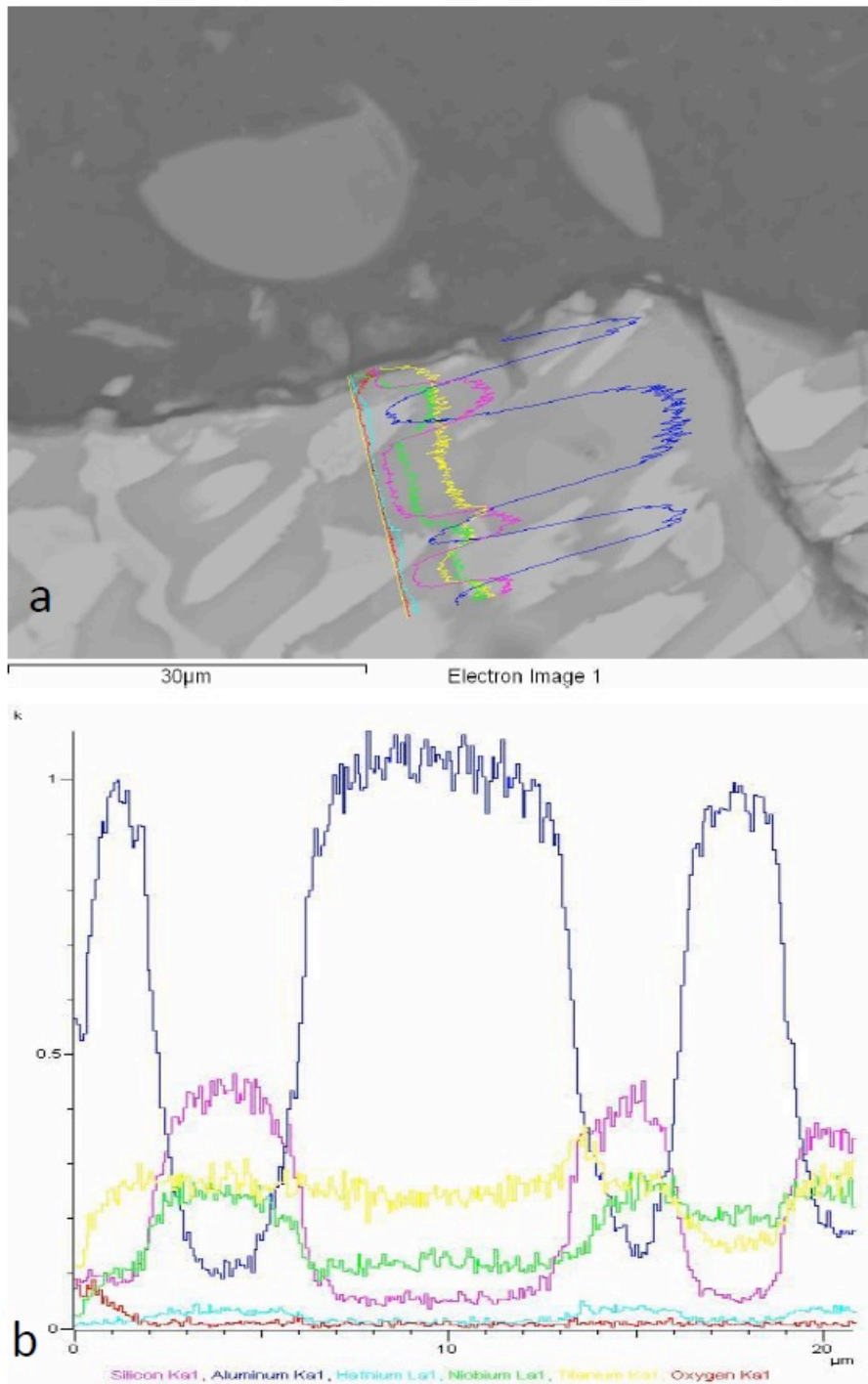


Figure 104: BSE image showing the near surface microstructure of the alloy MG6 oxidized at 800 °C (a) line scan, (b) associated data

Table 33: EDS analysis data (at%) of the near surface microstructure of the oxidized specimen at 800 °C

Spectra	Phase	Element					
		O	Nb	Si	Ti	Al	Hf
Spectrum 1	Al ₂ O ₃	64.3	2.4	4.5	3.2	24.9	0.5
Spectrum 2	Al ₂ O ₃	67.8	1.1	3.8	3.1	23.9	0.2
Spectrum 3	Al ₂ O ₃	59.4	1.6	5.4	5.2	28	0.4
Spectrum 4	Al ₂ O ₃	65.7	2.5	3.7	3.7	23.9	0.4
Spectrum 5	Nb ₅ Si ₃	5.7	21.8	36.6	27.8	3.1	4.9
Spectrum 6	Ti ₅ Si ₄	2.9	5.5	45.1	39.5	2.3	4.6
Spectrum 7	Nb ₅ Si ₃	5.2	20.6	35.8	27.8	5.7	4.9
Spectrum 8	Al ₃ TM	3.2	11.3	2.4	13.4	68.5	1.2
Spectrum 9	Ti ₂ Al ₅	3.7	10.5	2.9	13.8	68	1
Spectrum 10	Ti ₂ Al ₅	3.8	12.4	2.4	13.2	66.7	1.4
Spectrum 11	Al ₂ O ₃	65.1	2.2	1.6	4.4	26.3	0.3
Spectrum 12	Al ₂ O ₃	61.4	2	2	4.9	29.4	0.3

6.1.3.2.2 Isothermal oxidation at 1200 °C

The bulk composition of the oxidized specimen is given in table 34. Its Al+Si content was the same as the average of MG6-HT1200. The microstructure of the oxidized specimen is shown in figure 105. The microstructure was similar to that of MG6-HT1200 and there was evidence of melting near the surface, see figure 105b and compare with figure 94. The XRD data is shown in figure 106 and would suggest the presence of six phases, namely γ Nb₅Si₃, Ti₅Si₄, Ti₅Si₃, Al₃TM, TiAl₂ and Ti_{0.2}Nb_{0.07}Al_{0.23} plus alumina. The EDS analysis confirmed the presence of the six intermetallic phases, see table 34. A phase with composition corresponding to TM_{2.7}AlSi_{0.3} was also identified.

The oxidation at 1200 °C was not catastrophic and in agreement with the TG experiment. Adherent α -Al₂O₃ scale was formed on the specimen. This scale was thick and continuous even around corners, see figure 107. The α -Al₂O₃ in the Bragg-Brentano XRD data in figure 106 was in agreement with the GXRD in figure 100. The alumina scale was also confirmed by EDS, see figure 108, figure 109 and table 35. The line scan for oxygen (figure 108b) indicated very low oxygen concentration in the bulk of the oxidized specimen. The same was the case at 800 °C, see figure 104b. The EDS analysis confirmed the contamination of the microstructure by oxygen below the scale with more severe contamination of the 5-3 silicide compared with the aluminides.

Table 34: EDS analysis data (at%) of the alloy MG6 oxidized at 1200 °C in muffle furnace

Area and phase analysis		Elements					Al+Si
		Nb	Si	Ti	Al	Hf	
Large area	Bulk	13.1±0.4	22±1.8	22.4±0.5	38.7±2.4	3.7±0.2	60.7
		12.5-13.5	19.9-24.1	21.8-22.9	35.8-40.7	3.5-3.9	
Phase (spot) analysis		Aluminides and silicide					
	Al ₃ TM	12.3±1.4 10-14.2	1.4±1.7 0-5.6	13.3±0.9 11.7-14.7	72.3±3.2 64.5-74.3	0.7±0.3 0.3-1.3	73.7
	Ti ₅ Si ₄	9.9±2.7 4.2-13.2	45.9±3.4 35.7-47.7	34.4±3.5 30.9-42.4	2.5±3.1 1.1-11.6	7.4±1.4 3.8-8.9	48.3
	TM _{2.7} AlSi _{0.3}	2.6±0.7 2.1-3.1	7.5±0.8 7-8.1	64±0.1 64-64.1	24.7±1.7 23.5-25.9	1.1±0.1 1.1-1.2	32.3
	TiAl ₂	10.6±0.2 10.4-10.8	5.1±0.1 5.1-5.2	21.2±1.4 20.3-22.2	62.1±1.7 60.9-63.4	0.9±0 0.8-0.9	67.3
		5-3 silicide					
	(Ti,Nb) ₅ Si ₃	6±0.5	39.6±0.3	47.4±1.3	2.3±1.5	4.6±0.6	42
	γ (Nb,Ti) ₅ Si ₃	22.3±0.5 22-23	38.5±0.5 37.9-39	30.4±0.5 29.8-30.7	2.3±0.4 1.9-2.7	6.5±0.6 6.1-7.2	40.7

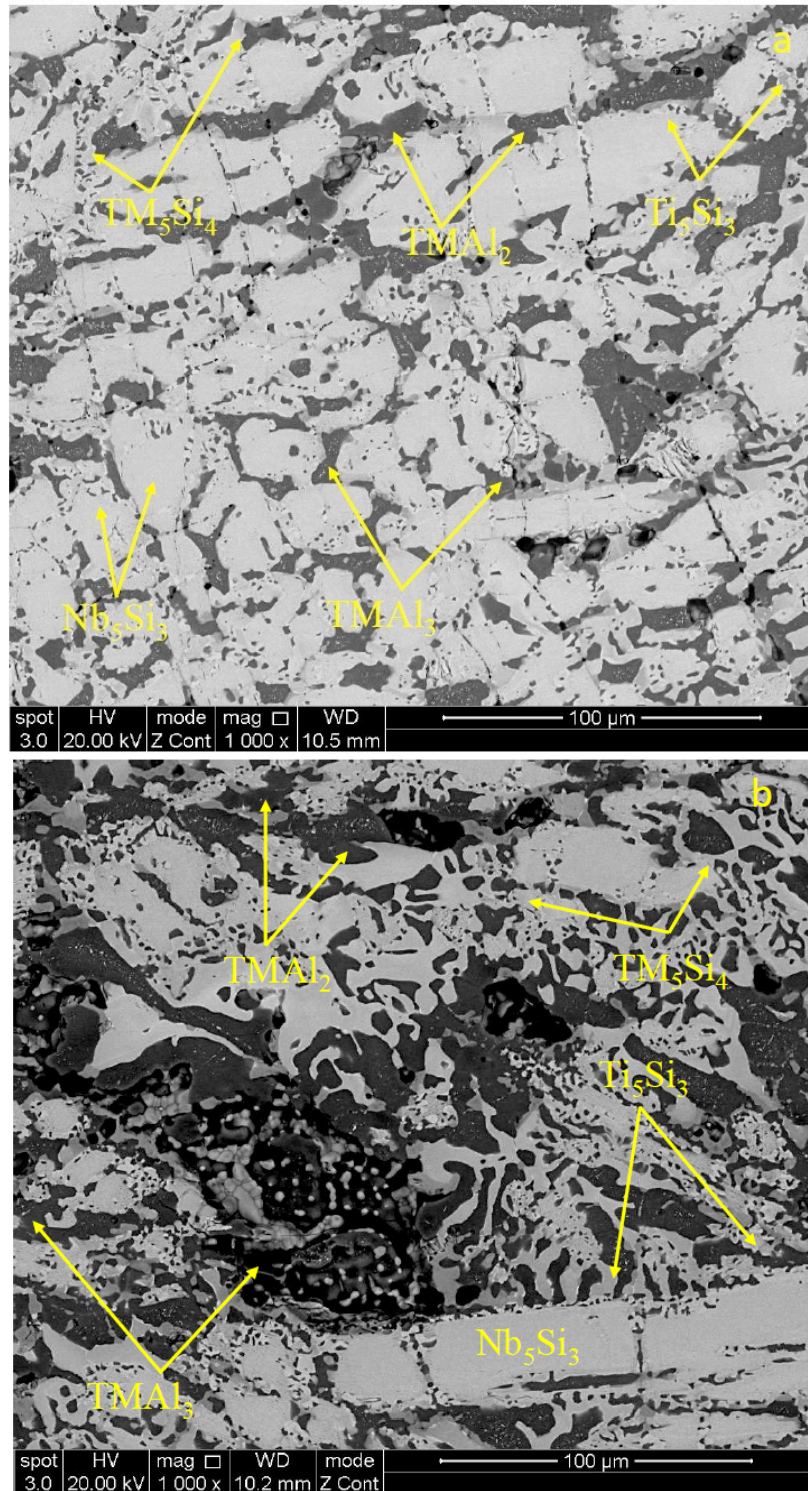


Figure 105: BSE images of the microstructure of the alloy MG6 in muffle furnace at 1200 °C, (a) bulk, (b) near the top

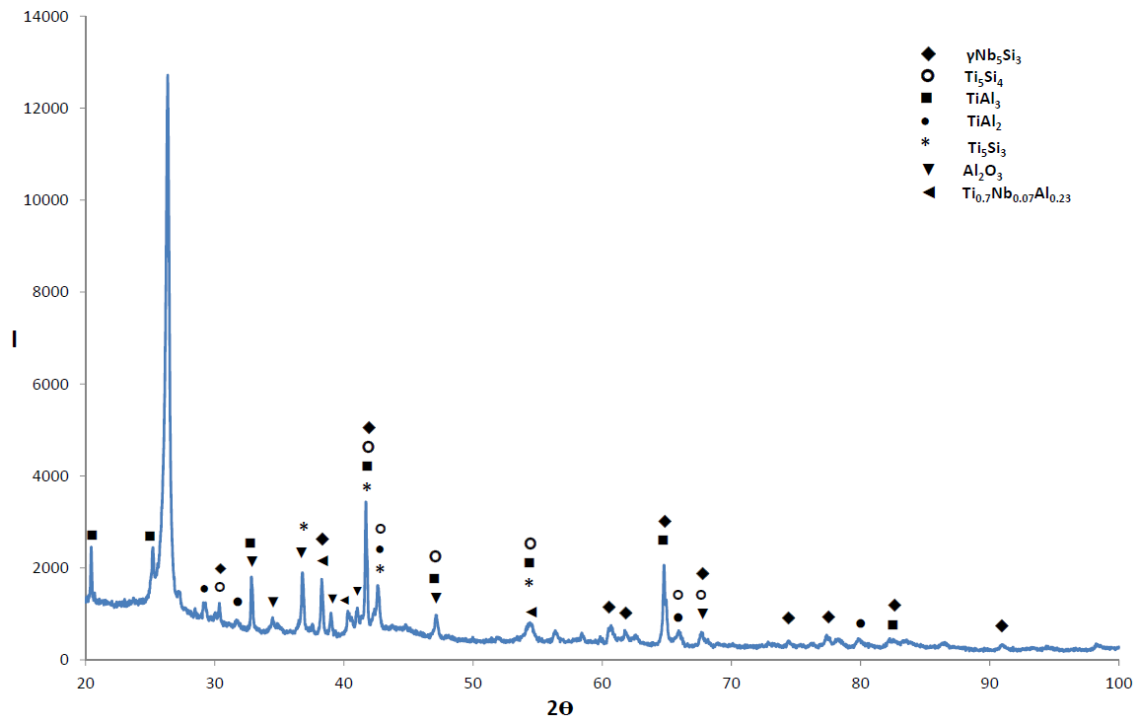


Figure 106: XRD diffractogram of the alloy MG6 oxidized at 1200 °C in muffle furnace

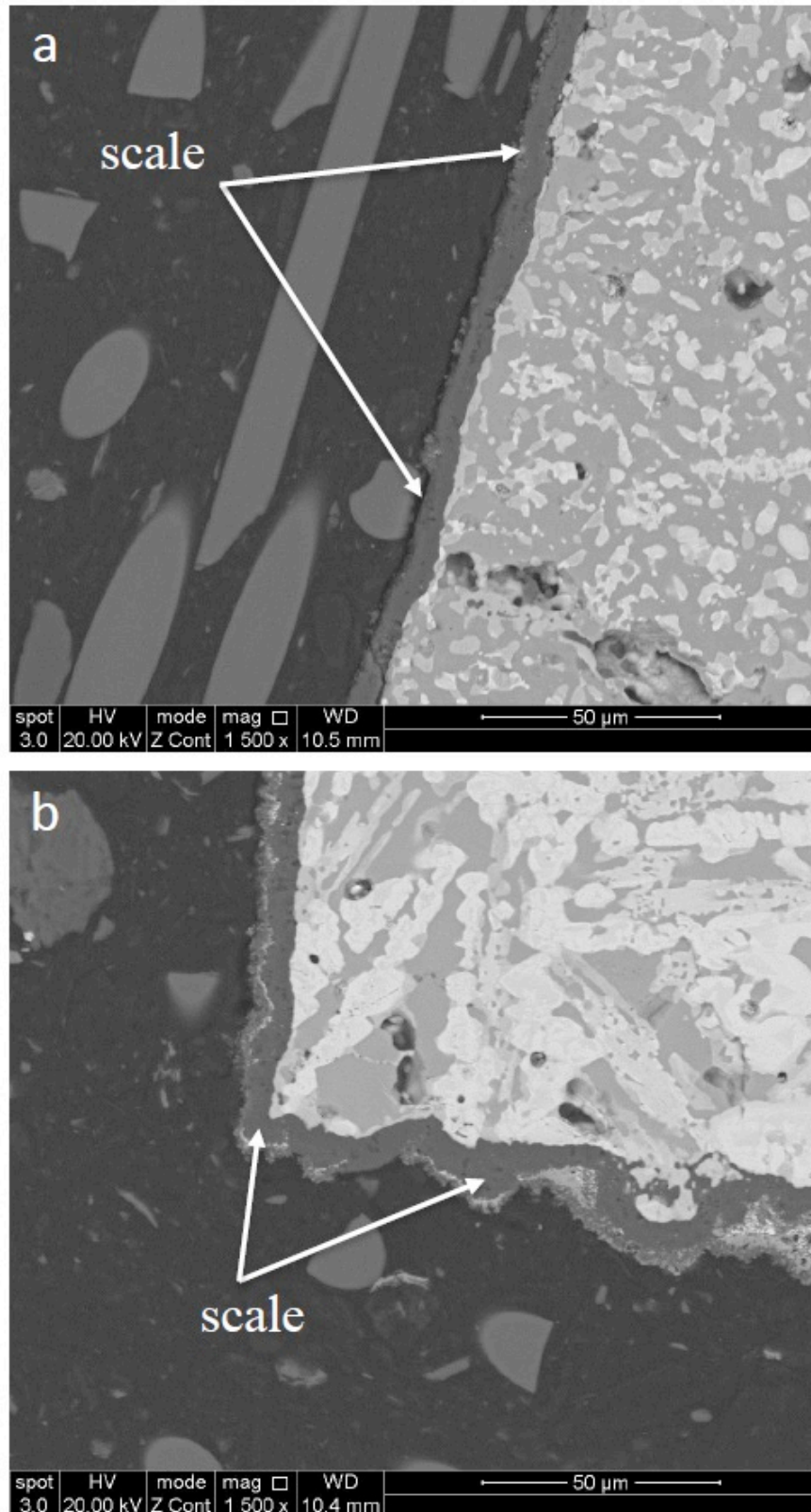


Figure 107: BSE images of cross section of the oxidized alloy MG6 in muffle furnace at 1200 °C showing the adherent alumina scale (a) away from a corner, (b) at a corner

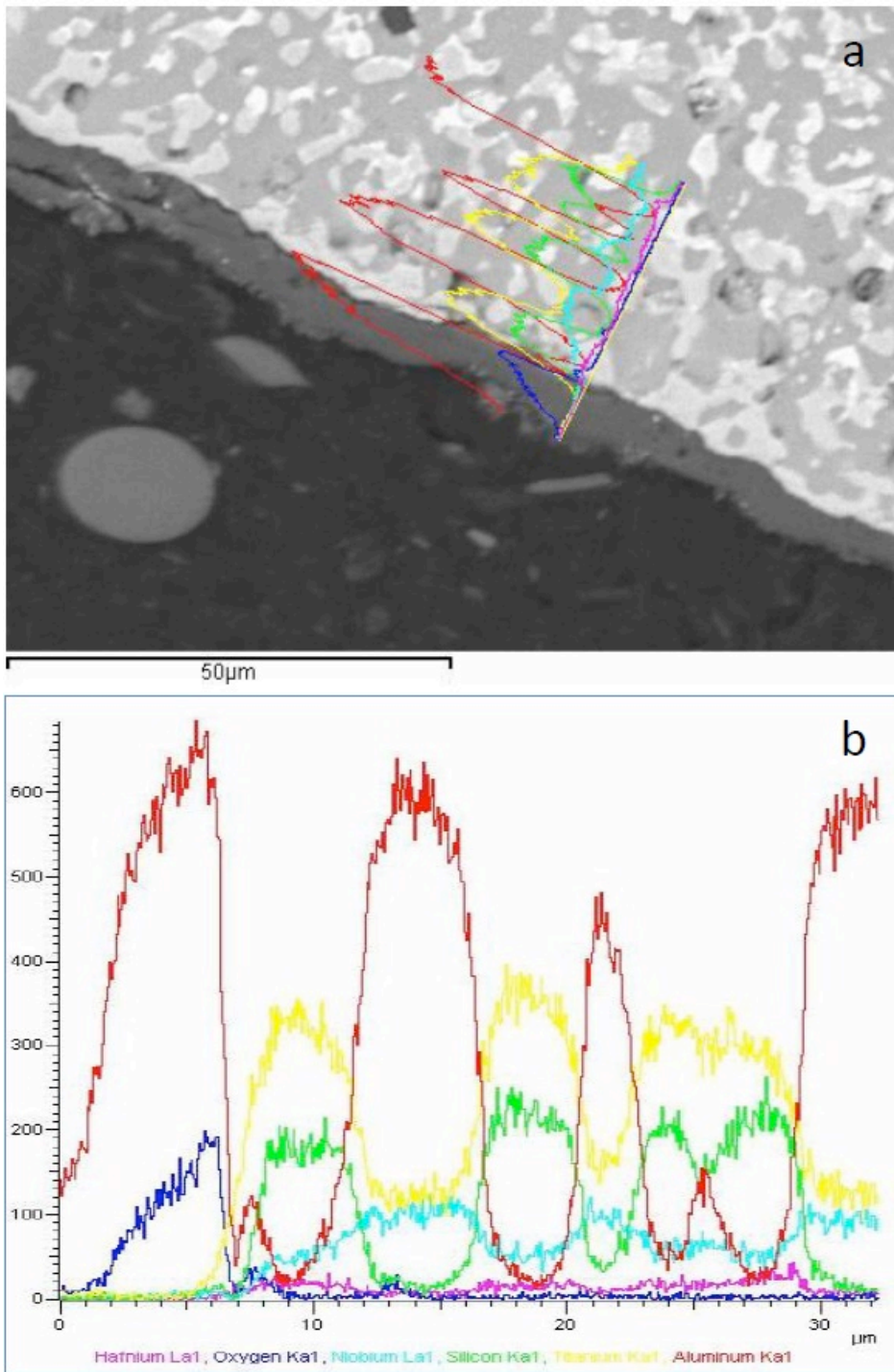


Figure 108: (a) BSE image of cross section of scale with superimposed line scan and (b) detailed line scan

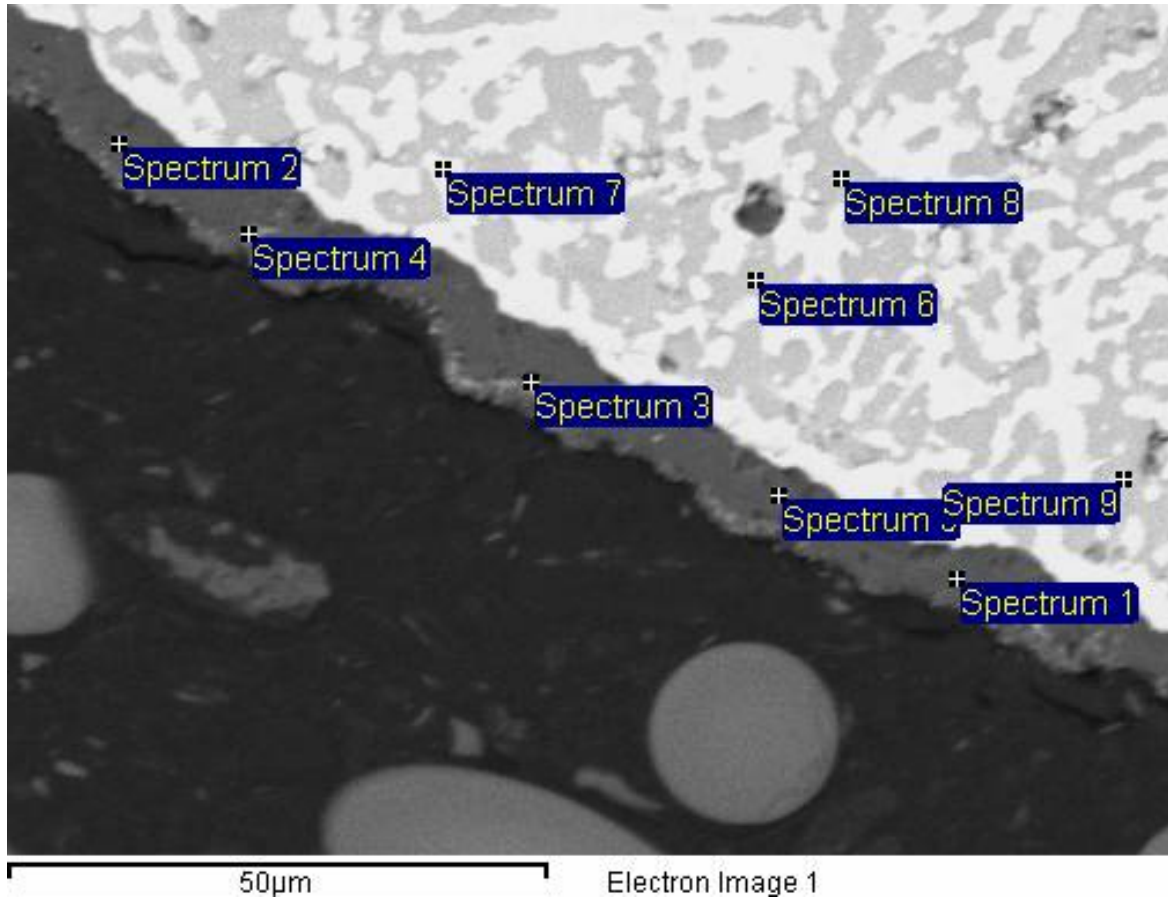


Figure 109: BSE image of the microstructure of the oxidized alloy MG6 at 1200 °C near the surface showing where point analyses data were collected from, see table 35

Table 35: EDS analysis data (at%) of the near surface microstructure of the oxidized specimen at 1200 °C

Spectra	Phase	Element					
		O	Nb	Si	Ti	Al	Hf
Spectrum 1	Al ₂ O ₃	58.6	0	0.4	0.1	40.8	0
Spectrum 2	Al ₂ O ₃	62.2	0	0.3	0.1	37.4	0
Spectrum 3	Al ₂ O ₃	70.1	1.3	3.5	7.4	17.2	0.5
Spectrum 4	Al ₂ O ₃	67.5	1.1	0.6	6.3	24.1	0.3
Spectrum 5	Al ₂ O ₃	62.4	0	0.1	0	37.3	0
Spectrum 6	Al ₃ TM	4.2	12.8	0.7	11.4	70.2	0.6
Spectrum 7	Ti ₅ Si ₃	6.2	7.9	33.6	40.6	7.6	4
Spectrum 8	Al ₃ TM	3.9	12.6	0.7	11.7	70.5	0.5
Spectrum 9	TiAl ₂	3.7	13.1	3.3	14.4	64.6	0.8

6.1.4 Discussion

The alloy MG6-AC exhibited macrosegregation of Al, Si and Ti. Compared with the alloy MG2-AC, the macrosegregation of Si and Ti was reduced respectively by about 15% and 75%, but that of Al had increased by about 12%. It should be noted that when the alloy MG5-AC was compared with the alloy MG2-AC, the macrosegregation of Si and Ti was reduced respectively by about 22% and 56%, but the macrosegregation of Al had increased by about 29%. These results supported the conclusion that Al is the solute element that controls the chemical inhomogeneity in the alloys of this research and that the Al/Si and Al/Ti ratios rather than the Ti/Si ratio must be further optimised to close the gap between maximum and minimum concentrations of Al and Si in the alloy.

The same phases were present in all parts of the ingot of MG5-AC, namely hexagonal $\gamma(\text{Nb,Ti})_5\text{Si}_3$ (isomorphous with Ti_5Si_3), $(\text{Ti,Nb})_5\text{Si}_4$, TiAl and Al_3TM tri-aluminide. The microstructure was finer in the bottom of the ingot, owing to the higher cooling rate(s) prevailing there during solidification, but compared with the alloy MG5-AC, this effect was not as strong. Compared with the alloy MG5-AC, the main difference was the replacement of TiSi by TiAl .

In the previous chapter the formation of the 5-4 silicide around the 5-3 hexagonal silicide was attributed to the peritectic reaction $\text{L} + \text{Ti}_5\text{Si}_3 \rightarrow \text{Ti}_5\text{Si}_4$. The fact that TiSi was not formed in MG6-AC means that the melt surrounding the bulky composite grains (composite here means 5-3 core surrounded by 5-4 silicide) did not reach the Si content where (i.e., was not so Si rich so that) the peritectic $\text{L} + \text{Ti}_5\text{Si}_4 \rightarrow \text{TiSi}$ reaction could occur (note that the Si content of the 5-4 silicide was higher in MG6 than in MG5).

The melting temperature of TiAl is lower than that of TiSi and Al_3X ($\text{X}=\text{Hf}, \text{Nb}$) but higher than that of Al_3Ti , thus in terms of decreasing melting temperature the ranking of intermetallics in MG6-AC should be hexagonal 5-3 silicide, 5-4 silicide, and then TiAl or Al_3TM depending on the composition of the latter two phases. In the microstructures of MG6-AC (figure 89) the tri-aluminide formed in the areas between the “composite” silicide grains, i.e., in the last to solidify melt. Thus, it is deduced that the melting temperatures of the 5-3 silicide and 5-4 silicide were higher than those of the tri-aluminide Al_3TM and TiAl , which supports the above discussion.

The fibrous (wool like) structure (nature) of the 5-4 silicide around the 5-3 silicide was more pronounced in the bottom of the ingot, see figure 89c. The latter was richer in Al compared with the bulk and top. It should be noted that the same effect (meaning strong fibrous nature of 5-4 silicide around 5-3 silicide) was observed in the top of MG5-AC, which was also richer in Al compared with bulk and bottom. These observations would suggest that the concentration of Al in the melt plays a role in the formation of the fibrous 5-4.

As the primary 5-3 silicide was formed the melt became poor in Hf, Nb, Si and Ti and rich in Al, from this melt the 5-4 silicide formed on the 5-3 silicide via a peritectic reaction (see above) and the melt became poor in Hf, Si, Nb and richer in Al and then (depending on the composition of the melt) from Al rich and Si and Hf poor melt formed the Al_3X and the surrounding melt became rich in Hf, Nb, Si, Ti and poor in Al and TiAl formed OR from the richer in Ti and not so rich in Al melt around the 5-4 silicide formed the TiAl and the surrounding melt became rich in Hf, Nb, Si and poor in Al and Ti and then the Al_3TM formed when the melt became Al rich.

It is suggested that the solidification path of MG6-AC was $L \rightarrow L + \text{hexagonal } Nb_5Si_3$ then $L + \text{hexagonal } Nb_5Si_3 \rightarrow TM_5Si_4$, then $L + \text{hexagonal } Nb_5Si_3 \rightarrow TM_5Si_4 + Al_3TM \rightarrow \text{hexagonal } Nb_5Si_3 + TM_5Si_4 + Al_3TM + TiAl$ OR $L \rightarrow L + \text{hexagonal } Nb_5Si_3$ then $L + \text{hexagonal } Nb_5Si_3 \rightarrow TM_5Si_4 \rightarrow L + \text{hexagonal } Nb_5Si_3 + TM_5Si_4 + TiAl \rightarrow \text{hexagonal } Nb_5Si_3 + TM_5Si_4 + TiAl + Al_3TM$. The latter path is supported by the results of Bulanova et al (2004), see below.

If the alloy MG6 is considered as (Ti,Nb,Hf)-Si-Al, primary hexagonal 5-3 silicide is in agreement with the results reported by Bulanova et al (2004) , and the liquidus projection, see figure 110. Bulanova et al (2004) also account for formation of TiAl via $L \leftrightarrow TiAl + Ti_5Si_3$ at 1420 °C and the formation of Al_3Ti as the temperature drops via $L + TiAl \leftrightarrow Ti_5Al_{11}$ at 1390 °C (~ 33Ti-6Si-61Al), $L \leftrightarrow Ti_5Al_{11} + Ti_5Si_3$, then $L + Ti_5Al_{11} \leftrightarrow Al_3Ti + Ti_5Si_3$ at 1380 °C (~ 30Ti-6.5Si-63.5Al), then $L + Ti_5Si_3 \leftrightarrow Ti_5Si_4 + Al_3Ti$ at 1356 °C (~ 21Ti-37Si-42Al) with the liquid solidifying to give $Al_3Ti + Ti_5Si_3 + Ti_5Si_4$.

The Pandat software was used to calculate the solidification path for the overall average composition of MG6-AC (the average composition in the bulk and bottom of the ingot was essentially the same as the overall average alloy composition). The following path was calculated: Solidification starts at 2002 °C with $L \rightarrow L + Ti_5Si_3$, then $L \rightarrow Ti_5Si_3 + Nb_5Si_3$ at 1704 °C, and the simulation stops at 1409 °C with three phases, namely $L + Ti_5Si_3 + Nb_5Si_3$, in other words the calculated solidification path cannot account for the formation of the 5-4 silicide, tri-aluminide and TiAl.

The following path was calculated for the top of MG6-AC. Solidification starts at 2017 °C with $L \rightarrow L + Ti_5Si_3$, then $L \rightarrow Ti_5Si_3 + Nb_5Si_3$ at 1699 °C, then $L + Ti_5Si_3 \rightarrow Nb_5Si_3 + HfSi$ at 1509 °C, then $L + HfSi \rightarrow Nb_5Si_3 + Ti_3Al_2Si_5$ at 1382.78 °C, then $L \rightarrow Nb_5Si_3 + Ti_3Al_2Si_5$ at 1382.77 °C, then $L + Nb_5Si_3 \rightarrow Ti_3Al_2Si_5 + DO22 Al_3X$ at 1153 °C, then $L + Ti_3Al_2Si_5 \rightarrow fcc Al$ at 663.4 °C and then $L \rightarrow fcc Al$ at 663.38 °C and solidification finishes at 578 °C with the last liquid forming fcc Al. This solidification path can account for the formation of the tri-aluminide but not for the 5-4 silicide and

TiAl. Furthermore, it predicts formation of TiSi, which is isomorphous with HfSi (oP8, Pnma, prototype FeB), and $Ti_3Al_2Si_5$ and fcc Al. The latter phases were not observed.

The calculated solidification paths would suggest that the cast microstructure of the alloy MG6 was very sensitive to melt composition, even though there were not very large differences in Al + Si between the different parts of the ingot. This was not supported by the experimental results.

The microstructure of MG6-HT800 consisted of the hexagonal γNb_5Si_3 , the aluminides TiAl and Al_3TM , the silicides Ti_5Si_4 and TiSi and a Si and Al rich $TM_9Si_7Al_4$ intermetallic, the structure of which is not known. In the latter Al + Si = 55.2 at%, and Al/Si \approx 0.6. Compared with the cast alloy, the TiSi and $TM_9Si_7Al_5$ were the new phases to form (in MG6-AC the XRD suggested the presence of TiSi but this was not confirmed by EDS analysis). The solubilities of Si and Al respectively in TiAl and Ti_5Si_4 were in agreement with the literature (Bulanova et al, 2004, Park et al, 2007) but the solubility of Al in TiSi was higher than that reported in Park et al (2007). The solubilities of Al, Hf and Ti in the 5-3 silicide were in agreement with the literature. Figure 111 shows the positions of the average MG6-HT800 composition in two Ti-Si-Al isothermal sections at 700 °C, the closest available to 800 °C. Table 29 shows that the actual average compositions in all parts of the MG6-HT800 were essentially the same. In both parts of figure 111 the overall average alloy composition is in the three phase Ti_5Si_3 , Ti_5Si_4 and Al_3Ti area.

The DSC trace (figure 91) showed an exothermic peak around 700 °C, which was accompanied by a small weight gain in the TG trace. This peak could be attributed to

the precipitation of $\text{TM}_9\text{Si}_7\text{Al}_5$ and/or precipitation of $\text{Ti}(\text{Al}_{1-x}\text{Si}_x)_3$ (tI8, I4/mmm, TiAl_3 (h)) with $0 < x < 0.15$ that is stable above 735 °C Perrot (2006), where the structure is DO22 – Al_3Ti for $x = 0$.

The microstructure of MG6-HT1200 consisted of the hexagonal $\gamma\text{Nb}_5\text{Si}_3$, the aluminides TiAl and Al_3TM , the silicides Ti_5Si_4 and TiSi and a Ti based aluminide with $\text{Al} + \text{Si} = 24.9$ at% and $\text{Al}/\text{Si} = 3.3$. Compared with the cast alloy, the TiSi was the new phase to form, and considering the results for MG6-HT800 it was concluded that the TiSi is a stable phase in MG6. This conclusion is supported by the 1200 °C isothermal sections for Ti-Al-Si in figure 112. In figure 112a the overall average alloy composition is in the three phase Ti_5Si_3 , TiSi and Al_3Ti area and in figure 112b the overall average alloy composition falls in the three phase Ti_5Si_3 , Ti_5Si_4 and Al_3Ti area but is very close to the two phase Ti_5Si_4 and Al_3Ti and the three phase Ti_5Si_4 , TiSi and Al_3Ti areas. The overall alloy composition is far away from areas where the TiAl is in equilibrium with Al_3Ti and Ti_5Si_3 . In MG6-HT800 the TiAl had $\text{Al} + \text{Si} = 64.2$ at% and $\text{Al}/\text{Si} = 19$, and in MG6-HT1200 it had $\text{Al} + \text{Si} = 64.3$ at% (unchanged) but $\text{Al}/\text{Si} = 2.5$, meaning that its composition moved towards the Ti rich corner of the Ti-Al binary. It should be noted that the one analysis of Ti_3Al (see table 30) gave $\text{Si} = 5.8$ at%, which is higher than the Si solubility in Ti_3Al of 1.5 at% given by Azevedo and Flower (2002).

The above discussion and the observation of a phase in MG6-HT1200 with composition close to Ti_3Al and the fact that it was easier to find the TiSi in MG6-HT1200 compared with MG6-HT800 while the opposite was the case for TiAl , would suggest that the TiAl aluminide might not be stable and that Ti_3Al might be stable in the alloy MG6. This

suggestion should be tested using longer heat treatment at 1200 °C. The $\text{TM}_9\text{Si}_7\text{Al}_5$ intermetallic is not a stable phase in MG6.

The DSC trace (figure 91) showed an endothermic peak on heating around 1100 °C with an accompanying rapid increase in weight gain in the TG trace. This could be associated with the reaction $\text{L} + \text{Ti}_5\text{Si}_4 \leftrightarrow \text{TiSi} + \text{Al}_3\text{Ti}$ at just above 1105 °C (Raghavan 2005) with TiSi having formed at a lower temperature as suggested by the results for MG6-HT800. It should be noted that alloy compositions of MG6-AC, from which the specimen for the DSC study was taken, fall in the three phase Ti_5Si_4 , TiSi, Al_3Ti area at 1105 °C in the solidus surface of the Ti-Al-Si system, see figure 113.

With the exception of localised melting at 1200 °C, formation of fibrous (wool like) Ti_5Si_4 in the cast, heat treated and oxidised alloy MG6 and “partitioning” of 5-3 silicide grains was observed, as was the case in the alloy MG5. The same discussion applies to the alloy MG6 as that for the alloy MG5. Subtle differences between the two alloys were observed regarding (i) not stable (metastable) phases like $\text{TM}_9\text{Si}_7\text{Al}_4$ in MG6-HT800, $\text{TM}_8\text{Al}_{11}\text{Si}_3$ in MG5 oxidised at 800 °C, $\text{TM}_2\text{Si}_{1.5}\text{Al}$ in oxidised MG5 at 800 °C and 1200 °C compared with $\text{Ti}_{2.5}\text{AlSi}_{0.3}$ in MG6 oxidised at 1200 °C, which are attributed to the slightly different chemistries of the two alloys and (ii) the identification of Ti_2Al_5 with/out Al_3Ti in MG5 and mostly of the latter in MG6, which is attributed to difficulties in EDS analyses and the fact that the alloy MG6 was richer in Al than MG5 and Ti_2Al_5 and Al_3Ti have close compositions with the latter being more rich in Al.

The precipitation of a second phase in TiAl with contrast similar to that of the 5-3 and/or 5-4 and/or TiSi silicides was (perhaps) slightly more pronounced in the alloy MG6 compared with the alloy MG5 (see figure 94 in this chapter and figure 73 and figure 82 in the previous chapter) and in MG6 was observed near areas of localised melting. Could this be linked with the transformation $L + Ti_5Si_4 \leftrightarrow TiSi + Al_3Ti$ on cooling? No evidence of such a transformation was shown in the DSC trace. Alternatively, it could be precipitation of a second phase from TiAl (mother phase), see figure 114. This figure shows the TiAl region of the Ti-Al binary phase diagram with transformation of (precipitation from) TiAl to Ti_3Al or Al_2Ti , respectively from Al lean and Al rich TiAl, where the indicated Al concentrations are those in TiAl in MG6-HT1200 and MG6-HT800. In the former case the Ti_3Al would exhibit lighter contrast than TiAl (as observed in TiAl in MG6-HT1200) and in the latter case the Al_2Ti would exhibit darker contrast than TiAl (not exhibited by the precipitates in TiAl). There is solubility of Si in both phases (i.e., Al_2Ti and Ti_3Al) which could also explain the higher Si content of the TiAl in MG6-HT1200, see table 30 and table 34. Given the contrast of the fine second phase in TiAl in MG6-HT1200, the absence of a peak in the cooling DSC trace of MG6 and the fact that one analysis corresponds to Ti_3Al , it is suggested that the fine precipitates were Ti_3Al aluminide.

The alloy MG6, like the alloys MG2 and MG5, had exceptional oxidation behaviour at 800 °C and 1200 °C. The alloy did not pest at 800 °C, it did not oxidise catastrophically at 1200 °C, in both temperatures it formed a thin and adherent scale which did not spall off at all at 1200 °C and during subsequent handling of the oxidised specimen, and alumina scale was formed at both temperatures. The alumina scale was thicker at 1200 °C and seemed to adhere better to the MG6 alloy substrate.

According to GXRD, the alloys MG2, MG5 and MG6, which can be considered as belonging to the same family of alloys, formed α -Al₂O₃ in their scales at 1200 °C, which was confirmed by EDS for the latter two alloys, and also at 800 °C, which was confirmed only by EDS for the alloys MG5 and MG6. All three alloys did not pest at 800 °C. Compared with the alloy MG2, which exhibited parabolic oxidation kinetics at 800 °C, the alloy MG6 followed linear oxidation kinetics. At 1200 °C, the alloy MG2 followed parabolic oxidation kinetics up to 14 h with $k_p = 6 \cdot 10^{-11} \text{ g}^2\text{cm}^{-4}\text{s}^{-1}$ and then linear kinetics, with an overall parabolic rate constant $k_p = 2 \cdot 10^{-10} \text{ g}^2\text{cm}^{-4}\text{s}^{-1}$ while the alloy MG6 had parabolic oxidation kinetics throughout (indicative of inherently better oxidation) but with higher rate constants at the early stages (due to localised melting?) compared with the alloy MG2, see table 31, and a lower overall parabolic rate constant $k_p = 3 \cdot 10^{-13} \text{ g}^2\text{cm}^{-4}\text{s}^{-1}$, indicative of superior oxidation behaviour compared with MG2. Compared with the single crystal Ni superalloy CMSX-4, the oxidation of MG6 at 1200 °C was exceptional, with $k_p^{\text{MG6-1200}}/k_p^{\text{CMSX4-1200}} = 0.03$.

There were similarities regarding the type of phases formed below the scale in the alloys MG5 and MG6 and their contamination by oxygen. The latter was more severe for 5-3 silicide grains compared with 5-4 silicide grains, and the contamination of the latter was the same as that of aluminides. The same discussion applies for the oxidation of the alloy MG6 as that for the alloy MG5. Regarding the contamination of the alloy further below the scale and towards the bulk, the alloys MG5 and MG6 exhibited better behaviour compared with the alloy MG2.

The alloys of this study contain Nb and Ti, form oxide(s) of these metals and their oxides can form binary (mixed) oxides, namely the titanium niobates that were formed

on the alloys studied in this thesis. The latter have also been reported to form in the scales of oxidised Nb silicide based alloys (Zelenitsas and Tsakirooulos, 2006, Geng et al, 2006). Could the type of niobate(s) in the scale play a role concerning its adhesion to the substrate?

Niobium has +2, +4 and +5 stable oxidation states. In the Nb-O binary phase diagram the stable oxides are NbO, NbO₂ and Nb₂O₅. NbO has a solubility range (NbO_{0.982} to NbO_{1.008}) and cubic structure. NbO₂ has no solubility range and body centred tetragonal structure. Nb₂O₅ has monoclinic structure and was originally reported as Nb₂O_{4.8}. The high temperature form of niobium pentoxide, H-Nb₂O₅, has a solubility range on the metal-excess side at 1300-1400 °C (Kimura 1973, Schafer et al., 1969). H-Nb₂O₅ is the stable form in air above 900 °C. Ti⁴⁺ can substitute for Nb⁴⁺ in the sub-stoichiometric H-Nb₂O₅. The Me⁴⁺/Me⁴⁺ ratio can be changed via changes to Ti-Nb oxides.

According to Roth and Coughanour (1955) there exist the binary oxides TiO₂-Nb₂O₅ and TiO₂-3Nb₂O₅. They reported a room temperature solid solubility limit of approximately 18 at% niobium in TiO₂. The TiO₂-3Nb₂O₅ binary oxide was later suggested to be the Ti₂Nb₁₀O₂₉ oxide by Wadsley (1961a, 1961b) and that it can have monoclinic or orthorhombic structure. The most often reported niobate on Nb silicide based alloys is TiNb₂O₇. The crystal structure of this oxide is based on the ReO₃ structure and contains blocks of corner-sharing MeO₆ octahedra (Me = Nb, Ti). This structure is responsible for the variety of niobates that can form.

The different stoichiometries and structures of the binary oxides are attributed to variations in the size of these blocks and the way they are joined together. The metal

positions in the structures are occupied by one or other of these elements in a random manner. Defects are caused by the presence of intergrowth. Each metal atom (Ti and Nb) is coordinated to six oxygens (Wadsley, 1961b, Von Dreele and Cheetham, 1974) forming an octahedral grouping (TiO_6 and NbO_6). In TiNb_2O_7 these blocks contain 9 MeO_6 octahedra and form a linear column along the b-axis of the unit cell. In all cases, the b axis, which is the short axis of the structures, is ≈ 3.8 Å. The latter is the length of the octahedral body diagonal of the structures. Perpendicular to the b-axis the columns are bound by crystallographic shear planes. Across the shear planes the MeO_6 octahedra share edges.

The Ti^{4+} ion has a preference for the octahedra at the corners and edges of the blocks (i.e. those octahedra which lie along the shear planes and share, therefore, one or two edges with other octahedra) (Von Dreele and Cheetham, 1974, Casperin, 1984). The crystal structure shows an analogy with the rutile structure. Marinder and Magneli (1958) found the ideal tetragonal rutile structure over a very wide range of composition in the $\text{Ti}_{(1-x)}\text{Nb}_x\text{O}_2$ system.

In systems that exhibit crystallographic shear the mechanism by which shear planes are formed and how they move is important. Magneli reported the “shear-type” $\text{Ti}_n\text{O}_{2n-1}$ structures (nowadays known as Magneli phases) with $4 \leq n \leq 10$. These are made up of layers of rutile structure with a width of n TiO_6 octahedra. The successive layers are offset such that the first Ti in the new layer is in an interstitial position relative to the last Ti of the preceding layer. The TiO_6 octahedra share faces across this discontinuity or crystallographic shear plane and thereby reduce the O:Ti ratio as required by the oxygen deficiency. Disorder is created by Nb^{5+} as a dopant in TiO_2 .

There is anisotropy of oxygen diffusion in H-Nb₂O₅. Sheasby and Cox (1968) reported that both in stoichiometric and slightly reduced Nb₂O₅, the diffusion coefficients for oxygen are up to 200 times greater parallel to the b axis than perpendicular to this direction.

In the literature, black Ti niobate is often reported as TiNb₂O₇. Single compound TiNb₂O₇ is known to grow as white and very friable needles whereas the TiNb₂O_{6.42} is black and very resistant to fracture. These properties are thought to be reversible (the time for thermodynamic equilibrium will be longer than that to achieve the oxidized state). The change of the colour of the scale formed at 800 and 1200 °C might thus be linked with slight changes in the stoichiometry of the Ti niobates formed in the scale, with the latter depending on the “shear-type” Ti_nO_{2n-1} structure(s) formed (n values), variations in the size of R₃O₃ type blocks and corner-sharing MeO₆ octahedra (Me = Nb, Ti) and the way they are joined together. If we were to accept that the TiNb₂O_{6.42} is very resistant to fracture, the improved adhesion of the scales formed on the alloys MG2, MG5 and MG6 could be attributed to oxidation conditions that promoted alumina formation and also stabilised the TiNb₂O_{6.42} in the scale.

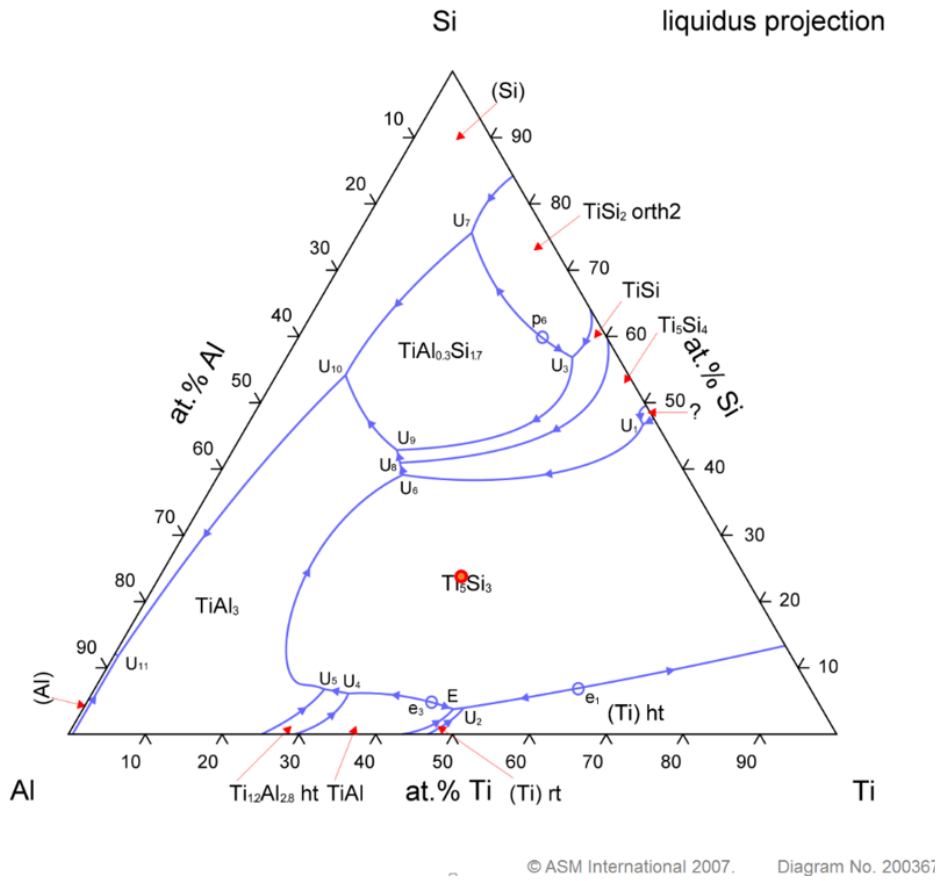
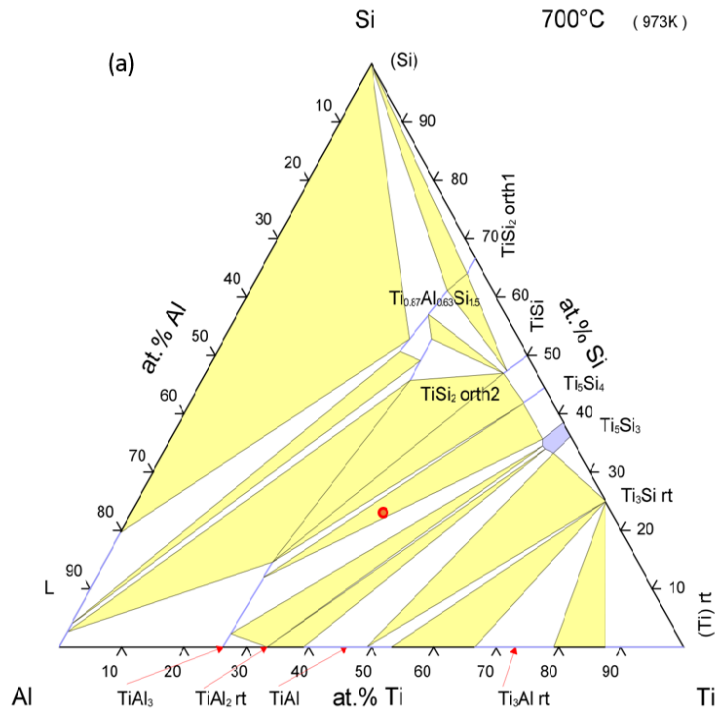
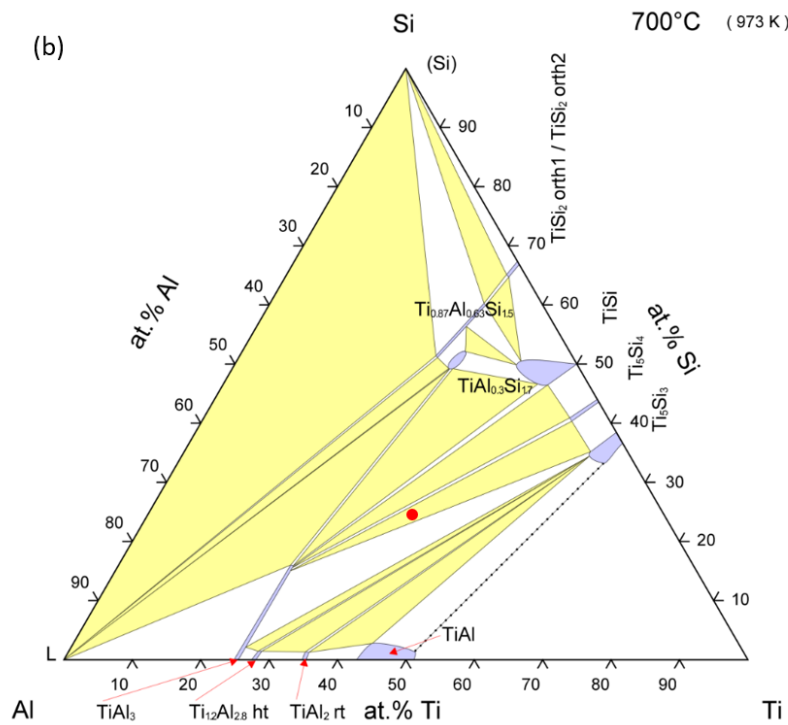


Figure 110: Liquidus projection of the Ti-Al-Si system



© ASM International 2007. Diagram No. 1300218



© ASM International 2006. Diagram No. 976532

Figure 111: Ti-Al-Si isothermal sections at 700 °C from (a) Perrot, (b) Raman, Red is for the overall average alloy composition

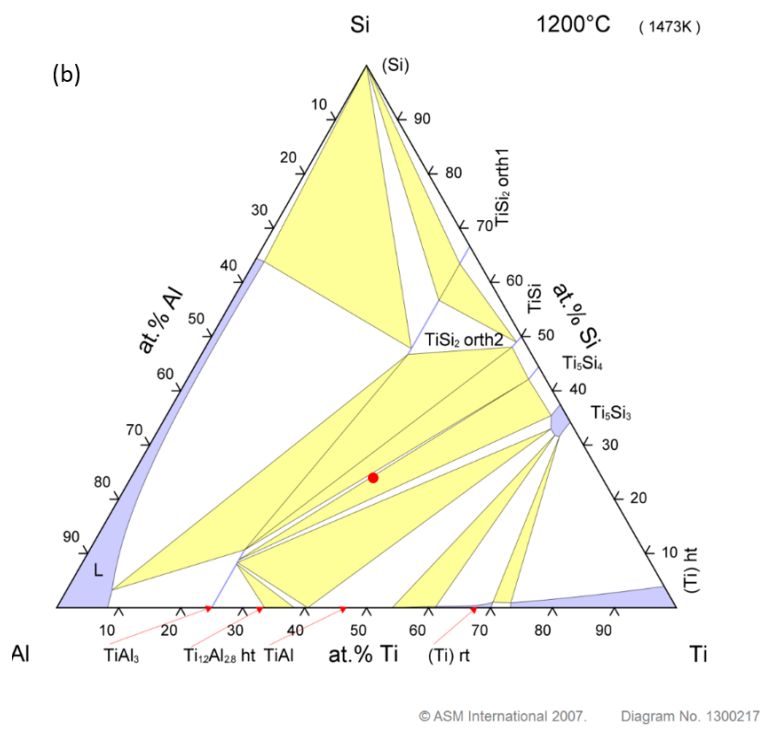
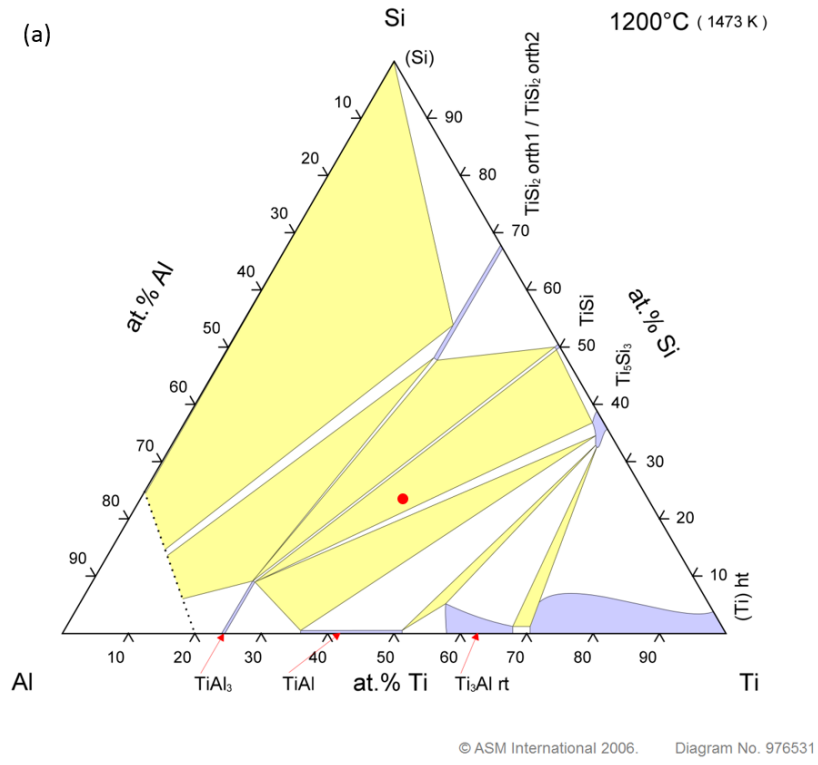


Figure 112: Ti-Al-Si isothermal sections at 1200 °C from (a) Schob, (b) Perrot, red for overall and bottom compositions

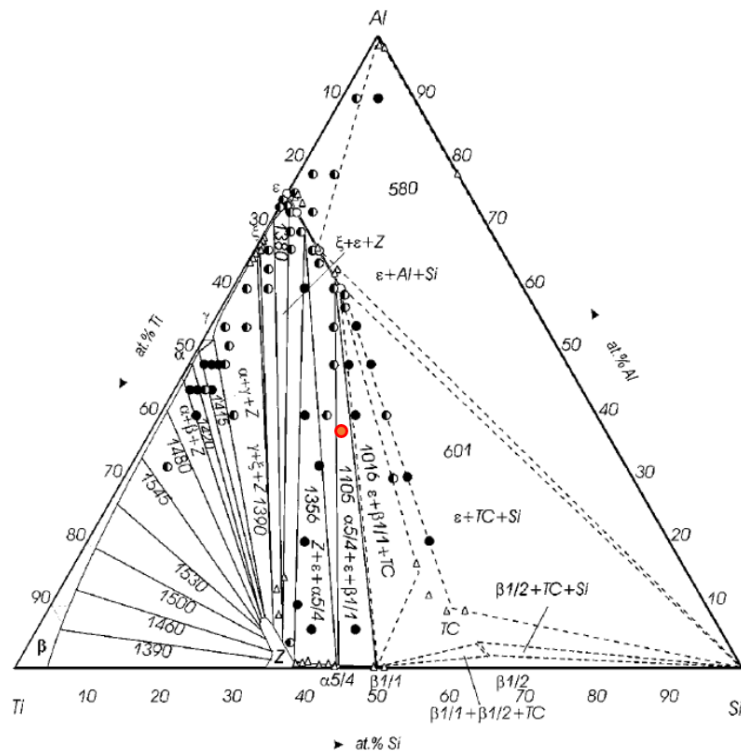


Figure 113: The solidus surface of the Ti-Si-Al system (Bulanova et al, 2004)

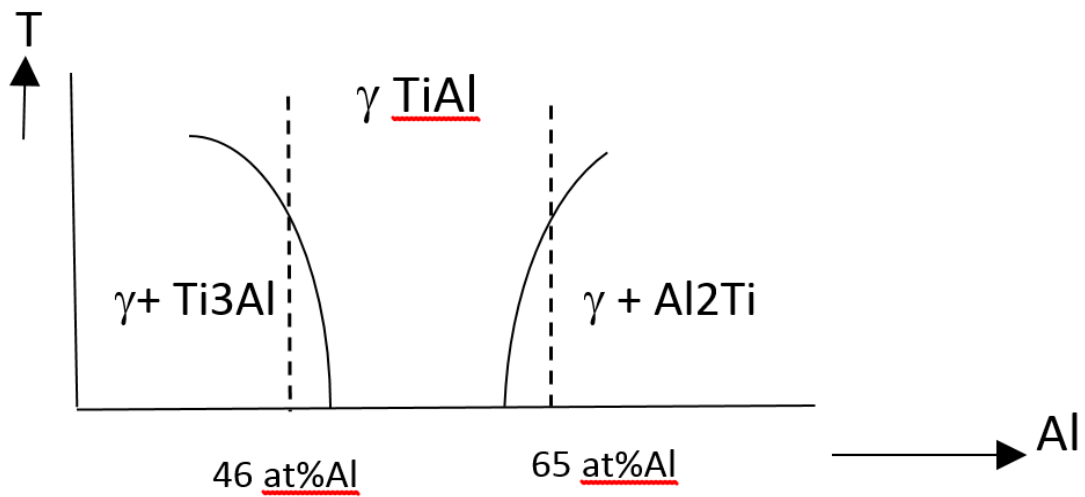


Figure 114: Schematic of TiAl region of the Ti-Al binary phase diagram

6.1.5 Summary

The Al rich alloy MG6 (compared with the alloys MG2 and MG5) was selected to study phase stability, oxidation behaviour and in particular whether alumina scale could form at 800 °C and/or 1200 °C, owing to the even higher Al concentration in this alloy. There was macrosegregation of Al, Si and Ti in MG6-AC. Compared with the alloy MG2, the macrosegregation of Si and Ti was reduced but that of Al was increased.

The same microstructures were observed in the top, bulk and bottom of MG6-AC and that in the bottom was finer. The phases present in these parts of the ingot were $\gamma\text{Nb}_5\text{Si}_3$ (primary phase), Ti_5Si_4 , the tri-aluminide Al_3TM and TiAl . Compared with the alloy MG5-AC, the TiSi in MG5 was replaced by TiAl in MG6. The fibrous structure of Ti_5Si_4 around Nb_5Si_3 was more pronounced in the bottom of the ingot, which incidentally was also Al rich.

The microstructure of the heat treated alloy at 800 °C for 100 h, MG6-HT800, exhibited significant chemical inhomogeneity for Al, Si and Ti and consisted of the $\gamma\text{Nb}_5\text{Si}_3$, the aluminides TiAl and Al_3TM , the silicides Ti_5Si_4 and TiSi and the $\text{TM}_9\text{Si}_7\text{Al}_4$ intermetallic. The formation of the $\text{TM}_9\text{Si}_7\text{Al}_4$ intermetallic could be linked with the exothermic peak in the DSC trace at around 700 °C, the latter however could also be due to the formation of $\text{Ti}(\text{Al}_{1-x}\text{Si}_x)_3$ (tI8, I4/mmm, TiAl_3 (h)) with $0 < x < 0.15$ that is stable above 735 °C.

The microstructure of the heat treated alloy at 1200 °C for 100 h, MG6-HT1200, exhibited chemical inhomogeneity for Al and Si and consisted of the hexagonal $\gamma\text{Nb}_5\text{Si}_3$, the aluminides TiAl and Al_3TM , the silicides Ti_5Si_4 and TiSi and Ti_3Al . There

was localised melting in areas of the microstructure where the phases Ti_5Si_4 , Al_3Ti , TiSi and TiAl were present. In the TiAl near these areas there was precipitation of a second phase, likely Ti_3Al or silicide. The localised melting was associated with the endothermic peak in the DSC trace on heating around $1100\text{ }^\circ\text{C}$, which was accompanied by rapid increase in weight gain in the TG trace, and could be associated with the reaction $\text{L} + \text{Ti}_5\text{Si}_4 \leftrightarrow \text{TiSi} + \text{Al}_3\text{Ti}$ occurring on heating at just above $1105\text{ }^\circ\text{C}$ with TiSi having formed at a lower temperature.

The two heat treatments confirmed that the TiSi is stable in this alloy and that the $\text{TM}_9\text{Si}_7\text{Al}_4$ intermetallic is not a stable phase. Formation of fibrous (wool like) Ti_5Si_4 in the heat treated and oxidised alloy MG6 and “partitioning” of 5-3 silicide grains was also observed.

The alloy MG6 had exceptional oxidation behaviour at $800\text{ }^\circ\text{C}$ and $1200\text{ }^\circ\text{C}$. The alloy did not pest at $800\text{ }^\circ\text{C}$, but oxidised linearly, it did not oxidise catastrophically at $1200\text{ }^\circ\text{C}$ and followed parabolic oxidation, at both temperatures it formed a thin and adherent scale which did not spall off at all at $1200\text{ }^\circ\text{C}$ and during subsequent handling of the oxidised specimen, and alumina scale was formed at both temperatures. The alumina scale was thicker at $1200\text{ }^\circ\text{C}$ and seemed to adhere better to the MG6 alloy substrate. The oxidation at $1200\text{ }^\circ\text{C}$ was better than that of the single crystal Ni superalloy CMSX-4.

At $800\text{ }^\circ\text{C}$ the scale consisted of Ti niobates, TiO_2 , SiO_2 , Nb_2O_5 , TiAl_2O_5 and HfO_2 . At $1200\text{ }^\circ\text{C}$ the same oxides were present in the scale plus $\alpha\text{Al}_2\text{O}_3$. The latter was thick and continuous even around corners and did not spall off during handling of the

oxidised specimen. There was a change in the colour of the scale between 800 °C and 1200 °C.

The oxidised microstructure at 800 °C consisted of $\gamma\text{Nb}_5\text{Si}_3$, Ti_5Si_4 , TiSi , Al_3TM , TiAl and TiAl_2 . The silicides and aluminides below the scale were contaminated, the former more severely than the latter, with worse contamination of Nb_5Si_3 compared with Ti_5Si_4 . The oxidised microstructure at 1200 °C exhibited evidence of localised melting. The microstructure consisted of $\gamma\text{Nb}_5\text{Si}_3$, $(\text{Ti,Nb})_5\text{Si}_3$, Ti_5Si_4 , Al_3TM , $\text{TM}_{2.7}\text{AlSi}_{0.3}$ and TiAl_2 .

Chapter 7: Conclusions and Suggestions for future work

7.1 Conclusions

The alloys studied in this thesis were selected in order to find out how the synergy of Al, Hf and Ti, which are three key elements that control the properties of Nb silicide based alloys, affects phase stability and oxidation behaviour when the Al concentration in the alloy increases at the expense of Nb. In particular we were interested to find out whether the above synergy promotes the stability of specific type(s) of silicide(s), whether the Nb_3Si is stabilised, what the effect is on the stability of the bcc Nb_{ss} and which other phase(s) is (are) stabilised in the microstructures. Given that Al has an adverse effect on the toughness of the Nb_{ss} at concentrations exceeding 5 at%, the study of the Al rich alloys was particularly interested to discover if in Al rich alloys $\alpha\text{Al}_2\text{O}_3$ could form and whether pest oxidation is suppressed. Alumina forming high temperature alloys are of particular interest as potential components of a multi-material bond coat in a coating system for Nb silicide based alloys.

In the four alloys investigated in this study, Al was not the only element with the potential to improve oxidation resistance via alumina formation. The concentrations of Si and Ti were also high and thus we were interested to find out whether Al niobate could form in the scales and whether SiO_2 and TiO_2 could form, particularly since the latter can form binary oxides with Nb oxides, namely niobates and the former could be problematic owing to the well-known CMAS issues with coating systems on Ni based superalloys.

Macrosegregation

Macrosegregation was present in all the alloys studied. The simultaneous existence of Al and Hf in the alloys increased the macrosegregation of Si. When the Al concentration in the alloys increased there was macrosegregation of Al, Si and Ti. Owing to macrosegregation different solidification paths were followed in the alloy MG2. The chemical inhomogeneity resulting from the macro-segregation of the aforementioned solute elements persisted in the heat treated microstructures.

Integrity of Ingots

The heavily macrosegregated ingots of the alloys were cracked, particularly of the alloys with increased Al concentration, where the bcc Nb_{ss} was not stable and other intermetallics than just Nb₅Si₃ were formed. The most brittle of all the studied alloys was the alloy MG5. The above would suggest that applying and using the Al rich alloys of this study in a coating system would not be straight forward.

Phase transformation and phase stability

Nb₃Si

All four alloys confirmed that the synergy of the Al, Hf and Ti did not stabilise the Nb₃Si.

Nb₅Si₃

The synergy of the Al, Hf and Ti suppressed the $\beta\text{Nb}_5\text{Si}_3 \rightarrow \alpha\text{Nb}_5\text{Si}_3$ transformation and tended to stabilise the hexagonal $\gamma\text{Nb}_5\text{Si}_3$, meaning that hexagonal 5-3 silicide was the stable one in these alloys. This should be confirmed using longer heat treatments.

Nb solid solution

The microstructures of the alloys MG2, MG5 and MG6, i.e., the alloys with high Al concentration also confirmed that at high Al contents the bcc Nb_{ss} was not stable.

Aluminide intermetallic phases

Metastable intermetallic phases were formed in the cast alloy MG2-AC and heat treated alloy MG6-HT800, respectively the TM_{3,7}Al₃Si and TM_{2,35}Al_{1,65}Si in the former and the TM₉Si₇Al₄ in the latter. With the exception of the aforementioned metastable intermetallics, the microstructures of the Al rich alloys were remarkably stable. In all three Al rich alloys MG2, MG5 and MG6 the tri-aluminide Al₃TM and TiAl were stable. In the MG2 the Ti₂Al₅ was also stable and in the alloys MG5 and MG6 the Ti₅Si₄ and TiSi silicides were stable. Thus, by increasing the Al concentration in the alloy Al rich aluminides were stabilised and by keeping Si/Ti ≥ 1 two extra silicides were also stabilised in the microstructure. In other words, by increasing the Al content the bcc Nb_{ss} was suppressed and the microstructure consisted of phases that could act as reservoirs of Al and Si during oxidation.

Localized melting

By increasing the Al content in the alloy MG6 localised melting was observed in MG6-HT1200.

Oxidation at 800 °C

The synergy of Al and Hf was very effective in suppressing pest oxidation in all the alloys of this study. This would suggest that high Al concentration is not essential for suppressing pest. The alloys MG1 and MG2 followed parabolic oxidation kinetics at

800 °C but the oxidation rate constant of the alloy MG6 was linear, probably due to the formation of the metastable $\text{TM}_9\text{Si}_7\text{Al}_4$ at around 700 °C.

The evidence for alumina in the scale formed at 800 °C increased with Al content from the alloy MG2 to the alloy MG6 but there was no evidence from GXR and EDS for alumina in the scale of the alloy MG1.

Oxidation at 1200 °C

The synergy of Al and Hf was able to suppress scale spallation at 1200 °C only in the Al rich alloys MG2, MG5 and MG6. This would suggest that high Al content is essential for improved adhesion of the scale.

The presence of $\alpha\text{Al}_2\text{O}_3$ scale was confirmed by GXR and EDS in the Al rich alloys MG2, MG5 and MG6, after isothermal oxidation at 1200 °C.

The uniformity and continuity of scale and its adherence to the substrate even around corners was improved as the Al increased to that in the alloy MG6. The latter exhibited the best overall parabolic rate constant and its oxidation was superior to that of the single crystal Ni superalloy CMSX-4. Considering the localised melting observed in the alloy at around 1105 °C, and its linear oxidation at 800 °C, this was an impressive result and pointed to inherent oxidation resistance of alloy(s?) near the composition of the alloy MG6. This could be tested in future research.

Phases in scale

The GXRD data of all the oxidised alloys suggested the presence of Nb_2O_5 , SiO_2 , TiO_2 , HfO_2 and Ti niobates at 800 °C and 1200 °C plus the TiAl_2O_5 at 800 °C for the Al rich alloys and TiAl_2O_5 and $\alpha\text{Al}_2\text{O}_3$ at 1200 °C for the Al rich alloys.

EDS provided clear evidence for $\alpha\text{Al}_2\text{O}_3$ on the Al rich alloys but not for SiO_2 , Nb_2O_5 , and TiO_2 and Ti niobates.

The colour of the scales formed was consistent with that reported for Ti niobates.

It is considered unlikely that suppression of TiO_2 and Ti niobates is possible in alloys with Ti content similar to that of the alloys of this study. However, the results for the Al rich alloy would suggest that the type of Ti niobate that forms plays a key role regarding the adhesion of the scale. This could be tested in future research.

Contamination of microstructure of oxidation

Contamination of the phases present in the substrate below the scale was not suppressed by the synergy of Al, Si and Ti in the alloys of this study, but the extent of contamination towards the bulk was reduced with increasing Al concentration.

The Nb_{ss} was the most severely contaminated phase followed by the 5-3 silicide and then the aluminides TiAl and Al_3TM , the contamination of which was essentially similar.

The Ti_5Si_4 silicide was more resistant to contamination compared with the 5-3 silicide and remarkably was also less contaminated than Ti_2Al_5 . This would suggest that it is worth studying alloys where the 5-4 silicide is the only silicide present together with Al rich aluminides in the microstructure.

7.2 Suggestions for future work

The stability of hexagonal 5-3 in Al and Hf containing Nb silicide based alloys should be investigated further, and alloys with low and high Al concentrations should be considered. This study would require prolonged heat treatments.

This study confirmed the formation of $\alpha\text{Al}_2\text{O}_3$ scale on the Al rich alloys. The stability of this scale upon prolonged oxidation should be studied. Furthermore, the behaviour of the scale under thermal cycling should be studied.

The results for the oxidation of the Al rich alloys of this study would suggest that there exist alloy composition(s?), probably between those of the alloys MG5 and MG6, where best oxidation resistance with no pest oxidation and formation of stable adhering continuous $\alpha\text{Al}_2\text{O}_3$ scale is possible. Given the remarkable low contamination of 5-4 silicide compared with 5-3 silicide, this research should explore alloy compositions where the microstructure consists of 5-4 silicide and Al_3TM and TMAI aluminides.

The type of Ti niobate formed in alloys with different Si/Ti ratio and Al content should be studied to establish the exact type (chemistry and structure) of niobate formed. This research would require TEM studies of the scales formed on such alloys after short, long and prolonged isothermal and cyclic oxidation.

References

- Abbaschian A.B and Gokhale G.J. 1989. "The Hf-Si (Hafnium-Silicon) System." *Alloy Phase Diagram* 10 (4): 390-393.
- Alyamovskii S.I, Gelp P.V and Matveenko I. 1962. "concentration of stability of niobium silicide at 1250 °C." *Russ J. Inorg. Chem* 7: 432-435.
- Anton D.L, Shah D. M, Duhl D. N, Gaimei A.F. 1989. "Selecting high temperature structural intermetallic compounds: The engineering approach." *Metals* 41 (9): 12-17.
- Azevedo C.R.F, H.M Flower. 2002. "Experimental and Calculated Ti-rich Corner of the Al-Si-Ti Ternary Phase Diagram." *Calphad* 26: 353-373.
- Bewlay B.P., Lewandowski J.J., and Jackson M.R. 1997. "Refractory Metal-intermetallic In-Situ Composites for Aircraft Engines." *JOM* (Springer) 49 (8): 44-45.
- Bewlay B.P and Jackson M.R. 2003. *Comprehensive composite materials*. Chapter 3.22, page 579-615. Edited by Anthony Kelly and Karl Zewben. Elsevier.
- Balsone S.J, Bewlay B. P., Jackson M.R., Subramanian P.R., Zhao J.c., Chatterjee A and Heffernan T. M., 2001. "Materials beyond superalloys: Exploiting high temperature composites." In *structural intermetallics*, Jackson Hole, 99-108. WY: Third international symposium on structural intermetallics.

Bywater G. 2017. “ A Study On The Microstructure And High Temperature Oxidation Of Nb-Silicide Alloys With Hf And Ge Or Al Additions And The NbCr₂ Laves Phase”. *PhD Thesis*. University of Sheffield.

Batzner C, Beuers J., Hoch M. and Schmid F R. 1993. “Aluminium-Niobium-Silicon, Ternary Alloys.” *Ternary Alloys, VCH 7*: 370-374.

Bewlay B.P, Bishop R.R, Jackson M.R. 1999a. “The Nb-Hf-Si ternary phase diagram: liquid-solid phase equilibria in Nb- and Hf-rich alloys.” *Z. Metallkd* 90 (6): 413-422.

Bewlay B.P, Jackson M. R, Sutliff J. A, Lipsitt H.A , Reeder W.J. 1995b. “Solidification processing of high temperature intermetallic eutectic-based alloys.” *Mater. Sci. Eng. A* A192-193 (2): 534-543.

Bewlay B.P., Jackson M.R, Lipsitt H.A. 1997. “The Nb-Ti-Si ternary phase diagram: evaluation of liquid-solid phase equilibria in Nb and Ti-rich alloys.” *J. Phase Equilibria* 18 (3): 264-278.

Bryant R.T. 1962. “The Solubility Of Oxygen In Transition Metal Alloys.” *Journal of the Less-Common Metals* 4: 62-68.

Brukl C, , Nowotny H., Benesovski. 1961. “Investigation of the ternary systems V-Al-Ti, Nb-Al-Ti, Cr-Ti-Si, Cr(Mo)-Al-Si.” *Montash. Chem.*, 92: 967-980.

Bulanova M, Tretyachenko L, Golovkova M and Meleshevich K. 2004. "Phase equilibria in the α -Ti-Al-Si region of the Ti-Si-Al system." *Journal of Phase Equilibria and Diffusion* 25 (3): 209-229.

Bulanova M, Fartushna I. 2010. *Niobium - Silicon - Titanium*. Vol. 11E3, in *Refractory metal systems: Landolt-Börnstein - Group IV Physical Chemistry*, by MSIT Materials Science International Team, edited by S. Ilyenko G. Effenberg, 505-522. Stuttgart: Springer-Verlag Berlin Heidelberg.

Hernandez-Negrete Ofelia. 2017. "Study Of Intermetallic Alloys For High Temperature Applications -Beyond The Ni Superalloys- ". *PhD Thesis*. University of Sheffield.

Casperin M. 1984. "Refinement of $TiNb_2O_7$ structure and cation reactivation." *J. Solid State Chem* (53) 144.

Chan K.S. 2002. "Alloying effect on fracture mechanism in Nb-based intermetallic in-situ composites." *Materials Science and Engineering* 329: 513-522.

Chan K.S. 2005. "Alloying effects on the fracture toughness of Nb-based silicides and laves phases." *Material Science and Engineering A* 409: 257-269.

Chan K.S. 2002. "Modeling creep behavior of niobium silicide in situ composites." *Materials Science and Engineering A* 337: 59-66.

Chan S.K. 2004. "Cyclic oxidation response of multiphase Niobium-Based Alloys." *Metallurgical and Materials Transactions A* 35-A: 589-597.

Davidson D.L, Chan K.S. 1999. "The fatigue and fracture resistance of a Nb-Cr-Ti-Al alloy." *Metallurgical and Materials Transactions A* 30 (no. 8): 2007-2018.

Davidson D.L, Chan K.S. 2001. "Delineating brittle-phase embrittlement and ductile phase toughening in Nb-based in situ composites." *Metallurgical and Materials Transactions A* 32 (11): 2717-1727.

Davidson D.L, Chan K.S. 1999. "Effect of Ti Addition on cleavage fracture in Nb-Cr-Ti solid-solution alloys." *Metallurgical and Materials Transactions A* 30A: 925-939.

Dezellus O, Gardiola B, Andrieux J, Lomello-Tafin M, and Viala JC. 2014. " On the Liquid/Solid Phase Equilibria in the Al-Rich Corner of the Al-Si-Ti Ternary System." *JPEDAV* 35: 137-145.

Dieter. G E. 1986. *Mechanical Metallurgy*. Third. Boston: McGraw-hill Boston.

Felten. J.E. 1969. "The Interaction of The Alloy Niobium-25Titanium With Air,Oxygen And Nitrogen, I. The Unusual Oxidation Behavior Of Nb-25Ti At 1000 °C. *J. Less-Common Metals* 185-197.

Felten. J.E. 1969. "The Interaction of The Alloy Niobium-25Titanium With Air, Oxygen And Nitrogen, II. The Reaction Of Nb-25Ti in Air And Oxygen Between 650 °C And 1000 °C." *J. Less-Common Metals* 199-206.

Fleischer, R.L. 1994. *Miscellaneous Novel Intermetallics*. Vol. 2, in *Intermetallic compounds*, edited by R.L. Fleischer J.H Westerbrook, 237-256. John Wiley & Sons Ltd.

Grammenos. I, Tsakirooulos. P. 2010. "Study of the role of Al, Cr and Ti additions in the microstructure of Nb-18Si-5Hf base alloys." *Intermetallics* 18 (2): 242-253.

Geng. J, Tsakirooulos. P , Shao. G. 2007. "A Thermo-Gravimetric And Microstructural Study Of The Oxidation Of Nb_{ss}/Nb₅Si₃-Based In Situ Composites With Sn Addition ." *Intermetallics* 15 (3): 270-281.

Geng. J, Tsakirooulos. P , Shao. G. A. 2006 .A441. "Oxidation of Nb–Si–Cr–Al in situ composites with Mo, Ti and Hf additions ." *Materials Science and Engineering* 26-38.

Geng T, Li C , Bao J , Zhao X , Du Z and Guo C. 2009. "Thermodynamic assessment of the Nb–Si–Ti system ." *Intermetallics* 17: 343-357.

Geng. J, Tsakirooulos. P , Shao. G. A. 2007. "A study of the effect of Hf and Sn additions the microstructure of Nb_{ss}/Nb₅Si₃ based in situ composites." *Intermetallics* 15: 69-76.

Groubner, J, Mirkovic´. D, Schmid-Fetzer. R. 2005. “Thermodynamic Aspects of Grain Refinement of Al–Si Alloys Using Ti And B .” *Materials Science and Engineering A* 395: 10-21.

Ghosh G, Olson G.B. 2007. “Integrated design of Nb-based superalloys: Ab initio calculations, computational thermodynamics and kinetics, and experimental results.” *Acta Materialia* 55: 3281–3303.

Gupta. S.P. 2003. “Intermetallic compounds in diffusion couples of Ti with an Al–Si eutectic alloy .” *Materials Characterization* 49: 321-330.

Grabke H. J., Meier G. H. 1995. “Accelerated oxidation, internal oxidation, intergranular oxidation, and pesting of intermetallic compounds.” *Oxidation of Metals* 44 (1): 147–176.

Hou P.Y. 2010. *Oxidation of Metals and Alloys*. “Shreir's corrosion: basic concepts, high temperature corrosion” Vol. 1, 195-239. Elsevier .

Jackson M.R., Bewlay B.P., Zhao J,-c. and Subramanian P.R.. 2003. “A Review of Very High Temperature Nb-silicide-Based Composites.” *Metallurgical and Meterials Transactions A* 34A: 2043-2052.

Jackson M.R., Bewlay B.P, Rowe R.G., Skelly D.W. and Lipsitt H.A. 1996. “High Temperature Refractory Metal-Intermetallic composites.” *JOM* 48 (1): 36-44.

Kelkar H.A, Carim G.P. 1995. "Phase Equilibria in the Ti-Al-O System at 945 °C and Analysis of Ti/Al₂O₃ Reactions." *Journal of the American Ceramic Society* 78 (3): 572-576.

Kimura S. 1973. "Phase Equilibria in the System NbO₂-Nb₂O₅: Phase Relations at 1300 and 1400 °C and Related Thermodynamic Treatment". *J. Solid State Chem* (6) 438-449.

Kimura Y, Mishima Y, Yamaoka H, Sekido N. 2005. "Processing, microstructure, and mechanical properties of (Nb)/Nb₅Si₃ two-phase alloys." *Metallurgical and Materials Transactions A* 36 (3): 483–488.

Kim W, Tanaka H, Kasama A, Hanada S. 2001. "Microstructure and room temperature fracture toughness of Nb_{ss}/Nb₅Si₃ in situ composites." *Intermetallics* 9: 827-834.

Knittel S, Mathieu S, Vilasi M. 2012. "Oxidation behaviour of Arc-melted and uniaxial hot pressed MoSi₂ at 500oC." *Intermetallics* 18: 2267-2274.

Kocherzhinskii Y. A., Yupko L. M and Shishkin E. A. 1980. "Equilibrium Diagram of the Nb-Si system." *Izv. Akad. Navk SSSR Met* (1): 206-211.

Kumar K.S. 1994. *Silicides: Science, Technology and Applications*. Vol. 2, in *Intermetallic Compounds (Principles and Practice)* , edited by J.H. Westerbrouk and R.L. Fleischer, 211-235. John Wiley & Sons Ltd.

Li.Z. 2012. *PhD Thesis*. University of Sheffield.

Liang. H, Chang Y.A. 1999. “Thermodynamic modeling of the Nb–Si–Ti ternary system .” *Intermetallics* 7 (5): 561-570.

Li Y, Li C.R , Du Z.M, Guo C.P, Zhao X.Q. 2013. “As-cast microstructures and solidification paths of the Nb–Si–Ti ternary alloys in Nb₅Si₃–Ti₅Si₃ region .” *Rare Metal* 32 (5): 502-511.

Liu S, Weitzer F, Schuster J.C, Krendelsberger N, and Du Y. 2008. “On the reaction scheme and liquidus surface in the ternary system Al-Si-Ti.” *Int.J. Mater. Res* (99(7)): 705-711.

Massalski T.B., Subramanian P.R., Okamoto H, Kacprzak L. 1990. “Binary alloy phase diagram.” *ASM International* (Materials Park) 3.

Mathieu S, Knittel S, François M, Portebois L, Mathieu S and Vilasi M. 2014. “Towards the improvement of the oxidation resistance of Nb-silicides in situ composites: A solid state diffusion approach .” *Corrosion Science* 79: 119–127.

Mathieu S, Knittel S, Berthod P, Mathieu S and Vilasi S. 2012. “On the oxidation mechanism of niobium-base in situ composites.” *Corrosion Science* 60: 181-192.

Marinder B. O, Magneli A. 1958. “ Rutile-Type Phase in Some Systems of Mixed Transition Metal Dioxides.” *Acta Chem. Stand.* (12) 1345.

McAdam G.D. 1964. "Substitutional Niobium Alloys for High Creep Strength ." *Journal of Inst.Met* 93: 59-64.

McCaughey C M. 2017. "The Solidification of Niobium Silicides for Next Generation Gas Turbine Engines." *PhD Thesis*. University of Sheffield.

Meier G.H. 1989. "A Review of Advances in High-temperature Corrosion ." *Materials Science and Engineering A120*: 1-11.

Meier G.H, Perkins R.A. 1990. "The Oxidation Behavior and Protection of Niobium." *JOM* 17-21.

Mitra R. 2006. "Mechanical Behaviour and Oxidation Resistance of Structural Silicides." *International Materials Reviews* 51: 13-64.

Murakami T., Sasaki S., Ichikawa K., Kitahara A. 2001a. "Microstructure, mechanical properties and oxidation behaviour of Nb-Si-Al and Nb-Si-N powder prepared by spark plasma sintering." *Intermetallics* 9 (7): 621-627.

Menon E.S.K, Parthasarathy T.A., Mendiratta M.G. 2004. "Microstructural Effects And Kinetics Of High Temperature Oxidation In Nb-Si Base Alloys ." *Metallic Materials With High Structural Efficiency* . Amsterdam: ©2004 Kluwer Academic Publishers Dordrecht . 315-326.

Menon E.S.K., Mendiratta M.G., Dimiduk D.M. 2001. "Oxidation behavior of complex niobium based alloys ." *Proceedings of the International Symposium Niobium 2001, Niobium science & technology : held in Orlando, Florida, USA, December 2-5, 2001*. Orlando, Florida: Bridgeville, Pa. : Niobium 2001 Ltd., ©2001-2002. 121–145.

Meier G.H., Pettit F.S. 1992. "High temperature oxidation and corrosion of intermetallic compounds." *Materials Science and Technology* 331-338.

Mendirata M.G., Lewandowski J. J, Dimiduk D.M. 1991. "Strength and Ductile-Phase toughening in the Two-Phase Nb/Nb₅Si₃ Alloys." *Metallurgical Transactions A* 22A: 1573-1583.

Murayama Y, Hanada S. 2002. "High Temperature Strength, Fracture Toughness And Oxidation Resistance Of Nb-Si-Ti-Al Multiphase Alloys." *Science And Technology Of Advanced Materials* 3: 145-156.

Nelson J. 2015. "Study Of The Effects Of Cr, Hf And Sn With Refractory Metal Additions On The Microstructure And Properties Of Nb-Silicide Based Alloys". *PhD Thesis*. University of Sheffield.

Ohnuma I, Fujita Y, Mitsui H, Ishikawa K, Kainuma R and Ishida. K. 2000. "Phase equilibria in the Ti-Al system." *Acta Matereritalia* 48: 3113-3123.

Papadimitriou. I, Utton. C, Tsakirooulos. P. 2017. *Unpublished research*. University of Sheffield.

Park J. S., Cho J, Hur B. Y., and Perepezko J. H. 2007. "Interface Reactions and Reaction Synthesis of a High Temperature Composite System." *Metals And Materials International* 13: 1-12.

Park J.S , Kim J.M. 2010. "Interface Reactions and Synthetic Reaction of Composite Systems." *Materials* 3: 264-295.

Pint B.A., Distefano J.R., Wright I.G. 2006. "Oxidation resistance: One barrier to moving beyond Ni-base superalloys." *Materials Science and Engineering (A 415)*: 255-263.

Pan V. M., Latysheva V.L., Kulik O. G., Popov A. G. , Litvinenko E. N., 1984. "The Nb-Nb₃Al-Nb₅Si₃ phase diagram ." *Russ Metall.*, 4: 233-235.

Perepezko J.H. 2009. "The hotter the engine, The better." *Science*. vol 326: 1068-1069.

Perrot. P. 2006. *Al-Si-Ti (Aluminium - Silicon - Titanium)*. Vol. 114A, in *Light Metal Systems. Part 4, Light Metal Ternary Systems: Phase Diagrams, Crystallographic and Thermodynamic Data Author: Effenberg, G. ed., by MSIT Materials Science International Team, edited by S. Ilyenko G. Effenberg, 1-15. Springer-Verlag Berlin Heidelberg : Materials Science International Team MSIT®.*

Raghavan V. 2009. "Al-Si-Ti (Aluminium-Silicon-Titanium) ." *Journal of phase equilibria and diffusion* 30 (1): 82-83.

Raghavan V. 2005. "Al-Ti (Aluminium-Titanium)." *Journal of phase equilibria and Diffusion* 26 (2): 171-172.

Raman A., and Schubert K. 1965. "The Constitution of Some Alloy Series Related to $TiAl_3$. II. Investigations in Some Ti-Al-Si Systems. " *Z. Metallkd* 56(1): 44-52.

Ravichandran K.s. 1992. "A survey of toughness in ductile phase composites" *Scripta Metallurgica et Materialia* 26: 1389-1393.

Roth R.S, Coughanour L.W. 1955. "Phase Equilibrium Relations in the Systems Titania-Niobia and Zirconia-Niobia". *J. Res. Nat. Bur. Stand.* (55) 209.

Raghavan V. 2006. "Al-Nb-Si (Aluminum-Niobium-Silicon)." *Journal of Phase Equilibria and Diffusion* 27: 163-165.

Rahmel A, Spencer P. 1991. "Thermodynamic Aspects of $TiAl$ and $TiSi_2$ Oxidation: The Al-Ti-O and Si-Ti-O Phase Diagrams." *Oxidation of Metals* 35: 53-68.

Schafer H, Bergner D, Gruehn R, Anorg Z. 1969. The thermodynamic stability of the seven phases existing between (NbO_2 and $NbO_{2.5}$). *Allgemeine Chemie* (31) 365.

Sekido N, Kimura Y, Miura S and Mishima Y. 2004. "Solidification Process and Mechanical Behavior of the Nb/ Nb_5Si_3 Two Phase Alloys in the Nb-Ti-Si System ." *Materials Transactions* 45: 3264-3271.

Schlesinger M.E., Okamoto H., Gokhale A.B, Abbaschian R. 1993. "The Nb-Si(Niobium-Silicon) System." *Journal of phase equilibria* 14 (4): 502-509.

Schob O, Nowotny H, Benesovsky F. 1962. "The Ternary Systems Formed by Ti, Zr and Hf with Al and Si" (in German), *Planseeber, Pulvermetall* 10: 65-71 (Equi. Diagram, Experimental, 26)

Sheasby J. S, Cox B. 1968. "Oxygen Diffusion In Alpha-Niobium Pentoxide" *J. Less-Common Metals* 15: 129-135.

Subramanian P. R., Parthasarathy T. A., Menediratta M.G and Dimiduk D.M. 1995. "Compressive creep behavior of Nb₅Si₃." *Scripta Metall. et Mater* 32 (8): 1227-1232.

Subramanian P.R., Mendiratta M.G., Dimiduk D.M. 1996. "The development of Nb-based Advanced intermetallic alloys for structural applications." *Journal of Metals* 48 (1): 33-38.

Subramanian P.R., Mendiratta M.G., Dimiduk D.M, Stucke M.A. 1997. "Advanced intermetallic alloys-beyond gamma titanium aluminides." *Materials science and engineering A* 13 (1): 239-240.

Subramanian P.R., Mendiratta M.G , Dimiduk D. M. 1994. "Microstructures and Mechanical behaviour of Nb-Ti Base Beta + Silicide alloys." *Mat, Res, Soc, Symp. Proc.* 491-502.

Tian Y.X, Guo J.T, Zhou L.Z, Cheng G.M and Ye H.Q. 2008. "Microstructure and room temperature fracture toughness of cast Nbss/silicides composites alloyed with Hf." *Materials Letters* 26 (17-18): 2567-2660.

Taub A.I., Fleischer R.L. 1989. "Intermetallic compounds for high temperature structural use." *Science* 243: 616-621.

Thandorn T. 2009. " Experimental Study Of The Effect Of B Additions On Phase Equilibria And Properties Of Nb Silicide Based Alloys". *PhD Thesis*. University of Sheffield.

Tsakiropoulos P. 2014. "On the Macrosegregation of Silicon in Niobium Silicide Based Alloys." *Intermetallics* 55: 95-101.

Tsakiropoulos. P, Zelenitsas. K and Vellios. N. 2011. "Study of the effect of Al, Cr and Sn additions on the microstructure and properties of Nb silicide based alloys ." *Mater. Res. Soc. Symp. Proc.* Cambridge University Press. 367-372.

Tsakiropoulos P. 2001. "Beyond Nickel-Based superalloys." In *Encyclopedia of Aerospace engineering*, edited by Richard Blockley and Wei Shyy. John Wiley & Sons.

Tsakiropoulos. P. 2016. *private communication*. University of Sheffield.

Tweddle A. 2015. “Study of the effect of Ge and Y additions on the microstructure, phase stability and environmental degradation of Nb silicide alloys”. *PhD Thesis*. University of Sheffield.

Vazquez A and Varma S.K. 2011. “High-temperature oxidation of Nb-Si-Cr alloys with Hf additions.” *Journal Of Alloys And Compounds* (509): 7027-7033.

Van Heerden D, Weihs T. P, Subramanian P. R, Foecke T, Gavens A. J. 2001. “The stability of Nb/Nb₅Si₃ microlaminates at high temperatures.” *Metallurgical and Materials Transactions A* 32 (9): 2363–2371.

Von Dreele R.B, Cheetham A.K.1974. “The structures of some titanium-niobium oxides by powder neutron diffraction”. *Proc. Roy. Soc. London Sect. A* (338) 311.

Voglewede B, Victoria Rangel R, Varma S.K. 2012. “The effects of uncommon silicides on the oxidation behaviour of alloys from the Nb-Cr-Si system.” *Corrosion Science* 123-133.

Wadsley A. D. (1961a) . Mixed Oxides of Titanium and Niobium I. *Acta Cryst* (14) 660.

Wadsley A. D. (1961b). “Mixed Oxides of Titanium and Niobium. II. The Crystal Structures of the Dimorphic Forms of Ti₂Nb₁₀O₂₉”. *Acta Cryst* (14) 664.

Yang Y, Bewlay B.P and Chang Y.A. 2007. "Liquid-Solid Phase Equilibria in Metal-Rich Nb-Ti-Hf-Si Alloys." *Journal of Phase Equilibria and Diffusion* 28 (1): 107-114.

Yang Y, Bewlay B.P , Chang Y.A. 2007. "Thermodynamic modeling of the Hf-Ti-Si Ternary System." *Intermetallics* 15: 168-176.

Zelenitsas. K, Tsakirooulos. P. 2006. "Effect of Al, Cr and Ta additions on the oxidation behaviour of Nb-Ti-Si in situ composites at 800 °C ." *Materials Science and Engineering A* 416: 269-280.

Zelenitsas. K, Tsakirooulos. P. 2005. "Study of the role of Al and Cr additions in the microstructure of Nb-Ti-Si in situ composites." *Intermetallics* 13: 1079-1095.

Zelenitsas. K, Tsakirooulos. P. 2006. "Study of the role of Ta and Cr additions in the microstructure of Nb-Ti-Si-Al in situ composites." *Intermetallics* 14: 639-659.

Zhao J.C, Bewlay B.P and Jackson M.R. 2001. "Determination of Nb-Hf-Si phase equilibria." *Intermetallics* 9: 681-689.

Zhao J.c, Jackson M. R, Peluso L.A.,. 2004. "Mapping diffusion of the Nb-Ti-Si phase diagram using diffusion multiples." *Materials science and engineering A* 372: 21-27.

Zhao J.C, Peluso L.A., Jackson M.R, Tan L. 2003b. "Phase diagram of the Nb-Al-Si ternary system." *Journal of alloys and compounds*, 360: 183-188.

Zheng N, Fischer W, Gruebmeier H, Shemet V and Quadackers W.J. 1995. "The Significance Of Sub-Surface Depletion Layer Composition For The Oxidation Behavior Of γ -Titanium Aluminides." *Scripta Metallurgica et Materialia* 33: 47-53.